UNIVERSITÀ DEGLI STUDI DI PARMA
Dottorato di ricerca in Fisica
Ciclo XXIX

Gravitational-wave signal from binary neutron star merger simulations with different equation of state and mass ratio

Coordinatore:
Chiar.mo Prof. Cristiano Viappiani

Tutor:
Chiar.mo Prof. Roberto De Pietri

Dottorando: Francesco Maione

To Rosa

Abstract

This work is focused on the determination of the gravitational-waves signal emitted by binary neutron stars when they finally merge to form either a Black Hole or a remnant neutron star that will, likely, eventually also collapse to Black Hole. This research is based on the use of general relativistic numerical simulations that are the only tool available to study the evolution of a binary neutron star system through its coalescent, merger and post-merger phase.

In particular, the gravitational signal emitted by different initial binary neutron star configurations has been analysed, evaluating the effects on the signal due to the total mass, the mass ratio, the equation of state and the initial stellar separation. The research focused on the post-merger phase, were analytical descriptions of the GW signal are still absent, both in the case when a (hyper)massive neutron star or a black hole surrounded by an accretion disk is formed. The gravitational waves phase evolution, the radiated energy and angular momentum and the post-merger gravitational waves spectrum have been determined. In particular, in the case of the post-merger gravitational signal, various possible interpretation of its spectral features have been analysed performing a close comparison with the recent literature.

Emphasis has been given to analysing some sources of systematic errors, such as the initial data, the orbital eccentricity, the finite-resolution errors in the time evolution determined by the choice of different numerical methods, and the gravitational waves extraction methodology. For the latter, several data analysis techniques were developed, applied and extensively tested on the simulation data.

The main interest for this research topic comes from the fact that binary neutron star mergers are the main target for Earth-based gravitational waves interferometric detectors, after the recent first detection of a gravitational signal from binary black hole mergers. They are characterized by a rich phenomenology, which includes microphysical effects and electromagnetic emissions. In particular, the most interesting challenge is to constraint the equation of state of the nuclear matter inside the neutron star core, which is still unknown from a theoretical point of view. In order to recognize a GW signal inside the detectors noise and perform source parameters estimation from it, the comparison with theoretical models coming from numerical simulations is a necessary and essential tool.

This work has a central point on the study of binary neutron star simulations with public codes, in particular the `The Einstein Toolkit` and the `LORENE` library. All the code enhancements for the binary initial data and evolution, the parameter files, and the post-processing scripts developed for this work have been made publicly available, making all the results presented here reproducible, following the simple instructions described in the appendix.

Contents

Chapter 1

Introduction

After the recent first direct detections of gravitational waves (GW) from binary black-hole mergers by the Advanced LIGO interferometers [1, 2], the era of gravitational wave astronomy has begun. Now we have a new channel to look (or, with a better analogy, to listen) to the sky, studying high energy astrophysics and testing gravity in the strong field regime.

Besides binary black holes (BBH), the next target for direct GW detection are binary neutron star (BNS) mergers. When all three LIGO/Virgo interferometers will be active at design sensitivity, a range of 0.2-200 BNS mergers detections per year is predicted [3]. At least ten binary neutron star systems have been already detected in our galaxy, with observations of pulsars orbiting in a binary system with a companion in the mass range for being a neutron star (see sec. 2.1.2 for details) [4, 5]. Among them, the Hulse-Taylor pulsar (B1916+13) gave the first indirect proof of gravitational waves existence, for which the 1993 Nobel prize was awarded [6–8].

Binary neutron star mergers have a particularly rich and interesting phenomenology, compared with BBH, for the presence of matter and, hence, the possibility of electromagnetic and microphysical effects. The (still unknown) equation of state for the matter inside the neutron star core, at densities higher than the nucear equilibrium one, will leave imprints on the BNS system evolution and on its emitted gravitational wave signal [9–14]. Therefore, BNS mergers can be used as an astrophysical laboratory to investigate the properties of nuclear matter in extreme conditions. Several electromagnetic counterparts can also be present in a BNS merger, since most neutron stars have a strong magnetic field (see sec. 2.3). BNS mergers are believed to be the central engines for short gamma ray bursts [15–18], even if the exact mechanism for their emission is still investigated with astrophysical modelling and numerical simulations [19–28]. Other EM emissions, both in the coalescent phase (before the merger, from the interaction of the stars magnetosphere [29, 30]), and in the post-merger phase (such as fast radio bursts [31, 32], or dipolar spin-down emissions [33, 34]) have also been predicted. Another peculiar signal expected from BNS mergers is the so called *macronova* (sometimes called kilonova), an EM emission coming from the radioactive decay of elements produced via nuclear r-process in the matter ejected during and after the merger [35–37]. All these EM counterparts could be used to complement information from GW detections, trying to recover the source parameters.

In order to detect a GW signal from a BNS merger inside the detector noise, and to perform parameter estimation from it, a bank of templates of the predicted GW signal from merging neutron stars with different, plausible, characteristics (total mass, EOS, mass ratio, spin, eccentricity) is needed [38]. For the pre-merger coalescent phase, analytical techniques to compute the GW signal,

based on post-newtonian approximations, have been developed, and, recently, they also included tidal effects, which distinguish the BNS to the BBH coalescence and contain an imprint from the neutron star EOS. Among them, the Effective One Body model [39–42] has been particularly successful. Three different research groups developed so far EOB codes which includes also tidal effects contributions [11, 43–47]. In particular, lately, also dynamical tidal effects were considered, coming from the interaction between the tidal field and the stars quasi-normal modes of oscillation [47, 48]. To study the merger and post-merger phases, instead, full three dimensional general relativistic numerical simulations are the only available tool. Numerical relativity is still also important for the study of the coalescent phase, since the EOB models must be calibrated to numerical relativity simulations, in order to account for the unknown post-Newtonian coefficients.

Numerical simulations involving the solution of Einstein's equations became viable after the crucial breakthroughs of 2005 [49–51]. Nowadays, simulations of BNS mergers are performed by different groups in the world. The advancements in this field of research have highly benefited from the realization of public numerical relativity codes, such as the `LORENE` library [52, 53], `The Einstein Toolkit` [54], and LIGO's `LAL` library, which were used in this thesis, respectively, for generating the initial data, evolving the BNS systems in time, and part of the data analysis in post-processing. Public, open source, scientific codes are a key to scientific progress, since they guarantee the reproducibility of simulation results, and they reduce efforts replications in different research groups. For these reasons, all my thesis work is based uniquely on adopting already existing public community codes, to which I contributed with small enhancements where needed for my project, or writing new data analysis codes which were made publicly available by the Parma University Gravity research group (see appendix C).

Current active research topics in numerical BNS simulations include the computation and evolution of a richer variety of initial configurations, like spinning stars [55–58], eccentric binaries [58, 59], parabolic encounters and dynamical captures [56, 60, 61] and unequal mass systems [62–68]. The latter are particularly interesting, since we know for sure that unequal mass systems exist in nature, having recently detected one with a large mass asymmetry in our galaxy [4], while highly spinning neutron stars in binaries or eccentric orbits are not expected in most cases, when the stars will be close enough to enter in the Earth GW detectors frequency band, except rarer or more difficult to detect events, like the merger of BNS systems in globular clusters, which could have eccentric orbits due to the interaction with the dense surroundings, or stars with a low rotational period and a week magnetic spin-down, which will leave a dynamically relevant spin even close to the merger.

Another very active direction, which will not be explored in this work, is to include in the simulations a progressively richer microphysical phenomenology, with finite-temperature tabulated nuclear equations of state and neutrino emission and absorption [57, 69–73], which can change some of the properties of the evolution of the post-merger remnant, either a (hyper)massive neutron star [74], or a black hole surrounded by an accretion disk. Finally, another very important characteristic to model is the stars magnetic field evolution. Different numerical techniques have been developed to ensure the conservation of the magnetic field zero divergence constraint, both in ideal [71, 75–85] and resistive MHD [29, 86–88]. However, magnetized BNS mergers simulations are still in their infancy, since there are difficulties in interpreting their results, in particular due to magnetic instabilities which cannot be fully resolved with the currently available codes and computational resources (see ref. [26, 89] and sec. 2.3.1). For this reason, as a preliminary stage in my research program, in this thesis I focused only on non-magnetized BNS mergers.

Despite all that progress, there are still some uncertainties in BNS simulations results. An accurate evaluation of all the possible systematic error sources, and the development of new numerical and data analysis techniques to reduce those errors is fundamental, in order to be able to compare simulation results with GW observation, or with analytical models, retaining the ability to distinguish the gravitational signal from different sources, for example, to be able to measure EOS-related effects, like tidal deformations in the final part of the pre-merger phase [90, 91].

The initial configurations (computed assuming some approximations about symmetries and the gravitational potential, see sec. 3.3) are one possible source of error, which, however, has started to be investigated as such only very recently, looking at the validity of some approximations [92], comparing simulations with initial data computed by different codes [93], or comparing simulations of the same model with different initial separation between the stars (see sec. 4.1.2 and ref. [94]). In particular, one important error for which is responsible the initial data computation procedure, is the presence of a small but not negligible eccentricity in the evolved orbits (see sec. 4.1.1). This effect is one of the most important problems to overcome in order to get accurate waveforms for numerical simulations. Some solutions to obtain low eccentricity initial data have been implemented recently [58, 95], but they are not yet publicly available.

Another important possible source of error is the technique used to extract gravitational waves from the numerical simulation data. In general, in BNS simulations, GW extraction errors are much lower than the evolution code finite-resolution errors (see sec. 3.4 and ref. [94]), but only if some care is taken in the extraction algorithms.

Finally, the errors linked to the finite grid resolution of the evolution code need of course to be measured and kept under control. However, there is not yet a consensus in the literature about which is the best way to measure the code convergence properties, or to extrapolate, from simulations at different resolutions, results in the *infinite resolution* limit [96–98] (see appendix A.1 for details). Nevertheless, it is important to test the code convergence and to identify the convergence properties of different numerical methods, in order to be able to choose which are the most appropriate ones, in the different resolution ranges. The convergence analysis should be done looking at different observables, in order to select the best resolution for performing simulations targeted at studying different effects. More details on this point can be found in appendix A.1.

This thesis has the following organization: the first chapter is an introduction to the neutron stars physics and the astrophysical knowledge we have about binary neutron stars systems. The second chapter is a review of state-of-the-art numerical methods for solving Einstein's equations coupled with general relativistic hydrodynamics, as implemented in `The Einstein Toolkit`. The chapter is closed by a discussion on gravitational wave extraction techniques and the improvement I have tested in that area, for the most part already presented in ref. [94]. The third chapter contains an analysis of the results one can obtain from BNS simulations, with examples taken from the Parma Gravity group simulations, presented in ref. [68, 94, 99]. The pre-merger stage is investigated looking, in particular, at some error sources present in numerical simulations, like the orbital eccentricity (sec. 4.1.1) and the effect of the initial stars separation (sec. 4.1.2). A closer attention is devoted to the post-merger phase, where numerical relativity is the only available investigation tool. For the models which form an hyper-massive neutron star after the merger, the impact of different source parameters on the post-merger spectrum and radiated energy is analysed (sec. 4.2.1), including the role of the EOS, which one hopes to be able to constraint by looking at the post-merger spectrum of future detected signals from BNS mergers. Extensive comparisons with the existing literature are made, using different data analysis techniques, such as Fourier spectrograms and Prony's method.

Finally, models collapsing to black hole during the simulation time are also investigated (sec. 4.2.4). This work is completed by three appendices, about code convergence, the initial parameters of the presented simulations, and a short guide on how to perform numerical simulations of BNS mergers with public codes.

All computations have been done in geometrical units (hereafter denoted as CU) in which $c = G = M_\odot = 1$. Results are reported in cgs units, except where explicitly otherwise stated. CU are also used to denote resolutions, e.g., $dx = 0.25$ CU, and there they mean the resolution on the finest grid at initial time (which for most cases is the same for the entire evolution). Masses are reported in terms of the solar mass $M_\odot$. Finally, one should note that, as is usual in most of the work on this subject, matter is described using the variable ρ (baryon mass density), ϵ (specific internal energy) and p, instead of, as usually used in Astrophysics, $\overline{\rho}$ (energy density), $\overline{n}$ (baryon number density) and p. Their relation is the following: $\overline{\rho} = e = \rho(1 + \epsilon)$ and $\overline{n} = \rho/m_B$ (m_B is the baryon mass). In all the mathematical expressions in the remaining of this manuscript Greek indexes are used for specetime variables, and run from 0 to 3, and Latin indexes are used, instead, for space only variables, and run from 1 to 3.

Chapter 2

Physical background: neutron stars and gravitational waves

2.1 Neutron stars

With the term "Neutron star" (NS) we intend nowadays a compact star with a mass approximately between 1 and $3M_{\odot}$, a radius in the range $9-15$ km and a central density which is 3 to 10 times the nuclear equilibrium density $n_0 = 0.16\,\mathrm{fm}^{-3}$ [100], in which the gravitational pressure cannot be compensated by the electrons fermi gas pressure, like in a white dwarf, but is, instead, equilibrated by the strong nuclear interactions. A neutron star interior is neutron-rich, although, despite the name, a fraction of protons is still present (and a corresponding fraction of electrons and/or muons to neutralize the matter), and more complex nuclei can be found in the external layer, called "crust", as well other states like mesons, hyperons [101], and even deconfined quarks [102] could appear in the inner core, at densities above n_0 (see next subsection for more details).
Neutron stars are among the most dense objects in the universe. The matter is held together by a strong gravitational field, for witch a correct treatment of general relativistic effects is important: for a typical neutron star with mass $1.4\,\mathrm{M}_{\odot}$ and radius 10 km, the radius is only 2.4 times the Schwarzschild radius of a non-rotating black hole with the same mass. This gravitational field cannot be compensated only by the Fermi pressure of a free Neutron gas, as already demonstrated by Oppenheimer and Volkov and independently by Tolman in 1939 [103, 104], because it will lead to a neutron star maximum mass of $0.7\,\mathrm{M}_{\odot}$. The pressure to sustain the star against gravitational collapse is given, instead, by repulsive nuclear forces [105].

Neutron stars are born from the collapse of massive stars at the end of their life cycle, when the gravitational force cannot be sustained anymore by the internal pressure due to the thermonuclear reactions fuelling the star [106]. When the inner density of the star reaches the nuclear equilibrium density n_0, the stellar matter bounces back, producing a shock wave generated at the outer layer of the inner stellar core. The inner core, in this first phase, is hot, optically thick for neutrinos and lepton-rich. It is still not clear which is the mechanism responsible for the reviving of the shock front, which first halts at around $100-200$km from the star center, in order to have a successful supernova explosion. The main candidates are neutrinos emitted in the core and then reabsorbed in the stellar medium [107–109] or magnetic instabilities redistributing angular momentum and developing turbulence [110, 111]. If the shock front gets revived, the stellar envelop is stripped from its center, leaving behind a proto-neutron star. In the first $\simeq 10$ ms it undergoes a highly

dynamical phase dominated by turbulence and hydrodynamical instabilities, during which energy and angular momentum are emitted, mainly by neutrino radiation. During this first phase, stellar oscillation modes can be excited, and they will be responsible for the emission of gravitational waves [112–115]. The neutrino emission is linked with electron captures, which deleptonize the star, leaving it neutron-rich. In the following phase, called the "Kelvin-Helmholtz" phase, the proto neutron star evolves in a quasi-stationary manner, cooling down, shrinking, slowing down its rotation rate, and becoming transparent to neutrinos [116, 117]. During the collapse, the magnetic field of the progenitor star increases by several orders of magnitude, mainly due to flux conservation, but also due to the winding linked with the star differential rotation. In regular neutron stars the magnetic filed reaches values around $10^8 - 10^{12}$ Gauss. A special class of neutron stars, called "magnetars", have magnetic fields up to 10^{15} Gauss. The magnetar formation process is still unknown, but is believed to be linked with magnetic instabilities which develop in the protoneutron star after the stellar bounce [111].

Due to their external dipolar magnetic field, which could be misaligned with the rotation axis, several neutron stars can be observed as pulsars, emitting regular, pulsated electromagnetic signals in the radio band [118, 119] (but, in some cases, also in X-rays and even gamma-rays [120, 121]). This pulses are due to the electromagnetic radiation emitted by charged particles accelerated along magnetic field lines. Each pulse is visible when the star magnetic axis (and then its radiation beam) crosses the observer's line of sight, therefore the pulsation period is equal to the neutron star rotation period. The first experimental discovery of a neutron star happened in 1968 in the Mullard Radio Astronomy Observatory [122].

In order to compute the equilibrium configuration for a non-rotating neutron star, one has to solve the Tolman-Oppenheimer-Volkov (TOV) equations, which, in the simplified modelling of the star as a barotropic fluid (valid for a cold neutron star, which has already cooled down after the progenitor collapse), are:

$$\frac{dP}{dr} = \left(\rho\left(1+\epsilon\right)+p\right)\frac{m+4\pi r^3 p}{r\left(r-2m\right)}, \tag{2.1}$$

$$\frac{dm(r)}{dr} = 4\pi\rho\left(1+\epsilon\right)r^2. \tag{2.2}$$

Where all variables are functions of the single independent variable r (because of spherical symmetry). This system must be closed by a prescription for the (barotropic) equation of state of the matter, in the form $P = P(\rho)$.

An important information which can be gathered from solving the TOV equation is the mass-radius relationship for a cold neutron star given a particular EOS model. This can help confronting different proposals for the neutron star EOS with experimental data. In order to do so, it is important to be able to measure the masses and the radii of observed neutron stars [5]. The masses can be measured from pulsars in binary systems, for which the orbital parameters are determined by pulsar timing and accounting for the Doppler effect [123]. From those Keplerian parameters, it is possible to construct a mass function:

$$f \;=\; \frac{\left(M_c \sin i\right)^3}{M_T^2} \;=\; \left(\frac{2\pi}{P_b}\right)^2 \left(a \sin i\right)^3, \tag{2.3}$$

where $M_T = M_p + M_c$ is the total mass of the system, M_p is the pulsar mass and M_c is the companion mass, P_b is the orbital period, a is the semimajor axis and i is the inclination angle between the orbital angular momentum of the system and the line of sight.

The mass function has 3 unknowns (the two star masses and the angle i), therefore two more equations are needed for deriving the mass values. These come from the so called "post-Keplerian" (PK) parameters, which measure relativistic corrections to the Keplerian orbit of the binary. The five PK parameter used in practice are:

1. The periastron rate of advance $\dot{\omega}$, analogous to the perihelion advance of Mercury's orbit, it can be measured precisely in highly eccentric systems after a long observation period. From its measurement the total mass of the system can be constrained:

$$\dot{\omega} \;=\; 3\left(\frac{P_b}{2\pi}\right)^{-5/3} M_T^{2/3}\left(1-e^2\right)^{-1} \tag{2.4}$$

2. The Einstein delay γ, due to the gravitational redshift and the time dilation effect present in eccentric orbits. It also requires high eccentricities and long time observations for a precise measurement.

$$\gamma \;=\; e\left(\frac{P_b}{2\pi}\right)^{1/3} M_T^{-4/3} M_c\left(M_p + 2M_c\right) \tag{2.5}$$

3. The orbital period derivative $\dot{P}_b$, which is negative due to the energy and angular momentum emission in gravitational waves. It is measurable in double neutron star systems only, after years of observations.

4. The range r and the shape s of Shapiro delay [124], which is the delay of the pulsar signal due to its passage into the spacetime curved by the gravitational field of the companion star. The Shapiro delay measures of NS masses are the most accurate one to date, including for example PSR J1614—2230 [125], which was the first observed neutron star with a mass close to $2\,\mathrm{M}_\odot$. The Shapiro delay parameters are easier to measure for systems with a massive companion and with a high inclination angle.

$$r = M_c \qquad\qquad s = a\sin i\left(\frac{P_b}{2\pi}\right)^{-2/3} M_T^{2/3} M_c^{-1}. \tag{2.6}$$

I want to remark that the relationship between the star masses and post-Keplerian parameters is dependent upon the choice of an underlying theory of gravity (which, in the case of the formulas written before, is General Relativity). This means that those mass measurements cannot be used as a test of GR, but instead assume its validity, even in the strong-filed regime of the neutron stars interior.

The neutron star radii, instead, are more difficult to measure directly. The current most common technique is based on spectroscopic measurements of the neutron stars angular size, based on their flux of surface thermal emission [5, 126, 127]. These observations are complicated by the need for a general relativistic treatment (neutrons stars lense their own surface emission [128]), the presence of non-thermal magnetosphere emissions, which are very difficult to model, and the difficulty to measure the NS distance. A preferred laboratory for radius measurements are quiescent low-mass X-ray binaries (qLMXRB), in which, during the quiescent phase, the mass accretion from the companion to the pulsar ceases, reducing the non-thermal emission background [129]. Another interesting technique is to measure photospheric radius expansion events due to X-ray thermonuclear bursts [130]. A third, frequently used, analysis to infer the NS radius is to model

the periodic oscillations in the pulse profile originated by temperature anisotropies on the surface of rotating neutron stars [131, 132]. These oscillations depend of the characteristics of the NS spacetime, hence on its mass and radius, which can be determined, given a theoretical model for the temperature profile on the stellar surface and the radiation beaming.

Different radial measurements have been obtained with these techniques, constraining the NS equation of state in different subregions of the M-R diagram (for example, radial measures from qLMXRB point to the presence of very compact stars with a radius around 9.5 km for a standard mass of $1.4\,M_\odot$ [133, 134], while other analysis from pulse X-ray spectroscopy point to stars with larger radii, 14 km for stars with a mass around $1.5-1.8 M_\odot$). The problem is that all those techniques are highly depending on the surface emission and NS atmosphere modeling, which is still an active field of research. Forthcoming results in X-ray spectroscopy from missions like Athena [135], NICER [136] and LOFT [137] should increase the precision in radius direct measurements.

Indirect measure of the NS radii can be obtained analysing the gravitational wave emission from binary neutron star coalescence, merger, and their post merger remnant (if there is not a prompt collapse to black hole). Most of this Ph.D. thesis is devoted to prepare the needed gravitational signal theoretical modelling for succeeding in that task. See sections 4.1 and 4.2.1 for more details.

2.1.1 The neutron stars equation of state

The equation of state of the nuclear matter inside neutron stars cores is still largely unknown. The extreme conditions present there (in terms of density, pressure, gravitational potential) can not be reproduced in experiments on Earth, and it is not possible to perform theoretical finite-density QCD calculations in that parameter region just from first principles [138, 139].

As a first approximation, we are interested in the equation of state of cold nuclear matter in beta equilibrium, which is suitable to represent neutron stars when they have cooled down from the protoneutron star phase (this is also the physical condition of neutron stars at the beginning of merger simulations, and during all the coalescent phase). Different techniques have been developed to compute EOS models. I will briefly illustrate, as an example, the ones used to develop the four EOSs that were employed in the simulations whose results will be analysed in chapter 4.

The equation of state model should be able to describe the nuclear matter in a large density region, from the neutron star crust, where $\rho < \rho_0$ (with ρ_0 the nuclear equilibrium density) and the matter is composed only by the ordinary constituents, namely neutrons, protons, electrons, and simple atomic nuclei, up to the highest densities in the liquid inner core, where, for $\rho > 4\rho_0$, neutrons overlap and new non-nucleonic degrees of freedom can be present, such as hyperons, mesons condensates or deconfined quarks. Unfortunately, even for the crust case, calculation of an exact EOS staring from the bare two and three nucleon interactions experimentally measured in vacuum are not feasible, due to the complexity of the many-body problem concerning heavy nuclei immersed in a neutron gas, as happens in the NS crust. For this reason, one common technique is to use an effective nuclear hamiltonian in a mean-field scheme, containing effective two and three nucleon interactions. These effective nuclear interactions usually have a large number of free parameters, fixed by fitting atomic nuclei properties measurements and the results of nucleon-nucleon scattering experiments, and then extrapolated to higher densities and nuclear matter asymmetries. In order to avoid problems linked with those extrapolations, the first EOS models we used, the **SLy** EOS [140, 141], based on the Skyrme-Lyon nucleon-nucleon effective interaction, modifies the nuclear forces to take into account also the results of microscopic calculations for pure neutron matter, and also more recent experimental results on neutron-rich nuclei. In particular, it requires the consistency

with the UV14+VII EOS of neutron matter in the range $n_0 < n < 1.5\ fm^{-3}$ and uses a general procedure for fitting the properties of doubly magic nuclei. The SLy EOS is widely accepted as the right modelling for the NS crust, which is described using the Compressible Liquid Drop Model, and for this reason all of our stellar models use the same parametrized version of SLy for describing the low density matter, but the matching point between the SLy crust and the core EOS changes for every high density EOS model. One big advantage of using the SLy EOS also for the high density matter is that it allows to be consistent employing the same effective nuclear interaction at all regimes, instead of having different approximated approaches in different regions of the star.

A similar EOS is the **APR4** model [142], also based on an effective Hamiltonian approach, expanding it in one, two, three, ..., many body contributions, using a variational chain summation method. The nucleon-nucleon interaction is based on the Argonne v_{18} potential, but relativistic boost corrections and three nuclear interactions are also included in the computed Hamiltonian.

A different approach, instead, is followed by the other two EOS models that were used in the simulations of [94, 99], the **H4** EOS [101] and the **MS1** EOS [143]. They are based on a relativistic mean field framework, in which the strong nuclear interactions are modelled as a meson exchange (scalar σ, vector ω and isovector ρ) between nucleons. The starting point is the construction of an effective lagrangian containing free-particle terms for each particle considered (nucleons, electrons, mesons), plus meson-baryon interaction terms and pertubative meson self-interactions. In this approach, too, free interaction parameters are fixed in order to reproduce the results of low-energy terrestrial experiments. However, some parameters remain unsufficently constrained, but can be further selected confronting the resulting neutron star models with observations, such as the neutron star maximum mass lower limit.

The H4 EOS [101] includes also hyperons, which in that model start to be produced at densities higher than $2\rho_0$. The most relevant hyperons are Λ and Σ_-, because they have the lowest masses and so are more easily produced. In this model new parameters are present, such as the ones controlling the meson-hyperon interactions. Some of them are fixed from the properties of lambda hypernuclei, while others, in particular the coupling constant between σ mesons and hyperons, remain free to construct different EOSs models. In the H4 EOS these parameters are fixed in order to have the stiffest possible EOS sill consistent with the maximum neutron star mass and observed gravitational redshift of photons leaving a NS surface.

It is common, in binary neutron star merger simulations, to parametrize the EOS as a piecewise polytrope, following the work of [144]. This was also done in the Parma gravity group simulations, analysed in chapter 4 and ref. [68, 94, 99]. We used seven polytropic pieces, each corresponding to a different density interval. The four lower density pieces are the same for each EOS and come from the fitting of the crust and low density matter modelled with the SLy EOS [140]. They represent, in increasing density order, a non-relativistic electron gas, a relativistic electron gas, the neutron drip regime, and the NS inner crust in the density interval between neutron drip and the nuclear saturation density. The three high density pieces, instead, are different for each NS core EOS model. In each density interval $[\rho_i, \rho_{i+1}]$, the pressure P and specific energy density ϵ of a cold neutron star in beta equilibrium are given by:

$$P_{cold} = K_i \rho^{\Gamma_i} \tag{2.7}$$

$$\epsilon_{cold} = \epsilon_i + \frac{K_i}{\Gamma_i - 1} \rho^{\Gamma_i - 1} \tag{2.8}$$

The coefficients K_i and Γ_i and the separation densities ρ_i are reported in table 2.1 for the four low density pieces and in table 2.2 for the three high density pieces. The coefficients K_i can be fixed

i	$\rho_i[g/cm^3]$	K_i	Γ_i
0	-	6.801×10^{-11}	1.584
1	2.440×10^{7}	1.062×10^{-6}	1.287
2	3.784×10^{11}	5.327×10^{1}	0.622
3	2.628×10^{12}	3.999×10^{-8}	1.357

Table 2.1: Parameters of the low density piecewise polytropic EOS. ρ_i and K_i are expressed in cgs units. Note that the units of K_i depend on the corresponding values of Γ_i, so they are not directly comparable in magnitude.

EOS	Γ_4	Γ_5	Γ_6	$\rho_4[g/cm^3]$
APR4	2.830	3.445	3.348	1.512×10^{14}
SLy	3.005	2.988	2.851	1.462×10^{14}
H4	2.909	2.246	2.144	0.888×10^{14}
MS1	3.224	3.033	1.325	0.942×10^{14}

Table 2.2: Parameters of the high density EOS, parametrized as picewise polytrope, for the four different models analysed in this thesis, in increasing order of stiffness. Γ_4 and K_4 are the coefficients for the polytropic piece between the reported ρ_4 and $\rho_5 = 10^{14.7} g/cm^3$. Γ_5 and K_5 are, instead, the coefficients of the polytrope valid between ρ_5 and $\rho_6 = 10^{15} g/cm^3$.

given only K_0 and imposing the continuity of the pressure. Similarly, the coefficients ϵ_i are fixed to impose the continuity of the specific energy density, with $\epsilon_0 = 0$. The density threshold between the crust EOS and the inner core EOS (ρ_4) is different for each EOS model, and is selected, again, to impose continuity between the common low density EOS and the specific high density one. Its values are reported in table 2.2 too.

In fig. 2.1a are displayed the mass-radius relationships for a non-rotating neutron star with the four EOS mentioned before. It can be seen that all four EOS are consistent with the maximum mass limit of 2.01 $M_\odot$ imposed by the observation of PSR J0348+0432 [125]. The relativistic mean field EOSs are stiffer and lead to larger NS radii respect to the effective n-body nuclear interaction methods. Those four chosen EOSs cover all the range of most plausible NS radii, given the few observations available. In fig. 2.2 are shown the density profiles of a 1.4 $M_\odot$ neutron star in a binary system with a distance of 60 km from the companion neutron star, taken from the initial data of the simulations presented in [94].

In figure 2.1b, instead, is reported the pressure for each EOS, respect to the mass density of a star region. The relativistic mean field theory EOS (H4 and MS1) are joint at a lower density to the crust EOS (see also the values of ρ_4 in table 2.2) and are stiffer (with a higher pressure support) in the interval between the nuclear density and $\rho_6 = 10^{15} g/cm^3$. This allows them to support stars with larger radii. The other two EOSs (APR4 and SLy), instead, are very similar (leading also to similar curves in the M(R) plot fig. 2.1a). They are softer in the $10^{14} - 10^{15} g/cm^3$ density range, but have, instead, a larger pressure support at the highest densities. These density values beyond $10^{15} g/cm^3$, however, are not present in ordinary cold, irrotational, neutron stars in binary systems, which are used as initial data in the simulation analysed in this work. They could be reached, however, in the post-merger phase, if there is not a prompt collapse to black hole, especially in high total mass and equal mass models (see sec. 4.2 and, in particular, figure 4.14).

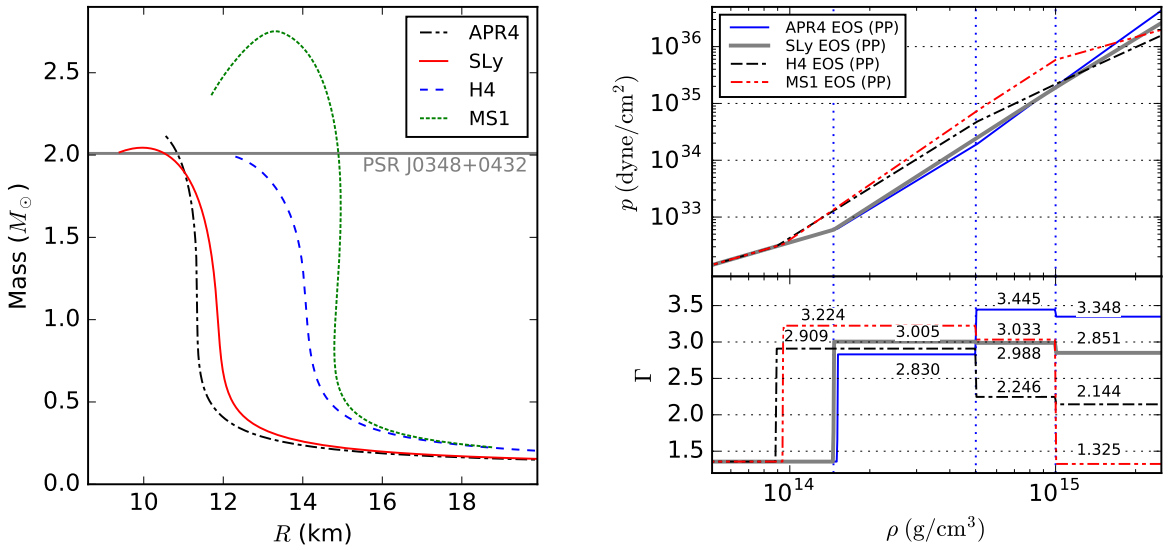

(a) $M(R)$ curves (b) $p(\rho)$ curves

Figure 2.1: Left figure: mass over radius relationships for a cold non-rotating neutron star with the four EOS models analysed in this thesis. The grey horizontal line represents the maximum mass limit of the observed pulsar PSR J0348+0432 [125].
Right figure: the top panel shows the pressure versus mass density curves for the same four EOSs. The bottom panel shows, instead, the adiabatic indexes Γ for the piecewise polytropic representations of those EOSs.

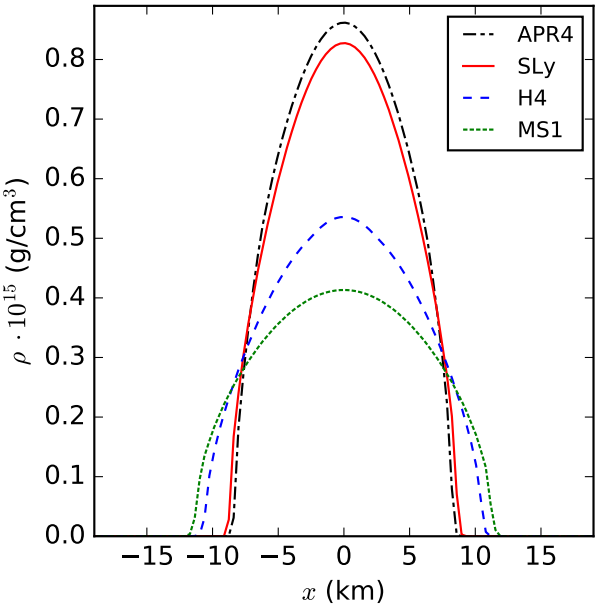

Figure 2.2: Density profiles for a cold neutron star in a binary system with a baryonic mass of 1.4 $M_\odot$ and a distance from the companion of 60 km. They are taken from the initial data of simulations presented in [94], using the APR4, SLy, H4 and MS1 EOSs. See also appendix B for more details on these and others simulated models initial configuration details.

2.1.2 Double neutron stars systems

Up to now, eleven double neutron star systems have been detected in our galaxy, through pulsar timing (the nature of the pulsar companion of one of those systems, PSR J1906+0746 as being a neutron star is still debated). Among those systems, only six have precise measurements of the masses of both stars, while for four others we have only an estimate for the total mass of the system. Two additional double neutron star systems have been detected in globular clusters, but the nature of the pulsar companion in one of them is not certain.

Table 2.3 list all those detected DNS systems with their relevant parameters. In particular, for each double nutron star system, it was computed the eccentricity that the system will have when it will enter in the Advanced LIGO/Virgo band (whith a emitted GW frequency of 10Hz) with the following expression (approximated at the Newtonian level), from ref. [145]:

$$\frac{10Hz}{f_i} = \left(\frac{e_{10Hz}}{e_i}\right)^{18/19} \left(\frac{1-e_{10Hz}^2}{1-e_i^2}\right)^{3/2} \left(\frac{304+121e_i^2}{304+121e_{10Hz}^2}\right)^{1305/2299}, \tag{2.9}$$

where f_i is the frequency of the gravitational waves emitted by the binary in its current state, computed as twice the orbital frequency, e_i is the current eccentricity of the orbit and e_{10Hz} is the desired eccentricity at a GW frequency of $10Hz$. It was also computed the time τ_g needed for each binary to merge, only for systems for which the individual masses of each star are known, with the following approximate formula from ref. [118]:

$$\tau_g \simeq 9.83 \times 10^6 \,\mathrm{yr} \left(\frac{P_b}{hr}\right)^{8/3} \left(\frac{m_1+m_2}{M_\odot}\right)^{-2/3} \left(\frac{\mu}{M_\odot}\right)^{-1} \left(1-e^2\right)^{7/2}, \tag{2.10}$$

where P_b is the binary rotation period, m_1 and m_2 are the masses of the two stars and $\mu = \frac{m_1 m_2}{m_1+m_2}$ is the reduced mass.

From table 2.3 it can be noted that the mass of neutron stars in double neutron star systems are constrained in a small range around $1.35\,\mathrm{M}_\odot$, and the mass ratios are close to one. This is different from the general distribution of neutron star masses,measured in binaries with regular stars or white dwarves, which is much broader and peaked at slightly higher masses [5, 123]. An exception to this trend, however, is the most recently observed BNS system with the pulsar J043+1559 [4], which has a high total mass and a large mass asymmetry (with a mass ratio of 0.75, never observed before). The pulsar in that system has by far the highest mass measured for a neutron star in a BNS system ($1.559\,\mathrm{M}_\odot$), while its companion has the lowest one ($1.174\,\mathrm{M}_\odot$). The discovery of this system has been very important, because it testifies the need for studying with numerical simulations also binaries with large mass asymmetry (which have been neglected in the literature before 2015, with few exceptions [62–64]) and lower (or higher) masses than what are usually considered (see for example ref. [68, 69] for a first step in these directions).

Double neutron star system are formed form regular star binary systems. The first star collapses, creating a neutron star. This first neutron star accretes from the companion, spinning up becoming recycled. When the companion grows to become a red giant, a common envelope will engulf the neutron star. This will cause it to spiral-in, creating a tightly close binary. The energy released by accretion and friction in this process will lead the hydrogen envelope to be expelled, leaving a close binary formed by a neutron star and an helium star [157, 158]. Due to large tidal effects this system has a perfectly circular orbit. When the second star will undergo a supernova explosion, creating a second neutron star, a relevant fraction of its mass will be ejected. This would cause the binary

Pulsar	M_T $[M_\odot]$	m_P $[M_\odot]$	m_C $[M_\odot]$	q	P_b [days]	e_i	e_{10Hz}	τ_g [Gyr]	Ref.
J1765-2240	-	-	-	-	13.638	0.303	2.574×10^{-8}	-	[146]
J1756-2251	2.570	1.342	1.231	0.92	0.320	0.181	7.207×10^{-7}	1.67	[147]
J1811-1736	2.57	-	-	-	18.779	0.828	3.044×10^{-7}	-	[148]
J1807-2500B*g	2.572	1.366	1.206	0.88	9.957	0.747	3.053×10^{-7}	1032	[149]
J0737-3039	2.587	1.338	1.249	0.93	0.102	0.088	1.118×10^{-6}	0.086	[150]
J1829-2456	2.59	-	-	-	1.760	0.139	8.927×10^{-8}	-	[151]
J1930-1852	2.59	-	-	-	45.060	0.399	1.101×10^{-8}	-	[152]
J1906+0746*	2.613	1.291	1.322	0.98	0.166	0.085	6.454×10^{-7}	0.31	[153]
B1534+12	2.678	1.333	1.345	0.99	0.421	0.274	8.853×10^{-7}	2.76	[154]
B2127+11Cg	2.713	1.358	1.354	1.00	0.335	0.681	7.220×10^{-6}	0.22	[155]
J1518+4904	2.718	-	-	-	8.634	0.249	3.234×10^{-8}	-	[156]
J043+1559	2.734	1.559	1.174	0.75	4.072	0.112	2.93×10^{-8}	1456	[4]
B1913+16	2.828	1.440	1.389	0.96	0.323	0.617	5.32×10^{-6}	99.6	[6]

Table 2.3: List of all detected binary neutron star systems, in increasing order of total mass. For entries marked with * the neutron star nature of the pulsar companion is still debated. Entries marked with **g** have been observed in globular clusters. For each system we list the pulsar name, the total adm mass M_T, the gravitational mass of the pulsar m_P and its companion m_C, the mass ratio q (by convention always less than 1), the binary orbital period P_b (from which the gravitational wave frequency can be computed as $\frac{2}{P_b}$), the system eccentricity in its current state e_i and when the GW frequency will reach $10Hz$ (e_{10Hz}), the approximated merger time τ_g and the original article reference for the system discovery.

to become unbound, unless the explosion impressed also a kick velocity to the newly born second neutron star. Studying the distribution of plausible kick velocities and mass ejecta for all the 13 BNS systems detected and reported in table 2.3, in ref. [159] was shown that there is evidence for two different formation channels for BNS systems: a mechanism with high kicks and ejected mass, coming from a regular supernova, which produced the systems with high pulsar spin periods and high orbital eccentricity (like the Hulse-Taylor BNS B1913+16), and a different mechanism with low kicks and ejecta, coming from an electron-capture supernova, which produced the systems with faster rotating pulsars and lower eccentricities.

2.2 Gravitational waves

Gravitational waves (GW) are one of the key prediction of Einstein's General Relativity (GR), already formulated in 1916, a few months after the first publication of GR field equations [160]. Gravitational waves are perturbations of spacetime, and a mandatory consequence of imposing a relativistic nature for gravitational interactions. Gravitational waves are generated by the bulk motion of massive sources, if they have a quadrupolar (or higher multipolar) component, and they propagate at the speed of light, with their amplitude decaying like the inverse of the distance from the source. The more commonly familiar electromagnetic waves, instead, are generated by the incoherent superposition of the motions of microscopic charges, and have a dipolar nature.

The quest to directly detect gravitational waves begun in the late 60s with the pioneering work of Joseph Weber with bar detectors. This incredible scientific endeavour finally gave its results the 14th of September, 2015, with the first direct detection of GWs from a binary black hole merger by the interpherometers of Advanced LIGO [1]. Indirect proof of the existence of GWs in nature, however, was already available, thanks to neutron stars! The 1974 discovery of the pulsar B1913+16 in a BNS system by Hulse and Taylor [6] allowed to make precise timing measurements in the following 15 years, showing a remarkable agreement between the orbital shrinking observed and the prediction from General Relativity due to the quadrupolar emission of gravitational waves [7]. This results lead to the 1993 Nobel Prize for Hulse and Taylor. It has been updated with more recent data [161], which are reported in fig. 2.3.

2.2.1 Gravitational waves in linearised gravity

The presence of gravitational radiation can be computed easily from the GR field equations in the linearised approach. Far from compact sources such as black holes or neutron stars, we can consider the spacetime metric $g_{\mu\nu}$ as given by the Minkowski special relativistic metric $\eta_{\mu\nu}$ plus a small perturbation $h_{\mu\nu}$, with $|h_{\mu\nu}| \ll 1$.

$$g_{\mu\nu} \;=\; \eta_{\mu\nu} + h_{\mu\nu} \tag{2.11}$$

From this metric one can construct the Einstein tensor $G_{\mu\nu} = R_{\mu\nu} + \frac{1}{2} g_{\mu\nu} R$ and write Einstein's equations

$$G_{\mu\nu} = 8\pi T_{\mu\nu} \tag{2.12}$$

in the linearised gravity approximation:

$$\Box \bar{h}_{\mu\nu} \;-\; 2\partial_{(\mu}\partial^{\rho}\bar{h}_{\nu)\rho} \;+\; \eta_{\mu\nu}\partial^{\rho}\partial^{\sigma}\bar{h}_{\rho\sigma} \;=\; -16\pi T_{\mu\nu}, \tag{2.13}$$

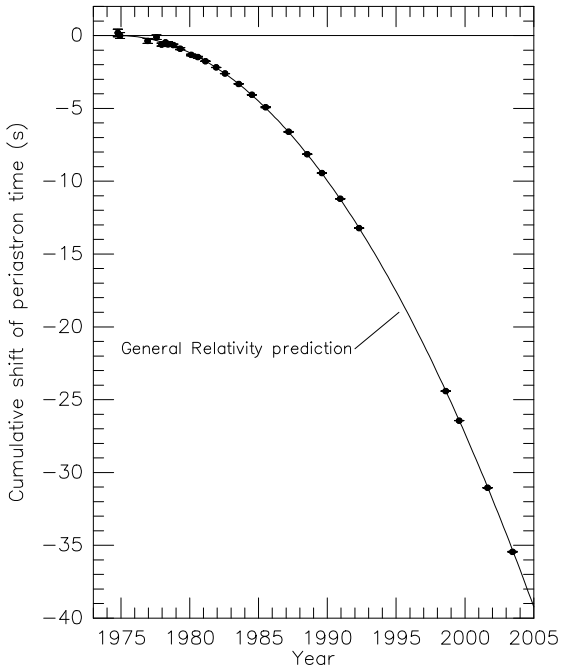

Figure 2.3: Cummulative shift of periastron time due to orbital shrinking in the Hulse-Taylor binary system in 30 years of observation. The solid line shows the general relativity prediction and is not a fit of the data points. Figure from ref. [8].

where it was practical to introduce the trace-reversed metric perturbation

$$\bar{h}_{\mu\nu} \;:=\; h_{\mu\nu} - \frac{1}{2} h \eta_{\mu\nu}, \tag{2.14}$$

where $h = \eta^{\mu\nu} h_{\mu\nu}$ is the trace of the perturbation.

The metric imposed by eq. (2.11) is not unique, because there is the freedom of performing an infinitesimal coordinate transformation $x^\alpha \to x^\alpha - \xi^\alpha$ which leaves eq. (2.11) untouched. This means that the linearised theory is invariant under the gauge transformation

$$h_{\mu\nu} \to h_{\mu\nu} + 2\partial_{(\mu}\xi_{\nu)}, \tag{2.15}$$

in the sense that this transformation will not change the field equations 2.13. To simplify the problem, one can make the choice of the Lorenz gauge:

$$\partial^\mu \bar{h}_{\mu\nu} = 0. \tag{2.16}$$

This is similar to what is usually done in electromagnetism, where the Faraday tensor $F_{\mu\nu}$ is invariant under the gauge transformation of the quadri-vector potential $A_\mu \to A_\mu + \partial_\mu B$, allowing for the imposition of the Lorenz gauge $\partial^\mu A_\mu = 0$, which simplifies Maxwell's equations. Equation (2.16) will lead to the following field equations:

$$\Box \bar{h}_{\mu\nu} \;=\; -16\pi T_{\mu\nu}, \tag{2.17}$$

which have the form of a wave equation for the quantity $\bar{h}_{\mu\nu}$, which propagates with the speed of light.

Considering the propagation of gravitational waves in vacuum, governed by the equation $\Box\bar{h}_{\mu\nu} = 0$, it can be easily shown the presence of two distinct polarization of the gravitational radiation. The metric perturbation can be decomposed with a Fourier transform:

$$\bar{h}_{\mu\nu} = \int A_{\mu\nu}(k)e^{ik_\rho x^\rho}d^4k, \tag{2.18}$$

The Lorenz gauge condition of eq. 2.16 does not fix uniquely the metric perturbations, but leaves room for another gauge transformation, because any generator ξ^μ which satisfies $\Box\xi^\mu = 0$ will preserve eq. (2.16). This gives the ability to fix the so called "Transverse Traceless" (TT) gauge, after having selected an observer with four-velocity u^μ, imposing the following conditions to the perturbation amplitude:

$$u^\mu A_{\mu\nu} = 0 \tag{2.19}$$

$$\eta^{\mu\nu}A_{\mu\nu} = 0. \tag{2.20}$$

The traceless condition implies $h = 0$ and so $h_{\mu\nu} = \bar{h}_{\mu\nu}$. In the TT gauge, in the rest frame of the observer u^μ, for a gravitational wave which propagates in the z direction, the metric perturbation can be written as:

$$h^{TT}_{\mu\nu} = \begin{pmatrix} 0 & 0 & 0 & 0 \\ 0 & h_+ & h_\times & 0 \\ 0 & h_\times & -h_+ & 0 \\ 0 & 0 & 0 & 0 \end{pmatrix} \tag{2.21}$$

where h_+ and $h_\times$ are the only two indipendent polarization of gravitational wave. Their names come from the effect that they make when they interact with matter: the plus polarization deforms a circle of particles with its center at the center of a Cartesian coordinate system by elongating it alternatively along the x and y axis, while the cross polarization deforms the particle circle along the two axis bisectors.

Considering, instead, the generation of gravitational waves by some matter sources, one can try to derive the generated metric perturbation, again, in the linearised gravity approximation. Starting from eq. (2.17), for each component $\bar{h}_{\mu\nu}(t,\vec{x})$ the linear wave equation can be solved with standard techniques, using the retarded time variable $t' := t - \left|\vec{x} - \vec{x'}\right|$:

$$\bar{h}_{\mu\nu}(t,\vec{x}) = 4\int \frac{T_{\mu\nu}(t',\vec{x'})}{\left|\vec{x} - \vec{x'}\right|}d^3x'. \tag{2.22}$$

This expression can be simplified under the assumption that we are interested in the emitted gravitational waves far from the source, which means that $r = |\vec{x}| \gg R_{source}$, allowing to substitute in the denominator $\left|\vec{x} - \vec{x'}\right| \simeq r$. Another possible simplification comes from the so called "slow source" approximation, considering that the wavelength λ linked with the characteristic source variation is much bigger than the source size: $\lambda \gg R_{source}$. This allows to approximate also the numerator, obtaining finally for the approximated eq. (2.22):

$$\bar{h}_{\mu\nu} = \frac{4}{r}\int t_{\mu\nu}(t - r,\vec{x'})d^3x'. \tag{2.23}$$

Another constraint is imposed by the conservation of the energy-momentum tensor, which, in the linearised gravity, is simply $\partial_\mu T^{\mu\nu} = 0$, without the covariant derivative of the full non-linear theory. Considering a volume containing the source but with its boundary outside it, one can write, for the time component of the $T^{\mu\nu}$ conservation,

$$\partial_0 T^{00} = -\partial_i T^{i0}. \tag{2.24}$$

Differentiating both sides respect to time and using the symmetry of $T^{\mu\nu}$ one can obtain:

$$\partial_0^2 T^{00} = -\partial_0 \partial_i T^{i0} = \partial_i \partial_j T^{ij} \tag{2.25}$$

using again the energy-momentum conservation in the last step. Multiplying both sides for $x^i x^j$ and integrating over the considered volume, one can integrate by parts the last term, because the source term will vanish due to the fact that the boundary of the considered volume is outside the source. Finally, one obtains:

$$\int T^{ij}(x) d^3x = \frac{1}{2}\partial_0^2 \int x^i x^j T^{00} d^3x. \tag{2.26}$$

Applying this to eq. (2.23) one finally obtains:

$$\bar{h}_{ij}(t, \vec{x}) = \frac{2}{r}\ddot{I}_{ij}(t - r), \tag{2.27}$$

where I_{ij} is the second mass moment:

$$I_{ij}(t) = \int \rho(t, \vec{x}) x_i x_j d^3x. \tag{2.28}$$

Finally, one can obtain the famous quadrupole emission formula, projecting eq. (2.27) in the TT gauge:

$$h_{ij}^{TT}(t, \vec{x}) = \frac{2}{r}\Lambda_{ij,kl}(\vec{n})\ddot{Q}_{ij}(t - r), \tag{2.29}$$

where $\Lambda_{ij,kl} = P_{ik}P_{jl} - \frac{1}{2}P_{ij}P_{kl}$ depends upon the projection operator $P_{ij} = \delta_{ij} - n_i n_j$, whith $\vec{n} = \vec{x}/r$, and Q_{ij}, the mass quadrupole moment, is the traceless part of eq. (2.28):

$$Q_{ij}(t) = \int \rho(t, \vec{x}) \left(x_i x_j - \frac{1}{3} |\vec{x}|^2 \delta_{ij} \right) \tag{2.30}$$

2.2.2 Beyond linearised gravity: the post-Newtonian expansion

Gravitational wave emission from real astrophysical sources which we can hope to directly reveal with Earth based (like LIGO, Virgo, Geo, Kagra and in the future the Einstein Telescope) or space based (like eLisa) detectors cannot be described in the linearised gravity approximation, because sources like compact objects (neutron stars and black holes) generate a strong gravitational field, and their dynamical evolution is influenced by the backreaction of their emitted gravitational waves, which is not considered in the linearised theory. The way to go beyond is the so called "post-Newtonian" expansion.

For a self-gravitating system the strength of the gravitational field is linked with the velocity of motion by the Virial theorem:

$$\frac{v^2}{c^2} \simeq \frac{R_s}{d}, \tag{2.31}$$

where d is the typical size of the source and R_s is the Schwarzschild radius $R_s = \frac{2Gm}{c^2}$, indicating also c and G for clarity. This means that an expansion in the parameter $\epsilon = \frac{v}{c}$ is both an expansion for slowly moving sources and for weekly self-gravitating ones. At the lowest post-Newtonian orders (usually indicated as half the maximum exponent of ϵ in the expansion) there is no effect of the radiation reaction on the source, so the problem can be considered symmetric under time-reversal. Since under time reversal the metric components g_{00} and g_{ij} are even and g_{0i} are instead odd, this forces the presence of only even(odd) powers of ϵ in their PN expansion, respectively. On the other hand, Einstein's equations impose to work at order ϵ^n in g_{00} and at the same time at order ϵ^{n-1} in g_{0i} and ϵ^{n-2} in g_{ij} (to be consistent with the expansion order in all terms). Therefore, the low-order expansion terms of the metric components are:

$$g_{00} = -1 + {}^{(2)}g_{00} + {}^{(4)}g_{00} + \cdots \tag{2.32}$$

$$g_{0i} = {}^{(3)}g_{0i} + \cdots \tag{2.33}$$

$$g_{ij} = \delta_{ij} + {}^{(2)}g_{ij} + \cdots \tag{2.34}$$

At the same time, the energy-momentum tensor is expanded in powers of ϵ. This simple expansion is correct until the 2.5PN order, when GW radiation reaction enters for the first time into play. This destroys the time reversal symmetry, because of the boundary condition of no incoming radiation at the beginning of the considered time interval. This complicates the mathematical formulation at higher PN orders. For more information, one can look at ref. [162–164].

The post-Newtonian expansion is not convergent in the latest stages of a compact binary merger, since velocities gets high (a fraction of the speed of light, for example the black hole speed at merger was 0.5 c for the system that generated the first detected gravitational wave signal GW150914). For this reason, series resummation techniques have been explored recently, with great success. In particular, the Effective One Body (EOB) model for the inspiral of binary black holes [39–41, 165] have been successful in producing templates for non-rotating and spinning black holes mergers, which are currently adopted in GW detector data analysis. Various formulations of the EOB model have been calibrated to numerical relativity simulations, in particular to fix unknown high-order PN coefficients. This is one reason for which numerical relativity simulations of compact binary mergers are still very important, even if not directly adopted in experimental GW searches data analysis, substituted by the much faster semi-analytical techniques. The EOB model has been extended recently also to the study of binary neutron star (and black hole - neutron star) mergers, with the inclusion of a description for tidal effects [43, 45, 47, 166].

2.2.3 Gravitational waves astrophysical sources

The primary target for current and near-future gravitational wave detectors is the merger of compact binaries. Two binary black hole mergers have been already detected [1, 167], and more will come in the future, once the sensitivity of interferometers like Advanced LIGO/Virgo will increase. The second most promising source are binary neutron stars and neutron star - black hole mergers. While several BNS systems have been observed already in our galaxy through pulsar timing (see sec. 2.1.2), no NS-BH system has been yet detected, making the computations of their merger and detection rate unreliable.

Besides compact binaries, also different systems can produce a varying quadrupole moment able to emit sufficient power of gravitational radiation to be detected on Earth. One example are isolated neutron stars, which can emit GW if there is any "mountain", or imperfection, on their

surface, making them non perfectly symmetric, while rotating fast. Another mechanism through which isolated neutron stars can emit gravitational waves are secular [168–170] and dynamical [171–174] instabilities, which can be triggered in differentially rotating neutron stars, like the ones newly born after a supernova core collapse, with a wide range of their EOS [175]. The detection of gravitational waves by neutron stars instabilities or oscillation modes will open the field of gravitational wave asterosysmology, which means studying the internal structure of neutron stars thanks to the GW coming from thier oscillation, like the internal structure of Earth can be studied looking at earthquakes.

Another widely studied source are core collapse supernovae [112, 176, 177]. Several different mechanism can excite the emission of gravitational waves during a supernova collapse. The fist and most studied one is rotation collapse and bounce, when, for conserving the angular momentum, the star reaches a considerable asphericity during collapse, which added to fast rotation provides a time-varying quadrupole moment which generates gravitational waves. Another more recently studied mechanism, thanks to the development of three dimensional simulations [109, 178, 179], is the post-bounce GW emission due to convection and convective instabilities. A third mechanism is the gravitational radiation due to asymmetric neutrino emission during the shock-revival phase. This mechanism, however, generates GWs with frequencies too low to be detected by current Earth-based gravitational wave detectors. A final emission source are the pulsations of the hot, newly born proto-neutron star [117].

2.3 Multimessenger astronomy with binary neutron stars

Besides emitting gravitational waves, binary neutron stars can emit also a wide range of electromagnetic signals and even neutrino signals. This allows to open the new field of multimessenger astrophysics. Different signals can be used to extract different and complementary information, to help reconstructing a picture of the source physics, for example to distinguish between different neutron star EOS models. Simple examples are EM-followup searches of a GW detection trigger: immediately after the detection of a plausible GW signal, telescopes in different frequency bands will receive from LIGO/Virgo the information about the source location (with currently is weekly constrained to hundreds or even thousands of square degrees because only two detectors are active [2]). EM instruments will point towards the GW source, looking for a signal decaying in time after the GW detection. This can help identifying the source of some known EM signals, like short gamma ray bursts (SGRB), by looking at the GW signal it emits, but can also help discriminating between possible candidate sources for the GW signal. Some examples of similar analysis, from the first two direct detections of gravitational waves, have been presented in ref. [180–183]. An opposite application of multimessenger astrophysics is the GW-followup search triggered by electromagnetic detections. Informations about the source location and energetics drawn by the electromagnetic emissions can help GW data analysis searches inside the detectors noise, requiring a smaller signal to noise ratio to have a GW detection.

Focusing on BNS mergers, the most promising GW source associated with known mechanism of EM emission, the two most interesting processes to study with multimessenger techniques are the identification of the central engine of SGRB, which have been linked with BNS (or NS-BH) mergers, but whose production mechanism is not yet clear, and the production of heavy elements in the matter ejected from the BNS merger remnant, with the so called “rapid neutron capture” or “r-process”.

2.3.1 The link between binary neutron star mergers and short gamma ray bursts

Gamma ray bursts (GRBs) are intense flashes of soft gamma rays detected from Earth. Two different families of GRBs have been distinguished: short (with a duration of less than 2 s and a harder spectrum) and long (with a longer duration and a softer spectrum). Long gamma ray bursts are believed to be produced in core collapse supernovae, see for example [111]. SGRB, instead, are emitted after the merger of BNS or NS-BH systems. A first evidence for this comes from the different source locations of short and long gamma ray bursts. The latter come from active star formation regions, while the former from early, but more often from late type galaxies. This points to an older stellar population in the source zones and a great spread in the source ages [16–19]. Another clue which points towards the link between SGRB and BNS mergers is the high energy released in SGRBs, in the order of $10^{48} - 10^{52}$ erg, which is available during BNS mergers, in the form of gravitational binding energy of the merger remnant, which can be several time 10^{53} erg [184]. A third clear link are the time-scales involved in the BNS merger dynamical evolution: the typical time scale of the properly defined merger phase and of the merger remnant evolution (for example, of its rotation, if it is a neutron star or a spinning black hole surrounded by an accretion disk) is some ms, correspondent to the time scale of variation of the SGRBs energy output, which is small to be reproduced with different hypothetical sources. At the same time, the total duration of a SGRB prompt emission is much longer, typically around $\tau_{SGRB} \simeq 0.3$ s. This time scale is also linked with BNS merger remnants, in particular to the viscous time scale of the thick accretion disk formed in high total mass BNS mergers after a black-hole collapse. The study of disks mass, accretion rates and dynamical evolution is one of the most interesting motivations for performing numerical relativity simulations of BNS mergers, in order to give reliable data for building of SGRB emission models.

The remaining open question about SGRB is the precise nature and mechanism of their central engine. There have been several different proposals to explain the prompt emission of an ultra-relativistic outflow. The three most common ones are the magnetar model, the standard picture of a jet launched by strong magnetic fields in a black hole - torus system and the more recent time reversal scenario. A fourth model which was commonly discussed in the literature, the relativistic outflow emission due to neutrino-antineutrino pair annihilation, was refuted recently by ref. [185], where it was shown that baryon pollution in the central engine atmosphere due to BNS merger ejecta will preclude the jet launch.

In the magnetar model [20, 23, 186] SGRBs are launched by a newly formed magnetar, after a BNS merger or a white dwarf accretion-induced collapse. A similar model can be used also to explain long gamma ray bursts, whose central engine would be a magnetar formed by a core collapse supernova. The SGRB prompt emission, in this model, is powered by accretion onto the rapidly rotating protomagnetar from a disc formed during the BNS merger or WD collapse. This model is also able to explain the extended emission (on a time scale of 10-100 s) seen in some SGRBs, and in particular internal plateaus in the SGRB light curves with a rapid decay after the plateaus end. In the magnetar model these extended emissions are produced by the matter accelerated by the star fast rotation and ejected by the magnetic field via magnetic propelling [23]. The X-rays plateau is modelled as magnetic dipole spin-down emission, while its sudden decay is explained by the collapse of the supra-massive magnetar to balck hole, when, after its spin-down, rotation is not able to sustain it any more.

The standard black hole - torus model, which has been the dominant one until the discovery of

extended emissions, is based on the collapse of the BNS merger remnant in few ms after the merger, with the formation of a thick, magnetized, accretion disk around a Kerr black hole. Energy can be extracted from the system, to power a relativistic outflow, via the Blandford-Znajek (BZ) mechanism [187]. This requires, however, the presence of a strong magnetic field, close to equipartition, in the black hole egosphere. Several numerical simulations of magnetized BNS mergers have been performed in the last years (mainly in the ideal MHD approximation), in order to study the magnetic field amplification mechanism, its geometrical structure after the collapse to black hole (an ordered, poloidal magnetic field oriented along the BH spin axis is needed to power the jet) and if a relativistic outflow can be reproduced. The first simulation to show the formation of an ordered poloidal magnetic field structure was reported in ref. [21], starting from a realistic magnetic field structure inside two $1.5\,M_\odot$ neutron stars (with a maximum strength of 10^{12} Gauss) and using an approximated ideal fluid EOS. They did not see, however, the formation of a relativistic outflow. The same result was also confirmed in [87], performing resistive GRMHD simulations of a similar BNS system. The subsequent work of ref. [83], starting with a higher 10^{14} Gauss magnetic field, using a piecewise politropic approximation of the H4 EOS, similar to the one described in sections 2.1.1, and adopting a much higher resolution, found instead no organized magnetic field structure in the BH-torus system. This difference has been attributed to a different method for reconstructing magnetic field lines [26], or to the higher ejected matter (due to a different EOS) whose infalling pressure must be overcome by the magnetic pressure to launch a jet [27]. The only simulations in which a mildly relativistic outflow has been seen are the one of ref. [27], with a really high initial magnetic field of 10^{15} Gauss (justified to reproduce the magnetic amplification due to instabilities unresolved in the numerical evolution), both inside the star or as an external dipolar field. The most recent simulations of ref. [26] found the formation of an organized magnetic field structure, independent of the NS EOS, the initial magnetic field orientation and the stars mass ratio. They were not able to show a jet, however, because of the use of realistic initial magnetic field values (10^{12} Gauss).

Magnetic field amplification in BNS mergers happens mainly due to the Kelvin-Helmotz (KH) instability during the merger phase [89], the magneto-rotational instability (MRI) in the massive neutron star or the accretion disc formed after the merger and the magnetic field winding due to the differential rotation of the merger remnant. The KH instability creates vortices in the shear layer after the two neutron stars come into contact, that amplify the magnetic field, converting kinetic energy into turbulent energy and stretching the magnetic filed lines, producing a magnetic field exponential growth [89]. The MRI [188] is a local shear instability which amplifies exponentially the magnetic field strength in the presence of a negative radial gradient of angular velocity, as happens in the massive neutron stars formed after the merger. MRI effects are difficult to resolve in grid-based BNS simulations, because they require a spatial resolution about 10 times smaller than the MRI wavelength. Ref. [24, 83, 189] are the first to have reported the development of MRI in hyper massive neutron stars formed after a BNS merger, adopting resolutions under 100 m, which are not currently feasible for performing many simulations in a large parameter study. Realistic simulations of magnetized BNS merger are still difficult because of the resolution requirements to fully resolve all magnetic instabilities, starting from a plausible magnetic field value. A possible future direction is the development of subgrid models able to reproduce the energy extracted from lengthscales smaller than the simulation resolution [71, 190].

The third and most recent model of SGRB emission, developed to reconcile the BH-torus model, which has had partial confirmation of its ability to power relativistic jets from numerical

simulation, with the X-rays plateaus in the extended emissions, is the so called "time reversal scenario" [22, 25, 33, 34]. In this model, after a BNS merger a supra-massive NS is formed, which collapses in a much longer time-scale than the one we can study with numerical simulations, from seconds to hundreds of seconds. After merger, the supra-massive NS generates an optically thick atmosphere consisting of a photon-pair nebula and baryon-loaded ejecta. Spindown radiation emitted by the rotating magnetized NS is diffused in such atmosphere in a long timescale, up to $10^4, 10^5$ s. After the collapse to BH, a relativistic jet is launched, producing the SGRB prompt emission. The jet easily travels past the atmosphere, becoming detectable before at least some part of the spindown emission, even if it was produced after it. This mechanism provides the "time reversal" necessary to explain why the extended emission are seen long after the prompt gamma ray emission.

Although in this work there are no simulations considering also the effect of magnetic fields, the study of the effects of the NS EOS, the mass ratio, the initial data and the adopted numerical methods on the properties of the merger remnant (its collapse time, the mass of the produced accretion disc, the rotational profile of the remnant neutron star, the ejecta mass and composition) are key to calibrate and constrain the different SGRB central engine models.

2.3.2 Merger remnants as r-process sites and related macronova signals

Heavy elements beyond Fe are produced by neutron capture. After a supernova explosion, there is a balance between neutron capture and β decays. The difference between their time scales gives two different processes: the slow (s-process) and the rapid (r-process) neutron capture. Supernovae have been considered the site of r-process nucleosynthesis for many years, until more recent simulations have shown that neutrino-driven winds do not have the right physical conditions to explain all the heavy elements galactic abundance patterns, in particular around the third r-process peak (at $A \simeq 195$) [191]. Therefore a new paradigm gained consensus, hypothesizing BNS merger remnant as the principal sites for r-process. Matter ejected in BNS mergers has the right neutron abundance and velocity profile to start the needed nuclear reactions [192]. Moreover, it was shown that BNS merger ejecta nucleosynthesis is able to reproduce the solar system heavy elements abundance independently of the astrophysical characteristics of the BNS system, such as the two star masses, mass ratio, EOS [193]. This is linked with the ejecta being extremely neutron-rich. On the other hand, the nucleosynthesis is much more sensitive to the nuclear physics parameters.

It is therefore very important to accurately study the mass ejection mechanism in a BNS merger remnant. Dynamical mass ejection (through hydrodynamical processes or gravitational torques) has been accurately studied recently in numerical relativity simulations [44, 61, 66, 70]. Their results point towards a maximum ejecta of $\simeq 0.01\,\mathrm{M}_\odot$ with velocites around $0.1 - 0.2c$. In particular, two different processes have been found to be responsible for mass ejection: tidal interactions and shock heating. Shock heated matter is ejected in a quasi-spherical manner. The general-relativistic treatment of gravity is essential to reconstruct the correct shock-heated ejecta, because they are largely underestimated in Newtonian gravity. The shock-heated ejecta plays a stronger role for softer EOS (smaller neutron star radii). They are also less neutron-rich respect to tidal interactions ejecta, because their high temperature (above 1 MeV) allows electron-positron pairs production, which get captured by protons and neutrons respectively, emitting electronic neutrinos and antineutrinos. Given the much larger abundance of neutrons respect to protons, there are many more positron captures, leaving the matter with a higher electron fraction Y_e. Tidal-driven ejecta are, instead, emitted mostly in the orbital plane, and are very neutron-rich. Tidal ejecta are dominant in BNS mergers with high mass asymmetries. In that case, the merger is less violent, because the low mass

star gets tidally deformed already in the early merger phase (see chapter 4, and, in particular, figure 4.2 for more details), so the shock heating is less strong. This leads also to globally more neutron-rich ejecta. The effect of the mass ratio has been found to be more important in the stiff EOS models (with larger radii)[65, 66]. Another two less investigated but potentially important mass ejection channels are the neutrino-driven winds and the magnetic-driven winds [85, 194].

r-process nucleosynthesis in BNS merger ejecta is very important for multimessenger astrophysics because it can lead to a clearly identifiable electromagnetic signal, the so called "macronova" or "kilonova". It consists in an optical or near-infrared emission powered by radioactive decays of r-process nuclei [184, 195, 196]. At the beginning this radiation is trapped inside the matter, which is optically thick and expanding thanks to radioactive heating. The macronova radiation will be seen only when the EM diffusion time-scale will become similar to the matter expansion time-scale. This happens in a time frame of the order of 1 week after the BNS merger. Two candidate macronova signals have been observed so far [35, 36, 197] looking at the afterglows of short gamma ray bursts. In particular, the first candidate linked with GRB130603B has been identified thanks to the observation of a near-infrared source present in the Hubble Space Telescope data after 9 days from the GRB prompt emission, but not present either in the observation after 30 days and in the Earth-telescopes observations in the first two days after the GRB. Macronovae observations are a compelling proof for the link between SGRBs and BNS mergers, and can be used, by inferring the mass, velocities and neutron richness of the ejecta needed for generating such radioactive decay signal, to constrain the source parameters, in particular the most relevant for mass ejection, such as the NS EOS and the mass ratio. This will be complementary to the information gathered by a possible coincident GW detection.

As remarked before, ejecta characteristics can be predicted only by fully general relativistic numerical simulations. Therefore, enquiring a large spectrum of the possible parameter space for BNS systems is an important scientific endeavour to be able to correctly interpret future EM and GW signals from BNS mergers.

Chapter 3

Numerical background: how to solve Einstein's and hydrodynamics equations on a computer

The numerical solution of hyperbolic PDEs (like Einstein's equations and the general relativistic hydrodynamics (GRHD) equations) requires dedicated algorithms which have been developed in the last thirty years. The starting principle is representing continuous functions of space and time at several discrete time steps, and, at each time step, in a discrete spatial grid, with a finite number of points, in order to be able to apply to the spacetime fields discrete operations which a computer is able to perform. The spatial grid (in our case, a three dimensional Cartesian grid) represents a finite region in space which we are interested to evolve in time. In the case of BNS simulations, the grid is much bigger than the initial distance between the two stars, because there is the need to extract gravitational waves far from the source (see section 3.4) and to avoid (or at least delay) the interaction between the physical evolved fields and spurious matter and radiation infalling or bouncing back at the grid external boundaries.

In order to be evolved in time, equations must be written as a system of first order in time PDEs, in the form:

$$\partial_t U_i(t,\vec{x}) \;=\; RHS\left(U_i(t,\vec{x}), \partial_{\vec{x}} U_i(t,\vec{x}), \partial^2_{\vec{x}} U_i(t,\vec{x}), t, \vec{x}\right), \tag{3.1}$$

where U_i is a vector of our evolved variables. We start setting up initial data for each variable in each grid point. The grid points (in each refinement grid, see later) are distanced one another by the uniform spatial resolution Δx. Then initial data are evolved from the initial time t_n to the subsequent time $t_{n+1} = t_n + \Delta t$, using the so called "method of lines", handled by the `MoL` Cactus thorn. MoL consists in computing the right hand side of a PDE like eq. 3.1 approximating the spatial derivatives with appropriate methods (which are discussed in the following sections). In this way, for each grid point, the fields U_i depend only on the time variable t, leaving a system of ordinary differential equations. They can then be solved with standard numerical techniques, for example the fourth-order Runge-Kutta method [198, 199], which can be used in `The Einstein Toolkit` to evolve the solution at time t^n, denoted with U_i^n, to time t^{n+1}, computing U_i^{n+1} in four

different steps:

$$U_i^{(0)} = U_i^n \tag{3.2}$$
$$U_i^{(1)} = U_i^{(0)} + \frac{1}{2}\Delta t\ RHS(U_i^{(0)}) \tag{3.3}$$
$$U_i^{(2)} = U_i^{(0)} + \frac{1}{2}\Delta t\ RHS(U_i^{(1)}) \tag{3.4}$$
$$U_i^{(3)} = U_i^{(0)} + \Delta t\ RHS(U_i^{(2)}) \tag{3.5}$$
$$U_i^{(4)} = \frac{1}{6}\left(-2U_i^{(0)} + 2U_i^{(1)} + 4U_i^{(2)} + 2U_i^{(3)} + \Delta t\ RHS(U_i^{(3)})\right) \tag{3.6}$$
$$U_i^{n+1} = U_i^{(4)} \tag{3.7}$$

The spatial resolution and the temporal resolution are not independent, but are linked by the so called Courant factor

$$\eta = \frac{\Delta t}{\Delta x}. \tag{3.8}$$

This is both needed for compatibility with special relativity and for archiving stability in the adopted numerical methods. In all simulations analysed in the next chapter a Courant factor of 0.25 has been chosen.

One problem of solving GRHD equations is the need of both a very large grid (in the simulations of chapter 4 it is a cube with an half-edge of approximatively 1063 km ($720\,M_\odot$ in geometric units)) and at the same time achieving a very high spatial resolution (low Δx) near the evolved stars, to be able to resolve all hydrodynamical features and to have low numerical dissipation. This problem was solved by Berger-Oliger Adaptive Mesh Refinement (AMR) [200], which in the Einstein Toolkit is implemented by the thorn `Carpet`. In particular, a simpler, common choice, in BNS merger simulations, is to use only Fixed mesh refinement (FMR). This consists in having multiple nested grids, one inside the other, each (smaller) grid with a resolution double respect to the parent level (meaning two times the density of points, hence half the points distance Δx). As an example, the grid structure used in the simulations performed by the Parma group can be found in table A.2. The code FMR handles the time evolution via subcycling. An example of this algorithm, for just two refinement levels, with spatial resolutions Δx and $2\Delta x$, is:

1. The coarse level, (which has also a larger temporal resolution) evolves one step in time, from t to $t + 2\Delta t = t + 2\eta\Delta x$;

2. At the fine level boundary, the coarse level points are interpolated in space (with fifth order polynomial interpolation) and time (with second order polynomial interpolation), to be used as boundary conditions for the fine level evolution (this step is called *prolongation*);

3. The fine level evolves two steps in time (from t to $t + \Delta t$ and, after, from $t + \Delta t$ to $t + 2\Delta t$), to be aligned with the coarse one;

4. The fields values in coarse level points whose position in space coincides also with a fine level point are copied from the field values in the latter (this step is called *restriction*). Is possible to do just a simple copy, without interpolation, because `Carpet` uses a vertex centred grid, which means that where a finer grid points exists, there is also a corresponding point with the same Cartesian coordinates in each coarser grid.

This FMR scheme, coupled with a multi-step time evolution like RK4, brings problems at refinement boundaries: the fine grid evolution will need also boundary conditions, provided by prolongation, at each intermediate time step in the RK4 algorithm. This will, however, reduce convergence to first order at refinement boundaries [201]. In practice, BNS simulations without any additional technique to solve this problem showed a great loss of accuracy globally in preliminary tests which were performed. The solution adopted in `Carpet` is to use buffer zones at refinement boundaries, which means evolving 12 grid points more for each edge of any finer refinement level (3 ghost points for each of the four RK4 substeps). At each RK4 step, a set of three points becomes invalid, and is not used any more. These points, although evolved regularly like any other one (instead of filling their values with prolongation), are used only as boundary for the evolution of the regular (inner) points in the finer level. This of course leads to higher computational and memory costs, and in particular worsen the code scaling ability when thousands of computing cores are used. A promising alternative solution, which requires a modification of the Runge-Kutta algorithm, but avoids the use of buffer zones, have been proposed in ref. [202], and will be tested and implemented in `Carpet` in the near future.

3.1 Curvature evolution

The numerical solution of Einstein's equations, allowing in particular long-term black hole dynamical simulations, has been a challenge for many years, until the success of the first many-orbits BBH mergers simulations of 2005 [49–51].

In order to simulate the time evolution of a system regulated by Einstein's equations, one must first re-write them in a so called 3+1 formulation, separating a time coordinate, along which the system is evolved, from the spatial coordinates which label the spatial grid at each time step. The 3+1 formalism was originally indtroduced by Darmois (1927), Lichnerowitz (1944) and Choquet-Bruhat (1952). It was then used by Arnowitt, Deser and Misner for developping an Hamiltonian formulation of general relativity, known as the ADM formulation [203].

The first step is to foliate the spacetime in spacelike hypersurfaces Σ_t, which are level functions of a scalar field t (the time coordinate). The timelike, future-directed unit normal to each surface n is linked with the gradient of t by the relation

$$n^\mu := -\alpha \nabla^\mu t. \tag{3.9}$$

This equation is the definition of the lapse function α, which is given by $\alpha = -\sqrt{\nabla^\mu t \nabla_\mu t}$, to ensure that the vector n^μ has norm $n^\mu n_\mu = -1$. In the previous expressions the spacetime metric $g_{\mu\nu}$ is implicitly used to lower the vector indexes, and to define the operator

$$\nabla_\mu \;=\; g_{\mu\nu}\nabla^\nu. \tag{3.10}$$

It is possible to select a privileged observer , denominated the Eulerian observer, which is the one with four-velocity n^μ. This means its evolution is normal to Σ_t, which, therefore, can be viewed as the set of events which are simultaneous for the Eulerian observer. From α, one can also define the normal evolution vector $m^\mu := \alpha n^\mu$. It is characterized by:

$$\nabla_m t = m^\mu \nabla_\mu t = 1. \tag{3.11}$$

This means that the vector $m^\mu \delta t$ carries the hypersurface Σ_t into $\Sigma_{t+\delta t}$. Finally, one can define a spatial metric on each hypersurface

$$\gamma_{\mu\nu} := g_{\mu\nu} + n_\mu n_\nu. \tag{3.12}$$

The next step is to decompose Einstein's equations into a spatial part (on each hypersurface) and a component orthogonal to the foliation. This is done with the projection operators:

$$\gamma^\mu_\nu = \delta^\mu_\nu + n^\mu n_\nu \tag{3.13}$$
$$\alpha^\mu_\nu = -n^\mu n_\nu, \tag{3.14}$$

where δ^ν_μ is the Euclidean metric.

After some computations, it can be shown that the spatial projection of the four dimensional Ricci tensor is:

$$\gamma^\mu_\alpha \gamma^\nu_\beta {}^{(4)}R_{\mu\nu} = -\frac{1}{\alpha}\mathcal{L}_{\mathbf{m}} K_{\alpha\beta} - \frac{1}{\alpha} D_\alpha D_\beta \alpha + R_{\alpha\beta} + K K_{\alpha\beta} - 2K_{\alpha\mu}K^\mu_\beta, \tag{3.15}$$

where $R_{\alpha\beta}$ is the spatial Ricci tensor on Σ_t, D_μ is the spatial covariant derivative, computed with the metric $\gamma_{\mu\nu}$, and K is the trace of the extrinsic curvature $K_{\mu\nu}$, which is defined by:

$$K_{\mu\nu} = -\gamma^\mu_\alpha \gamma^\nu_\beta \nabla_{(\mu} n_{\nu)} = -\frac{1}{2}\mathbf{n}\gamma_{\mu\nu}, \tag{3.16}$$

where the round brackets indicate a symmetrization respect to the indexes they contain. It can be either seen as the projection on Σ_t of the gradient of its unit normal, or the rate of change of the spatial metric. The projections of the energy-momentum tensor, instead, are:

$$S_{\mu\nu} = \gamma^\alpha_\mu \gamma^\beta_\nu T_{\alpha\beta} \tag{3.17}$$
$$e = n^\mu n^\nu T_{\mu\nu} \tag{3.18}$$
$$j_\mu = -\gamma^\alpha_\nu n^\beta T_{\alpha\beta}, \tag{3.19}$$

where e can be interpreted as the energy density and j_μ as the the momentum density measured by the Eulerian observer.

The final step to write the full set of ADM equations is to introduce a coordinate system, adapted to the foliation, in order to write the previous tensorial expressions as a system of PDEs. One first introduces coordinates x^i, $i \in [1,3]$ on each hypersurface Σ_t. Then, a coordinate t is defined, such as the vector ∂_t is tangent to the lines of constant spatial coordinates. This defined vector ∂_t is dual to the 1-form dt, just like the normal evolution vector $\mathbf{m}$, defined before in eq. (3.11), so like $\mathbf{m}$ drags the hypersurfaces Σ_t. But m^μ and ∂_t in general differ, and their difference is defined as the shift vector β:

$$\beta^\mu := \partial^\mu_t - m^\mu. \tag{3.20}$$

From this definition of β and the definition of m of eq. (3.11), one can derive

$$\partial^\mu_t = -\alpha n^\mu + \beta^\mu, \tag{3.21}$$

and, for the Lie derivatives,

$$\mathcal{L}_m = \mathcal{L}_{\partial_t} - \mathcal{L}_\beta. \tag{3.22}$$

One can also express the components of the normal unit vector n^μ and its dual one-form n_μ in terms of the lapse and the shift:

$$n^\mu = \left(\frac{1}{\alpha}, -\frac{\beta^i}{\alpha}\right) \tag{3.23}$$

$$n_\mu = \left(-\alpha, \vec{0}\right). \tag{3.24}$$

This allows to decompose the four-dimensional metric $g_{\mu\nu}$ and write it respect to the just defined coordinate system:

$$ds^2 = g_{\mu\nu}dx^\mu dx^\nu = -\left(\alpha^2 - \beta^i\beta_i\right)dt^2 + 2\beta_i dx^i dt + \gamma_{ij}dx^i dx^j. \tag{3.25}$$

The physical interpretation of the lapse function and the shift vector is the following: the lapse represents a measure of the proper time (for an Eulerian observer) between two adjacent hypersurfaces:

$$d\tau^2 = -\alpha^2(t, x^i)dt^2; \tag{3.26}$$

while the shift vector represents the relationship between spatial coordinates of two adjacent hypersurfaces:

$$x^i_{t+\delta t} = x^i_t - \beta^i(t, x^i)dt. \tag{3.27}$$

They characterize the choice of the coordinate system for the time evolution, and as such, in general relativity they are gauge variables whose evolution can be freely chosen. This choice is very important, as it is discussed in the next subsection, to guarantee numerical stability, in particular for simulations involving black holes.

Now it is finally possible to derive the full set of ADM equations, projecting the Einstein's equations and writing them in the chosen coordinate system. Projecting them twice in the direction normal to Σ_t one obtains, after some algebric manipulation:

$$R + K^2 - K_{ij}K^{ij} - 16\pi e = 0, \tag{3.28}$$

where $R = g_{\mu\nu}R^{\mu\nu}$ is the curvature scalar. Equation 3.28 is the so called *Hamiltonian constraint*. Similarly, making a mixed space-time projection, one obtains:

$$D_j K^j_i - D_i K - 8\pi j_i = 0, \tag{3.29}$$

which are the *Momentum constraints*. These four constraints are elliptic equations, valid in each hypersurface Σ_t. In the numerical scheme implemented in `The Einstein Toolkit`, they are not solved during the numerical evolution, but, instead, one should carefully monitor the constraints violations at each time step due to numerical errors. A high constraint violation means that the physical state of the system computed by the numerical code is not a solution of Einstein's equation, therefore it's not a physical state.

Projecting the Einstein's equations two times on the hypersurface Σ_t, instead, one obtains, starting from the expression of eq. (3.15) for the projected Ricci tensor and writing the equations as $R_{\mu\nu} = 8\pi\left(T_{\mu\nu} - \frac{1}{2}g_{\mu\nu}T\right)$, where T is the trace of the energy-momentum tensor, an evolution equation for the extrinsic curvature:

$$\begin{aligned}\partial_t K_{ij} = &-D_i D_j \alpha + \alpha\left(R_{ij} - 2K_{ik}K^{kj} + KK_{ij}\right) + \\ &- 8\pi\alpha\left(R_{ij} - \frac{1}{2}\gamma_{ij}\left(S - e\right)\right) + \mathcal{L}_\beta K_{ij},\end{aligned} \tag{3.30}$$

which describes how the spacetime geometry changes going from one hypersurface to the future adjacent one. These three equations (six evolution equations for the extrinsic curvature and 4 constraint equations) should be supplemented by the relationship between the spatial metric and the extrinsic curvature, which, using eq. (3.22) and eq. (3.16), can be written as:

$$\partial_t \gamma_{ij} = -2\alpha K_{ij} + \mathcal{L}_\beta \gamma_{ij}. \tag{3.31}$$

3.1.1 The BSSN formulation

Unfortunately ADM equations (eq. 3.30 and 3.31, with the constraints 3.28 and 3.29) can not be used in practice for GR numerical simulations, since they are only weekly hyperbolic, and would quickly lead to numerical instabilities causing our codes to crash. In the late 1990s and first 2000s a new formulation of the Einstein's equations was developed by several groups, called today the BSSN-OK formulation, from the initials of its main developers (Baumgarte, Shapiro, Shibata, Nakamura, Oohara and Kojima) [204–206] [1].

Instead of evolving the spatial metric γ_{ij} and the extrinsic curvature K_{ij}, new variables can be introduced and evolved separately. First, a conformal spatial metric is constructed:

$$\tilde{\gamma}_{ij} := e^{-4\phi} \gamma_{ij}, \tag{3.32}$$

with the conformal factor

$$\phi := log\left(\frac{1}{12} det\left(\gamma_{ij}\right)\right) \tag{3.33}$$

promoted to evolved variable. Then the conformal, trace-free extrinsic curvature is defined (and evolved):

$$\tilde{A}_{ij} := e^{-4\pi}\left(K_{ij} - \frac{1}{3} g_{ij} K\right), \tag{3.34}$$

with $K = g^{ij} K_{ij}$. The indexes of $\tilde{A}_{ij}$ are raised or lowered with the conformal metric $\tilde{\gamma}_{ij}$. Finally, the conformal connection functions are introduced:

$$\tilde{\Gamma}^i := \tilde{\gamma}^{jk} \tilde{\Gamma}^i_{jk} = \partial_j - \tilde{\gamma}^{ij}, \tag{3.35}$$

where $\tilde{\Gamma}^i_{jk}$ are the Christoffel symbols of $\tilde{\gamma}_{ij}$ and the last equation comes from the fact that the conformal metric has determinant equal to one. Separating the trace part and the trace-free part

[1] The contribution of the last two authors (Oohara and Kojima) is often forgotten, and the formalism is usually simply referred at as BSSN in numerical relativity publications.

of the ADM evolution equations 3.30 and 3.31, one finally obtains the full BSSN system:

$$\left(\partial_t - \beta^j\partial_j\right) K = -\gamma^{ij}\tilde{D}_i\tilde{D}_j\alpha + \alpha\left(\tilde{A}^{ij}\tilde{A}_{ij} + \frac{1}{3}K^2\right) + 4\pi\left(e + \gamma^{ij}S_{ij}\right) \tag{3.36}$$

$$\left(\partial_t - \beta^j\partial_j\right)\phi = -\frac{1}{6}\left(\alpha K - \partial_k\beta^k\right) \tag{3.37}$$

$$\begin{aligned}\left(\partial_t - \beta^j\partial_j\right)\tilde{\Gamma}^i = &-2\tilde{A}^{ij}\partial_j\alpha + 2\alpha\left[\tilde{\Gamma}^i_{kl}\tilde{A}^{kl} + 6\tilde{A}^{ij}\partial_j\phi - \frac{2}{3}\tilde{\gamma}^{ij}\partial_j K\right] \\ &- \tilde{\Gamma}^j\partial_j\beta^i + \frac{2}{3}\tilde{\Gamma}^i\partial_j\beta^j + \frac{1}{e}\tilde{\gamma}^{ik}\partial_j\partial_k\beta^j + \tilde{\gamma}^{jk}\partial_j\partial_k\beta^i - 16\pi\alpha\tilde{\gamma}^{ik}j_k\end{aligned} \tag{3.38}$$

$$\left(\partial_t - \beta^j\partial_j\right)\tilde{\gamma}_{ij} = -2\alpha\tilde{A}_{ij} + 2\tilde{\gamma}_{k(i}\partial_{j)}\beta^k - \frac{2}{3}\tilde{\gamma}_{ij}\partial_k\beta^k \tag{3.39}$$

$$\begin{aligned}\left(\partial_t - \beta^j\partial_j\right)\tilde{A}_{ij} = &\, e^{-4\pi}\left[\alpha\tilde{R}^{\phi}_{ij} - \tilde{D}_i\tilde{i}_j\alpha\right]^{TF} + \\ &+ \alpha K\tilde{A}_{ij} - 2\alpha\tilde{A}_{ki}\tilde{A}^k_j + 2\tilde{A}_{k(i}\partial_{j)}\beta^k - \frac{2}{3}\tilde{A}_{ij}\partial_k\beta^k - 8\pi\alpha e^{-4\pi}S^{TF}_{ij},\end{aligned} \tag{3.40}$$

where TF stands for "trace-free", $\tilde{D}_i$ is the covariant derivative associated with the conformal spatial metric and the Ricci tensor has been divided in two components, one containing the terms with derivatives of the conformal metric and its Christoffel symbols ($\tilde{R}_{ij}$), and the other containing only the terms with covariant derivatives of the conformal factor (R^{ϕ}_{ij}). In deriving these equations, the Hamiltonian and momentum constraint relationships have been used. In particular, it is key to use the momentum constraint to eliminate the divergence of $\tilde{A}_{ij}$ from the evolution equations for the conformal connection $\tilde{\Gamma}^i$, to ensure numerical stability. This system of 17 PDEs was rigorously proven to be strongly hyperbolic in ref. [207, 208], even if it is not easy to see it at glance. It has introduced, however, five additional constraints which should be verified at each evolution step:

$$det\left(\tilde{\gamma}_{ij}\right) = 1 \tag{3.41}$$

$$Tr\left(\tilde{A}_{ij}\right) = 0 \tag{3.42}$$

$$\tilde{\Gamma}^i = \tilde{\gamma}^{jk}\tilde{\Gamma}^i_{jk}. \tag{3.43}$$

The first two constraints are actively enforced by the code at each time step. The third one, instead, is not enforced (like the Hamiltonian and momentum constraints of eq. 3.28 and 3.29). However, to help keeping its violation low, the evolved $\tilde{\Gamma}^i$ are used only where their derivatives are needed, but where they are needed without any derivative, $\tilde{\gamma}^{jk}\tilde{\Gamma}^i_{jk}$ is used, instead.

This evolution system must be supplemented with a choice for the gauge variables $\alpha(t, x^i)$ and $\beta^j(t, x^i)$. A simplistic choice, like the geodesic slicing ($\alpha = 1$ and $\beta^i = 0$) does not work, and leads to code crashes when evolving spacetimes containing black holes. This happens because it is not singularity avoiding, therefore, starting a simulation from BH initial data with a future singularity, that singularity is reached quickly in the numerical evolution. There is, therefore, a need for a singularity-avoiding slice condition on α. The lapse can not be constant everywhere, but should approach the Minkowski value of 1 in the asymptotic flat region near the grid outer boundaries and should become close to zero in the vicinity of a black hole, to avoid reaching the singularity. This causes the additional problem that, because time advances "faster" in the far region and is almost frozen near the BH, the grid (or, more precisely, each hypersurface Σ_t) gets strongly distorted (this phenomenon is known as grid stretching), with grid points falling inside the black hole horizon,

even if points inside it are excised from the numerical evolution. This causes the code to crash, due to the large gradients in the metric functions. To fix this problem, one needs to set also a spatial gauge condition for the shift vector β^i, which should also change in space and time.

One common solution for the lapse is the *maximal slicing* condition $K = 0$, or the related *K-freezing* condition $\partial_t K = 0$ (equivalent in the case of $K = 0$ set in the initial data). The K-freezing condition, however, leads to the need of solving an elliptic equation for the lapse at each time step, which is computationally expensive:

$$\Delta\alpha = \beta^i \partial_i K + \alpha K_{ij} K^{ij}. \tag{3.44}$$

An efficient alternative solution, is to contruct an hyperbolic slicing condition, called the *K-driver* condition, making $\partial_t^2 \alpha$ proportional to $\partial_t K$ [209, 210]:

$$\partial_t \alpha - \beta^i \partial_i \alpha = -2\alpha K. \tag{3.45}$$

With this particular choice of parameters, this condition takes the name of "1+log" slicing.

As spatial gauge condition, to avoid grid stretching one can, in the same way, impose the *Gamma-freezing* condition $\partial_t \tilde{\Gamma}^i = 0$, which implies solving elliptic equations for β^i, or impose it dynamically with the hyperbolic *Gamma-driver* condition, as implemented in the Einstein Toolkit:

$$\partial_t \beta^i - \beta_j \partial^j \beta^i = \frac{3}{4} B^i \tag{3.46}$$

$$\partial_t B^i - \beta_j \partial^j \beta^i = \partial_t \tilde{\Gamma}_i - \eta B^i, \tag{3.47}$$

where the additional evolved variable B^i has been introduced. The "Beta driver" η is a parameter which acts as a damping factor, driving B^i (and then $\partial_t \beta^i$) to zero, so the shift vector will tend to a constant in a stationary spacetime (in other words, this is a symmetry-seeking gauge condition). Being a damping factor with dimensions $[1/T]$, it sets, depending on the numerical integration method, a Courant-like limitation for the time step size, but independent from the spatial resolution. Since in FMR simulations with subcycling in time Δt is much larger near the grid boundaries than in the interior, a constant choice for the η parameter can lead to numerical instabilities in the coarser grid [211]. For this reason, a simple space-varying prescription for η is implemented in the Einstein Toolkit:

$$\eta(r) \;:=\; \frac{2}{M_{TOT}} \begin{cases} 1 & \text{for} \quad r \le R \quad \text{(near the origin)} \\ \frac{R}{r} & \text{for} \quad r \ge R \quad \text{(far away)} \end{cases}, \tag{3.48}$$

where r is the distance from the coordinates origin and M_{TOT} is the total gravitational mass of the simulated system.

These BSSN-OK equations are implemented in the Einstein Toolkit in the `McLachlan` thorn [54, 212], auto-generated as highly efficient vectorized code from a Mathematica script written in tensorial notation with `Kranc` [213]. The spatial partial derivatives in the right hand sides of equations are computed with a fourth order finite differencing representation: given f_n the value of a function f in the n-th grid point in the x-direction, for example, its derivative is expressed as:

$$\partial_x f = \frac{1}{12} f_{n-2} - \frac{2}{3} f_{n-1} + \frac{2}{3} f_{n+1} - \frac{1}{12} f_{n+2}. \tag{3.49}$$

The advection terms $\beta^i \partial_i$, instead, are computed using a fourth order upwind scheme, instead of a centred differences, to have a better numerical stability. Finally, Kreiss-Oliger fifth-order dissipation

[214] is applied to the evolved curvature variables, with a strength of $\epsilon_{diss} = 0.01$, in order to damp high-frequency oscillations.

The BSSN-OK system of evolution equations must be supplemented by suitable boundary conditions at the external edges of the computational grid. This is a non-trivial problem in numerical relativity, because one wants to obtain a stable evolution at the boundary, with constraints preservation, and more importantly, one wants that gravitational waves will propagate out of the grit and will not be reflected back inside. Or, stated differently, one wants to impose a no-incoming-radiation boundary condition. In the Einstein Toolkit this is done in an approximated way adopting Sommerfeld-type radiative boundary conditions [215]: for each evolved variable tensor component X, the main part of the boundary condition looks like

$$X = X_0 + \frac{u\,(r - v_0 t)}{r}, \tag{3.50}$$

behaving like an outgoing radial wave with speed v_0. Here u is a spherically symmetric perturbation and X_0 the component value at spatial infinity. This assumes that the waves at the boundary have a spherical wavefront, which is true if the boundary is far enough from the source. In practice, this condition is implemented deriving it in time and obtaining the following differential equation, which is easier to impose in a finite-difference code:

$$\partial_t X = -\frac{v_0 x^i}{r}\partial_i X - v_o \frac{X - X_0}{r}. \tag{3.51}$$

The spatial derivatives are computed with second order central finite differencing when possible, and with one-sided finite differencing otherwise. To account also for those parts in the solution which does not behave like a pure outgoing wave, the time derivative term $\partial_t X$ is modified with:

$$(\partial_i X)^* = \partial_t X + \left(\frac{r}{r - n^i \partial_i r}\right)^p n^i \partial_i \left(\partial_t X\right), \tag{3.52}$$

where n^i is the unit normal vector of the considered boundary face, and this correction decays with a power $p = 2$ of the radius in our simulations. These conditions are implemented in The Einstein Toolkit by the thorn `newrad`.

3.1.2 Z4 family formulations

An always-present concern during GR numerical simulations with BSSN-OK are the constraint violations either present in the initial data or developed during the numerical evolution. To alleviate this problem, a new formulation of the Einstein equations, the $Z4$ formulation, started being adapted for numerical relativity by different groups [216–220]. The $Z4$ formulation can be derived from the following Lagrangian, with a Palatini-type variational principle [221]

$$L = g^{\mu\nu}\left(R_{\mu\nu} + 2\nabla_\mu Z_\mu\right). \tag{3.53}$$

It possesses an extra vector term Z_μ in addition to the standard Hilbert action. This vector measures the distance of a solution from the Einstein equations, and the algebraic constraint $Z_\mu = 0$ takes the place of Hamiltonian (3.28) and momentum (3.29) constraints of the ADM formulation. In order to damp the constraints violation, extra terms can be introduced, to make Einstein's equation solutions

an attractor for the full $Z4$ system solutions. In covariant form, the $Z4$ system with constraint damping is:

$$R_{\mu\nu} + \nabla_\mu Z_\nu + \nabla_\nu Z_\mu + k_1 \left[n_\mu Z_\nu + n_\nu Z_\mu - (1+k_2) g_{\mu\nu} n_\rho Z^\rho \right] = \\ = 8\pi \left(T_{\mu\nu} - \frac{1}{2} g_{\mu\nu} T \right). \tag{3.54}$$

The coefficients k_i are linked to the characteristic times of the constraint violation decay. This system, as the original Einstein's equations, can be written in 3+1 form, and, then, it is possible to develop a conformal decomposition, similar to the one of BSSN-OK. Two different conformal Z4 formulations have been studied: the `CCZ4` formulation [220, 222], which retains the full equations and in this way is a covariant formulation, at the price of greater differences respect to BSSN-OK and the need to introduce an additional parameter k_3 to be able to evolve also spacetimes containing black holes and the `Z4c` [218, 219, 223] formulation, which retains only the principal part of the equations, in order to be as close as possible to BSSN-OK, but is not fully covariant and needs the introduction of ad-hoc constraint preserving boundary conditions in order to avoid constraint violations being reflected back inside the grid at the outer boundaries [224]. Since in `McLachlan` only the CCZ4 formulation is implemented, I will describe that in the following paragraphs.

After the standard BSSN-OK conformal decomposition, and the separation of traceless and trace parts, the CCZ4 systems is the following, where I have marked in red the terms added respect to standard BSSN-OK (3.41), and in blue the ones added for constraints violation damping:

$$\left(\partial_t - \beta^j \partial_j\right) K = -\gamma^{ij} \tilde{D}_i \tilde{D}_j \alpha + \alpha \left(R + K^2 + 2 D_i Z^i - 2\Theta K \right) + \\ - 3\alpha k_1 (1+k_2) \Theta + 4\pi \left(e + \gamma^{ij} S_{ij} \right) \tag{3.55}$$

$$\left(\partial_t - \beta^j \partial_j\right) \phi = -\frac{1}{6} \left(\alpha K - \partial_k \beta^k \right) \tag{3.56}$$

$$\left(\partial_t - \beta^j \partial_j\right) \hat{\Gamma}^i = -2\tilde{A}^{ij} \partial_j \alpha + 2\alpha \left[\tilde{\Gamma}^i_{kl} \tilde{A}^{kl} + 6 \tilde{A}^{ij} \partial_j \phi - \frac{2}{3} \tilde{\gamma}^{ij} \partial_j K \right] + \\ + 2\tilde{\gamma}^{ki} \left(\alpha \partial_k \Theta - \Theta \partial_k \alpha - \frac{2}{3} \alpha K Z_k \right) + 2k_3 \left(\frac{2}{3} \tilde{\gamma}^{ij} Z_j \partial_k \beta^k - \tilde{\gamma}^{jk} Z_j \partial_k \beta^i \right) + \\ - \tilde{\Gamma}^j \partial_j \beta^i + \frac{2}{3} \tilde{\Gamma}^i \partial_j \beta^j + \frac{1}{e} \tilde{\gamma}^{ik} \partial_j \partial_k \beta^j + \tilde{\gamma}^{jk} \partial_j \partial_k \beta^i - 16\pi\alpha \tilde{\gamma}^{ik} j_k \tag{3.57}$$

$$\left(\partial_t - \beta^j \partial_j\right) \tilde{\gamma}_{ij} = -2\alpha \tilde{A}_{ij} + 2\tilde{\gamma}_{k(i} \partial_{j)} \beta^k - \frac{2}{3} \tilde{\gamma}_{ij} \partial_k \beta^k \tag{3.58}$$

$$\left(\partial_t - \beta^j \partial_j\right) \tilde{A}_{ij} = e^{-4\pi} \left[\alpha \tilde{R}^\phi_{ij} - \tilde{D}_i \tilde{i}_j \alpha + D_i Z_j + D_j Z_i \right]^{TF} + \\ + \alpha \tilde{A}_{ij} \left(K - 2\Theta \right) - 2\alpha \tilde{A}_{ki} \tilde{A}^k_j + 2 \tilde{A}_{k(i} \partial_{j)} \beta^k - \frac{2}{3} \tilde{A}_{ij} \partial_k \beta^k - 8\pi\alpha e^{-4\pi} S^{TF}_{ij} \tag{3.59}$$

$$\left(\partial_t - \beta^j \partial_j\right) \Theta = \frac{1}{2} \alpha \left(R + 2 D_i Z^i - \tilde{A}_{ij} \tilde{A}^{ij} + \frac{2}{3} K^2 - 2\Theta K \right) - Z^i \partial_i \alpha + \\ - \alpha k_1 (2 + k_2) \Theta - 8\pi\alpha e. \tag{3.60}$$

The four-vector Z^μ have been separated in Z_i and $\Theta = Z_0$. The conformal connections has been substituted by $\hat{\Gamma}^i := \tilde{\Gamma}^i + 2\gamma^{i\tilde{j}} Z_j$. In this particular implementation, in the equation for the trace of the extrinsic curvature K the Ricci scalar is not substituted using the Hamiltonian constraint. This is done, instead, in the Z4c formulation. The 1+log and Gamma-freezing gauge conditions must

also be slightly modified, to account for the new variables:

$$\partial_t \alpha - \beta_j \partial^j \alpha = -2\alpha \left(K - 2\Theta\right) \tag{3.61}$$

$$\partial_t \beta^i - \beta_j \partial^j \beta^i = \frac{3}{4} B^i \tag{3.62}$$

$$\partial_t B^i - \beta_j \partial^j B^i = \partial_t \hat{\Gamma}_i - \beta_k \partial^k \hat{\Gamma}^i - \eta B^i \tag{3.63}$$

The term with k_3 has been added in [220] to alleviate numerical instabilities in evolving black holes: a value $k_3 = 1$ is used to keep full covariance, while a value $k_3 = \frac{1}{2}$ makes the black hole evolution possible. This is not necessary, instead, in the Z4c formulation.

The Z4 family formulations bring two main advantages over BSSN-OK: first, it is possible to define a natural constraint-damping scheme for every constraint, which is not the case for BSSN. This is useful, for example, when evolving constraint-violating initial data, as done for example in [57] for evolving spinning binary neutron stars. The constraint violations get dumped quickly by at least a couple of orders of magnitude respect to BSSN-OK. Second, the constraint subsystem in BSSN-OK has a characteristic with speed 0. This means that constraint violations remain on the numerical grid where they are generated by numerical errors, and do not propagate. This is a problem when evolving a physical system for which the interesting parts are always at the same grid locations, like a single star or black hole, for example after the merger of a BNS system. In the Z4 formulation, instead, all the constraint characteristics have a speed of ± 1. This means that the generated constraint violations propagate out of the numerical grid with the speed of light.

One disadvantage of the CCZ4 formulation, already discussed in [220], and confirmed by our simulations (see ref. [68] and appendix A.1) is that a higher resolution is needed to enter in the convergent regime, respect to BSSN-OK, because the Hamiltonian constraint, even if damped, enters directly in the evolution equations, while is assumed to be fully satisfied and as such put to zero in the BSSN-OK equations. Another possible problem of all Z4-family formulations is the choice of a correct value for the damping parameters. In our simulations, following [222], we used $k_1 = 0.05$, $k_2 = 0$ and $k_3 = 1$.

3.2 Matter evolution

For simulating neutron stars, the spacetime evolution described in the previous section must be coupled with the hydrodynamical evolution for the matter. Working always in a 3+1 decomposition framework, with a spacetime metric given by eq. (3.25), an additional important variable to consider is the fluid four-velocity u^μ (which, from a different point of view, is the velocity of an observer comoving with the fluid), which, like the Eulerian observer velocity n^μ, has module $u^\mu u_\mu = -1$ and is timelike. The GRHD equations will be written in the Eulerian observer reference frame, so it is also important to consider the spatial projection v^i on each hypersurface Σ_t of the fluid four-velocity measured by the Eulerian observer. This is given by

$$v^i = \frac{\gamma^i_\mu u^\mu}{-u^\mu n_\mu} = \frac{1}{\alpha}\left(\frac{u^i}{u^0} + \beta^i\right). \tag{3.64}$$

It is interesting to note that in the case $\alpha = 1$ and $\beta^i = 0$ one recovers the special relativistic expression $v^i = \frac{dx^i}{dt} = \frac{u^i}{u^0}$, with $u^i = \frac{dx^i}{d\tau}$. With simple algebra, using the unitary of the u^μ module,

it is easy to show that

$$\alpha u^0 = \frac{1}{\sqrt{1 - v_i v^i}} := W, \tag{3.65}$$

where we have defined W as the Lorenz factor of the fluid.

The next step is to consider the ideal-fluid energy momentum tensor:

$$T^{\mu\nu} = \rho h u^\mu u^\nu + p g^{\mu\nu}, \tag{3.66}$$

where ρ is the mass density (contrary to the notation often used in the astrophysics literature, where the letter ρ indicates the energy density), $h = 1 + \epsilon + \frac{p}{\rho}$ is the relativistic specific enthalpy, ϵ is the specific energy density and p is the pressure. The equations to solve for evolving the hydrodynamical variables are:

$$\nabla_\mu T^{\mu\nu} = 0 \tag{3.67}$$

$$\nabla_\mu (\rho u^\mu) = 0, \tag{3.68}$$

where (3.67) is the energy-momentum conservation and (3.68) is the baryon number conservation. This system of equations should be closed with a choice for the matter EOS (see sec. 2.1.1 for a discussion about the neutron star EOS and its piecewise polytropic approximation often used in numerical relativity), in the form $p = p(\rho, \epsilon, ...)$.

The code `GRHydro` [225], which is the official, open source, GRHD module in `The Einstein Toolkit`, uses the so called *Valencia formulation* of the GRHD equations [77, 79, 226–229]. It is a conservative formulation, in which instead of the "natural" five *primitive* variables $\left(\rho, \epsilon, v^i\right)$ a set of derived *conserved* variables is evolved, in order to be able to write the hydrodynamics equation in the conservative form

$$\partial_t \mathbf{U} = \partial_i \mathbf{F}^{(i)}(\mathbf{U}) + \mathbf{S}(\mathbf{U}), \tag{3.69}$$

where $\mathbf{U}$ is the state vector containing the five conserved variables, $\mathbf{F}^i$ are the flux vectors, one for each direction, and $\mathbf{S}$ is the source vector, which does not contain derivatives of the state vector variables. A conservative (and strongly hyperbolic) formulation for the evolution equations helps with their numerical implementation, since any finite differences algorithm will automatically conserve the conserved variables in the theory and, moreover, thanks to Lax-Wendroff 1960 theorem, the numerical solution, if the code is in a convergent regime, will converge to a weak solution of the system (a solution to its integral representation). The conservative formulation is an essential hypothesis for this theorem [230]. The Valentia formulation conserved variables are:

$$\begin{pmatrix} D = \sqrt{\gamma} W \rho \\ S_j = \sqrt{\gamma} \rho h W^2 v_j \\ \tau = \sqrt{\gamma}(\rho h W^2 - p) - D. \end{pmatrix} \tag{3.70}$$

The corresponding fluxes are:

$$F^i = \begin{pmatrix} D(\alpha v^i - \beta^i) \\ S_j(\alpha v^i - \beta^i) + p\delta^i_j \\ \tau(\alpha v^i - \beta^i) + p v^i \end{pmatrix} \tag{3.71}$$

And, finally, their source terms:

$$S = \begin{pmatrix} 0 \\ T^{\mu\nu}\left(\partial_\mu g_{\nu j} + \Gamma^\sigma_{\mu\nu} g_{\sigma j}\right) \\ \alpha\left(T^{\mu 0}\partial_\mu \log\alpha - T^{\mu\nu}\Gamma^0_{\nu\mu}\right) \end{pmatrix}. \tag{3.72}$$

Besides obtaining convergence to the right physical solution and conservation in the numerical evolution of the physically conserved variables, another requisite for an evolution scheme for hydrodynamics is the ability to treat consistently also solutions with shocks. Any non-linear, hyperbolic, PDE can develop shocks even starting from smooth initial data. Therefore we need a numerical algorithm able to capture efficiently those shocks, without crashing the computer code or loosing accuracy. The starting point is a finite-volume scheme, which helps both highlighting the conservation properties of the system and dealing with discontinuous solutions. Its main point is evolving, instead of the point-valued conserved variables U, their volume average in a numerical cell

$$\bar{U} = \frac{1}{\Delta V}\int_{x^1}^{x^1+\Delta x^1}\int_{x^2}^{x^2+\Delta x^2}\int_{x^3}^{x^3+\Delta x^3} U dx^1 dx^2 dx^3. \tag{3.73}$$

Integrating equation (3.69) in a spatial numerical cell, and using Gauss divergence theorem, one gets:

$$\begin{aligned}\partial_t \bar{U}(\vec{x},t) = &-\frac{1}{\Delta x^1}\left(\bar{F}_{23}(x^1+\Delta x^1) - \bar{F}_{23}(x^1)\right) - \frac{1}{\Delta x^2}\left(\bar{F}_{13}(x^2+\Delta x^2) - \bar{F}_{13}(x^2)\right) + \\ &-\frac{1}{\Delta x^3}\left(\bar{F}_{12}(x^3+\Delta x^3) - \bar{F}_{12}(x^3)\right) + \bar{S}(\vec{x},t),\end{aligned} \tag{3.74}$$

where $\bar{F}_{ij}$ is the surface average of the flux F on the i,j boundary face of the numerical cell volume:

$$\bar{F}_{ij}(x^k) = \int_{x^i}^{x^i+\Delta x^i}\int_{x^j}^{x^j+\Delta x^j} F(\tilde{x}^i,\tilde{x}^j,x^k) d\tilde{x}^i d\tilde{x}^j. \tag{3.75}$$

In order to show, in a simplified way, the key idea of the shock-capturing algorithm adopted in `GRHydro` (the so called "Godunov method", developed by Godunov in an appendix of his Ph.D. thesis [231]), it is useful to integrate eq. 3.74 also in time, in the arbitrary interval $[t_n, t_n+1]$:

$$\begin{aligned}\bar{U}_{ijk}(t^{n+1}) = \bar{U}_{ijk}(t^n) &+ \frac{\Delta t}{\Delta x^i}\left(\hat{F}_{i+1/2jk} - \hat{F}_{ijk}\right) + \frac{\Delta t}{\Delta x^j}\left(\hat{F}_{ij+1/2k} - \hat{F}_{ijk}\right) + \\ &+\frac{\Delta t}{\Delta x^k}\left(\hat{F}_{ijk+1/2} - \hat{F}_{ijk}\right) + \int S d^3x dt,\end{aligned} \tag{3.76}$$

where $\hat{F}_{ijk}$ is the *numerical flux function*:

$$\hat{F}_{ijk} = \frac{1}{\Delta t}\int_{t^n}^{t^{n+1}} \bar{F}_{ijk} dt. \tag{3.77}$$

Equation 3.76 is a recipe to evolve forward in time the hydrodynamical conserved variables from the time-level t^n to the time-level t^{n+1}, but it is not (yet) a numerical scheme, it's an analytical expression obtained without any approximation. In order to compute the evolved variables at t^{n+1}, however, one needs to know the time-averaged flux $\hat{F}$ on each surface of the considered numerical cell boundary, which depends on the solution for conserved variables at times $t > t^n$. In order to construct an appropriate numerical evolution scheme, one needs an approximation for $\hat{F}$, which is robust to the presence of shocks in the solution. Godunov's idea was to compute $\hat{F}$ using the solution of a one dimensional Riemann problem at each boundary in each Cartesian direction. The Riemann problem is given by a one dimensional conservation-form hyperbolic PDE (like 3.69, but

without any source term), with the following discontinuous initial conditions (around the separation face $x = x_0$):

$$\bar{U}(x, t_0 = 0) = \left\{ \begin{array}{lll} U_L & if & x < x_i \\ U_R & if & x > x_i \end{array} \right\}. \tag{3.78}$$

The Riemann problem is invariant under similarity transformations:

$$(x, t) = (ax, at), a > 0, \tag{3.79}$$

and, therefore, its solution is self-similar and depends on the variable $\frac{x-x_0}{t-t_0}$. The solution of a Riemann problem for the hydrodynamics equations consists of constant states separated by rarefaction waves (continuous self-similar solutions of the PDE), shock waves (where all hydrodynamical primitive variables are discontinuous) and contact discontinuities (where only the density is discontinuous and all other variables are continuous, like the neutron stars surface). This solution strategy imposes a Courant factor (see sec. 3), because the time step should be sufficiently small not to allow waves from neighbouring cells interfaces to interact:

$$\Delta t < \frac{\Delta x}{|v_{max}|}, \tag{3.80}$$

where v_{max} is the maximum wave speed in any point of the grid at a given time step.

The original first-order Godunov's scheme used eq. 3.76 for the time evolution, computing the numerical fluxes solving Riemann problems at cells faces with initial conditions given by a piecewise constant reconstruction: each conserved variable, inside each cell (and therefore also at the cell boundary, from the appropriate side) takes a constant value equal to its cell volume average.

To go beyond first-order convergence, one has to adopt a *High Resolution Shock Capturing* scheme (HRSC). First of all, in our finite-volume approach, one can approximate cell volume averages $\bar{U}$ and face surface averages $\bar{F}$ with their point-values at the numerical grid cell and face centres (U_{ijk} and F_{jk} respectively). This is exact up to second order in space (in the sense that the error made with this approximation is proportional to $(\Delta x)^2$). This is the approach adopted in `GRHydro`, and in all current finite-volume GRHD codes. To go beyond second order convergence, one has to include additional (complicated) steps to compute from the evolved volume-averaged conserved variables their values at each grid point at the desired approximation order (because they are used in the energy-momentum tensor for the finite-difference curvature evolution, see sec. 3), and also compute, from the point-valued fluxes given by the Riemann problem solution, the face-averaged numerical fluxes to be used in eq. 3.76 [232]. For this reason, the only GRHD codes formally able to go beyond second order convergence adopt a different finite differences Flux-Vector Splitting approach [96, 98, 233].

To increase the temporal resolution, in HRSC methods one adopts the Method of Lines (see sec. 3) starting from eq. 3.74. The numerical flux terms $\hat{F}$ are computed as solutions of a Riemann problem also in this case, because, thanks to their self-similarity property, they are guaranteed to be constant in time at the cell interface $x = x_0$. In the most recent numerical relativity works a fourth order RK method is often chosen also for the hydrodynamical variables. Even if second and third order RK methods adapted to keep the equation conservation properties exist, following most of the recent literature we found global lower errors adopting the same (and the highest-order possible, given the highest spatial finite difference order adopted) RK method for both the spacetime and the matter evolution (see [84, 179]).

To increase the spatial resolution beyond first order, instead, different reconstruction methods have been developed, in order to compute the initial values U_L and U_R for the Riemann problem, at the left and right interface of each cell boundary, from the cells volume averages. The common structure of these methods is the reconstruction of the internal profile of primitive variables inside each numerical cell with a polynomial interpolation. From these profiles, the limits at the cell boundaries P_L and P_R are computed, and from them the corresponding conserved variables. The polynomial reconstructions are supplemented with some kind of limiter, which limits the reconstruction profile slope, reducing the method to first order convergence near shocks. These limiters allows to overcome the limitations of Godunov's theorem, which states that any linear, higher than first order, reconstruction method may induce spurious oscillations near shocks.

In particular for this thesis were tested the Piecewise Parabolic method (PPM) [234], which is third order convergent in smooth flows, the Monotonicity Preserving method (MP5) [235], fifth order, and the Weighted Essentially Not Oscillatory method (WENO) [236, 237], also fifth order convergent. The latter was proven to be the best for archiving global second order convergence even at very poor resolutions in [68] (see appendix A.1, but also refs.[11, 98, 238] for similar findings about the WENO method). As explained in [225, 239], the use of a at least N^{th} order convergent ODE solver for the time evolution and an at least N^{th} order space discretization algorithm guarantees a global N^{th} order convergence (both are prerequisites, since the time and space discretization steps are linked by the Courant condition 3.8) in a MoL framework, if the right hand side in eq. 3.69 is first order convergent in time. The use of a Riemann problem solution to evaluate the fluxes at cell boundaries allows this final condition to hold.

To summarize the last section, the evolution of the GRHD equations in `The Einstein Toolkit` procedes as follows:

1. The source terms are computed from the primitive variables at cells centres;
2. The primitive variables are reconstructed to the left and right states near the cell faces;
3. The conserved variables are computed from the reconstructed primitives with simple algebraic expressions;
4. A Riemann solver algorithm finds an approximate solution to the Riemann problem at each interface, using the conserved variables right and left reconstructed states as initial conditions. The Riemann problem is solved independently along each spatial directions, finding all the flux components $\bar{F}^i$ of eq. 3.74;
5. The source and flux terms are summed up to build the right hand sides for the MoL time evolution;
6. At the same time, the primitive variables values at cell centres are used to construct the energy-momentum tensor, with which the right hand sides of BSSN-OK evolution equations are computed;
7. Both hydrodynamical conserved variables and curvature variables are evolved in time with a forth-order Runge-Kutta method;
8. From the cells centres values of the conserved variables in the new time-step the new primitive variables are computed, with a root-finding procedure, which checks also if they lie in a physically acceptable range.

3.2.1 Reconstruction methods

PPM

The first reconstruction method that was tried, is the widely adopted PPM, which is still the most common choice for numerical relativity codes (as, for example, [239, 240]), and which was already used by the Parma gravitational physics group in single-star simulations [173, 175]. The original PPM algorithm is slightly modified in `GRHydro`, adopting a formulation specialised to evenly-spaced grids, using the simplest dissipation algorithm and an approximated flattening algorithm which needs only three stencil points instead of the four of the original procedure.

The core of the PPM reconstruction is the interpolation of the reconstructed primitive variable a with a quadratic polynomial:

$$a_{i+1/2} = \frac{1}{2}(a_{i+1} + a_i) + \frac{1}{6}(\delta a_i - \delta a_{i+1}), \tag{3.81}$$

where δa_i is given by the approximation:

$$\delta a_i = min(\frac{1}{2}\left|a_{i+1} - a_{i-1}\right|, 2\left|a_{i+1} - a_i\right|, 2\left|a_i - a_{i-1}\right|) \cdot sign(a_{i+1} - a_{i-1}) \tag{3.82}$$

when

$$(a_{i+1} - a_i)(a_i - ai - 1) > 0$$

and is zero otherwise.

After this first step, the right and left states are equal $a_i^R = a_{i+1}^L = a_{i+1/2}$, and the solution will be third order convergent in space for smooth flows. This, however in not strictly monotonicity preserving (it could create new extrema in the reconstructed profile, which were not extrema of the original variable profile). In particular, it can happen that the interpolated a_i is not between a_i^L and a_i^R. Such problem arises when a_i is a local maximum or minimum, or when it is close to one of the reconstructed face averages, and then the interpolating parabola "overshoots". In such cases the reconstructed variables are modified:

$$a_i^L = a_i^R = a_i \text{ if } (a_i^R - a_i)(a_i - a_i^L) \leq 0 \tag{3.83}$$

$$a_i^L = 3a_i - 2a_i^R \text{ if } (a_i^R - a_i^L)\left(a_i - \frac{1}{2}(a_i^R + a_i^L)\right) > \frac{1}{6}\left(a_i^R - a_i^L\right)^2 \tag{3.84}$$

$$a_i^R = 3a_i - 2a_i^L \text{ if } (a_i^R - a_i^L)\left(a_i - \frac{1}{2}(a_i^R + a_i^L)\right) < -\frac{1}{6}\left(a_i^R - a_i^L\right)^2. \tag{3.85}$$

Before the monotonicity preserving procedure, another two steps may be applied: first, contact discontinuities could be steepened, to ensure sharp solution profiles. Next, a flattening procedure near shocks is applied, in order to reduce the convergence in that case towards first order (locally), and avoid oscillations in the solution. The reconstructed variables are modified as follows:

$$a_i^{L,R} = \nu_i a_i^{L,R} + (\nu_i) a_i, \tag{3.86}$$

where ν_i is an additional advection velocity, which produces the extra dissipation needed for avoiding oscillations near shocks:

$$\nu_i = max\left(0, 1 - max\left(0, \omega_2\left(\frac{p_{i+1} - p_{i-1}}{p_{i+2} - p_{i-2}} - \omega_1\right)\right)\right), \tag{3.87}$$

and, instead, $\nu_i = 1$ in smooth flows. The criteria for detecting a shock in this case are:

$$\omega_0 \; min(p_{i-1}, p_{i+1}) < |p_{i+1} - pi - 1| \;\; \textbf{and} \;\; v^x_{i-1} - v^x_{i+1} > 0. \tag{3.88}$$

This procedure is different from the original one of [234], but requires only thee points stencils, instead of four points ones, which would increase considerably the computational cost, especially when using mesh refinement.

MP5

Another reconstruction method which recently received some attention is the MP5 method [235]. It was adopted in the first higher-than-second order GRHD code [96, 233] and was found to be the most accurate in a simple single TOV star test in the `GRHydro` presentation paper [225]. MP5 is based on a fifth-order polynomial interpolation, followed by a limiter designed to keep high order convergence also near solution extrema, distinguishing them from shocks, which is not possible to do in third-order methods like PPM, and to preserve monotonicity when adopting a Runge-Kutta scheme for the time evolution. The core interpolation is given by:

$$a^L_{i+1/2} = \frac{1}{60}\left(2a_{i-2} - 13a_{i-1} + 47a_i + 27a_{i+1} - 3ai + 2\right). \tag{3.89}$$

The condition regulating if a limiter is applied is:

$$\left(a^L_{i+1/2} - a_i\right)\left(a^L_{i+1/2} - a^{MP} \leq 0\right) \tag{3.90}$$

$$a^{MP} := a_i + minmod\left(a_{i+1} - a_i, \alpha(a_i - a_{i-1})\right), \tag{3.91}$$

where $\alpha = 4$ is used. The minmod limiter function is given by:

$$minmod(x, y) = \frac{1}{2}(sign(x) + sign(y))min(|x|, |y|) \tag{3.92}$$

$$minmod(w, x, y, z) = \frac{1}{8}(sign(w) + sign(x))\,|(sign(w) + sign(y))(sign(w) + sign(z))| \times \\ \times\, min(|w|, |x|, |y|, |z|). \tag{3.93}$$

If eq. 3.90 is satisfied, a limiter is applied. To set it, four combinations of the interpolated variable are built:

$$a^{AV} = \frac{1}{2}(a_i + a_{i+1}) \tag{3.94}$$

$$a^{UL} = a_i + \alpha(a_i - a_{i+1}) \tag{3.95}$$

$$a^{MD} = a^{AV} - \frac{1}{2}D^{M4}_{i+1/2} \tag{3.96}$$

$$a^{LC} = a_i + \frac{1}{2}(a_i - ai - 1) + \frac{4}{3}D^{M4}_{i-1/2}. \tag{3.97}$$

a^{AV} stands for AVerage, a^{UL} for Upper Limit, a^{MD} for MeDian and a^{LC} for Large Curvature. $D^{M4}_{i\pm1/2}$ are built, instead, starting from finite-difference expressions for the second derivatives of the

reconstructed field:

$$D_i^- = a_{i-2} - 2a_{i-1} + a_i \tag{3.98}$$
$$D_i^0 = a_{i-1} - 2a_i + a_{i+1} \tag{3.99}$$
$$D_i^+ = a_i - 2a_{i+1} + a_{i+2} \tag{3.100}$$
$$D_{i+1/2}^{M4} = minmod\left(4D_i^0 - d_i^+, 4D_i^+ - D_i^0, D_i^0, D_i^+\right) \tag{3.101}$$
$$D_{i-1/2}^{M4} = minmod\left(4D_i^0 - d_i^-, 4D_i^- - D_i^0, D_i^0, D_i^-\right). \tag{3.102}$$

From those field combinations one can write the limited reconstructed variable:

$$a_{i+1/2}^L = a_{i+1/2}^L + minmod\left(a_{min} - a_{i+1/2}^L, a_{max} - a_{i+1/2}^L\right), \tag{3.103}$$

where

$$U_{min} = max(min(a_i, a_{i+1}, a^{MD}), min(a_i, a^{UL}, a^{LC})) \tag{3.104}$$
$$U_{max} = min(max(a_i, a_{i+1}, a^{MD}), max(a_i, a^{UL}, a^{LC})). \tag{3.105}$$

To obtain the reconstructed variables at the right interface, instead, it is sufficient to use the same algorithm, substituting $\{a_{i-2}, a_{i-1}, a_i, a_{i+1}, a_{i+2}\}$ with $\{a_{i+2}, a_{i+1}, a_i, a_{i-1}, a_{i-2}\}$.

WENO

The WENO reconstruction is an improvement on the Essentially Non Oscillatory (ENO) method [241]. In the original ENO method, two interpolation polynomials, with different stencils, are used. Then, based on the field smoothness, one of the two is selected, in order to avoid the one containing the discontinuous solution near shocks. This idea allows to keep high order convergence even near shocks and local extrema, which is not possible with single stencil methods with limiters like PPM and MP5. However, selecting just one of the stencils, the ENO method does not archive the maximum convergence order for the number of stencil points used, and is computationally intensive, requiring a lot of logical operations. The idea behind the WENO method (first developed in [236] and improved to reach fifth order convergence in [237]) is to use a combination of all the possible ENO reconstruction stencils, each weighed accordingly, with weight that tend to zero in the case of a discontinuity present in the corresponding stencil.

$$a_{i+1/2}^{L,1} = \frac{3}{8}a_{i-2} - \frac{5}{4}a_{i-1} + \frac{15}{8}a_i \tag{3.106}$$
$$a_{i+1/2}^{L,2} = -\frac{1}{8}a_{i-1} + \frac{3}{4}a_i - \frac{3}{8}a_{i+1} \tag{3.107}$$
$$a_{i+1/2}^{L,3} = \frac{3}{8}a_i + \frac{3}{4}a_{i+1} - \frac{1}{8}a_{i+2}. \tag{3.108}$$

Each of these approximations is third-order convergent, but an appropriate combination, spanning all the 5 points stencil from a_{i-2} to a_{i+2}, is fifth order convergent, when the weights w^i are all different from zero:

$$a_{i+1/2}^L = w^1 a_{i+1/2}^{L,1} + w^2 a_{i+1/2}^{L,2} + w^3 a_{i+1/2}^{L,3}. \tag{3.109}$$

WENO weights have sum one $\sum_i w^i = 1$ and are chosen starting from the so called *smoothness indicators* β^i:

$$\beta^1 = \frac{1}{3}\left(4a_{i-2}^2 - 19a_{i-2}a_{i-1} + 25a_{i-1}^2 + 11a_{i-2}a_i - 31a_{i-1}a_i + 10a_i^2\right) \tag{3.110}$$

$$\beta^2 = \frac{1}{3}\left(4a_{i-2}^2 - 13a_{i-1}a_i + 13a_i^2 + 5a_{i-1}a_{i+1} - 13a_ia_{i+1} + 4a_{i+1}^2\right) \tag{3.111}$$

$$\beta^3 = \frac{1}{3}\left(10a_i^2 - 31a_ia_{i+1} + 25a_{i+1}^2 + 11a_ia_{i+2} - 19a_{i+1}a_{i+2} + 4a_{i+2}^2\right). \tag{3.112}$$

From the smoothness indicators, the weights are obtained as follows:

$$w^i = \frac{\bar{w}^i}{\sum_i \bar{w}^i} \tag{3.113}$$

$$\bar{w}^i = \frac{\gamma^i}{(\epsilon + \beta^i)^2} \tag{3.114}$$

$$\gamma^i = \left\{\frac{1}{16}, \frac{5}{8}, \frac{5}{16}\right\}. \tag{3.115}$$

The problem with this weights is that ϵ is scale-dependent, and therefore setting a fixed value for it could lead to problems in simulating physical systems with a large variation in relevant scales (such as problems where turbulence or hydrodynamical instabilities are present). A solution to this was found in [242], and is adopted also in `GRHydro`: modified smoothness indicators are used, which depend on the scale of the reconstructed field, measured by its L^2 norm in the considered stencil $||a^2||$. The new smoothness indicators are:

$$\bar{\beta}^i = \beta^i + \epsilon\left(||a^2|| + 1\right). \tag{3.116}$$

In `GRHydro` a default value of $\epsilon = 1 \times 10^{-26}$ is used. As mentioned before, a stencil weights will go to zero (and, therefore, the corresponding stencil smoothness indicator will tend to infinity) when a discontinuity in the reconstructed field is present in its points, adaptively reducing the convergence order when needed, but keeping at least third order convergence near shocks.

3.2.2 The Riemann solver

In the Parma relativity group simulations (analysed in chapter 4), the approximate Riemann solver from Harten, Lax, van Leer and Einfeld (HLLE) [243, 244] was used (following what is done in most GRHD codes), because it is not computationally expensive, it is robust (see for example a comparison with the more accurate Marquina solver in [245], where the robustness of HLLE was found to be important for avoiding constraint violations at the boundary of the EOS politropic pieces (see sec. 2.1.1)), and because it is the only Riemann solver in `GRHydro` already extended for GRMHD evolutions, making it easier to develop a follow-up project including also magnetic fields. Differently for other common Riemann solvers (like the Roe and Marquina solvers), which use the so called *local characteristics approach* [77, 226, 228], based on the Jacobian matrices spectral decomposition of a linearisation of the GRHD equations (considering all five characteristics of GRHD), HLLE uses a two wave approximations, considering only the maximum and minimum wave speeds V_+ and V_-

at both sides of an interface, which generate a single state between them. The Riemann problem solution for a conserved variable U, in a point labelled by the variable $\xi = \frac{(x-x_{interface})}{\Delta t}$ is then:

$$U = \begin{cases} U_L & if \quad \xi < V_- \\ U^{HLLE} & if \quad V_- < \xi < V_+ \\ U_R & if \quad \xi > V^+ \end{cases} \tag{3.117}$$

The intermediate state U^{HLLE} can be computed starting from a one-dimensional form of eq. 3.76 in a control volume around the considered cell interface:

$$\int_{x_L}^{x_R} U(x, t+\Delta t)dx = \int_{x_L}^{x_R} U(x,t)dx + \int_t^{t+\Delta t} F(U(x_L,t')dt' - \int_t^{t+\Delta t} F(U(x_R,t')dt'. \tag{3.118}$$

The right hand side can be directly evaluated using the reconstructed variables U_L and U_R and the corresponding fluxes $F_L = F(U_L)$ and $F_R = F(U_R)$:

$$\int_{x_L}^{x_R} U(x, t+\Delta t)dx = x_R U_R - x_L U_L + \Delta t(F_L - F_R). \tag{3.119}$$

The left hand side, instead, can be divided into three parts, one at the left of the fastest left-going wave, one between the two waves, and one at the right of the fastest right-going wave:

$$\begin{aligned} \int_{x_L}^{x_R} U(x, t+\Delta t)dx = &\int_{x_L}^{\Delta t V^-} U(x, t+\Delta t)dx + \int_{\Delta t V^-}^{\Delta t V^+} U(x, t+\Delta t)dx + \\ &+ \int_{\Delta t V^+}^{x_R} U(x, t+\Delta t)dx = \\ &= \int_{\Delta t V^-}^{\Delta t V^+} U(x, t+\Delta t)dx + (\Delta t V^- - x_L)U_L + (x_R - \Delta t V^+)U_R. \end{aligned} \tag{3.120}$$

Inserting this result into eq. 3.119 and dividing both terms by $\Delta t(V^+ - V^-)$ one gets, finally, an expression for the average exact Riemann problem solution between the slowest and the fastest wave at time $t + \Delta t$, which is used as definition for the HLLE intermediate state:

$$U^{HLLE} = \frac{1}{\Delta t(V^+ - V^-)} \int_{\Delta t V^-}^{\Delta t V^+} U(x, t+\Delta t)dx = \frac{V^+ U_R - V^- U_L + F_L - F_R}{V^+ - V^-}. \tag{3.121}$$

To get from those solution states the corresponding numerical fluxes, one needs to invoke the *Rankine-Hugoniot* condition: given a shock propagating along $s(t)$ with speed $V = \frac{ds(t)}{dt}$, its flux functions are related with its states by

$$F(U(s_L,t)) - F(U(s_R,t)) = V\left(U(s_L,t) - U(s_R,t)\right). \tag{3.122}$$

It is straight-forward to derive eq. 3.122, starting from a one-dimensional representation of eq. 3.74 between x_L and x_R, splitting the left hand side in two parts, one on the left of the discontinuity $s(t)$ and the other on its right:

$$\frac{d}{dt}\int_{x_L}^{s(t)} U(x,t)dx + \frac{d}{dt}\int_{s(t)}^{x_R} U(x,t)dx = F(U(x_L,t)) - F(U(x_R,t)). \tag{3.123}$$

Using the formula for moving a time derivative inside an integral, one gets:

$$F(U(x_L,t))-F(U(x_R,t)) = V\left(U(s_L,t)-U(s_R,t)\right)+\int_{x_L}^{s(t)}\partial_t U(x,t)dx+\int_{s(t)}^{x_R}\partial_t U(x,t)dx. \quad (3.124)$$

Taking the limits $x_R \to s(t)$ and $x_L \to s(t)$, one recovers the Rankine-Hugoniot condition (3.122). Applying it to eq. 3.117, between the left and the intermediate state, or between the intermediate and the right state, one obtains to equivalent expressions for the HLLE numerical flux function:

$$F^{HLLE} = F_L + V^-\left(U^{HLLE}-U_L\right) \quad (3.125)$$

$$F^{HLLE} = F_R + V^+\left(U_R-U^{HLLE}\right). \quad (3.126)$$

Substituting the expression found for U^{HLLE} in eq. 3.119, one finally finds:

$$F^{HLLE} = \frac{V^+F_L - V^-F_R + V^+V^-(U_R-U_L)}{V^+-V^-}. \quad (3.127)$$

Of course, to get a numerical flux, one needs also to come up with a way for computing the minimum and maximum wave speeds. In `GRHydro` this is done computing the maximum and the minimum between all the analytically-computed eigenvalues of the GRHD system of equations using the left and right reconstructed states. Those eigenvalues, along the i-th direction, are [227]:

$$\lambda_0 = \alpha v^i - \beta^i (\text{triple}) \quad (3.128)$$

$$\lambda_\pm = \frac{\alpha}{1-v^2c_s^2}\left[v^i(1-c_s^2) \pm c_s\sqrt{(1-v^2)(\gamma^{ii}(1-v^2c_s^2)-v^iv^i(1-c_s^2))}\right]-\beta^i, \quad (3.129)$$

where $c_s^2 = \frac{\partial p}{\partial \rho}$ is the sound speed, computed from the equation of state. An important difference between these GR eigenvalues and the Euler's equations Newtonian ones is that in $\lambda_\pm$ (which in the Newtonian case are simply $\lambda_\pm^{Newt} = v^i \pm c_s$) there are also coupling with velocities in the other directions, through v^2.

3.2.3 Conservative to primitive conversion

The recovery of primitive variables from the evolved conservative ones, to be able to start the next time-evolution step, constructing the energy-momentum tensor and reconstructing hydrodynamical variables at cell interfaces, can not be done analytically, like the conversion from primitives to conservatives, but in pure hydrodynamics (without magnetic fields, or radiation) it is relatively straight-forward, requiring only a one-dimensional Newton-Raphson procedure to recover the unknown pressure.

First, the undensitised conserved variables are computed:

$$\hat{D} = \frac{D}{\sqrt{\gamma}} = \rho W \quad (3.130)$$

$$\hat{S}_i = \frac{S_i}{\sqrt{\gamma}} = \rho h W^2 v_i \quad (3.131)$$

$$\hat{\tau} = \frac{\tau}{\sqrt{\gamma}} = \rho h W^2 - P - \hat{D}. \quad (3.132)$$

Next, two additional auxiliary variables are defined:

$$Q := \rho h W^2 = \hat{\tau} + \hat{D} + P \tag{3.133}$$

$$\hat{S}^2 := \gamma_{ij}\hat{S}^i\hat{S}^j = (\rho h W)^2 \left(W^2\right) - 1, \tag{3.134}$$

where $\hat{S}^2$ is known from the evolved variables, and Q depends only on the unknown pressure P. Given the relation between Q and $\hat{S}$, one can construct expressions for the primitive variables ρ and ϵ which also depend only on P:

$$\rho = \frac{\hat{D}\sqrt{Q^2 - \hat{S}^2}}{Q} \tag{3.135}$$

$$\epsilon = \frac{\sqrt{Q^2 - \hat{S}^2} - PW - \hat{D}}{\hat{D}}, \tag{3.136}$$

where the Lorentz factor W can be expressed by:

$$W = \frac{Q}{\sqrt{Q^2 - \hat{S}^2}}. \tag{3.137}$$

Given an initial guess for the new pressure, one can compute the new density and specific energy density. Given those, a pressure value $P(\rho, \epsilon)$ can be computed using the EOS. With an iterative procedure such as the Newton-Raphson method, one will try to minimize the residual between the pressure value used to compute ρ and ϵ and the one obtained with the subsequent EOS call. This method, in particular, requires to know the pressure derivatives $\frac{\partial P}{\partial \rho}$ and $\frac{\partial P}{\partial \epsilon}$, which are given, again, by the equation of state. The *con2prim* routines are also responsible to check if the resulting primitive values are physical, for example if the pressure and the densities are positive, and if the velocities are less than one.

3.3 Initial data computation

Generating accurate initial data for binary neutron stars in quasi-circular orbits is a non-trivial first step, necessary for the fully dynamical evolution. In fact, the results of this work point to the presence of multiple errors in simulation results linked with the initial data computation technique (see sec. 4.1.1 and 4.1.2). For this thesis was used the only public code for BNS initial data, the `LORENE` library [53, 246].

BNS prior to the merger phase are believed to be in circular orbits, thanks to the circularization properties of the emitted gravitational radiation (see the predicted eccentricity values at $10Hz$ for the observed BNS binaries in table 2.3). Additionally, they will most likely be in an irrotational state, because the viscous forces are too weak and act on a time-scale too long respect to the gravitational radiation one in order to be able to successfully synchronize the stars spins with the orbital rotation. Initial data computation starts, therefore, assuming the existence of an *helicoidal* Killing vector, which, for an asymptotic inertial observer at rest respect to the binary, takes the form

$$I = \frac{\partial}{\partial t} + \Omega \frac{\partial}{\partial \phi}. \tag{3.138}$$

This assumption has important consequences, for example it implies ignoring the outgoing gravitational radiation, and its backreaction on the binary dynamics (since this radiation-reaction will enter in the post-Newtonian expansion at the 2.5PN order, this helicoidal symmetry can be exact up to 2PN). This is responsible for the lack of a radial component of the star velocity (which comes from radiation reaction in the real system) and consequently for the small orbital eccentricity once these initial data are evolved (see sec. 4.1.1). Another consequence of the helicoidal symmetry is that it leads to a non-asymptotically flat spacetime. Appropriate approximations should therefore be done in the curvature evolution to avoid diverging metric coefficients at infinity. In the `LORENE` code (and in most of the private code developed by different groups in the last years, for example [58, 247]) the so called *Conformal Thin Sandwich* approach is used, based on the Wilson and Mattews scheme [248]. In a 3+1 splitting like presented in sec. 3.1, the spatial metric is approximated as conformally flat:

$$\gamma_{ij} = A^2 \eta_{ij}. \tag{3.139}$$

This approximation is justified because it would be exact for spherically-symmetric spacetimes, it is a very good and commonly used approximation for constructing axisymmetric isolated neutron stars initial data, and it's a good description of the BNS spacetime when the stars are far apart. To further simplify the computations, one can build a coordinate frame compatible with the helicoidal symmetry, where $I = \frac{\partial}{\partial t}$. Defining the corotating shift

$$\omega^i = \beta^i + \Omega \frac{\partial}{\partial \phi}, \tag{3.140}$$

and using the Killing equation

$$\nabla_\mu I_\nu + \nabla \nu I_\mu = 0 \tag{3.141}$$

one can construct a relation for the extrinsic curvature K^{ij}:

$$\begin{aligned} K^{ij} &= -\frac{1}{2\alpha}\left(\nabla^i \beta^j + \nabla^j \beta^i\right) = \\ &= -\frac{1}{2A^2\alpha}\left(\partial^i \omega^j + \partial^j \omega^i - \frac{2}{3}\eta^{ij}\partial_k \omega^k\right). \end{aligned} \tag{3.142}$$

This relationship, thanks to the helicoidal symmetry, fixes all spatial components of the extrinsic curvature, given the corotating shift. This means fixing eq. 3.30 of the ADM formulation, leaving a free choice only for its trace K, which is fixed imposing a maximal slicing gauge condition ($K = \partial_t K = 0$, see also sec. 3.1.1). Taking into account the Hamiltonian and momentum constraints and the trace of the Einstein equations, one gets five elliptic equations to be solved for the variables ω^i, A, and α. In the `LORENE` code, the following alternative variables are defined:

$$\nu := ln(\alpha) \tag{3.143}$$

$$\beta := ln(\alpha A), \tag{3.144}$$

to get, finally, the following equations:

$$\nabla^2 \nu = 4\pi A^2 (e + S) + A^2 K^{ij} K_{ij} - \partial_i \nu \partial^i \beta \tag{3.145}$$

$$\nabla^2 \beta = 4\pi A^2 S + \frac{3}{4} A^2 K_{ij} K^{ij} - \frac{1}{2}\left(\partial_i \nu \partial^i \nu + \partial_i \beta \partial^i \beta\right) \tag{3.146}$$

$$\nabla^2 \omega^i + \frac{1}{3}\partial^i \partial_j \omega^j = -16\pi \alpha A^2 j^i + 2\alpha A^2 K^{ij} \partial_j \left(3\beta - 4\nu\right), \tag{3.147}$$

where all Laplacians are computed respect to the flat spatial metric. The remaining five Einstein's equations are not considered in this scheme, and are probably violated, reflecting the fact that this is only an approximation of the true BNS spacetime.

For describing the initial hydrodynamics variables profiles, instead, it is easier to trade the energy-momentum tensor and baryon number conservation with the following *uniformy canonical equations of motion*, if a recipe exists to obtain all thermodynamical variables from the specific enthalpy:

$$u^{\mu}\left(\nabla \times \mathbf{w}\right)_{\mu\nu} = 0 \tag{3.148}$$

$$\nabla^{\mu}\left(\rho u_{\mu}\right) = 0, \tag{3.149}$$

where $w_{\mu} = h u_{\mu}$ is the comomentum 1-form, and its exterior derivative

$$\left(\nabla \times \mathbf{w}\right)_{\mu\nu} = \nabla_{\mu} w_{\nu} - \nabla_{\nu} w_{\mu} \tag{3.150}$$

is the vorticity two-form. It is evident that a *potential flow*

$$w_{\mu} = \nabla_{\mu}\psi, \tag{3.151}$$

for which $\left(\nabla \times \mathbf{w}\right)_{\mu\nu} = 0$, is a solution to eq. 3.148. This is the GR generalization of a Newtonian irrotational flow. From the helicoidal symmetry definition, one has $\mathcal{L}_I w = 0$. Using Cartan's identity, this becomes:

$$I^{\mu}\left(\nabla \times \mathbf{w}\right)_{\mu\nu} + \nabla^{\mu}\left(I^{\nu} w_{\nu}\right) = 0, \tag{3.152}$$

which implies that

$$I^{\nu} w_{\nu} = const. \tag{3.153}$$

is a constant of motion. Using this first integral, the fluid motion is completely determined by the potential ψ, which must still satisfy eq. 3.149:

$$\frac{\rho}{h}\nabla^{mu}\nabla_{\mu}\psi + \nabla^{\mu}\psi\nabla_{\nu}\left(\frac{\rho}{h}\right) = 0. \tag{3.154}$$

In the 3+1 approach, this equation becomes, on every hypersurface Σ_t, the following elliptic Poisson-like equation:

$$\rho\partial_i\partial^i\psi + \partial^i\rho\partial_i\psi = -\frac{hW}{\alpha}\beta^i\partial_i\rho + \rho\left[\left(\partial^i\psi + \frac{hW}{\alpha}\beta^i\right)\partial_i ln(h) - \partial^i\psi\partial_i\alpha - \frac{\beta^i}{\alpha}\partial_i\left(hW\right)\right] + K\rho hW. \tag{3.155}$$

To conclude, BNS initial data are computed solving equations 3.145, 3.146, 3.147, 3.155, with appropriate asimptotic flatness boundary conditions at large radii:

$$\alpha \to 1 \tag{3.156}$$

$$\psi \to 1 \tag{3.157}$$

$$\omega^i \to \omega \times \vec{r}. \tag{3.158}$$

In `LORENE` this is done with an iterative procedure, using a multidomain spectral method. In this method, different numerical grids are built around each star center, defined as the point with maximum specific hentalpy, which could not coincide with the Newtonian center of mass of the

star. In Cartesian coordinates, each star is located on the x axis, and they are equidistant from the coordinates center, with a distance between the stars centres d fixed before the initial data computation (a comprehensive study of this initial distance impact on the simulation results can be found in [94] and in sec. 4.1.2 of this thesis). During each iteration, the stars do not move respect to the grid center, even if they have a different mass. The rotation axis position is, instead, changed at every step. Generating our initial data, we used four coordinates domains for each star: the inner domain covers the star interior, it has a ball topology, its inner boundary coincides with the star center and its outer boundary with the star surface. Two domains, then, cover the exterior of each star, starting from its surface and reaching a finite radius, with a spherical shell topology. The last domain, instead, reaches the spatial infinity, to be able to set the right asymtotical flatness boundary conditions, and it has a compactified coordinate representation. The equations to be solved are discretized with a *collocation spectral method*, meaning that the fields are expanded on a series of basis functions, and, in each domain, each field can be represented either by its spectral expansion coefficients or its values at particular grid points. In `LORENE` Chebyshev polynomials are used as basis in the radial coordinate, trigonometrical polynomials or associated Legendre functions in θ and a Fourier series in ϕ. In each domain, we decomposed a field with 33 points (or spectral coefficients) in the radial direction, 21 points in θ and 20 in ϕ, following the suggestion of [53].

For finding the equation solutions, the metric potential are split in the so called *autopotentials*, which are the potentials in a star domains generated by the same star gravitational field, and the *comp-potentials*, which are the potentials in a star domains generated by the companion field. In a typical code run, given as initial parameters the baryon mass of the two stars, their interbinary distance and their EOS, the first step (executed once) is to create two non-rotating equilibrium spherical neutron star configurations at the initial positions. Their orbital angular velocity is set according to a second-order post-Newtonian expression. Next, the iterative procedure starts. At every iteration, first, the orbital angular velocity and the position of the rotation axis x_c are computed, taking the gradient along the x direction of the first integral of motion 3.153. Imposing that the hentalpy is, by definition, maximal at star centres, one obtains two equations:

$$\frac{\partial}{\partial x}\, ln\left(W_0\right)|_{(x_{(1,2)},0,0)} = \frac{\partial}{\partial x}\left(\nu + ln\left(W_u\right)\right)|_{(x_{(1,2)},0,0)}\,, \tag{3.159}$$

where $W_0 = -n^\mu v_\mu$, $W_u = -u^\mu v_{mu}$ and $x_{(1,2)}$ are the positions of the two stellar centres. All the variables in these equations can be expressed as function of Ω and x_c, and they can be solved using a simple zero-finding secant method. Some care must be taken when highly unequal mass configurations are considered. In this simple approach, which we used, it is important to properly set the initial interval for the zero-finding procedure: big enough such that it contains the true x_c and Ω, but small enough to ensure that the numerical procedure can converge to the right solution. We slightly modified the `LORENE` code in order to more easily set and change those parameters. This was proven to be key in constructing initial data for unequal mass BNS, up to mass ratio values which have rarely been simulated in the past, also because of the difficulty in generating appropriate initial data for them. A different approach for solving the same problem is presented in ref. [249], where x_c is set in order to drive to zero the total linear momentum of the system, similarly of what is done for building BH-NS binaries initial data. After this first step, the hydrodynamics equation 3.155 is solved, using the specific hentalpy as variable. From h, new values of the thermodynamical quantities ρ, ϵ, p, are computed using the EOS, and are used to build the energy-momentum tensor for solving the Einstein equations 3.146, 3.147 and 3.145. Before the beginning of a new iteration step, some relaxation is applied to the fields, to help insuring convergence. Moreover, the comp-potentials are

not updated every code step, but every 8 steps. After the first 20 iteration, the code is also forced to converge to the right baryon mass for each star, multiplying the central specific entalpy of each star by a factor

$$\left(\frac{2+\xi}{2+2\xi}\right)^{1/4}, \tag{3.160}$$

where ξ is the difference between the baryon mass value for the star in question at the present code iteration and its requested baryon mass at the end of the computation. The code iterations end when the relative difference in the central specific hentalpy between two steps is less than 1×10^{-8}.

3.4 Graviational-wave signal extraction from simulations

The physical setting in a BNS simulation is different from the one in the simple linearised gravity case described in sec. 2.2.1. The central source is made of compact objects which generate a strong gravitational field and which needs the solution of full non-linear Einstein's equations to be able to predict its evolution. Therefore, the simple quadrupole formula (2.29), although used in some works, with appropriate modifications, is not the best tool to compute the gravitational wave strain emitted by the simulated system (the quadrupole formula is able to reconstruct quite accurately the frequency evolution of the signal, but has a big uncertainty in the waves amplitude [250, 251]). The two most common techniques for extracting the gravitational radiation signal from numerical simulations are the use of the Newmann-Penrose scalar Ψ_4, or the use of the Regge-Wheeler-Zerilli theory of metric perturbations of the Schwarzschild spacetime.

The first technique is based on the Newmann-Penrose (or Weyl) scalars, which can be defined starting from the Weyl tensor [252]

$$C_{\alpha\beta\mu\nu} = R_{\alpha\beta\mu\nu} - g_{\alpha[\mu}R_{\nu]\beta} + g_{\beta[\mu}R_{\nu]\alpha} + \frac{1}{3}g_{\alpha[\mu}g_{\nu]\beta}R \tag{3.161}$$

and contracting it appropriately with an orthonormal null tetrad $l^\mu, n^\mu, m^\mu, \bar{m}^\mu$, where $\bar{m}^\mu$ is the complex conjugate of m^μ and the following orthonormality relations apply:

$$l^\mu l_\mu = n^\mu n_\mu = m^\mu m_\mu = 0 \tag{3.162}$$

$$m^\mu n_{mu} = m^\mu l_\mu = 0 \tag{3.163}$$

$$l^\mu n_{mu} = -1. \tag{3.164}$$

This null tetrad is constructed starting from a orthonormal regular tetrad on each hypersurface Σ_t, based on spherical coordinates, $(e_R)^i, (e_\theta)^i, (e_\phi)^i$. Some care must be taken in interpreting the radial coordinate meaning. The propagation direction of outgoing gravitational waves is along the surface radial coordinate r, for which the 2-surfaces $r = t = const.$ have area $4\pi r^2$. This is the radial Schwarzschild coordinate in a non-spinning background. On the other hand, the radial coordinate R of the coordinate system most often used in numerical relativity (selected with the gauge conditions (3.45) and (3.46)) is not a surface radial coordinate, and asymptotically is close to the *isotropic* radial coordinate, linked with r, by:

$$r = R\frac{1+(M+a)}{2R}\frac{1+(M-a)}{2R}, \tag{3.165}$$

where a is the Kerr parameter $a = J/M$ (which is equal to zero in the non-rotating limit, giving the relation $r = R\left(\frac{1+M}{2R}\right)^2$, used in the following analysis and in ref. [68, 94, 99]). Here M is the

total ADM mass of the system and J is the total ADM angular momentum. Instead of using eq. 3.165, it is also possible to compute, during the simulation run, the areal radius

$$r_A = \sqrt{\frac{A(R)}{4\pi}}, \tag{3.166}$$

where $A(R)$ is the surface area of the proper sphere chosen for the gravitational wave extraction. We checked that, in our simulations, those two methods give the same results with a very good approximation.

The null tetrad more frequently used in numerical relativity, and implemented also in the thorn `WeylScalar4` of the Einstein Toolkit, is a modified version of the *psikadelia* tetrad [253, 254]:

$$\mathbf{l} := \frac{1}{\sqrt{2}}\left(\mathbf{e}_t - \mathbf{e}_R\right) \tag{3.167}$$

$$\mathbf{n} := \frac{1}{\sqrt{2}}\left(\mathbf{e}_t + \mathbf{e}_R\right) \tag{3.168}$$

$$\mathbf{m} := \frac{1}{\sqrt{2}}\left(\mathbf{e}_\theta - i\mathbf{e}_\phi\right). \tag{3.169}$$

Having defined a null tetrad, the associated Newmann-Penrose scalars are:

$$\Psi_0 = -C_{\alpha\beta\mu\nu} n^\alpha m^\beta n^\mu m^\nu \tag{3.170}$$

$$\Psi_1 = -C_{\alpha\beta\mu\nu} n^\alpha l^\beta n^\mu l^\nu \tag{3.171}$$

$$\Psi_2 = -C_{\alpha\beta\mu\nu} n^\alpha m^\beta \bar{m}^\mu l^\nu \tag{3.172}$$

$$\Psi_3 = -C_{\alpha\beta\mu\nu} n^\alpha l^\beta \bar{m}^\mu l^\nu \tag{3.173}$$

$$\Psi_4 = -C_{\alpha\beta\mu\nu} l^\alpha \bar{m}^\beta l^\mu \bar{m}^\nu. \tag{3.174}$$

The most important in this context is Ψ_4, because its asymptotic limit (for $r \to \infty$) describes the gravitational radiation:

$$\Psi_4 = \ddot{h}_+ - i\ddot{h}_\times := \ddot{\bar{h}}, \tag{3.175}$$

where from now on h is the complex gravitational wave strain $h = h_+ + ih_\times$. In numerical simulations Ψ_4 is computed in a spherical surface far from the sources using eq. 3.174, and then is expanded in spin-weighted spherical harmonics of weight -2:

$$\Psi_4(t, R, \theta, \phi) = \sum_{l=2}^{l_{max}} \sum_{m=-l}^{l} \Psi_4^{lm}(t, R)\, {}_{-2}Y^{lm}(\theta, \phi). \tag{3.176}$$

This is done in the Einstein Toolkit by the thorn `Multipole`. Thanks to the *peeling theorem*, the Newmann-Penrose scalars have an important property: in asymptotically flat spacetimes, Ψ_n falls off for $r \to \infty$ as r^{n-5}. For this reason, since Ψ_4 falls off as $\frac{1}{r}$, often results for $r\Psi_4$ (and, equivalently, for the strain rh) are reported and analysed. This is needed, for example, when one wants to compare waveforms extracted at spheres with different radii. Another necessary step for that purpose is to express the GW signals as functions of their retarded time (the time respect to the one in which the signal reaches the "detector" sphere). To evaluate the retarded time, we make the assumption

that the metric far from the sources is approximatively the Schwarzschild one, to get:

$$t_{ret} = t - R^* \tag{3.177}$$

$$R^* = R + 2Mlog\left(\frac{R}{2M} - 1\right), \tag{3.178}$$

where M is the system ADM mass and R^* is known as the tortoise coordinate. Further improvements in the retarded time determination, relaxing the Schwarzschild spacetime hypothesis, have been presented in [255]. All the GW results, unless otherwise specified, are presented from now on respect to the retarded time t_{ret}.

Ψ_4 is a gauge-invariant quantity, tensorially is a scalar quantity, but it's dependent upon the tetrad choice. However, if the tetrad is a small perturbation about the Kinnersley tetrad (which is the natural choice for a Kerr spacetime, for which all Weyl scalars but Ψ_2 vanish), Ψ_4 is tetrad-invariant at first order [252].

The two main difficulties in using Ψ_4-based GW extraction from a numerical simulation are the necessity of extrapolating the result to spatial infinity, for the relationship 3.175 to be valid, and performing the double time integration to get the gravitational wave strain (which is the final goal if one wants to compare the simulation results with future GW direct experimental detections). Some of my work for this thesis focused on solving these issues with simple, yet accurate, procedures, comparing their results with what is more commonly adopted in the literature (see next subsections for details).

Another technique for GW extraction which was tested in my work is the Regge-Weeler-Zerilli theory of metric perturbations of the Schwarzschildspacetime, in the gauge-invariant formulation of Moncrief [256, 257]. The extraction is based on the Regge-Weeler functions (for the odd perturbations, Ψ^o), and the Zerilli ones (for the even perturbations Ψ^e) computed by the code `WaveExtract` and related to the GW strain components by:

$$h_{lm} = \frac{1}{r\sqrt{2}}\left(\Psi^e_{lm} + i\Psi^o_{lm}\right). \tag{3.179}$$

Even if RWZ extraction has the advantage of not requiring any integration to obtain the GW strain, in practice we found it less accurate than the now more or less standard Ψ_4 extraction, both in the waveform convergence with the extraction sphere radius and in the presence of unphysical oscillations in the final part of the signal.

3.4.1 Integration of Ψ_4 signal

The natural procedure to integrate the Ψ_4 signal to get the GW strain is to numerically compute the double time integration, for example with a simple trapezoidal rule, and then set the two unknown integration constants fitting the resulting strain with a first order polynomial and subtracting it to the strain itself:

$$\bar{h}^{(0)}_{lm}(t,r) = \int_0^t dt' \int_0^{t'} dt'' \Psi_4^{lm}(t'',r) \tag{3.180}$$

$$\bar{h}_{lm}(t,r) = \bar{h}^{(0)}_{lm} - Q_1 t - Q_0, \tag{3.181}$$

where the fitted parameters have the natural interpretation

$$Q_1 = \left.\frac{\partial \bar{h}}{\partial t}\right|_{t=0} \tag{3.182}$$

$$Q_0 = \bar{h}(t=0). \tag{3.183}$$

It's important to underline that the integration in eq. 3.180 starts from the coordinate time $t = 0$ and not from retarded time $t_{ret} = 0$. In accordance with Appendix A of [40], we found out that the "more natural" use of the retarded time leads to oscillations in the first few milliseconds of the strain signal (even when using the more advanced integration techniques presented later in this section). This could be due to the lower values for the integration constants Q_0 and Q_1 when starting from $t = 0$, which lead to lower values in the fit errors.

The simple integration procedure (3.180), however, leads to the presence of unphysical oscillations and non-linear drifts in the resulting strain amplitude (even an order of magnitude relatively higher, as can be seen in fig 3.2). This phenomenon has been accurately documented and explained in [258], where it was attributed to the presence of high-frequency noise aliased in the low-frequency Ψ_4 signal (our typical run Nyquist frequency is about 50 khz) and amplified in the double integration process. The first solution we adopted in [68], but which was already proposed in [251], is to fit the integrated signal with higher-order polynomials, in particular with a second order one:

$$\bar{h}_{lm}(t,r) = \bar{h}^{(0)}_{lm} - Q_2 t^2 - Q_1 t - Q_0. \tag{3.184}$$

Although the additional constant Q_2 has no immediate physical interpretation, it gets lower as the extraction radius increases, therefore it can be partially interpreted as a correction of finite-radius extraction errors. This procedure, however, is satisfying only for the dominant strain component $h_{2,2}$, while it is insufficient to cure the unphysical behaviours in the subdominant modes (see figure 3.1). For them, even higher-order (beyond the second one) polynomials would be needed, as noticed also in [259]. This procedure would not be fully justified from the mathematical point of view.

The most commonly used alternative in numerical relativity is the *Fixed Frequency Integration* (FFI) proposed in [258]: the signal is integrated in the frequency domain, with the following prescription, to avoid the spectral leakage phenomenon:

$$\tilde{h}^{lm}(f) = -\frac{\tilde{\Psi}^{lm}_4(f)}{(2\pi f_0)^2} \text{ if } f < \frac{m f_0}{2} \tag{3.185}$$

$$\tilde{h}^{lm}(f) = -\frac{\tilde{\Psi}^{lm}_4(f)}{(2\pi f_0)^2} \text{ if } f \geq \frac{m f_0}{2}, \tag{3.186}$$

where $\tilde{}$ stands for the Fourier transform of its argument and f_0 have to be chosen on a case-by-case basis as the lowest frequency of the physically relevant radiated signal. This procedure is effectively equivalent to apply a high-pass filter in the frequency domain to the Ψ^{lm}_4 signal, damping the part of the signal spectrum below the frequency $\frac{m f_0}{2}$ multiplying it with a second-order transfer function

$$H_{FFI}(f) = \frac{f^2}{f_0^2} \qquad \text{if } f < \frac{m f_0}{2} \tag{3.187}$$

$$H_{FFI}(f) = 1 \qquad \text{if } f \geq \frac{m f_0}{2}. \tag{3.188}$$

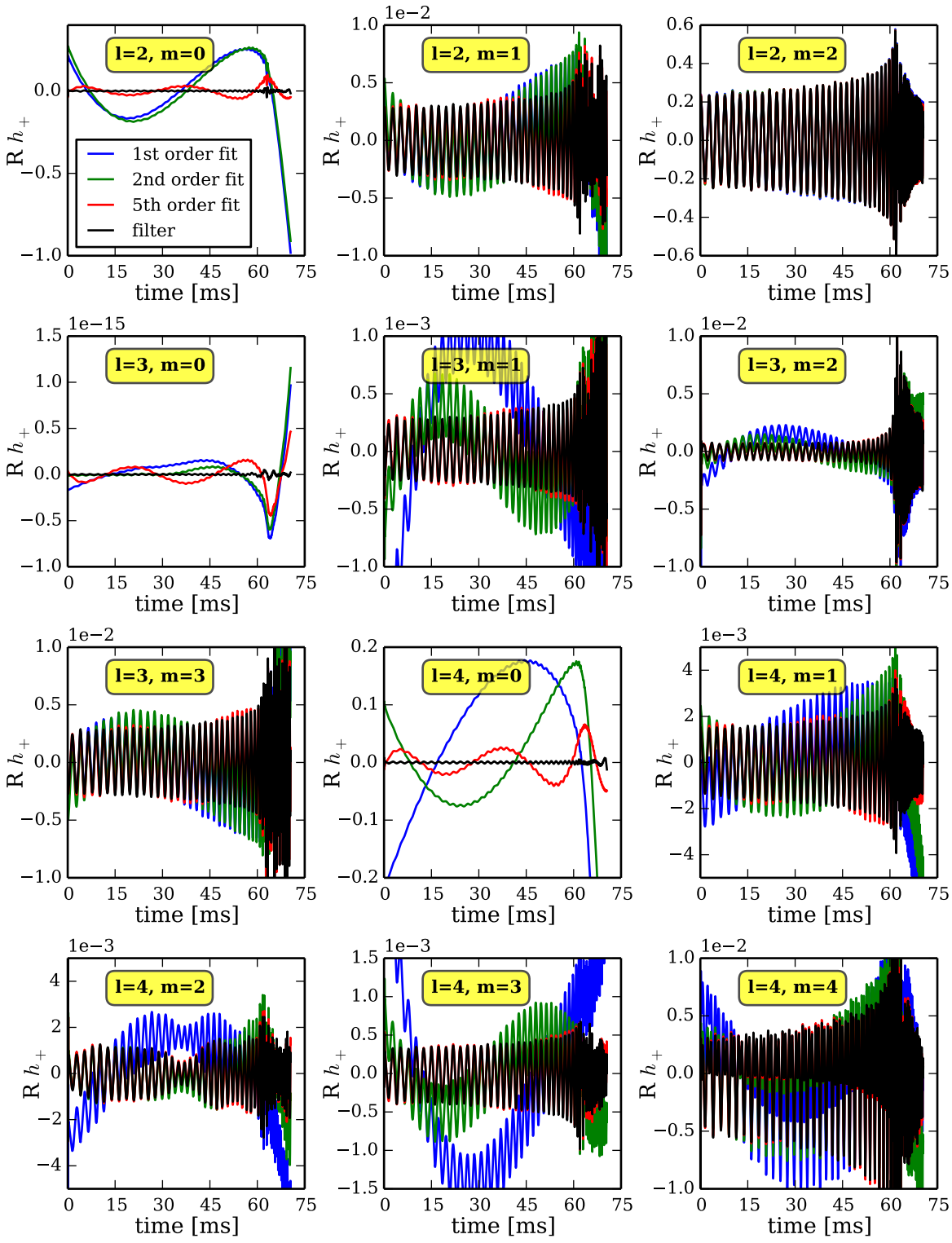

Figure 3.1: Real part of the gravitational-waves strain (corresponding to the GW polarization h_+) for different spherical harmonics components. The strains are computed from real simulations data of an equal mass BNS model with the SLy EOS, $M = 1.4\,\mathrm{M}_\odot$ for each star and a starting interbinary distance of 60 km (see appendix B for details), setting only the physical integration constants (blue line), subtracting a second order (green line) or fifth order (red line) polynomial fit or using our filtering procedure (black line). High order polynomial fitting can cure the unphysical drifts in the dominant $(2, 2)$ mode but does not work for the subdominant modes.

The FFI integration has been successfully applied to compute the GW strain from many different GR simulations (such as BNS, NS-BH, supernovae, etc.), and is able to handle quite well also the subdominant modes, thanks to the factor m in the cutting frequency computation, which comes from the spherical harmonics structure, but we found it has a couple of shortcomings:

- First, and most importantly, FFI integration has a filtering order which is too low to eliminate all unphysical drifts and GW amplitude oscillations in some cases. For example, this happens after the application of formula 3.197 (discussed in the next subsection) for extrapolating the Ψ_4 signal extracted at finite radii to spatial infinity. The integral terms in eq. 3.197 amplify the low frequency noise in Ψ_4, which get subsequently amplified again by the double time integration to get h. A possible solution to this problem would be to increase the filter order, multiplying for example the signal at frequency f lower than $\frac{mf_0}{2}$ by $\left(\frac{f}{f_0}\right)^4$. As I will show later, a smarter procedure is to filter the integral terms (both the ones in eq. 3.197 and the final strain h) after and not before the integration, to avoid an amplification of the low-frequency noise remaining after FFI filtering;

- Secondly, the FFI procedure requires a frequency-domain integration, which needs the application of a suitable window function to the original signal, in order to avoid Gibbs phenomenon related problems at the signal beginning and end. This leads to having to discard a relevant portion of the simulated signal, wasting part of the computational resources required by the simulation run (more data on computational requirements can be found in section A.2). On the other hand, a standard Butterworth digital filter application, like the one proposed here, leads only to small glitches in the last part of the signal, forcing to discard only a minimal fraction of it, way less than the one damped by most common window functions.

The new, simple, procedure we developed was to apply a simple digital Butterworth high-pass filter to the already-integrated Ψ_4 signal. We apply an Infinite Impulse Response (IIR) filter using the `signal` module of the `scipy` Python library. We require that the signal is cut at most by 0.01 dB at the lowest physically relevant frequency f_0 (computed as two times the initial orbital frequency of the binary) and an attenuation of -80 dB at $\frac{f_0}{10}$. The filter is applied as a forward-backward filter in order to avoid changes to the signal phase. A constant padding of the original unfiltered signal was found to be important to limit the Gibbs phenomenon and have a better result also near the signal end.

We compared the transfer function $H(f)$ for each integration procedure, defined as

$$\tilde{h}_i(f) = H(f)\tilde{h}_0(f), \tag{3.189}$$

where $\tilde{h}_i(f)$ is the Fourier transform of the GW strain computed with the i-th procedure (either 2nd or 5th order polynomial fitting, FFI, or our filter), and $\tilde{h}_0$ is the Fourier transform of the strain computed using only eq. 3.180 and first-order polynomial fitting to set the two mathematically-motivated integration constants. For simplicity we did the comparison on the dominant $l = m = 2$ mode only. All the strains are computed starting from the Ψ_4 signal extracted in a real BNS simulation, extrapolated to infinity with eq. 3.197. The results of this comparison are represented in figure 3.3. It is clear that the second order fitting is no longer sufficient to reduce low frequency noise after the infinite radius extrapolation, and a higher order polynomial would be needed. It is also visible that FFI has a worse performance than our high-pass filter at the lowest frequencies, because its filtering order is too low.

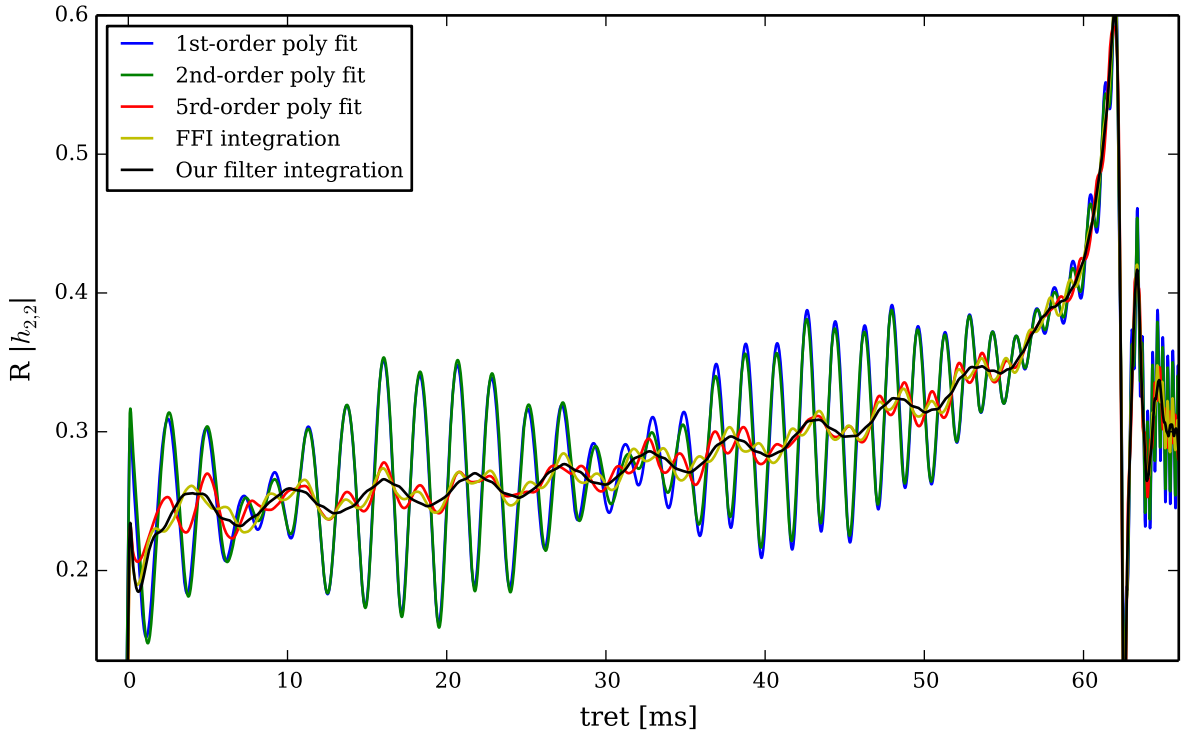

Figure 3.2: amplitude of the l=m=2 GW strain component, obtained with different integration techniques, starting from Ψ_4 extrapolated to infinity with eq. 3.197. The blue line represents the signal extrapolated fixing just the two needed integration constants. The green and red lines, the signal to which a higher-order polynomial fit is subtracted. The yellow line is the strain computed with FFI integration and, finally, the black line is obtained after the application of the digital filter developed in my work.

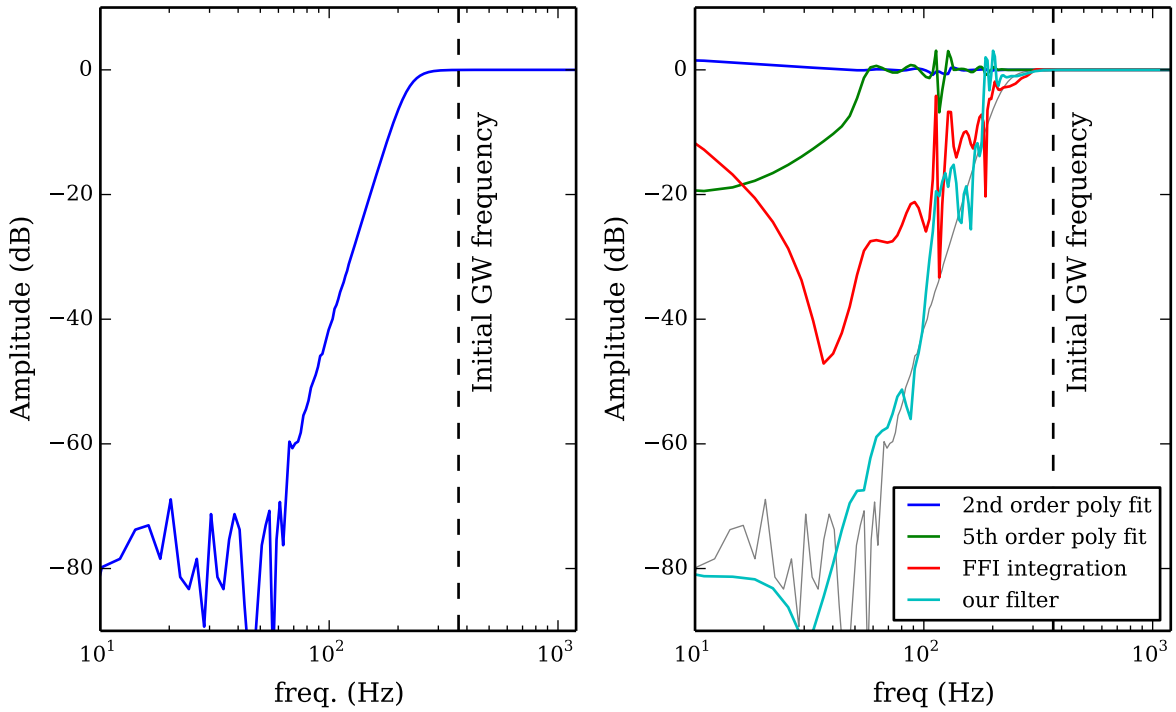

Figure 3.3: Left figure: theoretical transfer function for the high-pass Butterworth filter we applied. Right figure: effective transfer function of different integration procedures, computed with eq. 3.189 form real simulation data of an equal mass BNS model with the SLy EOS and $M = 1.4\,\mathrm{M}_\odot$ for each star, starting from $d = 60$ km.

3.4.2 Extrapolation of the extracted signal to infinity

As underlined before, equations 3.175 and 3.179 are valid only at large radii $r \to \infty$. Since the Ψ_4 or $\Psi^{e/o}$ components are, instead, computed on an extraction sphere with finite coordinate radius R during numerical simulations, one needs a technique to extrapolate those variables to spatial infinity in post-processing. In the numerical relativity literature three procedures have been developed for this task:

- Extracting the gravitational-waves signal at different radii and extrapolating it at infinite radius fitting the different signals with a polynomial in $\frac{1}{r}$ (see, for example, ref. [90, 162, 255, 260]);
- Extrapolating the signal extracted at finite radius using an analytic formula based on perturbation theory of the Schwarzschild or Kerr metric [261, 262];
- Performing a characteristic evolution of the metric, using as inner boundary conditions the metric and its derivatives on a timelike worldtube, extracted from the numerical simulation. This approach is commonly called *Cauchy-Characteristics Extraction* (CCE), and it's implemented in the Einstein Toolkit by the `PittNullCode` thorn [263, 264].

In this work and in ref. [94] we tested the first two approaches, comparing their results and their practicality. In particular, we tested for the first time in a BNS simulation the second order perturbative correction of [262], confronting it with the first order one, developed in ref. [261] and tested, for example, in [67, 97, 265]. Furthermore, in this thesis will be tested for the first time the corrections due to the real background spacetime being rotating (Kerr-like) and not stationary (Schwarzschild-like), which in [262] was computed but reported to be negligible, without presenting any test result.

For the polynomial extrapolation, following [255], the Ψ_4 components are divided in their amplitude and phase parts:

$$\Psi_4^{l,m} = A^{l,m}(r,t)e^{i\Phi^{l,m}(r,t)}. \tag{3.190}$$

Where r is the radius of the extraction sphere. Then, the variables $rA(r,t)$ and $\Phi(r,t)$ are fitted independently:

$$rA = a_0 + \frac{a_1}{r} + \frac{a_2}{r^2} \tag{3.191}$$

$$\Phi = b_0 + \frac{b_1}{r} + \frac{b_2}{r^2} \tag{3.192}$$

The extrapolation for $r \to \infty$ are, respectively, the fit parameters a_0 and b_0. The fitting polynomial was limited to second order because we used too few extraction radii to have a good result (avoiding overfitting) with a higher-order polynomial. This makes also more appropriate the comparison with the analytical second order correction of [262]. We extracted the gravitational wave signal at 7 different radii for each simulation, from $R = 400\,\mathrm{M}_\odot$ (approximatively 591 km) to $R = 700\,\mathrm{M}_\odot$ (1034 km).

The perturbative extrapolation approach is based on the asymptotic behaviour of the relevant wave-like function for each extrapolated variable. For example, at first order, in the case of the RWZ functions, one has:

$$\Psi^{e/o}_{l,m}(r,t) = h^{e/o}_{l,m}\Big|_{r\to\infty}(t) + \frac{l(l+1)}{2r}\int h^{e/o}_{l,m}\Big|_{r\to\infty}(t)dt + O(1/r^2), \tag{3.193}$$

where $h^{e/o}_{l,m}\Big|_{r\to\infty}(t)$ is the gravitational wave strain observed at infinity, and t is always the retarded time 3.178. Inverting this relationship, one obtains a formula for extrapolating the RWZ functions to infinite radius at first order:

$$\Psi^{e/o}_{l,m}\Big|_{r\to\infty} = \Psi^{e/o}_{l,m}(r,t) - \frac{l(l+1)}{2r}\int \Psi^{e/o}_{l,m}(t,r)dt. \tag{3.194}$$

The same logic can be followed for the Newmann-Penrose scalar Ψ_4, which in the Schwarzschild-background satisfies the Teukolsky equation [266], which, choosing the standard Boyer-Lindquist coordinates for the Kerr spacetime and the Kinnersley tetrad, is:

$$\begin{aligned}\left[\frac{(r^2+a^2)^2}{\Delta} - a^2 sin^2(\theta)\right]\frac{\partial^2}{\partial t^2}{}_{-2}\Psi + 4\frac{Mar}{\Delta}\frac{\partial^2}{\partial t\partial\phi}{}_{-2}\Psi + \left[\frac{a^2}{\Delta} - \frac{1}{sin^2(\theta)}\frac{\partial^2}{\partial\phi^2}{}_{-2}\Psi\right] + \\ -\Delta^2\frac{\partial}{\partial r}\left(\frac{1}{\Delta}\frac{\partial}{\partial r}{}_{-2}\Psi\right) - \frac{1}{sin(\theta)}\frac{\partial}{\partial\theta}\left(sin(\theta)\frac{\partial}{\partial\theta}{}_{-2}\Psi\right) + 4\left[\frac{M(r^2-a^2)}{\Delta} - r - iacos(\theta)\right]\frac{\partial}{\partial t}{}_{-2}\Psi + \\ +4\left[\frac{a(r-M)}{\Delta} + icotg(\theta)\right]\frac{\partial}{\partial\phi}{}_{-2}\Psi + (4cotg^2(\theta)+2){}_{-2}\Psi = 0,\end{aligned} \tag{3.195}$$

where a is the Kerr parameter $a = \frac{J}{M}$, where J is the total angular momentum and M the total mass of the system; $\Delta = r^2 - 2Mr + a^2$, and the Teukolsky's wave function ${}_{-2}\Psi$ is given by:

$${}_{-2}\Psi = (r - iacos(\theta))^4\,\Psi_4. \tag{3.196}$$

Using only the non-rotating (Schwarzschild) part of eq. 3.195 and taking its asymptotic limit, one can obtain the first and second order "Mass" perturbative corrections for the Ψ_4 extrapolation, as computed in detail in ref. [262]:

$$\begin{aligned}r\psi_4^{lm}(t_{\rm ret})\,|_{r=\infty} \;=\; &\left(1-\frac{2M}{r}\right)\Bigg(r\psi_4^{lm}(t_{\rm ret},r) \\ &- \frac{(l-1)(l+2)}{2r}\int dt\; r\psi_4^{lm}(t_{\rm ret},r) \\ &+ \frac{(l-1)(l+2)(l^2+l-4)}{8r^2}\int dt'\int dt\; r\psi_4^{lm}(t_{\rm ret},r)\Bigg).\end{aligned} \tag{3.197}$$

Where, in particular, the factor $\left(1-\frac{2M}{r}\right)$ comes from the difference between the Kinnersley tetrad used in the Teukolsky's formalism and the tetrad 3.167, used in our simulation code. As a step forward, also the second order in $\frac{1}{r}$ spin correction can be computed and applied. First, one has to keep in mind that, in the Teukolsky's formalism, the wave function is decomposed in spin-weighted spheroidal and not spherical harmonics, because they are the solution of the angular Teukolsky equation. In the frequency domain, the wavefunction is decomposed in:

$${}_{-2}\Psi = \int\sum_{l=0}^{l_{max}}\sum_{m=-l}^{l}{}_{-2}\Psi_{l,m,\omega}(r)\,{}_{-2}S^{a,\omega}_{l,m}(\theta,\phi)e^{-i\omega\phi}d\omega. \tag{3.198}$$

The spheroidal harmonics ${}_{-2}S_{lm}$ are linked with the spherical harmonics by:

$$ {}_{-2}S^{a\omega}_{lm} = {}_{-2}Y_{lm} + a\omega\Bigg[-\frac{2}{l^2}\sqrt{\frac{(l+2)(l-2)(l+m)(l-m)}{(2l-1)(2l+1)}}\,{}_{-2}Y_{l-1,m} + \\ + \frac{2}{(l+1)^2}\sqrt{\frac{(l+3)(l-1)(l+m-1)(l-m+1)}{(2l+1)(2l+3)}}\,{}_{-2}Y_{l+1,m}\Bigg] + O((a\omega)^2). \tag{3.199} $$

The Fourier and spheroidal harmonics components of the wave function ${}_{-2}\Psi_{lm\omega}$ can be found using an asymptotic solution of the radial Teukolsky equation, ignoring terms of order $O(1/(\omega r)^3)$. Inserting their expression and the spheroidal harmonics expression 3.199 in the wavefunction definition 3.198, one obtains the spherical harmonics expansion, in terms of the asymptotic strain h:

$$ \frac{1}{r^3}{}_{-2}\Psi_{lm\omega} = \int\Bigg[\left(1 + \left(-4\frac{ima}{l(l+1)} + i\frac{(l-1)(l+2)}{2\omega}\right)\frac{1}{r} - \frac{1}{8}\frac{l(l-1)(l+2)(l+1)}{\omega^2}\frac{1}{r^2}\right)h_{lm\omega} + \\ + a\omega\Bigg(-\frac{2}{l^2}\sqrt{\frac{(l+2)(l-2)(l+m)(l-m)}{(2l-1)(2l+1)}}\,h_{l-1m\omega} + \\ + \frac{2}{(l+1)^2}\sqrt{\frac{(l+3)(l-1)(l+m-1)(l-m+1)}{(2l+1)(2l+3)}}\,h_{l+1m\omega}\Bigg)\Bigg]e^{-i\omega t}d\omega + O((a\omega)^2, 1/(r\omega))^3) \tag{3.200} $$

The relationship between Ψ_4 computed in the Kinnersley and in the numerical relativity tetrad gives a contribution in the time domain relationship between the Ψ_4 signal extracted from numerical simulations and the Teukolsky wave function(3.196) (see [262, 267] and also [254, 268] for details about the computation):

$$ \frac{{}_{-2}\Psi_{lm}}{r^3} = \left(\frac{1}{2} - \frac{M}{r}\right) r\Psi^{NR}_{4lm} - i\frac{a}{r}\sum_{l'm'} C^{lm}_{l'm'} r\Psi^{NR}_{4l'm'}, \tag{3.201} $$

where

$$ C^{l'm'}_{lm} = \int {}_{-2}Y^*_{lm} cos\theta\, {}_{-2}Y_{l'm'} d\Omega, \tag{3.202} $$

which have non-zero values only for $m' = m$ and $l' = l$ or $l' = l \pm 1$. Putting everything together, one finally arrives at the second order in $1/r$ perturbative extrapolation of Ψ_4, which has also a background spin correction, first order accurate in $a\omega$:

$$ r\Psi_4^{lm}\Big|_{r\to\infty} = \left(1 - \frac{2M}{r}\right)\left(r\Psi_{4lm}(t,r) - \frac{(l-1)(l+2)}{2r}\int r\Psi_{4lm}(t,r)dt + \right. \tag{3.203} $$
$$ \left. + \frac{(l-1)(l+2)(l^2+l-4)}{8r^2}\int dt\int dt' r\Psi_{4lm}(r,t')\right) + $$
$$ + \frac{2i\ a}{(l+1)^2}\sqrt{\frac{(l+3)(l-1)(l+m+1)(l-m+1)}{(2l+1)(2l+3)}}\left(r\partial_t\Psi_{4l+1m}(t,r) - \frac{l(l+3)}{r}r\Psi_{4l+1m}(t,r)\right) + $$
$$ - \frac{2i\ a}{l^2}\sqrt{\frac{(l+2)(l-2)(l+m)(l-m)}{(2l-1)(2l+1)}}\left(r\partial_t\Psi_{4l-1m}(t,r) - \frac{(l-2)(l+1)}{r}r\Psi_{4l-1m}(t,r)\right). $$

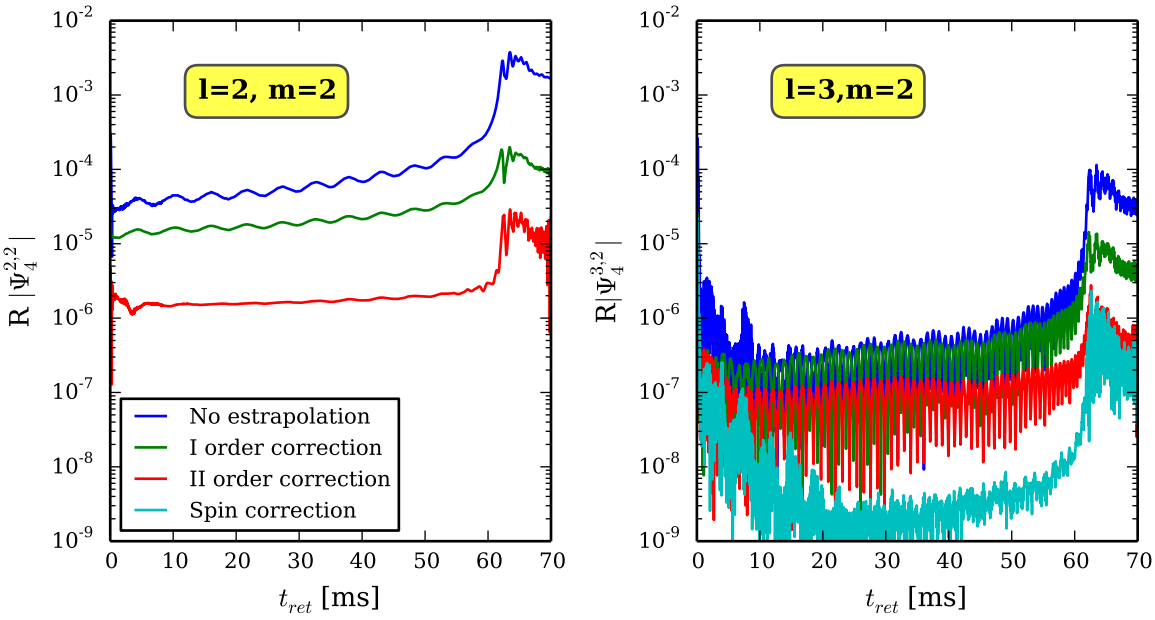

Figure 3.4: Left panel: amplitude of the $l = m = 2$ compontent of the Ψ_4 signal (blue line) and its first order (green line) and second order (red line) perturbative $1/r$ corrections. Right panel: amplitude of the $l = 3, m = 2$ component of Ψ_4, and its perturbative $1/r$ corrections, including the spin correction (cyan), which in the left panel would be several orders of magnitude smaller, around machine precision.

Computing the integral terms in eq. 3.197 or 3.203, the same amplitude oscillations problems described in section 3.4.1 arise. To solve them, filtering after integration is, again, required and the best solution. In order to be consistent with the filtering and the integration constants used in computing each term, we first computed the gravitational wave strain h from Ψ_4 extracted at finite radius (with the filtering procedure of the previous section), then we obtained from it the infinite radius extrapolation for Ψ_4, with the following modified version of eq. 3.203:

$$
\begin{aligned}
r\Psi_4^{lm}\Big|_{r\to\infty} &= \left(1-\frac{2M}{r}\right)\left(r\ddot{\bar{h}}_{lm}(t,r) - \frac{(l-1)(l+2)}{2r} r\dot{\bar{h}}_{lm}(t,r) + \right. \\
&\left. + \frac{(l-1)(l+2)(l^2+l-4)}{8r^2} r\bar{h}_{lm}(r,t)\right) + \\
&+ \frac{2i\ a}{(l+1)^2}\sqrt{\frac{(l+3)(l-1)(l+m+1)(l-m+1)}{(2l+1)(2l+3)}}\left(r\dddot{\bar{h}}_{l+1m}(t,r) - \frac{l(l+3)}{r} r\ddot{\bar{h}}_{l+1m}(t,r)\right) + \\
&- \frac{2i\ a}{l^2}\sqrt{\frac{(l+2)(l-2)(l+m)(l-m)}{(2l-1)(2l+1)}}\left(r\dddot{\bar{h}}_{l-1m}(t,r) - \frac{(l-2)(l+1)}{r} r\ddot{\bar{h}}_{l-1m}(t,r)\right).
\end{aligned}
\tag{3.204}
$$

To test the perturbative and polynomial fitting extraction methods, in [94] a comparison between the gravitational-wave signals extrapolated to infinite radius from an actual simulation was done. Here I extend the same comparison to other observables, including also the spin correction effect. First, it is useful to compare the different perturbative corrections (first and second order "mass"

corrections and the "spin correction") of a single Ψ_4 component, extracted at finite radius (in this example, our simulations outermost extraction radius $R = 700\,M_\odot$). In the left panel of figure 3.4, the amplitude of the $l = m = 2$ Ψ_4 component (multiplied with r) is shown (blue curve), together with the amplitude of the first order correction (green curve) and the second order one (red curve). The amplitude of the spin correction (cyan curve) is not visible, even in a logarithmic scale, because it is around machine precision. Therefore, the spin correction (which, in the case of the $(2, 2)$ mode, has only the h_{l+1m} term and not the h_{l-1m} term) is irrelevant when analysing the dominant GW component. On the other hand, the mass corrections are more important at the beginning of the simulations, and become progressively less relevant, compared with the original $\Psi_4^{2,2}$: when the GW signal reaches the extraction sphere, the first order correction amplitude is about $2/5(40\%)$ of the extracted signal, while the second order one is around 6%. After the merger, however, the first order correction amplitude has gone down to only 5.5% of the extracted signal, and the second order one is relatively diminished by an order of magnitude, to 0.6%. The spin correction could become relevant, as suggested in ref. [267], in subdominant modes. For example, in the left panel of figure 3.4 are shown the amplitude of the perturbative corrections to the $l = 3, m = 2$ component of Ψ_4. Here, the spin correction has an amplitude comparable to the mass second order correction, at the beginning and at the end of the signal. This is due to the fact that it depends directly from the dominant $h_{l-1m} = h_{22}$ mode. In this particular equal mass simulation example, the $(3, 2)$ mode has a much lower amplitude than the $(2, 2)$ mode, about 1%, so the spin correction is not really relevant to the total GW signal (in the case of binary optimal orientation, with the rotation axis aligned with the observational axis), even if the perturbative corrections are relatively more important for the (3,2) mode than for the (2,2) one, by almost an order of magnitude. The spin correction could turn out to be important in the case of binaries not optimally oriented and for which the subdominant modes are important due to some asymmetries in the initial configurations (eccentricity, spinning neutron stars, unequal mass systems) or the development of hydrodynamical instabilities (in particular, in the post-merger HMNS phase). To analyse the effect of the extrapolation techniques, and to estimate the remaining GW extraction error, it is best to look separately at the GW phase and amplitude. The strain phase accuracy in the inspiral is very important, since it can be used, comparing the simulated signal with a detected one, to estimate tidal effects and from them to constraint or pinpoint the neutron star EOS. For understanding if EOS informations can be extracted form tidal effects in the detected signals, a precise assessment of numerical simulations error budget is very important [90, 91, 260], including the extraction procedure, which, in ref. [269], was found to be the dominant source of error at the beginning of the signal in BBH simulations. Figure 3.5 shows the difference in accumulated phase between the signal extracted at the largest radius ($R = 700\,M_\odot$) and three other inner radii ($R = 600, 500, 400 M_\odot$), without any radius extrapolation (left panel), applying the first order perturbative correction to Ψ_4 (centre panel) or applying also the second order correction (right panel). The first order correction reduced the extraction error in phase by an order of magnitude, while the second order correction allows to gain another factor two. The resulting phase error, which is less than $0.01 rad$ before merger, is much lower than the expected finite-resolution numerical error of the evolution code, which is more than an order of magnitude greater, even when adopting higher order numerical methods [67, 96, 97]. It is also much lower than the evolution code error lower bound, for the same model, estimated in section 4.1.2 from the difference between simulations with different initial interbinary distance ($0.4 rad$ for the particular model in this example, see table 4.3).

In figure 3.6, instead, is reported a comparison, at the fixed extraction radius $R = 700\,M_\odot$,

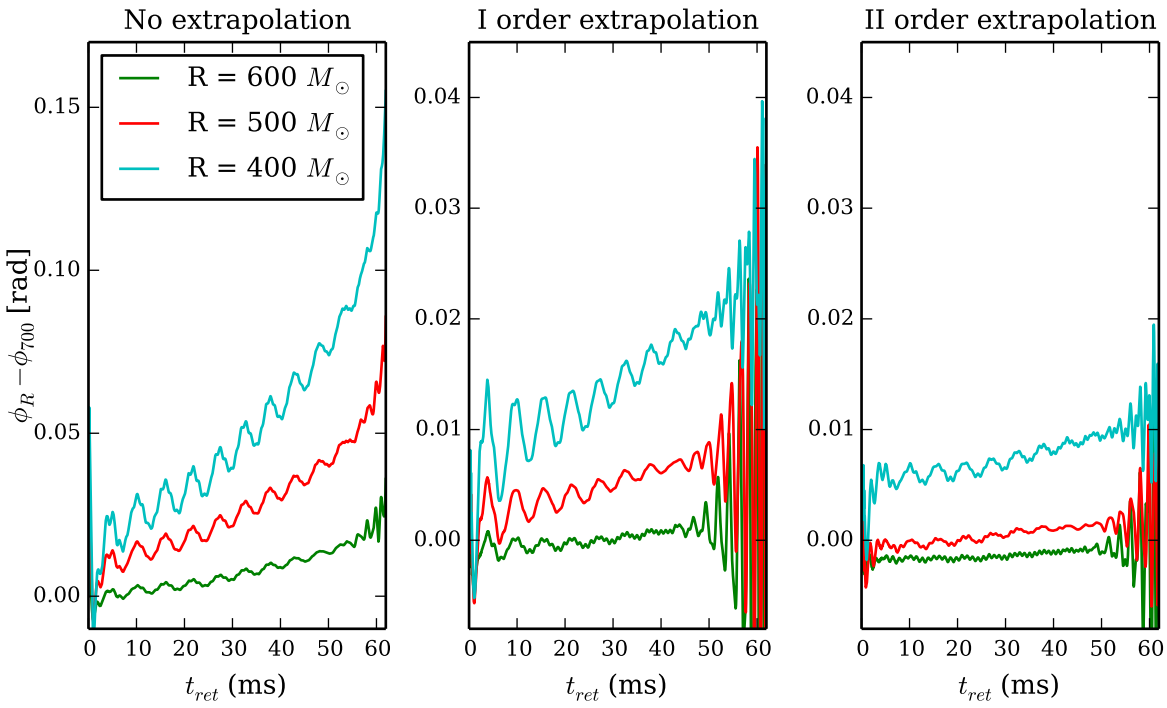

Figure 3.5: Difference in the accumulated phase between the (2,2) component of the GW strain computed extracting Ψ_4 at the outermost radius ($R = 700\,\mathrm{M}_\odot$)and other three inner radii ($R = 400, 500, 600 M_\odot$). The left panel shows the extracted signals without any extrapolation, the middle panel the signals to which is applied the first order perturbative correction, and the right panel the application of also the second order correction.

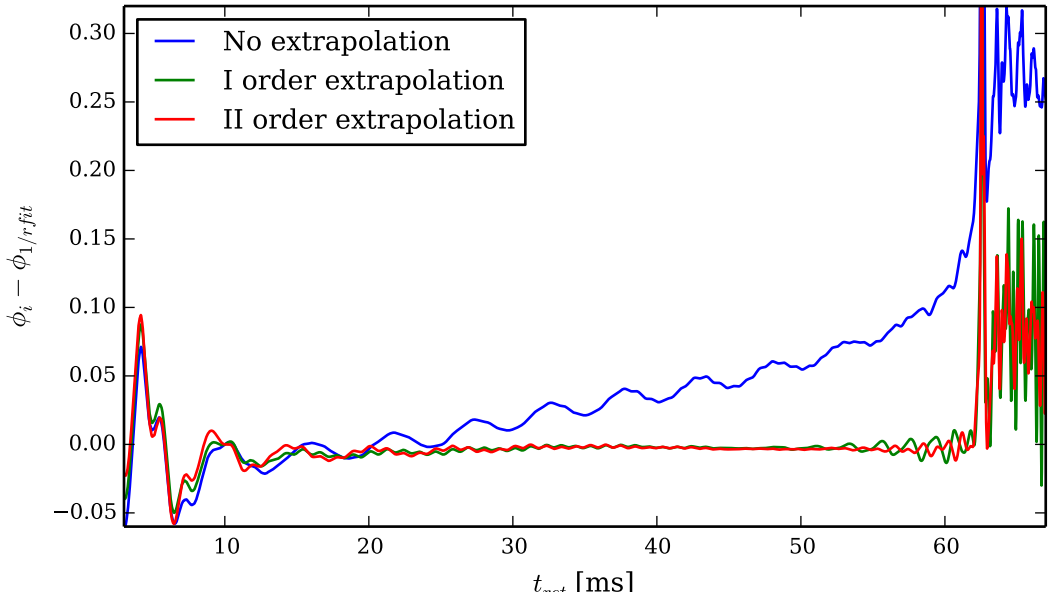

Figure 3.6: Difference in the accumulated phase between the GW strain extrapolated with the polynomial fit and the non-extrapolated one or the ones extrapolated with the perturbative formula 3.197 at the various orders.

Extrap. method	$\frac{E_{R=400}-E_{R=700}}{E_{R=700}}$	$\frac{J_{R=400}-J_{R=700}}{J_{R=700}}$
No extrap.	0.81%	-0.87%
I order extrap.	1.24%	1.58%
II order extrap.	0.50%	-0.14%

Table 3.1: Percentage difference between the radiated energy and angular momentum computed from the gravitational-wave signal extracted at the innermost ($R = 400\,\mathrm{M}_\odot$) and outermost($R = 700\,\mathrm{M}_\odot$) radius, with and without the application of the perturbative extrapolation formula 3.197

between the different perturbative extraction methods and the polynomial fitting method, plotting their accumulated phase difference. It is clearly visible that the polynomial fitting extraction gives a result very close in phase to both the first and second order extrapolation, with a difference of the order of 1×10^{-2} rad for all the inspiral part of the GW signal, and a higher difference, oscillating around $0.08 rad$, in the post-merger. On the other hand, as expected, the not extrapolated signal accumulates a phase error which, at merger, is $0.2 rad$, and in the post-merger phase is oscillating around $0.26 rad$. These errors could be comparable with the evolution numerical errors of high-resolution simulations. From this plot it is possible to conclude that some kind of extrapolation to infinite radius is needed for reducing the GW extraction error, but the difference between all the tested methods is really small, compared with other dominant error sources.

A different picture is theoretically expected for the amplitude corrections since, as explicitly showed in [267], it begins at the second order in $1/r$ and, therefore, the first order perturbative correction should not help reducing the amplitude extraction errors. I have evaluated this by looking at the energy and angular momentum radiated in gravitational waves, computed with equations

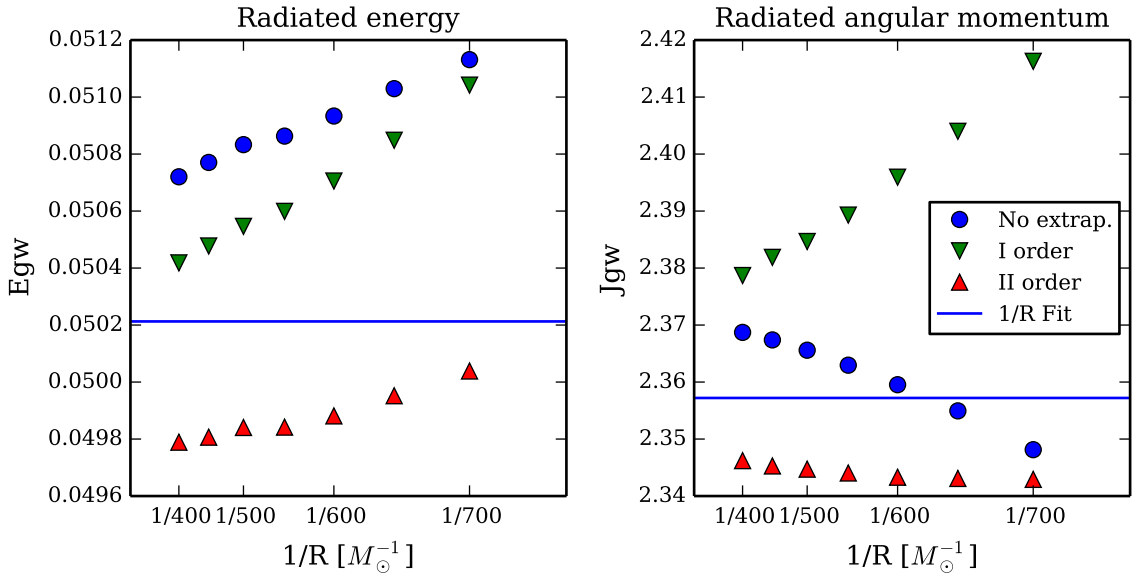

Figure 3.7: Left panel: total energy radiated in gravitational waves from the beginning of the simulation (of model SLy14vs14d60r25) to $5ms$ after the merger. The circles and triangles represents the GW signals extracted at different radii without any extrapolation (blue), with the first order perturbative extrapolation (green), and with the second order one (red). The black horizontal line represents the polynomial fit extrapolated signal.
Right panel: total radiated angular momentum in the z direction, from the beginning of the simulation to $5ms$ after the merger.

Extrap. method	$\frac{E-E_{no_extrap.}}{E_{no_extrap.}}$	$\frac{J-J_{noextrap.}}{J_{noextrap.}}$
I order extrap.	-0.60%	0.42%
II order extrap.	-1.84%	-0.95%
Polynomial fit extrap.	-1.00%	-0.49%

Table 3.2: Percentage difference between the radiated energy and angular momentum computed from the gravitational-wave signal extracted at the outermost($R = 700\,\mathrm{M}_\odot$) radius, using different extrapolation methods, respect to the ones computed from the not-extrapolated GW signal.

3.205, 3.206, because in ref. [262] was shown that the second order perturbative correction was essential for those radiated quantities to have the right convergence respect to the grid resolution. In figure 3.7 are shown the total energy (left panel) and angular momentum in the z direction (right panel) emitted from the beginning of the simulation to $5ms$ after the merger, respect to the extraction radius for the GW signal. Their fluxes are computed with the following expressions, from the gravitational wave strain:

$$\frac{dE^{gw}}{dt} = \frac{R^2}{16\pi} \int d\Omega \left| \dot{h}(t,\theta,\phi) \right|^2 \tag{3.205}$$

$$\frac{dJ_z^{gw}}{dt} = \frac{R^2}{16\pi} Re\left[\int d\Omega \left(\partial_\phi \, \bar{\dot{h}}(t,\theta,\phi) \right) h(t,\theta,\phi) \right], \tag{3.206}$$

then, the total radiated energy and angular momentum up to a point in time are simply computed integrating the above expressions.

The blue circles in figure 3.7 represent the not-extrapolated signal, the green triangles the one to which is applied the first-order perturbative correction only, and the red triangles the second-order extrapolated signals. Finally, the black horizontal lines are the results coming from the polynomial fit extrapolation. It is clearly visible than the difference in both the radiated energy and angular momentum computed extracting GWs at the outermost ($R = 700$) or innermost ($R = 400$) radius (which is proportional to the extraction error) is reduced by the second order perturbative correction, but it is actually increased by the first order one. Those differences, with their relative importance, are listed in table 3.1 and 3.2. In particular, the second order perturbative correction reduces the difference in the emitted energy by approximatively 40%, and in the angular momentum by a more relevant 85%. Even if these are small errors in absolute terms, on average around 1% of the radiated quantities, the fact that the first order correction actually increases them, while the second order one reduces them considerably, allows to conclude that it is important to use the second order perturbative extrapolation of ref. [262], even when it does not bring relevant advantages in reducing the phase extraction error. The energy coming from the polynomial fit extrapolation does not agree well with the energy coming from the second order perturbative extrapolation, in the sense that it cannot be the limit for infinite radius of the second order corrected radiated energy, but it is still closer to it than to the not-extrapolated signal.

Chapter 4

What can we learn from numerical simulations of binary neutron star mergers?

After the long introduction, it is time to look at which insights on the merger of binary neutron stars systems can be gathered from numerical relativity simulations. All the following analysis presented in this chapter are based on numerical simulations performed by the Parma numerical relativity group and presented in ref. [68, 94, 99]. Detailed information about the simulated models can be found in appendix B.

A typical evolution can be divided in three (or four) phases:

1. The inspiral phase, in which the two stars rotate rapidly one around the other, and their distance shrinks due to the energy and angular momentum radiated away by gravitational waves. In the last few milliseconds before merger, the tidal deformation of each star due to the gravitational field of the companion become important, speeding up the GW phase evolution. Tidal effects make the GW signal from coalescing binary neutron stars different from the binary black holes one, which can be predicted very accurately with semi-analytical techniques, based on the post-Newtonian expansion, such as the EOB model [39, 41], which, in its most recent implementations, is calibrated with numerical relativity simulations in order to estimate unknown high-order post-Newtonian coefficients. Recent development in analytical treatment of BNS coalescence has shown progress also in modelling tidal effects, either adiabatic [43, 45] or dynamically developed, by the interaction with the stars oscillation modes [47, 166]. The analysis of tidal effects in the late inspiral of BNS systems is very important, because it brings a signature of the neutron stars EOS, which influences the stars tidal deformability [11, 91, 97, 270].

2. The merger phase, in which the two stars come finally into contact, compressing their matter and giving rise to a complex hydrodynamical phenomenology, with instabilities and turbulence active inside the merger remnant, like the Kelvin-Helmotz instability, which can strongly amplify the stars magnetic fields, even if the maximum amplification has not been resolved yet in numerical simulations, due to the need for unfeasible resolutions to properly characterize the energy cascade from the smallest scales [89];

3. The post-merger phase, in which the neutron star formed during the merger evolves, with a different phenomenology depending on its mass, EOS, and angular momentum distribution. The remnant star is bar-deformed, rotates differentially, and emits gravitational waves with high luminosity. The GW emission slowly drives the evolution towards an equilibrium configuration, with uniform rotation, which, then, cools and spins down in a much longer timescale due to the effect of magnetic fields and neutrino emission;

4. The collapse phase, in which, if the merger remnant has a mass greater than the limit for a non-rotating neutron star imposed by its EOS, the neutron star collapses to a black hole, when its rotation has slowed down enough. This phase, depending on the initial stars parameters, could not happen at all, or could happen at different times from the merger, from a fraction of millisecond to hundreds of seconds or even more. The numerical simulations are currently able to track only a few milliseconds (up to 100 ms). After the collapse, an accretion disk is formed around the black hole, from the matter which is not immediately captured. The mass ratio between BH and disk strongly depends on the matter distribution and its angular momentum at the moment of collapse, which, in turn, depends on the collapse time and the physical evolution up to that point, conditioned by the star EOS, the initial stars mass ratio, the possible development of (magneto)hydrodynamical instabilities, the presence (and the correct modelling) of neutrino emission and magnetic fields, etc. The disk is then accreated on the black hole, but has in itself an interesting phenomenology, thanks to its oscillations (emitting gravitational waves, see [250, 271, 272]), possible instabilities (see ref [273–276]) and electromagnetic emissions (see also sec. 2.3).

All this phases can be distinguished very well in the evolution of two neutron stars with a baryonic mass of $1.5\,M_\odot$ and the SLy EOS, summarized in figure 4.1 with equatorial and meridional sections showing the evolution of the matter density ρ. The first panel shows the initial conditions, with the two stars centres separated by 40 km. The stars begin to rotate one around the other (second and third panel), shrinking their separation emitting gravitational waves. As can be seen in the third panel, low density matter from the two stars already comes into contact after a few milliseconds of evolution, way before the actual merger. The stars merge after 7.7 ms, resulting in a bar-deformed hyper-massive neutron star, which rotates differentially (fourth panel). Right after the merger, its remnant has still two high density cores (with $\rho > 1 \times 10^{15}\,\mathrm{g\,cm^{-3}}$, see panel 5), rotating around each other and oscillating radially. In less than a couple of milliseconds, the two cores also merge, as can be seen in the sixth panel. From that panel is also evident that the outer spiral arms structure rotates with a different group speed than the inner high-density structure. This has been liked with some features of the post merger spectrum (see ref. [277] and the extensive discussion in section 4.2.1). In the seventh panel, the star has become already more spherically symmetric (leading to a lower gravitational waves flux emission), and a large amount of low-density matter has been expelled far from the HMNS core. Finally, the eighth panel shows the star profile just before collapse, with a large, spherical, high density core, and the last panel shows the accretion disk low-density matter (with a density which quickly falls below the neutron-drip level, see section 4.2.4 for more details about collapsing models).
A different phenomenology is seen, instead, in unequal mass BNS systems, like the one depicted in figure 4.2, corresponding to the observed system PSRJ037+1559 (see table 2.3), modelled, again, with the SLy EOS. Initially the two stars start from a distance of 44 km (first panel). They start orbiting each-other, but after a few milliseconds, well before the merger, an evident mass transfer from the lower mass to the higher mass star is visible (third panel), even if, at the beginning,

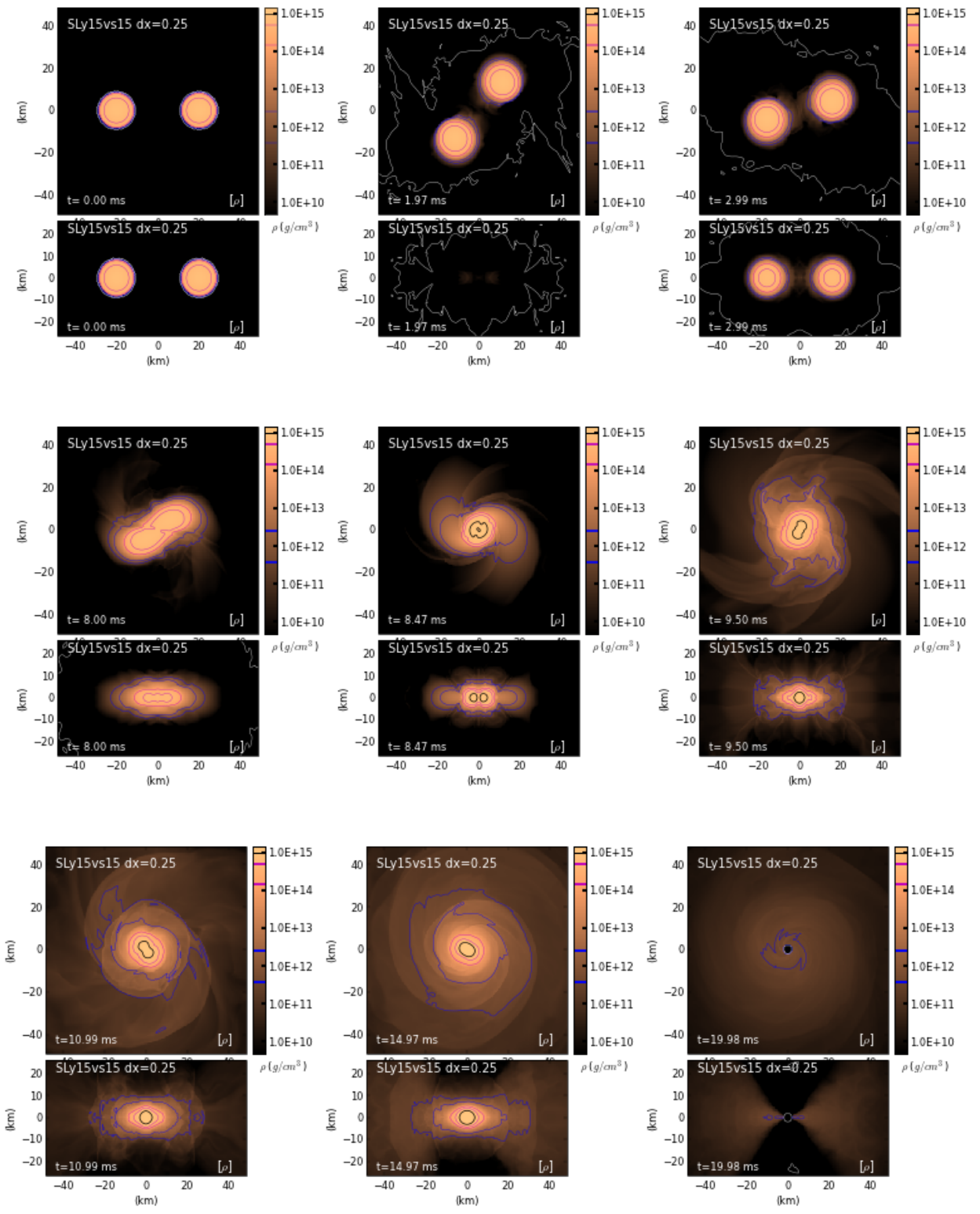

Figure 4.1: Dynamics of the evolution of an equal mass BNS model with $M = 1.5\,\mathrm{M}_\odot$ for each star, an initial distance between the star centres of 40 km, and using the SLy EOS for describing the nuclear matter. The simulation was performed with a grid resolution in the finer level $dx = 0.25\,\mathrm{M}_\odot$. It shows a relatively short inspiral phase (less than 8 ms), followed by an hyper-massive neutrons star phase and the collapse to black hole, surrounded by an accretion disk.

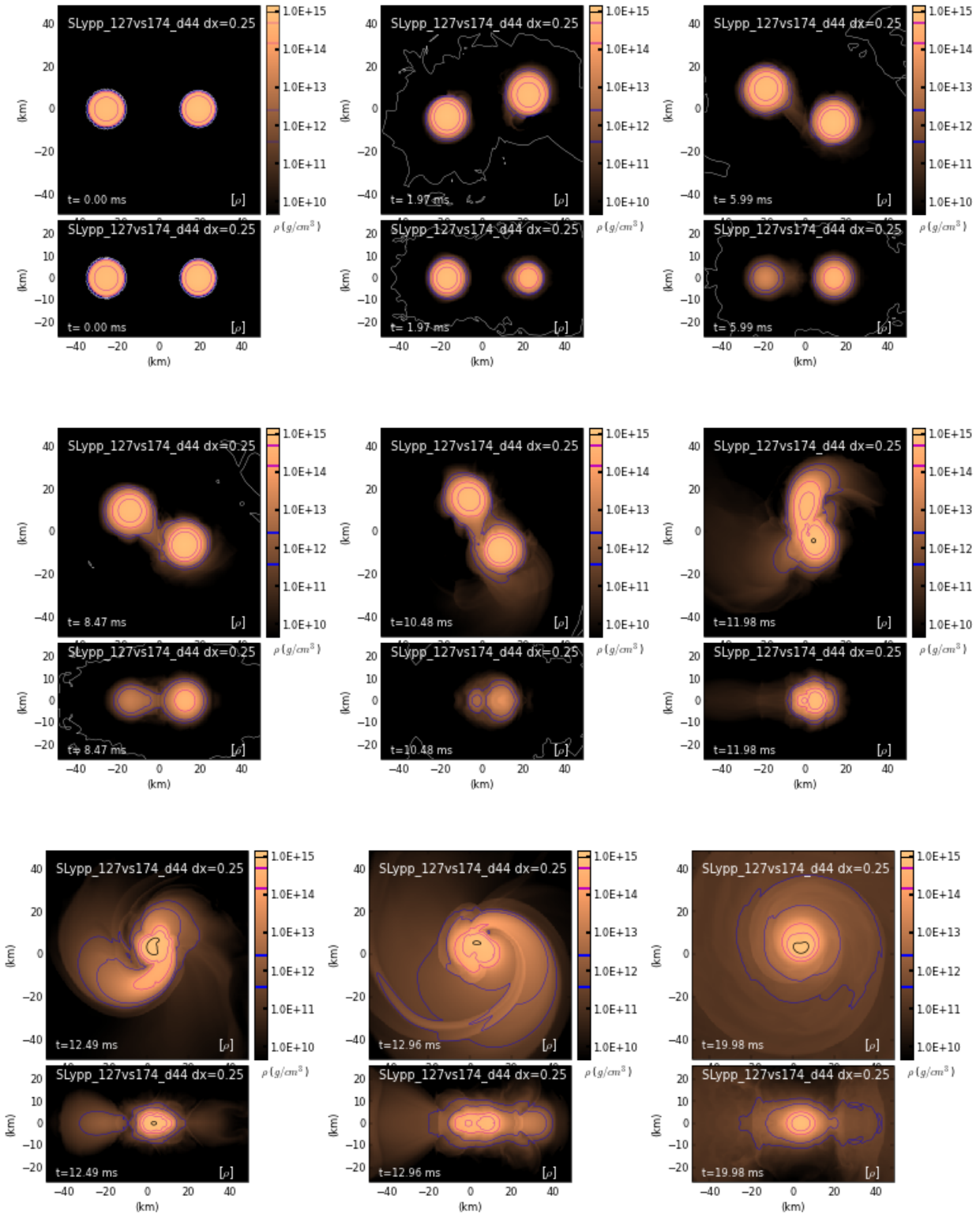

Figure 4.2: Dynamics of the evolution of an unequal mass BNS model with baryonic masses $M_1 = 1.27\,\mathrm{M}_\odot$ and $M_2 = 1.73\,\mathrm{M}_\odot$, corresponding to the parameters of the recently discovered pulsar PSRJ043+1559 system, the most asymmetric observed so far. The initial distance between the star centres is 44 km, and the SLy EOS was used for describing the nuclear matter. The simulation was performed with a grid resolution in the finer level $dx = 0.25\,\mathrm{M}_\odot$.

it concerns only low density matter, therefore does not effect the energy balance and the overall dynamical evolution. In the fourth panel, after 8.5 ms from the simulation start, the outer crusts come into contact, way before the actual merger (which happens, according to the most widely accepted definition, at 11.8 ms). In the fifth panel also the inner crust has merged, while the lower mass star is highly deformed by the tidal field of the companion. The low density matter ejected and left behind by the lower mass star starts to form a single spiral arm, often called a "tidal tail". The merger itself is visible in the sixth panel, where the lower mass star seems to be captured by the higher mass one. A high density region ($\rho > 1 \times 10^{15}\,\mathrm{g\,cm^{-3}}$) is formed at the centre of the higher mass star, but not in the lower mass one. The seventh panel shows the early post-merger phase, which looks very different from the equal mass case. Instead of a bar-deformed star, with a central double core structure, here we have a single spiral arm, with a single central high mass core, coming from the higher mass star, rotating around the center of symmetry. The outer core is still highly deformed by the tidal effects in play during the merger. In the following evolution (last two panels), much more matter gets ejected far from the central compact object than in the equal mass case, and a visible non-axysymmetric density perturbation is present even when the remnant moves towards an equilibrium configuration. It is interesting to note that, although this model has an higher initial ADM mass than the equal mass one presented before ($M_{ADM} = 2.708\,\mathrm{M_\odot}$ for the PSRJ0453+1559 and $M_{ADM} = 2.697\,\mathrm{M_\odot}$ for the 1.5-1.5 equal mass BNS), and the same EOS, this model does not collapse to black hole during the timescale of the simulation, because of the higher mass ejected far from the nucleus, the higher angular momentum transported towards the outer parts of the star, and the lower central density increase and central density oscillations amplitude (see figure 4.14).

Another general picture overview can be collected looking at the gravitational wave signals extracted from simulations of different BNS models. In figure 4.3 is reported the plus polarization of the dominant (2,2) mode of the gravitational wave strain (extracted applying the second order extrapolation formula 3.197 and integrated with our filtering procedure, see sec. 3.4) of different BNS models, together with its envelope constructed plotting $\pm|h_{22}(t)|$. The signals show some common features to all simulations: in the first phase (the so called *inspiral* phase) the gravitational waves progressively increase both their frequency and amplitude, generating a signal known as "chirp". The point of maximum amplitude is conventionally defined as the merger of the two stars. After the merger, the signal amplitude drops, during the turbulent rearranging phase, and then its amplitude raises again, at a higher frequency, which strongly depends on the EOS, for the GW emission due to the rotation of the bar-deformed neutron star remnant. The post merger GW emission amplitude decreases exponentially, due to the redistribution of angular momentum and the star approaching a more axisymmetric state, but it shows in some models interesting features, which will be analysed later (see sec. 4.2). The models collapsing to black hole are clearly recognizable, because after collapse the GW amplitude drops immediately to negligible values.

In the top-left panel, are shown five equal mass models with the same initial distance between the stars (40 km) and the same EOS (SLy), but different mass for each star ($1.2, 1.3, 1.4, 1.5$ and $1.6 M_\odot$). During the inspiral phase, the models with higher total mass emit gravitational waves with higher amplitude. They also have a shorter merger time (because they emit energy and angular momentum at a higher rate). After the merger, the model with $1.6\,\mathrm{M_\odot}$ stars collapses immediately, without any post-merger HMNS phase, and its GW signal, consequently, becomes flat, very close to zero amplitude. The model with $1.5\,\mathrm{M_\odot}$ stars, instead, as seen already in figure 4.1, collapses 7.7 ms after the merger. Its post-merger GW signal has a higher amplitude than the lower mass models,

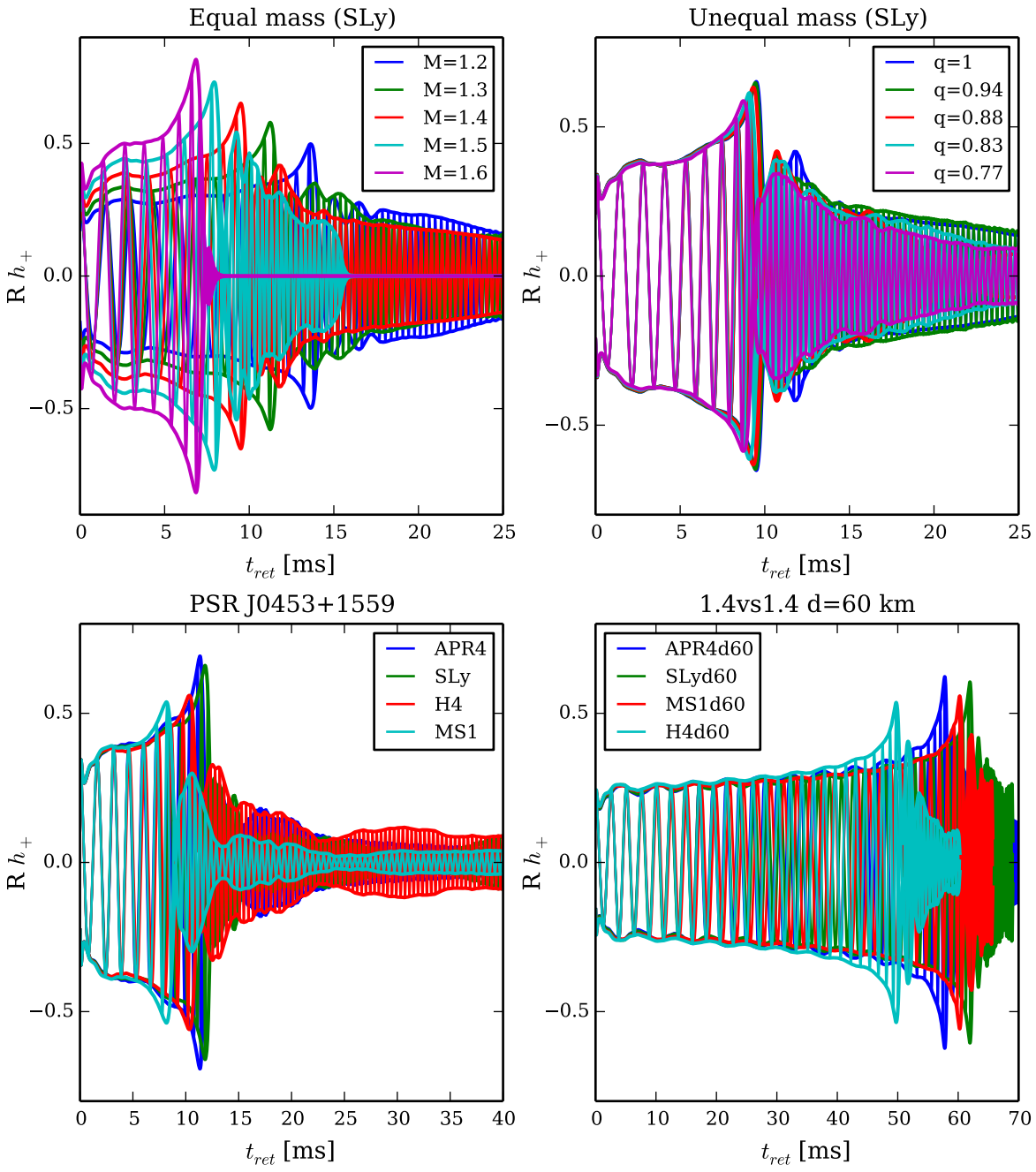

Figure 4.3: Plus polarization of the gravitational wave strain for different BNS simulated systems. In the top-left panel are represented five simulations of equal mass systems, with a baryonic mass of $1.2, 1.3, 1.4, 1.5, 1.6 M_\odot$ for each star, an initial distance of $40 km$ and the SLy EOS. In the top-right panel, instead, are represented unequal mass models with the same total baryonic mass of $2.8\,\mathrm{M}_\odot$, with mass ratios $q = 1, 0.94, 0.88, 0.83, 0.77$, with the same initial distance and EOS as before. The bottom panels contain, instead, a comparison of models with different EOS: the observed PSRJ0543+1559 system (left) and equal mass systems with total baryonic mass of $2.8\,\mathrm{M}_\odot$ (right), starting from a distance of 60 km apart. The employed EOSs are the one described in section 2.1.1.

but lasts only for the first phase, which, as described in depth in section 4.2, is characterized by several competing spectral components and emission modes growing and rapidly getting damped. In the non collapsing models, after a few milliseconds from the merger, the GW signal is, instead, characterised by a single oscillation mode, with exponentially decreasing amplitude.

In the top-right panel, instead, is reported the GW signal from five unequal-mass models, with a total baryon mass of $2.8\,M_\odot$, again with the SLy EOS, and mass ratios $q = 1, 0.94, 0.88, 0.83, 0.77$. The stars with the largest mass asymmetry merge slightly earlier than the more close to equal mass ones, because of the higher tidal deformation of the lower mass star. After the merger, decreasing the mass ratio, the damping time of the GW emission seems to decrease, even if some models ($q = 0.88, q = 0.77$) show evidence of the growth of different spectral modes after a sufficient decay of the principal emission mode.

This peculiar finding is confirmed by the system PSRJ0453+1559 (lower-left panel), simulated with different EOSs (described in sec. 2.1.1). All models, except the most compact stars with the APR4 EOS, show a secondary growth of the GW amplitude $10 - 15ms$ after the merger. This changes in the oscillations frequency and damping times and the rise of different oscillation modes can happen multiple times, as hinted by the simulation with the stiffest EOS (MS1). The different EOSs lead also to great differences in the merger times and in the GW phase evolution during the inspiral. The merger times are not perfectly ordered by EOS stiffness, because they are highly sensitive to the grid resolution (see appendix A.1), and the code convergence order can be different for the different EOSs, as reported, for example, in ref. [97].

The bottom-right panel, finally, shows more clearly the difference in the inspiral evolution due to the matter EOS and the consequent different tidal deformability of the stars. Here are reported results from simulations starting from a interbinary distance of 60 km. In the first couple of orbits (each orbit corresponds to two GW cycles), all the models have the same GW emission. This is because, at that distance, tidal effects are not yet relevant for their dynamics, and the GW emission is well approximated by a point-particles modelling (see sec. 4.1.2 for a comparison with post-Newtonian point-particle approximants). After that, the GW signals starts to diverge, because the less compact stars have, generally, a quicker phase evolution. In the specific case, the MS1 models merge way earlier than the other three models.

4.1 Inspiral gravitational waveform

Figure 4.3 already showed some of the main characteristics of the GW emission in the coalescent phase, before merger, and their dependence on different parameters, such as the stars mass, mass ratio and EOS. In order to quantitatively evaluate those differences, and, in particular, the one due to the EOS, about which we are interesting to gather information from GW detections data, all the error sources for the simulated signal should be under control [90, 91]. The problem of the GW signal extraction from simulations was already addressed in section 3.4, while the evolution code error and its convergence properties will be discussed extensively in appendix A.1. In this section, instead, I will analyse two other often ignored sources of errors, which, nevertheless, could be dominant and hide the true signal features due to tidal effects. The first error source is the eccentricity of the evolved orbits. As reported in table 2.3, all the observed BNS systems are believed to have a negligible eccentricity when they will enter in the LIGO/Virgo sensitivity band, due to the circularizing effect of GW emission. On the other hand, from the signals in figure 4.3, and in particular the longer ones in the bottom-right panel, one can clearly see by eye the presence of amplitude oscillations with

a fixed frequency. In the next subsection I will prove that they are not caused by GW extraction errors, but they are the imprint of a physical process, the eccentricity of the stars orbits. Another potentially important error source is linked with initial data, which are produced taking some approximations, like conformal flatness (see sec. 3.3). These possible errors could be evaluated by comparing simulation of the same model with initial data generated by different codes, as done in ref. [93]. Unfortunately, only one BNS initial data code is publicly available (the LORENE library), and so such comparison is difficult to reproduce. Instead, a different, interesting technique is to compare the results of simulations starting with a different initial interbinary distance (which means, a different initial orbital and GW frequency). This allows, also, to study which initial distance is the best for performing numerical BNS simulations, depending on which phase of the binary evolution one is most interested in studying.

4.1.1 Residual eccentricity

The presence of a residual orbital eccentricity in BNS numerical evolution is inevitable, if one imposes an Helical Killing vector in the initial data generation. It is a consequence of the resulting binary configuration having no radial velocity component, which in reality would be present due to the GW radiation reaction. The eccentricity can be measured from the stars orbits, and then the GW signals coming from the simulations can be compared with the ones predicted by post-Newtonian approximations of eccentric binaries. If they match, then we can confirm that the amplitude oscillations are indeed due to the eccentricity, and quantify how much they influence the accuracy of the simulated GW signals. The simplest way to compute the trajectory of a binary is to follow the stars centres, which can be defined as the points with maximum density (or minimum lapse α, given our singularity-avoiding gauge choice). A possible improvement on this technique, suggested also in ref. [95], is to compute the stars centres with a volume average, similar to a Newtonian center of mass computation:

$$x^i = \frac{\int_{star} \rho x^i d^3x}{\int_{star} \rho d^3x}. \tag{4.1}$$

To estimate the orbital eccentricity, a common procedure (see, for example, ref. [58, 95]) is to rely on the following Newtonian parametrization for the time derivative of the distance between the stars centres:

$$\dot{D}(t) \;=\; A_0 + A_1 t - e D_0 \omega_e sin\left(\omega_e t + \phi_e\right), \tag{4.2}$$

where e is the eccentricity, $D_0 = d$ is the initial distance and ω_e is the angular frequency of the eccentricity oscillations. If one computes the distance between the star centres from the simulation 3d output, it is possible to use eq. 4.2 to obtain the eccentricity value with a non-linear fit. The simplest, although incorrect, way of computing the distance is simply to take the coordinate distance between the centres. A better way would be to take, instead, the proper distance along a straight line between them. Finally, the correct procedure would be to compute the geodesic which passes through the two stars centres, and compute the proper distance along it. This will be, however, computationally expensive, because it should be repeated for every time-step for which one has 3d outputs. Therefore, in the following analysis, I adopted the simplest procedure, and verified afterwards its adequacy confronting the obtained eccentricity value with the one coming from the GW signal amplitude oscillations. It was chosen to fit the derivative of D and not D itself, because having one less free parameter brings an advantage greater than the error made by the numerical

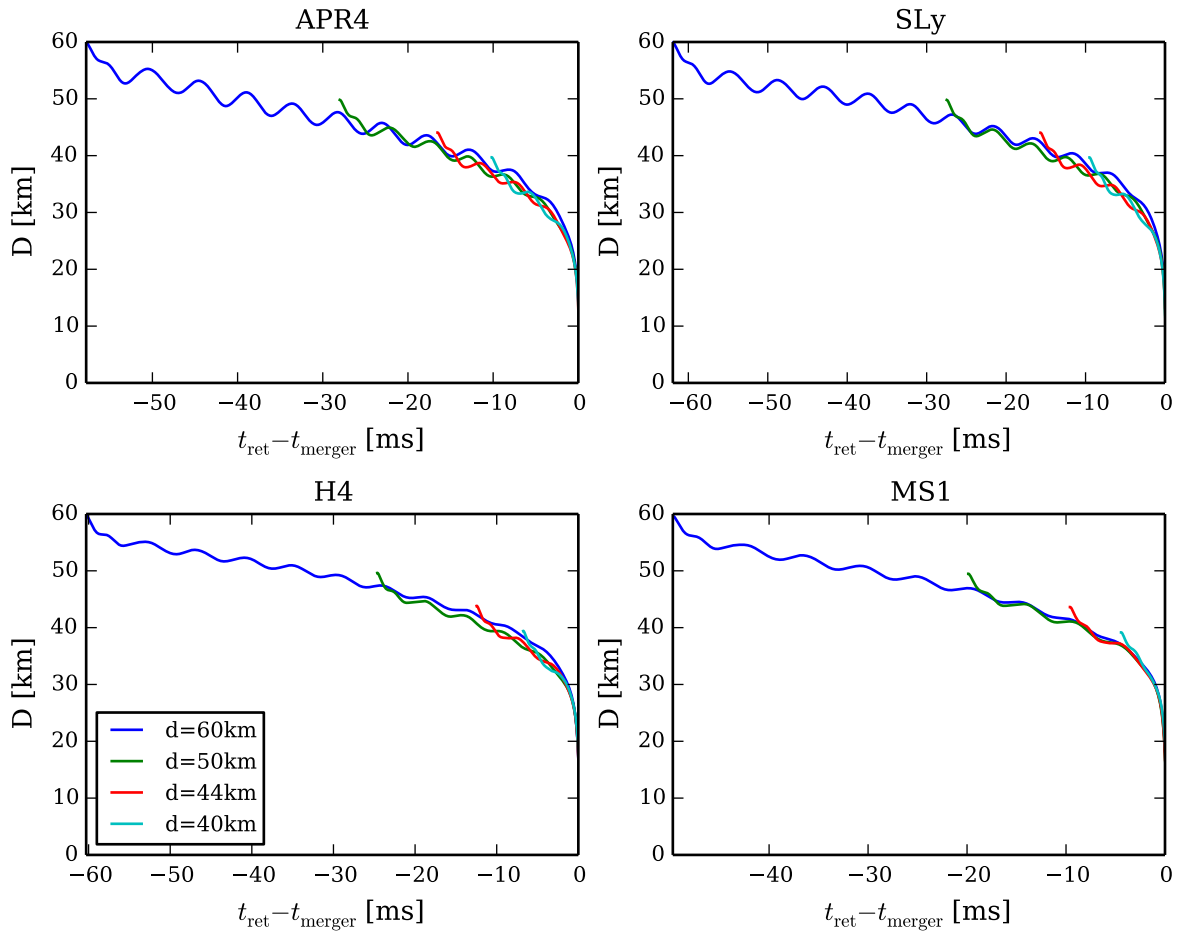

Figure 4.4: Evolution of the distance between the star centres, for equal mass BNS models with different EOS and initial separation. The oscillations in the distance are due to the residual orbital eccentricity, and are larger in the softer models.

derivative (which is performed using a fourth-order finite differencing operator). It was also tried to fit the evolution of the GW frequency, but the result was found to be much more noisy. The fit is performed starting from $t_{ret} = 3\,\mathrm{ms}$ (to avoid the spurious radiation emitted at the simulation beginning, see next paragraph) and $t_{ret} = \frac{2}{3} t_{merger}$ (to avoid the plunge phase, in which the stars come into contact and merge, and eq. 4.2 is no more a good representation for the distance derivative evolution).

The resulting evolution of the stars separation, for models with different EOS and initial distance, is shown in figure 4.4. In all the simulations is visible an initial sudden drop in the distance. This is due to an initial burst of unphysical spurious gravitational radiation (visible also from the signals in figure 4.3), which is due to a gauge readjustment because the initial spacetime did not have the right radiation content, which physically it should have due to the GW emitted by the binary up to that point of stars separation. This is a consequence of the *conformal flatness* approximation made in the initial data computation.

The subsequent evolution is again similar in all models, with the distance more rapidly decreasing

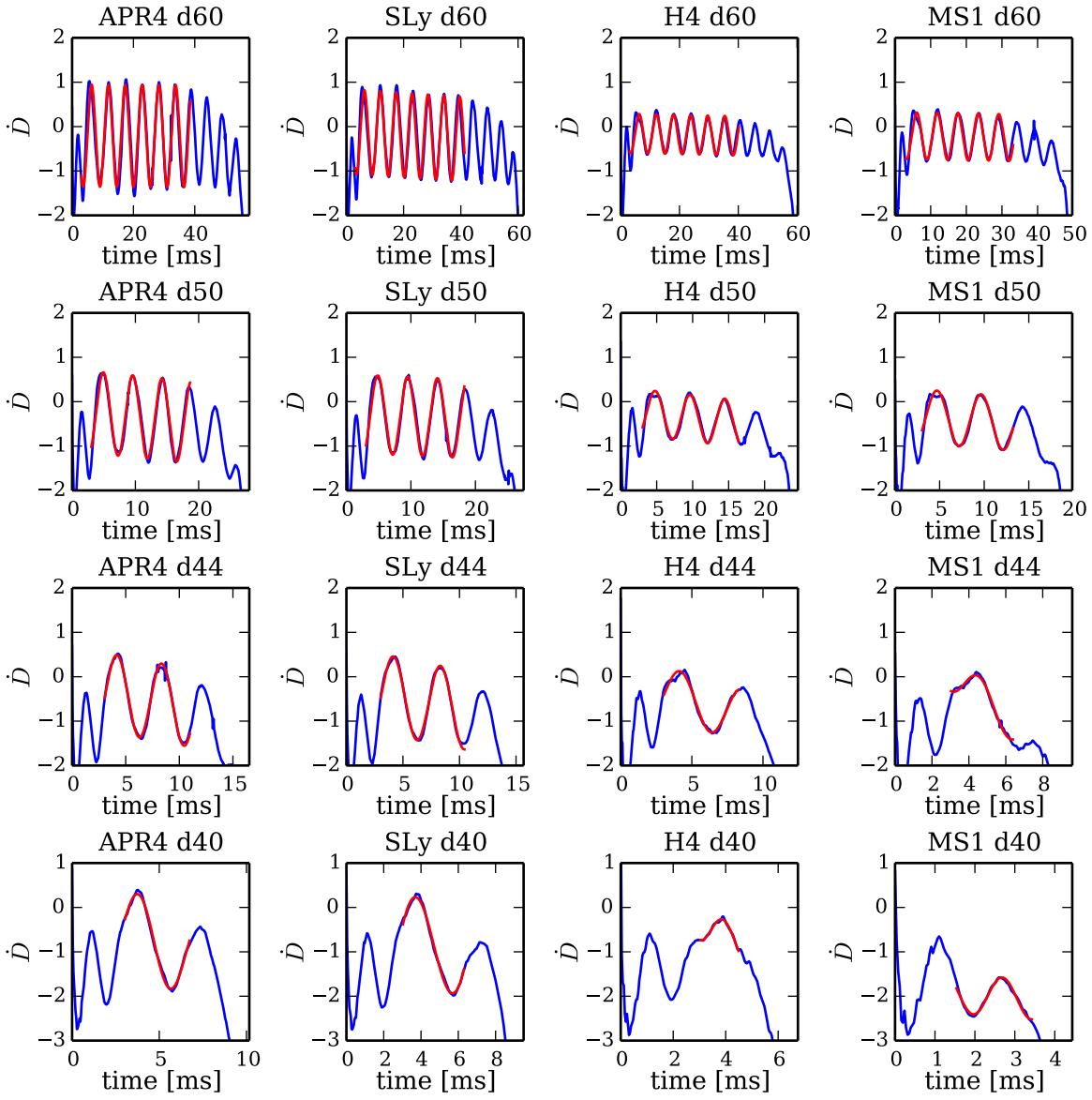

Figure 4.5: Evolution of the time derivative of the distance between the star centres, for equal mass BNS models with different EOS and initial separation. The oscillations in the distance derivative are due to the residual orbital eccentricity, and are larger in the softer models. The blue line represents actual data taken from the simulation output, while the red line is the result of the fit with eq. 4.2.

EOS	e $d = 60$km	e $d = 50$km	e $d = 44.3$km	$\|h_{T4} - h_{eT4}\|$ $R = 100$Mpc	R [Mpc] $\|h_{T4} - h_{eT4}\| = 1$
APR4	0.028	0.020	0.020	0.67	67
SLy	0.025	0.019	0.020	0.58	58
H4	0.012	0.012	0.014	0.33	33
MS1	0.014	0.014	0.007	0.35	35

Table 4.1: Results of the orbital eccentricity analysis. The first three columns show the eccentricity parameters obtained fitting equation 4.2. The fourth column shows the detectability of the eccentricity in a TaylorT4 approximate waveform with the same initial parameters of the model with the corresponding EOS and $d = 60$ km, for an optimally aligned binary at 100 Mpc. The fifth column shows the maximum optimally aligned binary distance for the eccentricity effect to be marginally detectable, calculated as $\|h_{T4} - h_{eT4}\|_{100Mpc} \times 100$ Mpc.

towards the merger (when the GW emission has a higher frequency and amplitude), and showing characteristic oscillations, typical of eccentric orbits. It is interesting to note that the evolution of models starting from a smaller initial separation is slightly different than the models starting from $d = 60$ km, with a faster orbital shrinking, in particular for the more compact stars (with APR4 and SLy EOSs). More on this phenomenon can be found in the next subsection.

The fitting curves are represented in red in figure 4.5, where the blue curves are the original distance data, instead. It is clear that at least one eccentricity cycle, before the plunge phase, when the parametrization of eq. 4.2 is probably not a good approximation anymore, is necessary for correctly estimating the orbital eccentricity. Therefore, the $d = 40$ km simulations will be excluded from the following analysis, and the results for the $d = 44$ km simulations with the stiffer EOS should be taken with care.

The resulting eccentricity values are reported in table 4.1. They are higher for the more compact stars, of about a factor 2.

To assess the correctness of the eccentricity computation procedure, and to evaluate if the GW amplitude oscillations are really an imprint of the orbital eccentricity, it is possible to compare the GW signal extracted from numerical simulations with one generated with post-Newtonian techniques for eccentric binaries. Recently, different groups have proposed techniques to generate analytical approximations of the inspiral waveforms for point particles in eccentric orbits [145, 278, 279]. These should be close to the BNS GW signal from numerical simulations, far from the merger phase, when tidal effects are not important. For this reason, many orbits simulations, with a large initial separation between the stars, are necessary to carry on this analysis. Figure 4.6 shows the GW amplitude for the BNS models of fig. 4.4 (black lines) and corresponding PN waveforms, generated following ref. [278] (accurate up to 2PN order in phase and Newtonian order in amplitude), and using the public LIGO Algorithm Library (LAL), with the same initial gravitational mass, eccentricity and frequency of the simulated model. At the beginning of the simulations, especially for the stiffer models, the PN approximant perfectly reproduces the simulated GW strain amplitude, including its oscillations. After a while, the simulated signal departs from the analytical one, because tidal effects and missing high-order post-Newtonian terms start to be important, but it keeps the same oscillations structure, until the final plunge phase. The difference between GWs from BNS simulations and point-particle PN approximations becomes farther from the merger in the most compact stars, in particular the ones with the APR4 EOS. This perfect match is less recognizable in the $d = 44$ km models, which

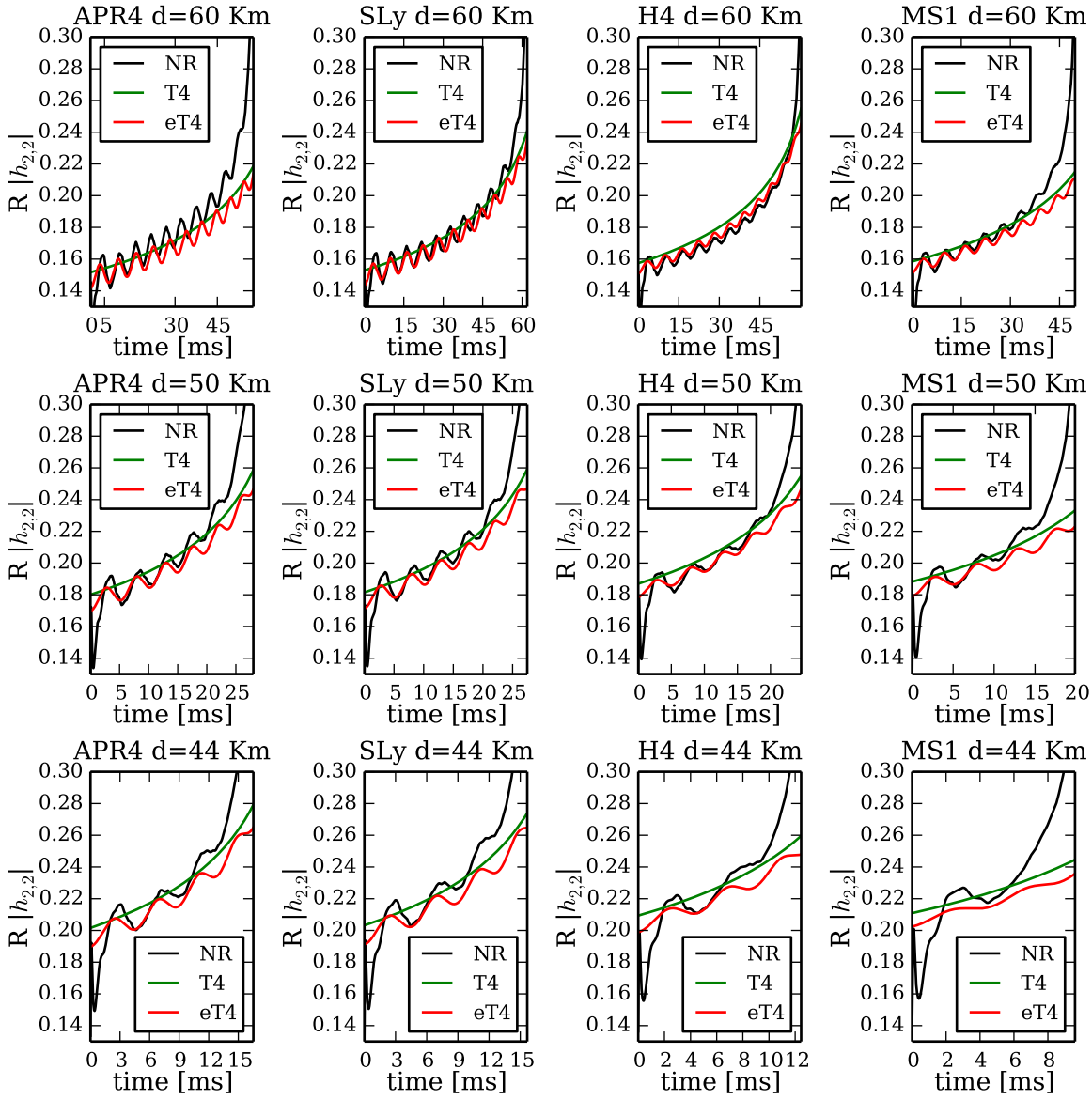

Figure 4.6: Gravitational wave strain amplitude for the same models of fig. 4.5. The black line represents the numerical simulation data, while the red line is a approximated post-Newtonian waveform for point-particles in an eccentric orbits (see ref. [278]).

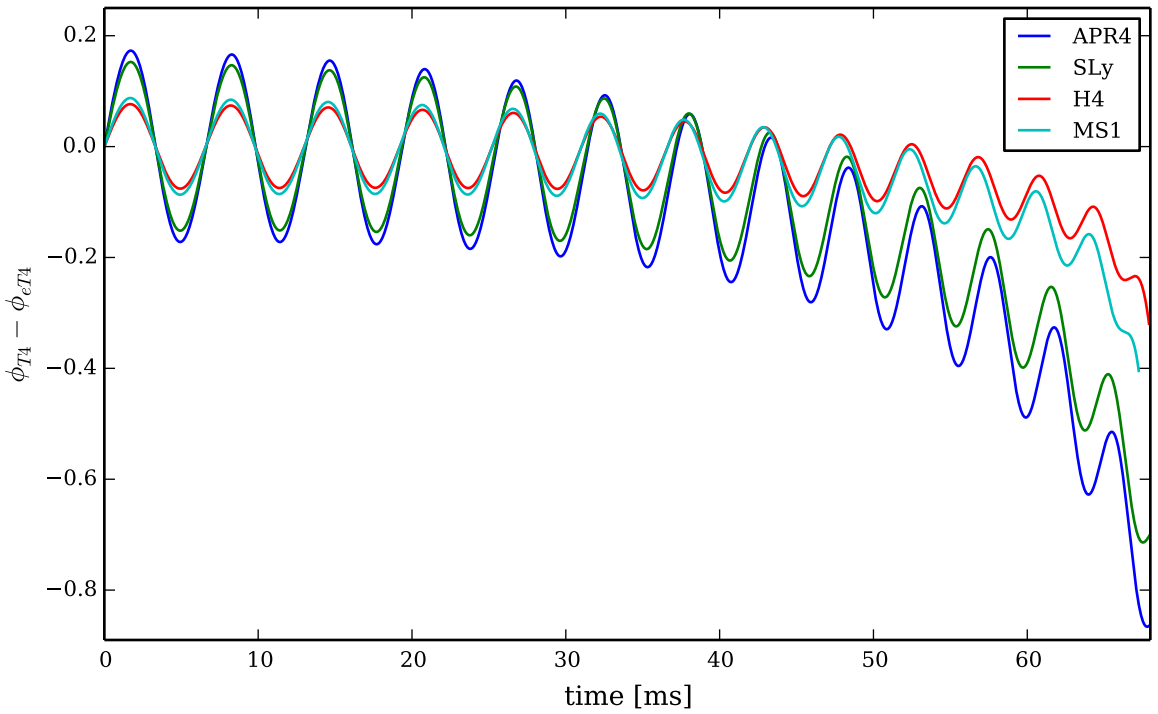

Figure 4.7: Difference in phase between a circular-orbits TaylorT4 approximant and a eccentric orbit post-Newtonian waveform, at the same PN order, starting from the same gravitational mass, frequency and eccentricity.

are close to the plunge phase already at the beginning of the simulations, and which have only a few eccentricity cycles (one for the H4 and MS1 models) before the merger. These results confirm that GW amplitude oscillations, remaining after our careful extraction procedure, are entirely due to the orbital eccentricity. I want to stress here, looking again at figure 3.2, that the use of the digital filtering after Ψ_4 integration is necessary for this comparison with the eccentric PN waveforms. With all the other strain amplitudes in fig. 3.2 computed with different integration methods, it would have been impossible to draw any conclusion from an analysis like the one in figure 4.6, due to the presence of a complex amplitude oscillations structure (given by noise and numerical integration errors), among which one cannot distinguish the physical oscillations caused by the orbital eccentricity.

It is interesting to assess which would be the impact of the orbital eccentricity introduced by quasi-circular initial data on GW detection and the following source parameters estimation. A possible first step in that direction is looking at the difference in phase between an eccentric post-Newtonian approximant, with the same gravitational mass and eccentricity of each of the simulated models in figure 4.4 with $d = 60\,\mathrm{km}$, and a standard TaylorT4 analytical waveform for point-particles coalescing in circular orbits, with the same masses. The result can be seen in figure 4.7. For the less compact models (with H4 and MS1 EOS, and an eccentricity around 0.01), the phase difference between the eccentric and the circular waveform oscillates around zero, with a maximum amplitude of about $0.1 rad$, which is most probably lower than the numerical errors of the evolution code (a lower bound of which is estimated in the next section). In the plunge phase, this difference raises

up to $0.4rad$. For the more compact models (with the APR4 and SLy EOSs, and an eccentricity between 0.02 and 0.03), instead, the phase difference oscillates around zero with an amplitude of $0.2rad$ for most of the inspiral, and can reach values close to a radiant at merger. This means that, while probably negligible in the less compact models, initial data eccentricity is a major source of error in numerical simulations of binary neutron stars inspiral for stars with a soft EOS. From figure 4.6, we already noted that eccentricity oscillations are the dominant factor in the difference between gravitational waveforms from many orbits BNS simulations (black lines) and point-particle post-Newtonian approximations (green lines), until the plunge phase, , even at low post-Newtonian order. This can make the assessment of tidal effects (and then EOS) impact on the gravitational signal more difficult, and hence can harm the efforts to pinpoint the neutron stars EOS from GW detections.

Another interesting evaluation is to measure the detectability, in the Advanced LIGO/Virgo interferometers, of the difference between eccentric and circular orbits waveforms. In particular, performing this computation starting from the initial frequency of the $d = 60\,\mathrm{km}$ simulations presented before, which are among the longest (in the inspiral phase) BNS simulations performed so far, allows to understand the importance of initial data eccentricity error in currently feasible BNS simulations, even if a detectability comparison should, in theory, be computed using a signal covering all the detectors frequency band. To do so, one can compute the distinguishability of two waveforms h_1 and h_2, using the following expression [13, 91, 280]:

$$||h_1 - h_2|| = min_{\Delta t, \Delta\phi} \sqrt{4 \int_{f_0}^{f_1} \frac{\left|\hat{h}_{+,1}(f) - \hat{h}_{+,2}(f) e^{i((2\pi f \Delta t + \Delta\phi)}\right|^2}{S_n(f)}}, \tag{4.3}$$

where $\hat{h}_{+,i}(f)$ are the Fourier transform of the plus polarization of the two compared strains, $f_0 = 9\,\mathrm{hz}$ and $f_1 = 7000\,\mathrm{hz}$ are, approximatively, the limits of the Advanced LIGO frequency band, and $S_n(f)$ is the one sided noise power spectral density for Advanced LIGO, in the *zero detuning, high power* configuration, which will be the best for detecting binary neutron stars mergers. Using this norm, it was shown in [280] that two detected gravitational waveforms will be distinguishable if $||h_1 - h_2|| \geq 1$. In particular, in the limit $||h_1 - h_2|| = 1$, the marginally distinguishable case, the two waveforms can be distinguished with a 1σ statistical significance.

In table 4.1 is reported the distinguishability between circular and eccentric orbits waveforms, computed for optimally aligned binaries at a distance of $R = 100Mpc$, and the corresponding minimum distance to have marginal distinguishability. The detectability of eccentricity effects at 100 Mpc is small, mainly because of the shortness of current numerical waveforms respect to the whole LIGO frequency band. When longer simulations will be available, especially to build hybrid analytical-numerical waveforms, able to cover the whole detectors band, this eccentricity effect will become more important.

Given these results, it is clear the importance of getting rid of the initial eccentricity of BNS orbits, in order to evaluate the difference between different EOSs and to model accurately tidal effects and other possible effects like stellar oscillations present in the inspiral phase. Work in this direction, mimicking what is already standard for binary black holes simulations, has been done by some groups [58, 95]. In particular, they use an iterative procedure, first evolving eccentric initial data, like LORENE's ones, and computing the eccentricity with eq. 4.2. Then, they correct accordingly the initial data, adding a radial velocity component, and start again the simulation. This process is repeated (usually three times), until a target value for the eccentricity is reached. For example,

for BBH simulations, the NRAR (Numerical Relativity and Analytical Relativity) collaborations prescribed $e < 2 \times 10^{-3}$, which is an order of magnitude lower than the one of LORENE's models. However, there is not yet a publicly available tool to generate low-eccentricity BNS initial data, which can be checked and evolved by anyone in the scientific community. I plan to dedicate some of my future work, immediately after this thesis, to create such tool.

4.1.2 Effect of the initial interbinary distance

Binary neutron star merger simulations presented in the literature start from a variety of initial values for the stars centres separation. As seen at the beginning of this section, long, many orbits, BNS simulations are necessary to perform comparisons with post-Newtonian approximations (either to construct longer hybrid analytical-numerical waveforms, to cover all the current GW detectors frequency band, or to evaluate the accuracy of different PN formulations and calibrate their free parameters), and to study tidal (and, more in general, EOS) effects on the inspiral waveform. On the other hand, when focusing on the post-merger signal, which is the primary target for three dimensional numerical investigations, for the lack of any analytical treatment so far, one wants to simulate the shortest possible inspiral, not to waste too many computational resources on that phase. From these necessities, several questions arise, such as:

1. How the numerical errors accumulate during many orbits evolutions? Which is the maximum number of orbits one can simulate with current numerical codes in order to keep a target accuracy?

2. How close to the merger a simulation can start, without propagating errors which can influence the post-merger results?

3. How accurate are the conformal thin sandwich initial data, depending on the stellar separation?

4. What is the difference between tidal deformations and stellar mode excitations developed during a numerical evolution starting from an initial large interbinary distance, or included in close-binaries initial data?

In order to answer all those questions, a first step is to compare simulations of the same model (in the case presented here, an equal mass model with a baryonic mass of $1.4\,\mathrm{M}_\odot$ for each star, and the four EOSs presented in sec. 2.1.1) starting from initial data with a different interbinary distance (which is equivalent to say that they have a different initial orbital frequency). The initial separations considered here are $60, 50, 44.3$ and 40 km. I can anticipate here that to give a complete answer to the previous questions, this work is not sufficient, and further explorations, using different numerical methods, and techniques to try to disentangle those errors sources, which are difficult to distinguish, are needed. This comparison can also be seen as using the full numerical 3D simulations to fill the gaps between several quasi-equilibrium configurations through which the binary must pass, evaluating with which accuracy are current numerical algorithms able to do so. Figure 4.8 gives a first overview of the difference between simulations with different initial stars separation. At the beginning of the shorter simulations, after the first "junk radiation" emission (explained in sec. 4.1.1), the signals of models with the same EOS agree very well, confirming that the dynamical evolution is able to connect LORENE's generated quasi-equilibrium configurations. However, in the last part of the coalescent phase, after the start of the $d = 40\,\mathrm{km}$ simulations, the signals start to diverge, with simulations starting from a closer interbinary distance having a faster phase evolution

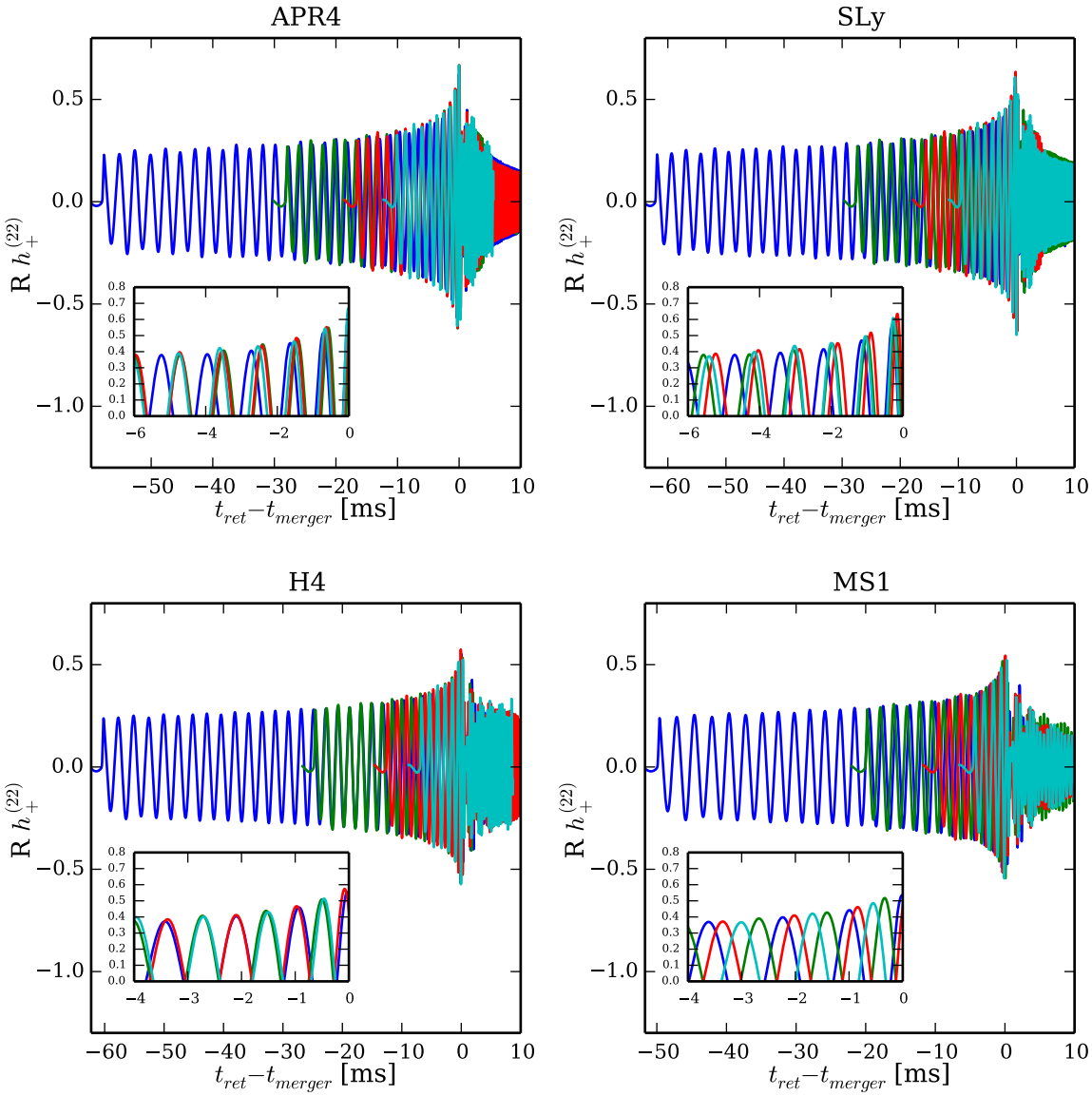

Figure 4.8: Gravitational wave strain plus polarization from simulations of an equal mass binary with $M = 1.4\,\mathrm{M}_\odot$ for each star, with different EOS and initial interbinary distance.

(see small boxes in figure 4.8). It is also interesting to note, contrary to what can be expected a priori, that the initial interbinary distance has also an impact on the GW amplitude in the post-merger phase. This could be potentially very important for numerical studies of the post-merger energy balance. A more quantitative analysis of these discrepancies can be found in section 4.2.3.

In order to investigate the differences in the phase evolution of simulations starting from different separations, during the inspiral, it is useful to align the simulations (with the same EOS) starting from $d = 50, 44.3, 40$ km with the longer ones, starting from 60 km. At first, the waveform are aligned at the time of the merger, considering them respect to the new time variable

$$\tilde{t} = t_{ret} - t_{merger}(d), \tag{4.4}$$

as they have already been shown in figure 4.8. Then, following a standard procedure, often used to compare waveforms of the same model generated with different techniques (see, for example, ref. [9, 11, 281]), the signals are aligned finding the time shift Δt and the phase shift $\Delta\Phi$, after defining the aligned GW phase

$$\Phi_{al1}(t) = \Phi_d(t - \Delta t) + \Delta\Phi - \Phi_{d=60}(t), \tag{4.5}$$

and then minimizing the following integral:

$$I(\Delta t, \Delta\Phi) \;=\; \int_{t_1}^{t_2} \left|\Phi_{al1}(\tilde{t})\right|^2 d\tilde{t}, \tag{4.6}$$

where the GW phase of the simulation starting from an initial interbinary separation d is defined from the gravitational wave strain h:

$$\Phi = arctan\left(\frac{h_X}{h_+}\right). \tag{4.7}$$

The integration limits are $t_1 = 3$ ms and $t_2 = min(20\,\text{ms}, t_{merger} - 2\,\text{ms})$, in order to avoid, as usual, the initial spurious radiation and the plunge phase.

In figure 4.9 are reported the differences between the aligned waves phase and the phase of the $d = 60$ km simulations waveforms. Outside the alignment interval, the phase evolutions between simulations starting from a different orbital frequency diverge quite significantly. This is more pronounced in the more compact stars, with the SLy and APR4 EOSs, showing a phase difference at merger of about 4 radiant. The stars with the H4 EOS have an intermediate behaviour, while the stars with the MS1 EOS show a much lower deviation, with a maximum phase difference at merger of 1 rad.

These results are not really satisfactory, showing a huge difference caused by the initial data separation, which can be mitigated by the alignement procedure in the alignement interval only. This last consideration leads to believe that eq. 4.5 is not the best for the signals scrutinized here. A different procedure to test, which can also help identifying the source of such huge phase discrepancies, is allowing for a dilatation of the time variable, as done in ref. [12, 97] to align waveforms of simulations with different resolutions, in order to compare them compensating for their different merger times. For each simulation with $d < 60$ km, one has to find the parameters η and $\Delta\Phi_2$ which, after defining

$$\Phi_{al2}(t) \;=\; \Phi_d(\eta \cdot t) + \Delta\Phi_2 - \Phi_{d=60}(t) \tag{4.8}$$

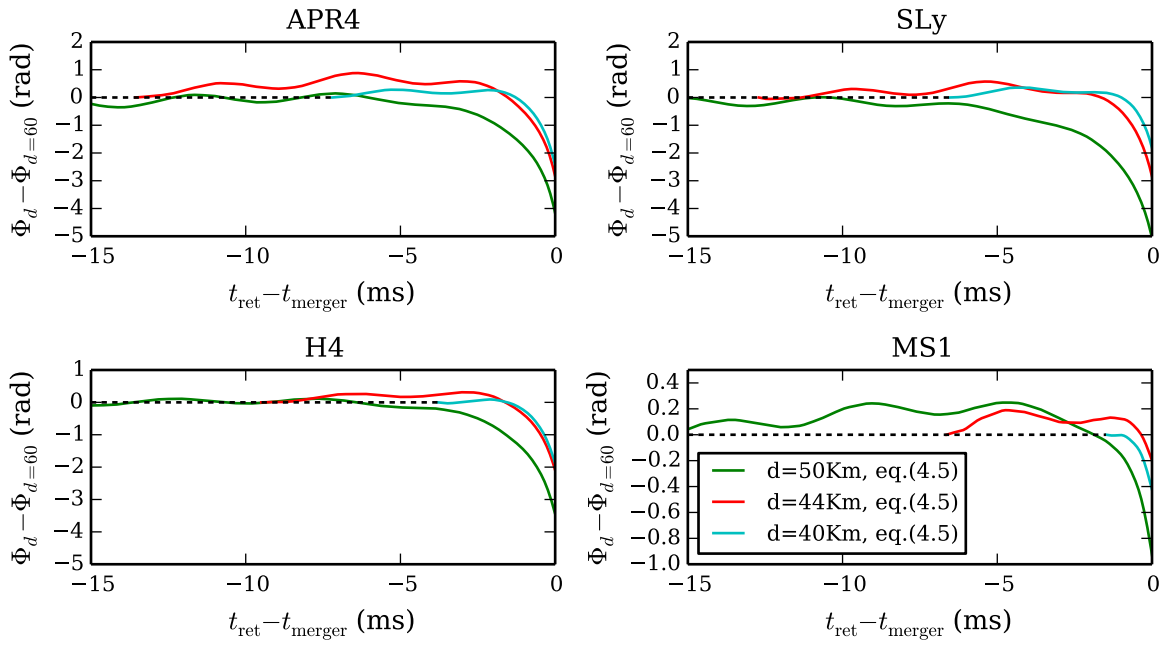

Figure 4.9: Difference in the accumulated phase between simulations starting from $d = 60\,\mathrm{km}$ separation and simulations starting from closer configurations, with the same EOS and star masses, aligned with eq. 4.5, allowing for a phase and time shift.

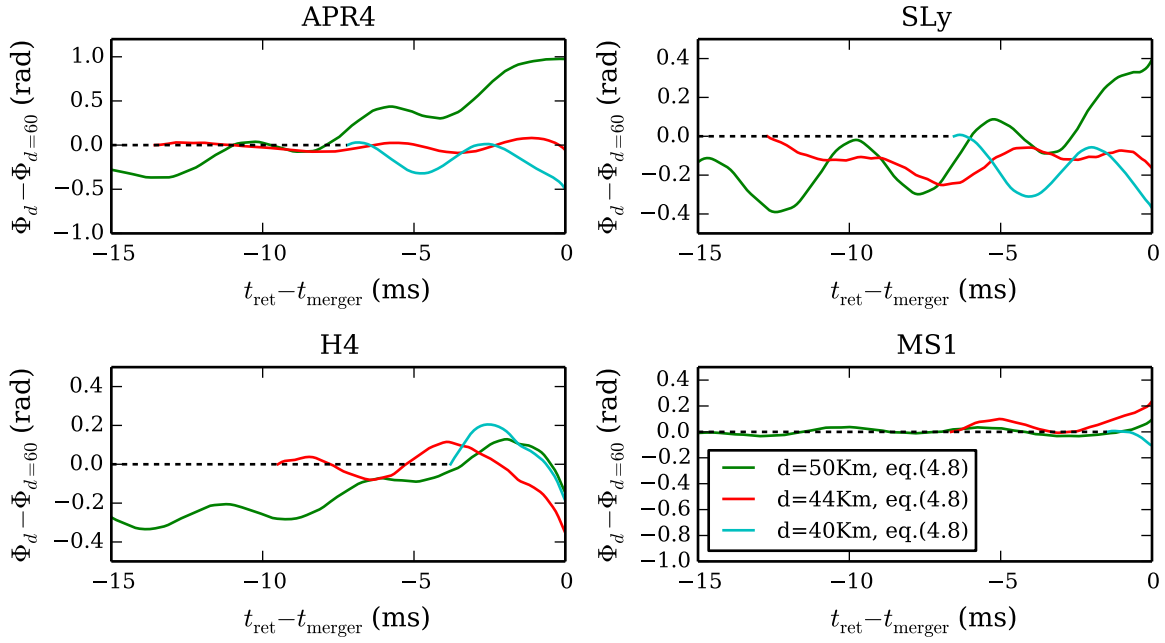

Figure 4.10: Difference in the accumulated phase between simulations starting from $d = 60\,\mathrm{km}$ separation and simulations starting from closer configurations, with the same EOS and star masses, aligned with eq. 4.8, allowing for a time dilation.

Model	Shift alignment (Eq. 4.5)		Dilatation alignment (Eq. 4.8)		
	Δt (ms)	$\Delta\phi$ (rad)	η	$\Delta\phi_2$ (rad)	$\Delta t_{\rm merger}$ (ms)
APR4(d=40 km)	1.40	6.26	1.112	-3.40	1.14
APR4(d=44.3 km)	1.71	6.07	1.096	-4.81	1.59
APR4(d=50 km)	1.82	5.76	1.047	-3.54	1.31
SLy(d=40 km)	1.53	6.83	1.140	-3.80	1.33
SLy(d=44.3 km)	2.02	7.46	1.111	-5.06	1.74
SLy(d=50 km)	2.34	7.51	1.056	-4.16	1.55
H4(d=40 km)	2.34	7.51	1.063	-1.26	0.43
H4(d=44.3 km)	1.56	5.82	1.075	-2.67	0.93
H4(d=50 km)	2.49	7.85	1.061	-3.92	1.52
MS1(d=40 km)	0.27	1.40	1.038	-0.30	0.17
MS1(d=44.3 km)	0.24	0.85	1.017	-0.51	0.17
MS1(d=50 km)	0.55	1.64	1.021	-1.16	0.42

Table 4.2: The first two columns represent the parameters Δt and $\Delta\phi$ which minimizes Eq. 4.6 for each model with $d < 60$ km. The next two columns show the parameters η and $\Delta\phi_2$ which minimize Eq. 4.9. The last column shows the effective merger time difference between the time-dilation aligned waveform and the original one $\Delta t_{\rm merger} = t_{\rm merger}(\eta - 1)$

minimize the following integral:

$$I(\eta, \Delta\Phi) \;=\; \int_{t_1}^{t_2} \left|\Phi_{al2}(\tilde{t})\right|^2 d\tilde{t}. \tag{4.9}$$

The result are presented in figure 4.10, again taking the phase differences between the aligned waveforms and the $d = 60$ km ones. With this different alignment, the phase differences are much smaller than before, and, more importantly, do not increase only outside the alignment interval. All the obtained values for the time dilation factor η are greater than one. This can be interpreted as the simulations starting from a closer initial binary configuration carry out more orbits compared with the ones starting from further apart, when comparing them over the same distance before merger. While this is always true comparing the simulations starting from $d = 60$ km with the ones starting closer, the effective merger times of simulations starting from 50, 44.3 and 40 km, instead, do not follow always the same trend, suggesting the presence of other sources of error, especially for the smallest initial distances.

The minimizing parameters for both alignment procedures, with the corresponding effective merger time difference, are reported in table 4.2. In table 4.3, instead, are reported the maximum phase differences, during the whole inspiral, between the aligned signals and the $d = 60$ km ones. In particular, the residual phase errors after the time dilation alignment (which corrects the effective merger time error) can be seen as lower bounds for the accumulated numerical errors by the evolution code, due to the finite grid resolution. As anticipated in sec. 3.4, these are much higher than the errors coming from the waveform extraction procedure, after the application of the second order perturbative extrapolation formula 3.197, even in the first part of the signal, contrary with what was found in [269] for binary black holes simulations.

This picture, coming from the GW phase differences, is consistent with the one given by the radiated energy and angular momentum. A common technique is to analyse the gauge-invariant

EOS	Shift alignment (Eq. 4.5) $\mathcal{E}_{\phi_{\rm al_1}}$ (rad)			Dilatation alignment (Eq. 4.8) $\mathcal{E}_{\phi_{\rm al_2}}$ (rad)		
	$d = 50$ km	44.3 km	40 km	$d = 50$ km	44.3 km	40 km
APR4	4.12	2.79	2.40	0.98	0.09	0.49
SLy	5.01	2.79	1.77	0.40	0.25	0.37
H4	3.41	2.06	1.85	0.33	0.35	0.20
MS1	0.91	0.19	0.41	0.09	0.23	0.10

Table 4.3: Maximum phase difference in the inspiral phase between waveforms from simulations starting from $d < 60$ km and simulations with $d = 60$ km, aligned according to Eq. 4.5 (first three columns) or Eq. 4.8 (second three columns).

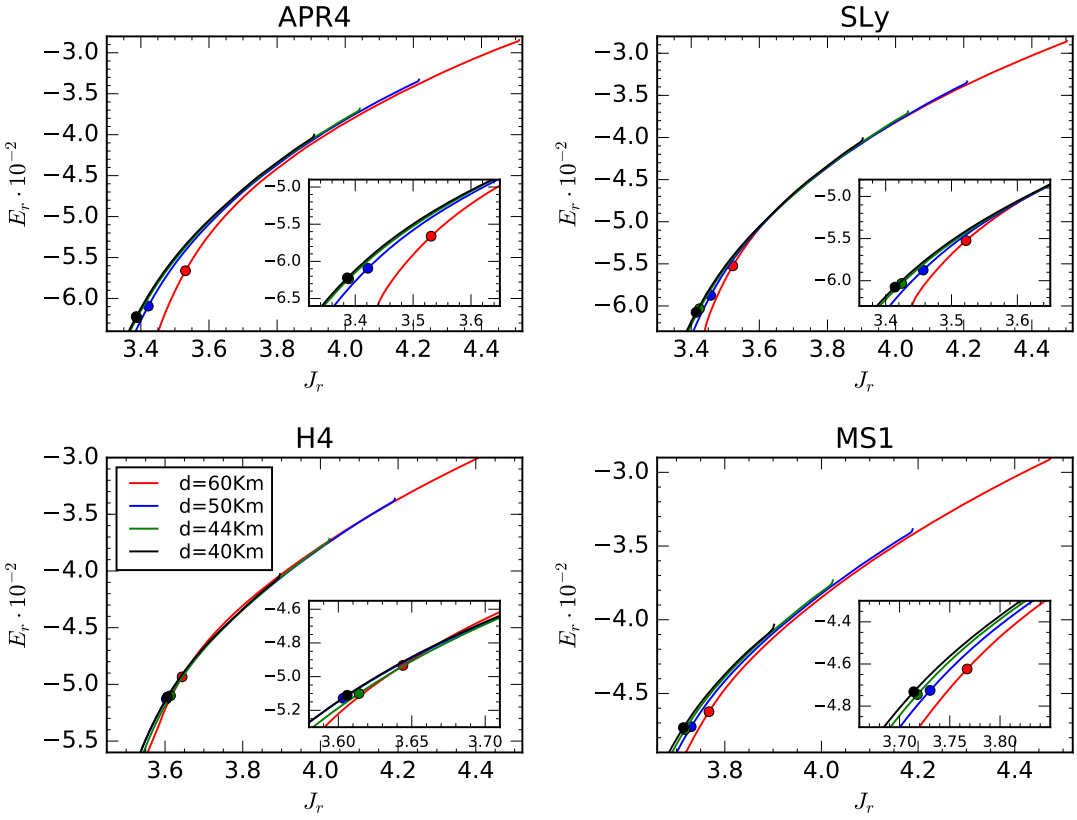

Figure 4.11: Gauge invariant reduced energy over reduced angular momentum curves, for the simulations presented in figure 4.8. The filled dots mark the binding energy and angular momentum at the time of the merger.

relation between the reduced radiated energy

$$E_r := \frac{\left(\frac{E}{M} - 1\right)}{\nu} \tag{4.10}$$

and the reduced radiated angular momentum along the z axis:

$$J_r := \frac{J_z}{M^2 \nu}, \tag{4.11}$$

where $E = M_{AMD} - E_{gw}$ and $J_z = J_{ADM} - J_{gw}$, with E_{gw} and J_{gw} computed from the gravitational wave strain using eq. 3.205 and 3.206. The initial ADM mass and angular momentum are taken from the output of the LORENE code, when importing initial data in the evolution code numerical grid. Finally, $M = M_1 + M_2$ is the sum of the two stars gravitational masses and $\nu = \frac{M_1 M_2}{M^2}$ is the reduced mass divided by M. The $E_r(J_r)$ curves are shown in figure 4.11, for each EOS and initial separation. They agree, in simulations with the same EOS, very well, until the start of the $d = 40\,$km simulations. After that point the simulations with d = 60 km start to diverge, resulting in a merger (marked with the filled circles in figure 4.11) at a higher energy and angular momentum. The other three simulations, instead, agree much better until the merger, and their merger energies and angular momenta are also close to each other. This has the natural interpretation that the simulations with a shorter effective merger time emit more energy and angular momentum during their faster approach to the merger, in which they carry out more orbits. In all the simulations starting from $d < 60$ km we observe a good agreement of the initial energy and angular momentum, after the short relaxation period, with the simulations starting from a larger interbinary distance, with a maximum difference of a few tenths of percent. This confirms again that, at least in the inspiral phase, our numerical evolutions, even at this resolution, are able to join the sequence of quasi-equilibrium states generated by the LORENE library. However, in the late inspiral and plunge phase, when the tidal effects start to be relevant, there are important differences.

This common picture can be naively interpreted considering that higher finite-resolutions errors accumulate during the longer simulations. In particular, this would explain why the $d = 60\,$km simulations are different from the other three, which are more similar, and why the phase differences are lower for the less compact stars (which have also a lower merger time). However, other explanations are possible.

A contribution to the difference between simulations starting from different separations can come from tidal effects, which are already important at the start of the $d = 40\,$km simulations, when the differences starts to show up in the $E_r(J_r)$ curves. As shown before, there are higher deviations in the $d = 60\,$km simulations with respect to the ones starting from further inward in the more compact stars. Tidal deformations developed in the dynamical evolution of models starting from a lower frequency could be different from the ones present in close binaries initial data, which are computed, with an approximate gravitational potential, by a spectral code and then interpolated in our cartesian grid. On the other hand, small tidal deformations could be present also in the d = 60 km initial configurations, but they could be under-resolved when we interpolate those initial data in our evolution code grid at our resolution. In ref. [93] has been shown that even small differences in initial data could be amplified during the evolution of the highly non-linear equations needed to describe BNS mergers in full general relativity, and this is particularly important for the the evolution of initial models with the higher merger times, which show the larger deviations between different initial separations.

The role of dynamical tidal effects was also recently underlined in ref. [47, 48]. These effects develop from the interaction of the tidal field with the stars quasi-normal modes of oscillation. These dynamic tides could be developed during a many orbits evolution, but are not considered in the calculation of the initial data used here. However, they should be more important for the less compact stars.

Another possible source of error is linked with the close binary initial configuration. In ref. [282] it is shown that initial BNS data computed in the conformal flatness approximation for the gravitational potential need to be evolved for more than 3 orbits to reach a true, stable, quasi-equilibrium configuration. This condition is not (or is barely) satisfied for the d = 40 km simulations (see table B.3).

From the available data it is impossible to disentangle all these error sources, evaluate their relative contributions, and fully answer to the questions posed at the beginning of this section. However, showing that there could be problems (or hidden physical effects) in many orbits BNS simulations, that their predicted inspiral GW signals do not match with the ones from shorter simulations, that these differences are EOS-dependent (they look higher in the more compact stars), and that they manifest themselves as a shorter effective merger time in the simulations starting from closer binaries configurations, are important and interesting first results, which can stimulate further enquiries about these subjects. In particular, new sequences of simulations of the same model starting from different separations, with better spatial resolution, are needed. More accurate numerical methods could also be employed, in particular Z4-family formulations of the Einstein equations (see sections 3.1.2), for their constraints damping property, and higher than second order methods for the hydrodynamics, as used for example in [93, 96, 98]. These more advanced numerical techniques, reducing the dynamical evolution errors, should reduce also the differences between the simulations with different initial interbinary distance, if that turns out to be their the dominant source. Another interesting direction would be to repeat this kind of simulations with a larger EOS sample, to better check the results dependency on the stars deformability, and, with that, on tidal effects. Also important is to perform a convergence study, to check if the differences reduces increasing the resolution. All these possible future studies, however, are very computationally expensive.

Finally, one last interesting direction is to compare different techniques for producing initial data, as already done in ref. [93]. This is made somewhat difficult by the fact that the LORENE code is the only BNS initial data code publicly available. However, being an object-oriented code, it is easy to add to it new algorithms for initial data generations, such as the use of the extended conformal thin sandwich formulation [283, 284], which tries to overcome the conformal flatness limitation.

In section 4.2.3 I will discuss more results coming from this comparison, about the impact of the initial interbinary distance on the post-merger GW signal.

4.2 Merger and post-merger dynamics

The merger and post-merger phases of binary neutron star systems evolution are the main target for numerical relativity, because, as already mentioned several times, they cannot be explored with analytical techniques.

The merger phase, difficult to properly define, is still largely unexplored, due to the turbulent nature of the (magneto)hydrodynamical processes happening when the two stars come into contact. For example, in ref. [89] was shown that, with current numerical relativity codes and using the highest currently feasible grid resolution, we are still not able to fully resolve the Kelvin-Helmotz

instability. This instability creates vortices in the shearing layer, by which, considering the star having infinite conductivity, the magnetic field is highly amplified, because the magnetic field lines are frozen with the fluid, and consequently are stretched in the small-scale vortices.

The post-merger phase, instead, is easier to study, because the remnant star evolves towards an equilibrium configuration (or collapses to a black hole). Its gravitational wave emission is dominated by a single mode (which, however, does not have constant frequency, but it varies slowly in time, as discussed more in detail in the next sections), due to the rotation of the bar-deformed neutron star. The dynamics of bar-deformed NSs and their development due to dynamical instabilities has been studied extensively in the past (see, for example, ref. [173, 175]). In BNS mergers, instead, the deformation is seeded by the tidal forces and the collision during the merger. In the subsequent evolution, while angular momentum is radiated in gravitational waves and redistributed in the remnant star, the degree of differential rotation decreases, and the star moves towards a more axisymmetric configuration, with a consequent diminishing of the emitted GW amplitude.

In the following section I will bring on the comparison between the models already presented in figure 4.3: five equal mass models with different total mass (and the same SLy EOS), five unequal mass models with different mass ratio (and the same total mass), four models of the observed PSR J0453+1559 system, with different EOSs, and four long ($d = 60\,\mathrm{km}$) simulations, with the same total baryonic mass and different EOS (and, consequently, a slightly different initial ADM mass too). In particular, I will compare the gravitational waves post-merger spectrum, and the energy radiated during the post-merger phase. This is useful to understand the role played by each of the main source parameters one hopes to be able to reconstruct from real GW signals observed in GW detectors.

4.2.1 The post-merger spectrum and its link with the neutron stars EOS

The most interesting aspect of the post-merger remnant evolution is the frequency spectrum of the emitted gravitational signal. In particular, the goal is to be able to connect its main features with some parameters directly linked with the neutron stars EOS.

Figure 4.12 shows the amplitude spectral density of the GW strain $|\tilde{h}|f^{1/2}$, where

$$|\tilde{h}| = \sqrt{\frac{|\tilde{h}_+|^2 + |\tilde{h}_\times|^2}{2}}. \tag{4.12}$$

The spectrum is computed, unless otherwise stated, from 8 ms before the merger to 15 ms after it. For the standard grid setup and finest resolution $dx = 0.25\,\mathrm{M}_\odot$ used in those simulations (see table A.2), this leads to a Nyquist frequency of 50.75 kHz and a spectrum frequency resolution of 43.48 Hz.

In all the different BNS models presented in figure 4.12, the spectrum shows an initial growth (given by the inspiral GW emission, whose spectrum is truncated at the lower end due to the limited number of simulated orbits), until a local maximum is reached (close to the merger instantaneous frequency, reported in tables 4.5, 4.6, 4.8 and 4.10). The GW emission at higher frequencies, instead, comes from the post-merger signal. In almost every model, a dominant peak is recognizable in the post-merger spectrum. This peak corresponds to the frequency f_2 (also called f_p, or f_{peak} in the literature) of the fundamental quadrupolar $m = 2$ oscillation mode of the bar-deformed neutron star [10]. This peak is not present only in models collapsing to a black hole right after the merger, like the equal mass one with $M = 1.6\,\mathrm{M}_\odot$ for each star and the SLy EOS (magenta line in the top-left panel of figure 4.12).

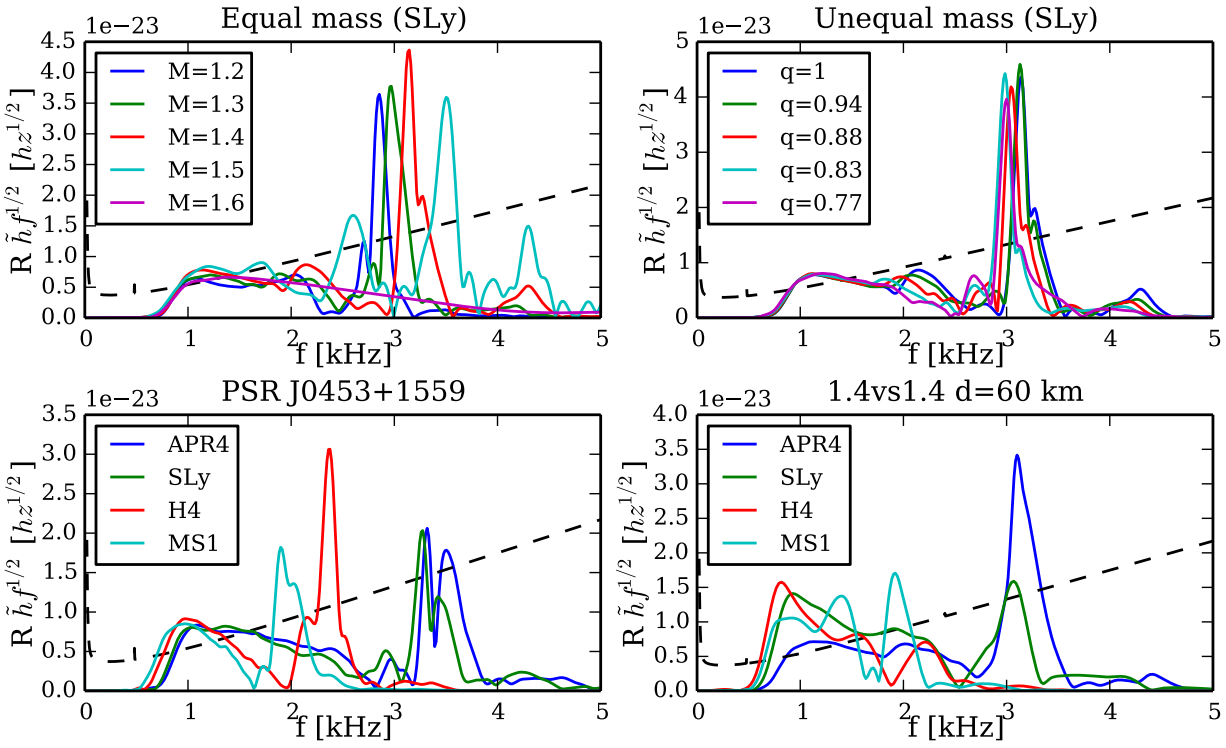

Figure 4.12: Amplitude spectral density for the (2,2) component of the GW strain, computed in an interval between 8 ms before the merger and 15 ms after it, except for models with a shorter inspiral phase (SLy1.5vs1.5, SLy1.6vs1.6) or a shorter simulated post-merger (SLyd60, H4d60, MS1d60). The spectral density values correspond to optimally oriented binaries at 100 Mpc from the detector. Here are highlighted the effect of total binary mass (top-left panel), mass ratio (top-right), and EOS in unequal (bottom-left) or equal (bottom-right) mass models. The black dashed line represents the sensitivity curve for Advanced LIGO detectors in the zero detuning - high power configuration, which will be the optimal one for detecting gravitational waves from BNS mergers.

Equal mass models with the SLy EOS and different total baryonic mass							
M_T $[M_\odot]$	f_1 [kHz]	f_1 from [285] [kHz]	f_{spiral} from [286] [kHz]	f_2 [kHz]	f_2 from [286] [kHz]	f_2 from [66] [kHz]	f_3 [kHz]
2.4	2.04	1.64	2.04	2.85	2.78	2.83	-
2.6	1.89 - 2.20	1.80	2.18	2.96	3.01	3.03	4.19
2.8	2.15	1.97	2.33	3.14	3.21	3.20	4.31
3.0	2.60	2.21	2.52	3.51	3.41	3.38	4.30

Table 4.4: Frequencies of the main spectral peaks for equal-mass models with the SLy EOS (top-left panel in figure 4.12). The frequencies f_1, f_2 and f_3 are computed from the simulation data interpolating the spectrum with a cubic spline (with resolution 1 Hz) and taking the frequencies of its local maxima. Predicted peak frequency values, according to empirical relations form ref. [66, 285, 286] are also reported for comparison.

Equal mass, SLy EOS			
M_T $[M_\odot]$	f_0 [kHz]	τ_0 [ms]	f_{merger} [kHz]
2.4	1.31	4.92	1.72
2.6	1.32	3.19	1.81
2.8	1.18	2.26	1.91
3.0	1.01	4.35	1.98

Table 4.5: Frequency and damping times for the $m = 0$ oscillation mode, obtained fitting the maximum density evolution after the merger, for equal mass models with the SLy EOS. The instantaneous frequency at merger is also reported.

Unqual mass models with $M_T = 2.8\,M_\odot$ and the SLy EOS						
q	f_1 [kHz]	f_2 [kHz]	f_3 [kHz]	f_0 [kHz]	τ_0 [ms]	f_{merger} [kHz]
1	2.15	3.14	4.31	1.18	2.26	1.91
0.94	2.10	3.13	4.27	1.18	1.88	1.90
0.88	1.98	3.05	4.17	1.23	1.44	1.81
0.83	1.83	2.98	4.11	1.26	1.54	1.73
0.77	-	3.00	-	1.28	1.96	1.63

Table 4.6: Frequencies of the main spectral peaks for unequal-mass models with the SLy EOS and total baryonic mass of $2.8\,M_\odot$ (top-right panel in figure 4.12). The frequencies f_1, f_2 and f_3 are computed from the simulation data interpolating the spectrum with a cubic spline (with resolution 1 Hz) and taking the frequencies of its local maxima. f_0 and τ_0 are computed fitting the post-merger maximum density oscillations. f_{merger} is the instantaneous frequency at the merger time.

Reproduction of the observed unequal-mass system PSRJ0453+1559 with different EOSs							
EOS	f_1 [kHz]	f_1 from [285] [kHz]	f_{spiral} from [286] [kHz]	f_2 [kHz]	f_2 from [286] [kHz]	f_2 from [66] [kHz]	f_3 [kHz]
APR4	2.39	2.45	2.76	3.32	3.57	3.67	4.63
SLy	2.26	2.26	2.56	3.27	3.43	3.41	4.24
H4	-	1.73	1.76	2.38	2.50	2.25	-
MS1	-	1.59	1.54	1.90	2.18	1.88	-

Table 4.7: Frequencies of the main spectral peaks for unequal-mass models based on the observed PSR J0453+1559 system, with different EOSs (bottom-left panel in figure 4.12). The columns correspond to the ones in table 4.4.

PSR J0453+1559			
EOS	f_0 [kHz]	τ_0 [ms]	f_{merger} [kHz]
APR4	1.10	1.47	1.87
SLy	0.99	1.51	1.67
H4	1.01	2.22	1.27
MS1	0.80	3.24	1.18

Table 4.8: Frequency and damping times for the $m = 0$ oscillation mode, obtained fitting the maximum density evolution after the merger, for unequal mass models reproducing the observed binary system PSRJ0453+1559, with different EOSs. The instantaneous frequency at merger is also reported.

Equal mass models with $M_T = 2.8\,M_\odot$ and initial $d = 60$ km, with different EOSs							
EOS	f_1 [kHz]	f_1 from [285] [kHz]	f_{spiral} from [286] [kHz]	f_2 [kHz]	f_2 from [286] [kHz]	f_2 from [66] [kHz]	f_3 [kHz]
APR4	2.03	2.08	2.51	3.10	3.34	3.47	4.41
SLy	1.91	1.97	2.33	3.07	3.21	3.20	4.12
H4	1.55	1.62	1.67	2.21	2.38	2.12	-
MS1	1.40	1.49	1.51	1.92	2.08	1.80	-

Table 4.9: Frequencies of the main spectral peaks for equal-mass models with total baryonic mass of $2.8\,M_\odot$ and different EOSs, starting from $d = 60$ km (bottom-left panel in figure 4.12). The columns correspond to the ones in table 4.4.

$M_T = 2.8\,M_\odot$ and $d = 60$ km			
EOS	f_0 [kHz]	τ_0 [ms]	f_{merger} [kHz]
APR4	1.30	2.10	1.86
SLy	1.25	1.82	1.72
H4	1.05	3.03	1.36
MS1	1.06	7.64	1.27

Table 4.10: Frequency and damping times for the $m = 0$ oscillation mode, obtained fitting the maximum density evolution after the merger, for equal mass models with total baryonic mass of $2.8\,M_\odot$ and different EOSs, starting from $d = 60$ km. The instantaneous frequency at merger is also reported.

In most models, another two subdominant peaks, one at each side of the dominant one, at frequencies called f_1 and f_3 (or, sometimes, f_- and f_+) are recognizable. Their physical origin has been the focus of a recent debate in the literature. They have been first interpreted as nonlinear combinations of the fundamental $m = 2$ mode with the quasiradial $m = 0$ oscillations [10, 287], which have frequency f_0 close to $\frac{f_1+f_3}{2} \simeq |f_2 - f_{1,3}|$. In more recent works, they have been, instead, attributed to the modulation of the main $m = 2$ mode by the nonlinear radial oscillations of the two rotating stellar cores in the first few milliseconds after the merger [14, 57, 245, 285]. Finally, in ref. [277, 286], a new mechanism was proposed for explaining the low frequency peak, in the stars with stiffer EOS: the GW emission at a new frequency $\hat{f}$ (also called f_{spiral}) due to the spiral arms created by the strong deformations during the merger, which rotate, in an inertial frame, at a frequency $\frac{\hat{f}}{2}$, slower than the central cores rotation.

It is important to note that, while the dominant post-merger peak is within the Advanced LIGO sensitivity curve for almost all models (with a reference distance of 100 Mpc and considering optimally aligned binaries), the subdominant peaks will be very difficult to detect in current interferometric detectors, and the next generation experiments, like the Einstein Telescope [288, 289], will be necessary for inferring the neutron star EOS properties from them.

In the top-left panel of figure 4.12, are compared the spectra of equal-mass BNS models with different total mass. The first characteristic one can note is that the post-merger spectrum of $1.6\,M_\odot$ merging stars (magenta line) does not have any high-frequency peak, but, instead, is monotonically decreasing after the first bump, relative to the inspiral GW emission. This happens because that model collapses to a black-hole right after the merger, so no (hyper)massive neutron star merger remnant is present in its evolution. The GW emission after collapse, due to disc oscillations or BH quasi-normal modes, is much weaker than the inspiral or post-merger NS emission, so it does not show up in the spectrum on this scale. Collapsing models are investigated more in depth in section 4.2.4. All the other systems show the dominant f_2 peak, which has a higher frequency and more power increasing the total mass of the system. An exception to this are the merging stars with $M = 1.5\,M_\odot$, which have less power in the f_2 peak than the $1.4\,M_\odot$ stars, because their remnant also collapses to black-hole before the end of interval in which the spectrum is computed, although after a short hyper-massive neutron star phase. Subdominant peaks, on each side of f_2, also become more important increasing the total mass. In particular, the f_3 peak is not recognizable in the $M = 1.2\,M_\odot$ system, while a low-frequency f_1 peak is present in the same model. Finally, it is possible to note that the $M = 1.5\,M_\odot$ system has also an additional peak at a frequency lower than all the other ones, below 2 kHz, which is not found in any other model.

The top-right panel of the same figure 4.12, instead, shows the effect of mass ratio on the GW spectrum. The main f_2 peak moves slightly towards a lower frequency increasing the mass asymmetry (in accordance with the results of [66, 67]). This effect, although small in the particular models analysed here, needs to be studied more in depth, with new simulations, adopting a wide range of total masses and EOSs, because it should be included in empirical relations linking the f_2 frequency with some characteristics of the initial stars or of their EOS. Since now, these relations are developed starting only from equal or close-to-equal mass systems [13, 245, 285–287, 290, 291], with the exception of the simple prescription in ref. [66]. Another effect of the mass ratio is the progressive disappearance of subdominant peaks, while the mass asymmetry increases. The most unequal mass system analysed here, with $1.2 - 1.6 M_\odot$ ($q = 0.77$), shows only one peak (at f_2) in its post-merger spectrum.

The bottom panels, finally, show the comparison of equal (right) and unequal (left) mass models

with different EOSs. The softer EOSs have the main peak at higher frequencies, with an effect which is much larger than the one due to the mass ratio. This is why the post-merger spectrum is one of the best candidate observables to reveal the neutron star EOS from observations of GW emitted by BNS mergers. In the unequal mass models, corresponding to the physical parameters of the observed system PSRJ0453+1559 ($q = 0.75$), no important secondary peaks are present, just as the $q = 0.77$ SLy models discussed above. Very small subdominant peaks are still present with the softer EOSs (APR4, and, more significantly, SLy), while they are totally absent with the stiffer EOSs (H4 and MS1). A very interesting and unique finding of these simulations is the presence of a double main peak in the model with the APR4 EOS. A change in time of the dominant mode frequency was already discussed in ref. [67, 285], but I am not aware of any other published simulation showing a split in the main spectral peak. This complicates further the phenomenology of the post-merger spectrum and its reconstruction with simple empirical prescriptions. This double peak could be linked with the finite-size of the simulated post-merger signal, and the higher-frequency peak, related to the fist few milliseconds after the merger (see also the spectrogram in figure 4.17), will have its weight reduced in a longer signal. However, most of the energy emission in gravitational waves happens during the simulated time (see section 4.2.2), therefore the damped gravitational waves emitted after 30 ms from the merger could qualitatively modify only slightly the overall frequency spectrum. A detailed analysis of this effect would require, first, an accurate study of the damping time resolution dependence, since the effect of numerical dissipation could be important. Such investigation is still a work in progress, starting from the data presented in appendix A.1 to study the convergence properties of the inspiral signal.

As mentioned in the last paragraph, several empirical universal relations have been proposed to link the frequencies of the main GW spectral peaks to some physical characteristics of the initial stars, independently of the neutron star EOS. If correct, these could be used to easily extract the source physical parameters from a GW detection, with a strong enough signal to be able to recognize also the post-merger (which, having a GW emission at higher frequency, is more difficult to be detected for current interferometers). These relations, however, are often based on a limited number of simulations, and, in particular, unequal mass systems are often ignored. As noted before, the inclusion of unequal mass BNS systems (which we now know that are existing in nature) will open a new direction in the parameter space and could, therefore, potentially break the empirical relations developed so far.

In particular, the fundamental quadrupolar oscillation mode, which is responsible for the f_2 peak, is known to be tightly correlated, in non-rotating stars, with the combination

$$\sqrt{\frac{M}{R^3}}. \tag{4.13}$$

This suggests that, if the remnant radius is related with the radius of a fixed mass non-rotating NS, in a EOS-independent way, there could be a relationship between f_2 and the NS radius. This was explored in ref. [286, 287], where, for fixed total mass of the (equal mass) BNS system, tight relationships where found between f_2 and the radius of a non-rotating neutron star with a mass higher than the one of the original coalescing stars (for example, the radius of $M = 1.6\,\mathrm{M}_\odot$ NSs for a system with total gravitational mass $2.7\,\mathrm{M}_\odot$), because the merger remnant central density is higher than the maximum density of the merging NSs. These relationships, however, do not scale so well when trying to parametrize also the contribution of the total mass of the system. The dependence of f_2 with the binary mass, could be itself dependent on the EOS, as shown in ref. [286]. Another interesting, and simple, way to connect f_2 with the physical parameters of the merging stars is

proposed in ref. [66], where it is connected, using a linear regression, and considering an inverse correlation with the total mass, with the conctact frequency of the merging stars, computed using an approximation from ref. [292] starting from the initial stars masses and radii. This allows, also, to take into account unequal mass systems, because they will have a slightly different contact frequency than the corresponding equal mass one with the same total mass. Comparing the f_2 predicted from those relations, and the results of the simulations in figure 4.12, one gets compatible frequency values, considering our Fourier transform sensitivity (see tables 4.4, 4.6, 4.7, 4.9). However the effect of mass ratio is underestimated by the relationship of ref. [66] (as is visible also in their figure 4), and both empirical relationships seem to work better for lower mass systems. Other interesting empirical relationships have been developed in ref. [245, 291], linking f_2 with the tidal coupling constant k_2. They are particularly interesting, because a single parameter is responsible for the EOS effect on the GW signal in both the inspiral and the post-merger phase.

The low-frequency subdominant peak has also been a target for universal relations linking it to the stellar mass and radius. In order to compare the leading physical interpretations for the subdominant peaks origin against the data discussed here, in figure 4.13 are plotted all the spectra of fig. 4.12, with vertical lines indicating the results of different prescriptions to forecast the frequencies f_1 and f_3, starting from the initial stars parameters. The low frequency green line is computed from eq. 18 of ref. [285], which comes from a fit of f_1 data from their simulations (which use numerical methods and EOSs very similar to the ones described in this thesis) against the initial stars compactness (or its average, in the case of unequal mass models). The corresponding high frequency line, approximating f_3, is computed simply as $f_3 = 2f_2 - f_1$, with f_1 taken from their empirical relation and f_2 directly from the simulations results. The cyan line marks the f_{spiral} frequency, computed with eq. 26 of ref. [285], which was obtained fitting the data from ref. [287] with a second order polynomial in the (average) compactness of the merging stars and their total gravitational mass.

The dashed red lines, instead, mark the frequency resulting from the combination of the $m = 2$ and $m = 0$ modes, at a frequency sometimes called $f_{2\pm0}$. They are simply computed as $f_2 \pm f_0$, with f_2 taken from the data and f_0 computed fitting the maximum density oscillations, with the following test function:

$$\rho = at + bt^2 + ce^{\frac{t}{\tau_0}} sin\left(2\pi f_0 t + \phi\right). \tag{4.14}$$

For the same purpose, it is also possible to fit the minimum lapse, instead, as done in ref. [68, 285]. The f_0 values obtained with both methods are compatible. The post-merger evolution of the maximum density can be seen in figure 4.14. ρ_{max} is growing quadratically, from the merger time, and has damped oscillations in the first few milliseconds. These oscillations have a similar frequency for every mass (except for the collapsing model with total mass $M_T = 3\,M_\odot$), mass ratio and EOS, but very different amplitudes and modulations. Their amplitude increases with the total mass of the system, as the power in the subdominant modes. This is consistent with the remnant getting closer to the threshold mass for quasi-radial collapse. The oscillations amplitude, instead, decreases with the mass asymmetry, while, again, also the power in the subdominant peaks decreases substantially. Models with a mass ratio far from one have also a limited growth of the average maximum density, respect to equal mass models. This happens because a larger amount of mass is driven away from the remnant core, as seen in the last panels of figure 4.2, due to the tidal disruption of the lower mass star. This difference is potentially very important, because it means that mass ratio can change significantly the collapse time of BNS merger remnant, influencing both the total energy emitted in GWs and the timescales for electromagnetic or matter emissions. For example, the PSR

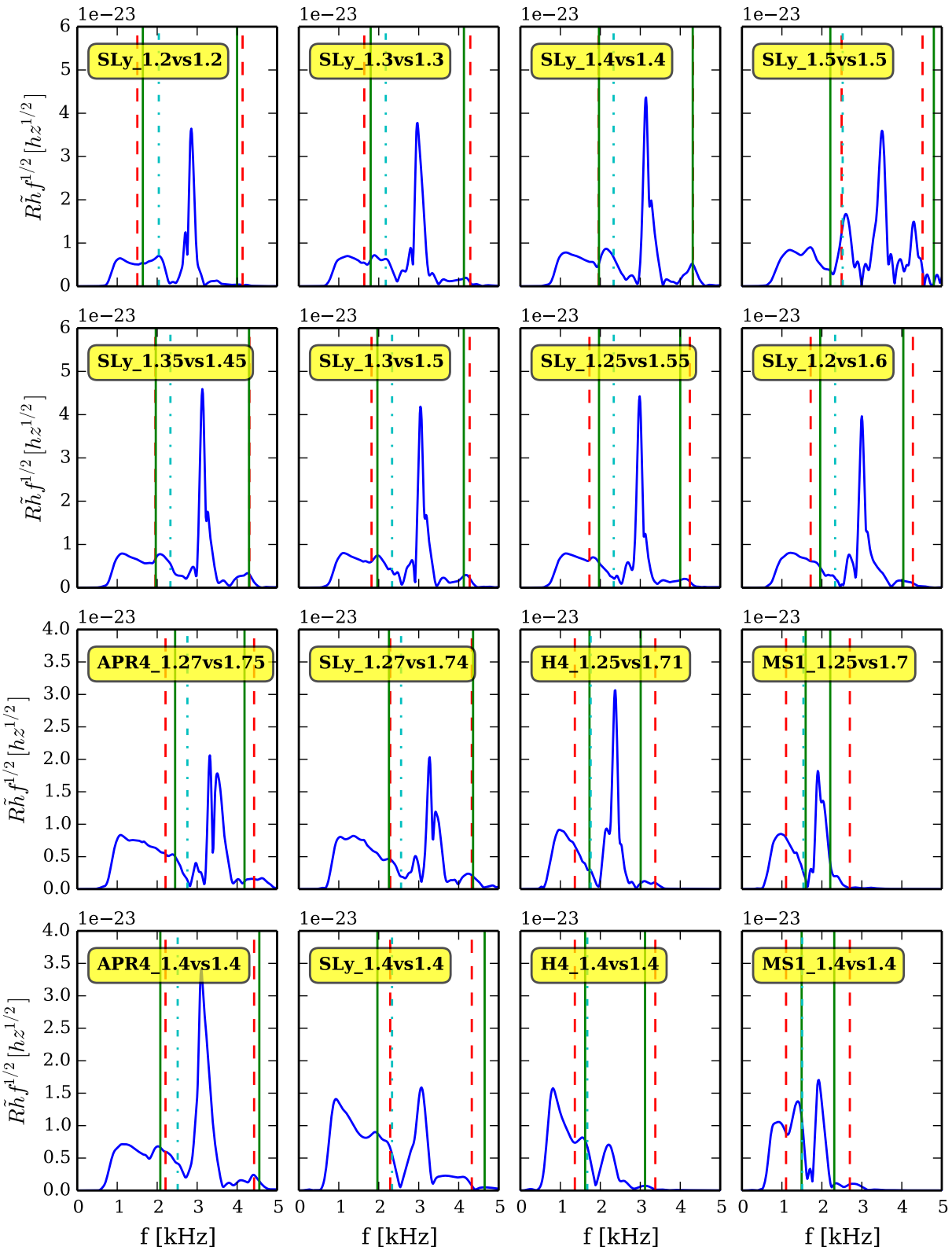

Figure 4.13: Amplitude spectral density of the GW strain, for the same models of fig. 4.12, for an optimally-aligned source at 100 Mpc from the detector. The vertical lines mark the subdominant modes frequencies predicted by empirical relations (green lines for f_1 and f_3 from ref. [14, 285] and cyan line for f_{spiral}, from the formula of ref. [285], extrapolated with the data of ref. [287]), or by mode composition (red dashed lines).

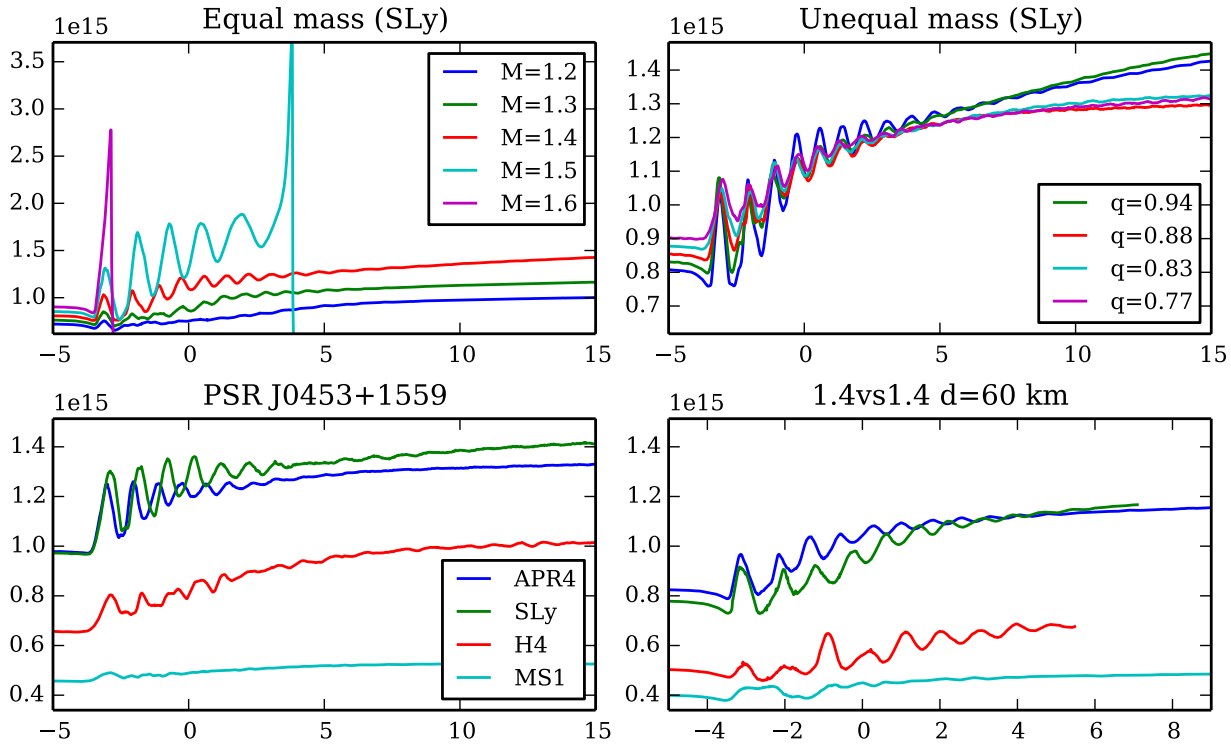

Figure 4.14: Evolution of the maximum density in the models presented in figure 4.13. Fitting its oscillations it is possible to compute the frequency of the quasi-radial $m = 0$ mode.

J0453+1559 model has a higher total mass than the equal mass SLy1.5vs1.5 model, but the former does not collapse to black hole in the simulation running time (about 30 ms after the merger), while the latter does collapse in a few milliseconds after the merger. The maximum density reached and its oscillations amplitude are also heavily influenced by the NS EOS (see bottom panels of figure 4.14, in which, for example, can be seen that the stars with MS1 EOS have way lower amplitude in their quasi-radial oscillations). In particular, in the stiffer EOSs, some modulations are present in the density oscillations. These have been found also in ref. [277, 286], where they have been interpreted as due to the slower rotation of the two antipodal bulges (forming the spiral arms of the bar-deformed remnant), producing a modulation with frequency $f_2 - f_{spiral}$. When the antipodal bulges and the central double cores are aligned, the compactness (and then, the maximum density) is lower, and when they are orthogonal the compactness and the maximum density are higher.

Looking at figure 4.13, it is still impossible to give a definitive answer for the physical origin of the subdominant peaks, because the frequency coming from the empirical relationship for f_1 is often close to the one for f_{spiral} (in the less compact models) or for $f_{2\pm0}$ (in the more compact models), as already noted in ref. [285]. However, some useful information can be gathered, which are in accordance with previous published works. Looking at the first row, the $M = 1.2\,\mathrm{M}_\odot$ system is consistent with the f_{spiral} model, because both the predicted f_1 and f_{2-0} fall at a frequency for which there is no peak in the spectrum. Moreover, no high frequency peak f_3 is found, which would be present if the low frequency peak came from an interaction between the $m = 2$ and $m = 0$ modes, but should be absent if only the emission at f_{spiral} was dominant, as it seems to be the case here. Increasing the masses (and, therefore, the compactness) of the merging stars, we find a model with a possible coexistence of both f_1 and f_{spiral} ($M = 1.3\,\mathrm{M}_\odot$), belonging to the category classified as "type II" in ref. [286]. The $M = 1.4\,\mathrm{M}_\odot$ model, instead, seems to have a low frequency peak in between the predicted f_1 (or the close f_{2-0}) and f_{spiral}. However, this oddness will be clear in the next paragraph, looking at the spectrogram. Finally, the $M = 1.5\,\mathrm{M}_\odot$ model shows two subdominant peaks which are closest to f_{2-0}, again in accordance with ref. [277], where is stated that the mode combination should be the dominant effect in models close to collapse. In the unequal mass PSR J0453+1559 system (third row of figure 4.13), there is only a recognizable subdominant peak for the softer EOSs, which is close to the predicted value for f_1 (and also for f_{2-0}, in the case of SLy), while the f_{spiral} prediction falls in a region without any spectral feature, consistently with what is expected for the more compact stars. The absence of subdominant peaks with the stiffer EOSs can be explained with the low amplitude of the density oscillations and the absence of a two-arms spiral structure, due to the high mass asymmetry. The last row shows the subdominant peaks being close to f_1 in all models, but also close to f_{spiral} in the least compact ones. In this case, contrary to the SLy1.2vs1.2 model, the presence of also an f_3 peak, close to $2f_2 - f_1$, makes a strong case for at least a contribution coming from the modulation of the dominant mode by the quasi-radial oscillation of the double rotating cores. However, the results from the spectrum of $d = 60\,\mathrm{km}$ simulations must be taken with care, since they can be biased by the numerical errors accumulated during the long inspiral numerical evolution, as argued in the following section 4.2.3.

The graviational waves post-merger spectrogram

Some recent works [67, 99, 285] highlighted the importance of not looking only at the main spectral features of the post-merger GW emission by computing its Fourier transform in a wide interval, but studying, instead, also its time evolution. The easiest and standard way of doing this is to build a Fourier spectrogram, computing signal Fourier transforms in small intervals (in this particular case,

5 ms intervals were used), with an high superposition between them (in this case, of 95%). For every Fourier transform, the time domain signal is first padded with zeros, to have a better frequency resolution, with a padding length of two times the original signal. The results are shown in figures 4.15, 4.16, 4.17 and 4.18, in which are also reported, with horizontal lines using the same color code of fig. 4.13, the estimates for f_1, $f_{2\pm0}$, f_{spiral} and f_3, together with a black line representing the f_2 values *measured* from the full spectrum.

The first interesting feature of the spectrograms, visible in all models, is that the secondary spectral peaks correspond to GW emissions only at most in the first five milliseconds after the merger. This is consistent with the time scales for the damping of the quasi-radial oscillations τ_0, reported in tables 4.5, 4.6, 4.8 and 4.10. At the same time, the dominant GW emission mode shows a change in frequency, right after the damping of the subdominant modes. The f_2 frequency, measured in the complete spectrum, corresponds to the frequency of the single exponentially damped remaining oscillation mode, after the first milliseconds. The main emission frequency in the first part of the post-merger, called f_{2i} in ref. [285], where this change in frequency was first recognized, can be computed like f_2 but from a short spectrum, ending 5 ms after the merger. For this reason, the $f_{2\pm0}$ frequencies should be computed using $f_{2i} \pm f_0$, because the mode combination could act only in the first few ms, before the $m = 0$ oscillation mode damping. This was done to draw the red dashed lines in figures 4.13 and on the spectrograms. Another interesting feature is that the frequency of the dominant mode, even after this initial "switch", is not constant, but increases in time, in particular in models closer to collapsing. This happens due to the redistribution of angular momentum in the remnant, which evolves towards a more compact configuration, causing the central double-core structure to rotate faster, increasing the main emission frequency. This change in the dominant mode frequency is less pronounced in the unequal mass models (see fig. 4.16 and 4.17), coherently with the slower increase in their central density, as seen in the top-right panel of figure 4.14.

A case for the usefulness of looking at the full spectrogram is made by the models SLy1.3vs1.3 and SLy1.4vs1.4 (figure 4.15). They show, in the first 2-3 ms, an emission at both the frequency predicted for f_{spiral} and the one for f_1 (or f_{2-0}, they appear to be very close for those two models). For the first model of the two, this is reflected also by the presence of two distinct peaks in the full spectrum of fig. 4.13. For the second one, instead, the f_{spiral} emission have more power but dies down in just a couple of milliseconds, while the f_1 (or f_{2-0}) emission lives for more than 5 ms, but has less power. The result, in the full spectrum, is a single peak, with a large width, in between the two frequencies. The model SLy1.2vs1.2, which in the full spectrum shows only one low-frequency peak close to f_{spiral}, in the spectrogram has, instead, also an emission close to $f_{2\pm0}$ (or f_1 and f_3), but with a low amplitude and not starting right at the merger, but only after some milliseconds.

In the unequal mass models, which have the same total mass and EOS of SLy1.4vs1.4 (figure 4.16), the f_{spiral} emission disappears even at moderate mass ratios, because the two spiral arms structure is replaced by a single spiral arm (coming from the deformation of the less massive star). The emission due to the interaction between the $m = 2$ and $m = 0$ modes, instead, gradually gets less power and also a shorter damping time, increasing the mass asymmetry, due to the parallel reduction of the density oscillations amplitude.

The interesting split peak in the post-merger GW spectrum of the PSRJ0453+1559 system with the APR4 EOS can be explained simply by the difference in the frequency of the main emission mode between the first 3 ms and the rest of the signal, which is bigger than in most of the other models, and by the fact that the remaining of the signal quickly loses power and its frequency does not increase with time. Another interesting feature of this system is a week, low frequency (1.7 kHz)

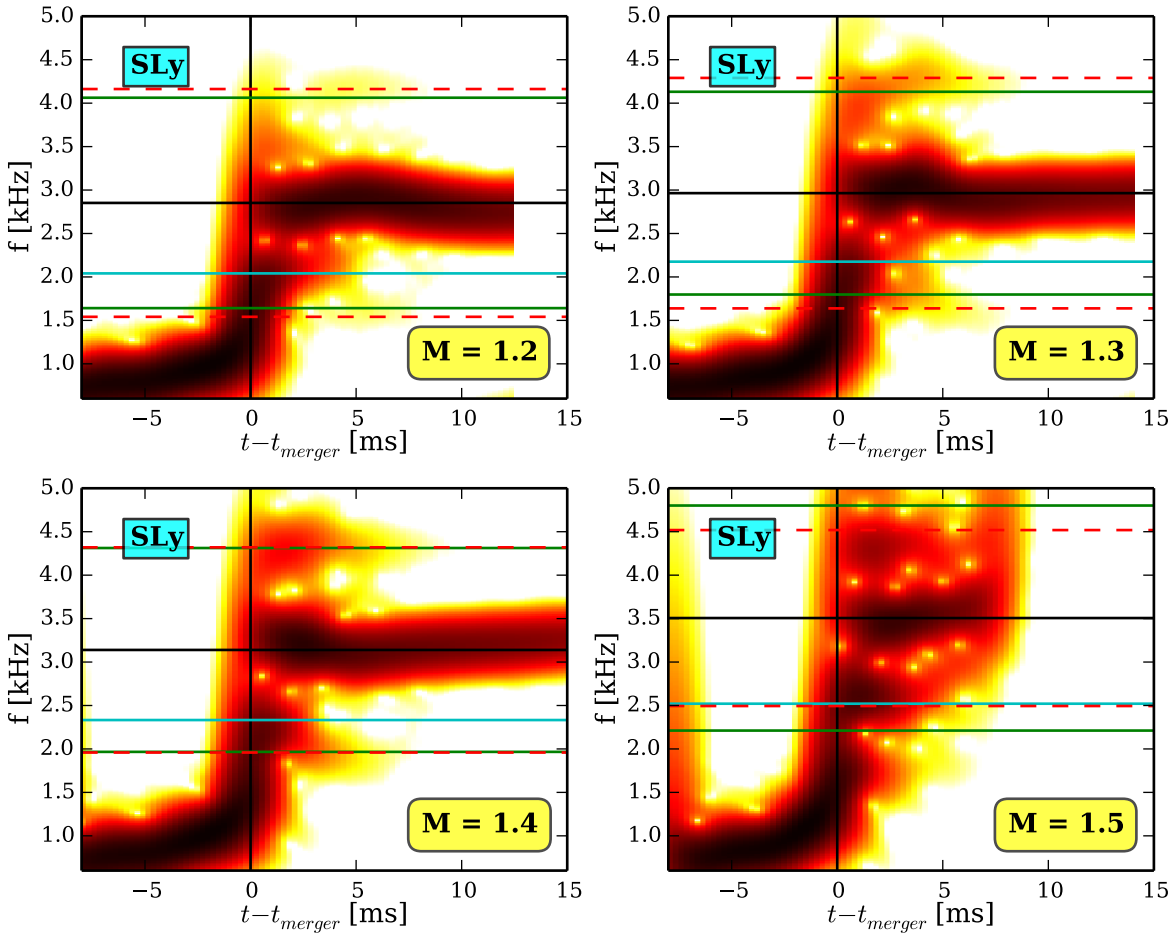

Figure 4.15: Fourier spectrograms of the post-merger GW signal for the equal mass models present in the top-left panel of figure 4.13, with the SLy EOS and different total mass. Detail of its computation can be found in the text. The coloured horizontal lines mark predicted frequencies for the subdominant peaks, with the same color-code of fig. 4.13. The black horizontal lines mark, instead, the peak frequency f_2 measured from the full spectrum.

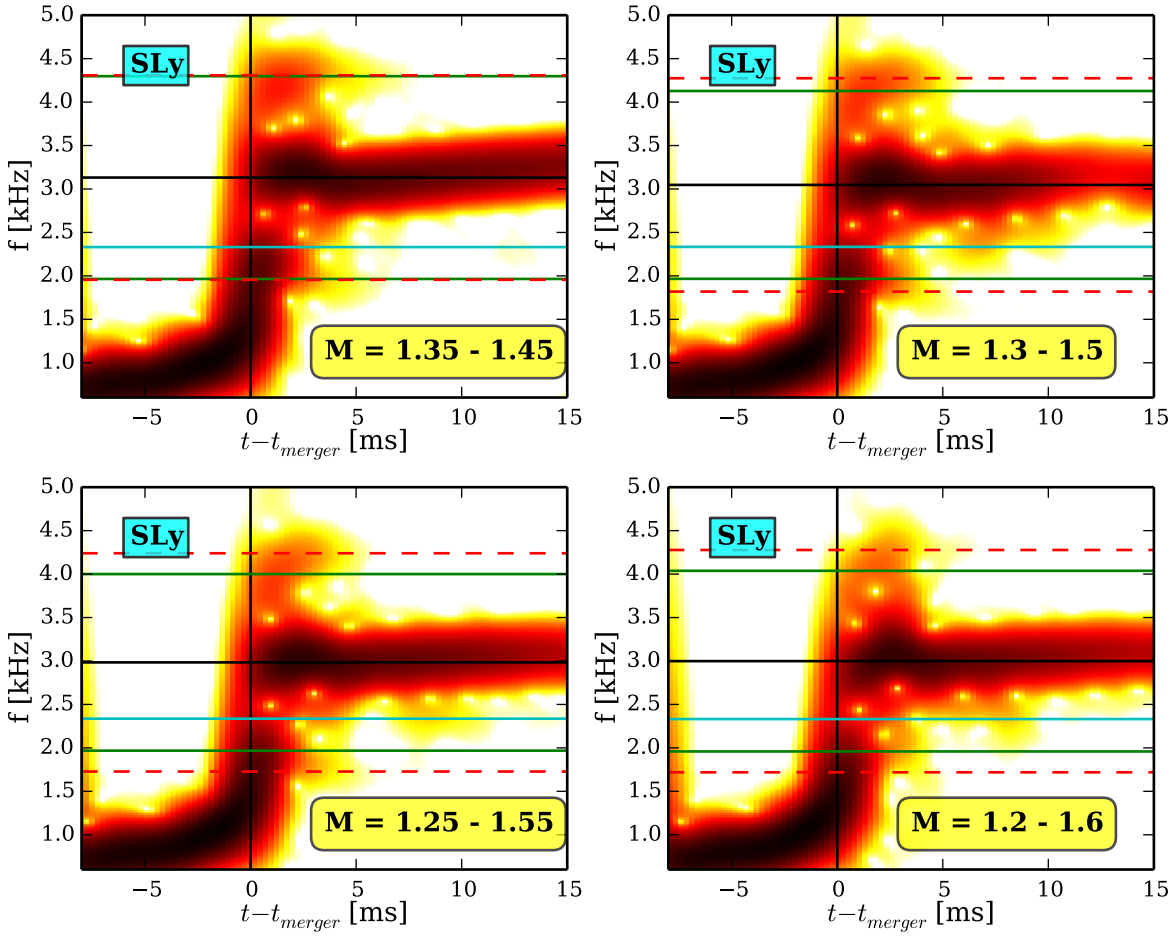

Figure 4.16: Fourier spectrograms for the (2,2) mode of the post-merger GW signal for the unequal mass models present in the top-left panel figure 4.13, with the SLy EOS, a total baryonic mass of $2.8\,M_\odot$ and different mass ratio, from $q = 1$ to $q = 0.77$. Detail of its computation can be found in the text. The horizontal lines mark predicted frequencies for the subdominant peaks, with the same color-code of fig. 4.13. The black horizontal lines mark, instead, the peak frequency f_2 measured from the full spectrum.

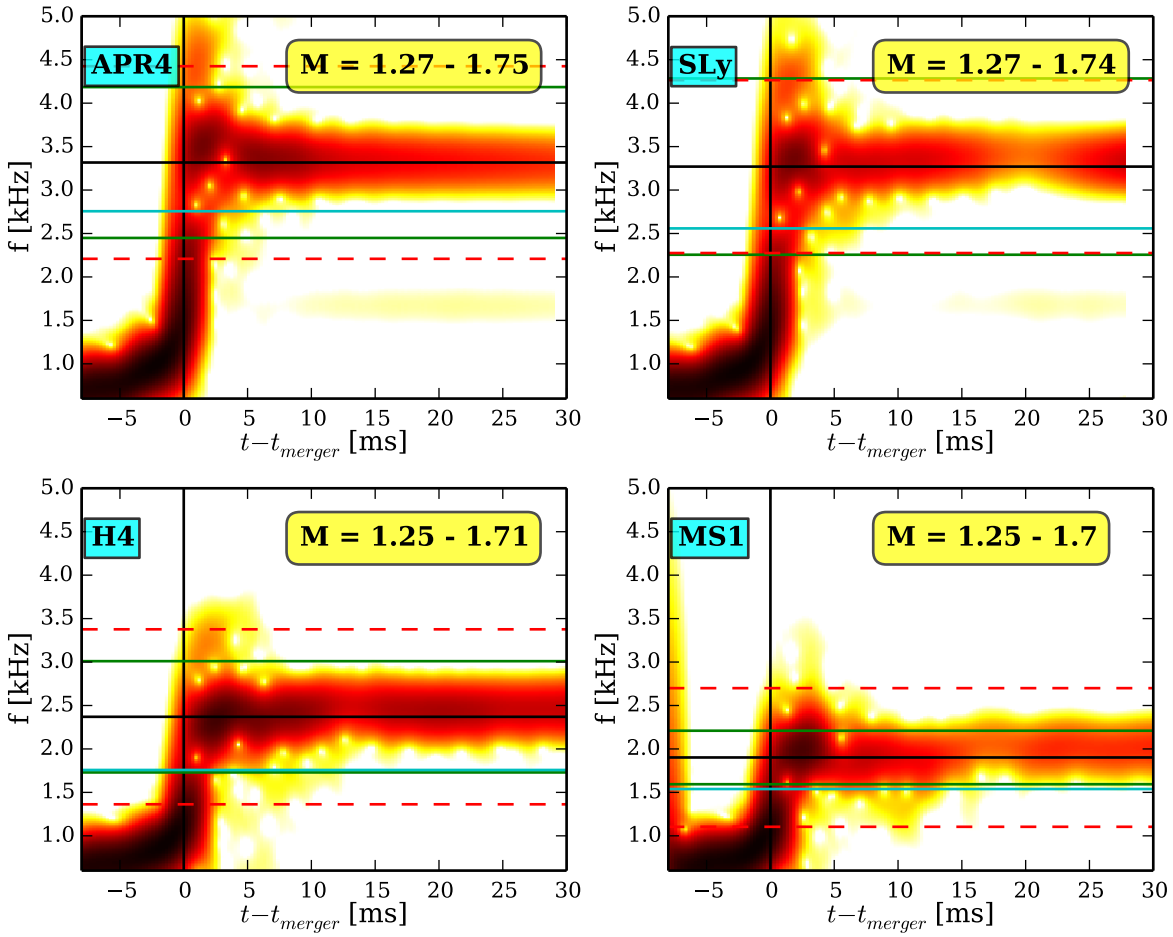

Figure 4.17: Fourier spectrograms for the (2,2) mode of the post-merger GW signal for the models present in the bottom-left panel of figure 4.13, based on the observed PSRJ043+1559 system, with different EOSs. Detail of its computation can be found in the text. The horizontal lines mark predicted frequencies for the subdominant peaks, with the same color-code of fig. 4.13. The black horizontal lines mark, instead, the peak frequency f_2 measured from the full spectrum.

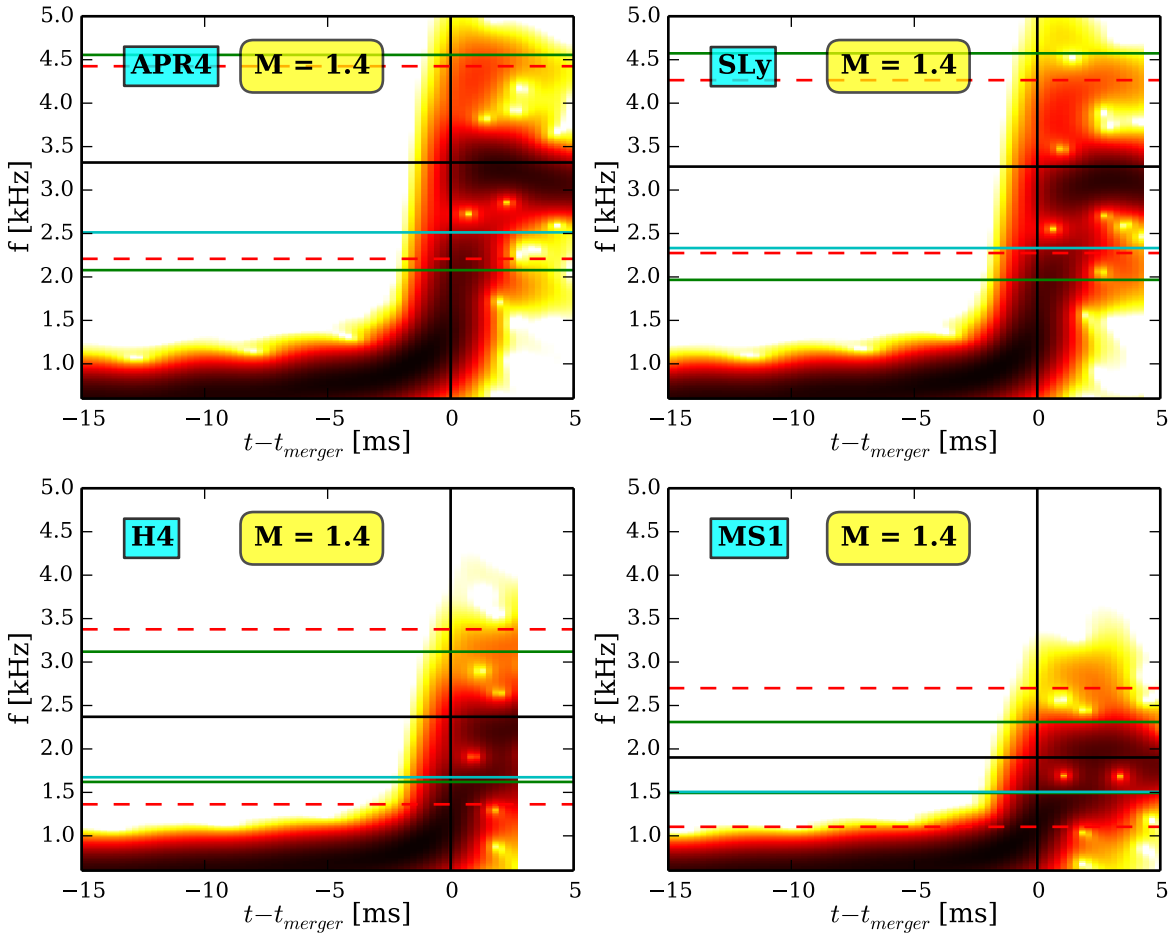

Figure 4.18: Fourier spectrograms for the (2,2) mode of the post-merger GW signal for the equal mass models present in the bottom-right panel of figure 4.13, with a total baryonic mass of 2.8 $M_\odot$ and different EOSs . Detail of its computation can be found in the text. The horizontal lines mark predicted frequencies for the subdominant peaks, with the same color-code of fig. 4.13. The black horizontal lines mark, instead, the peak frequency f_2 measured from the full spectrum.

GW emission mode which develops with the softer EOSs after 15 ms from the merger.

Prony methods for the post-merger spectrum analysis

The use of a Fourier spectrogram has some known drawbacks:

- It considers only the modulus of the gravitational waves strain, and not the full complex number.
- It does not allow to extract information about the damping times of the different excited modes, neither to know if they are positive or negative (if the mode is vanishing or growing in a particular time interval).
- The accuracy in time and in frequency are linked together by an "uncertainty principle" - like relationship (called the *bandwidth theorem* in this context, which states that longer intervals for the Fourier transforms allows for better frequency resolution, but worse time resolution). Therefore, it is not possible to archive a good accuracy in the emission frequencies in the first few milliseconds, where the subdominant modes are excited.

In the signal processing literature, an alternative technique to compute spectrograms is known, which overcomes all these limitations: the Prony method.

The goal of the Prony method is to fit a sum of complex exponentials (which means, of exponentially decaying or growing oscillating signals), sampled with discrete points, which, for each value of its discrete index $n \in [0, N-1]$, can be represented as:

$$h[n] = \sum_{k=1}^{M} A_k e^{(\alpha_k + i\omega_k)nT + i\phi_k} = \sum_{k=1}^{M} c_k z_k^n, \tag{4.15}$$

where M is the number of signal components, which a priori could be unknown. Fitting such a signal with standard least-squares methods it is known to be often problematic, when the data contain also a noise component and the number of exponential M is large, requiring to fit $4M$ free parameters [64, 286]. Another problem of using a standard least-square fit is the need of an initial guess for the parameters values, which is not needed, instead, adopting the Prony method.

The original method, developed by Prony in 1795, required knowing a-priori the value of M, and having a perfect signal without noise, sampled with 2M points. For $n \in [0, M-1]$, eq. 4.15 can be written in matrix form, as a Vandermonde linear system:

$$\begin{pmatrix} z_1^0 & z_2^0 & \cdots & z_M^0 \\ z_1^1 & z_2^1 & \cdots & z_M^1 \\ \vdots & \vdots & \ddots & \vdots \\ z_1^{M-1} & z_2^{M-1} & \cdots & z_M^{M-1} \end{pmatrix} \begin{pmatrix} c_1 \\ c_2 \\ \vdots \\ c_M \end{pmatrix} = \begin{pmatrix} h[0] \\ h[1] \\ \vdots \\ h[M-1] \end{pmatrix}. \tag{4.16}$$

The goal of the Prony method, is to find, in an independent way, a solution for the complex exponentials z_k, which gives the frequencies and the damping times of the signal components. Once they are known, one can solve the system 4.16 with standard techniques, to get also the amplitudes

and the phases, encoded in the coefficients c_k. The starting point is to construct an M-grade polynomial, whose zeros are the first M z_k:

$$p(z) = \prod_{k=1}^{M} (z - z_k) = \sum_{k=0}^{M-1} a_k z^k + z^M, z \in \mathcal{C}, \tag{4.17}$$

where the coefficient a_M has been arbitrarily set to one. Starting from these *Prony polynomials*, one can find the following relation, for each $m \in \mathcal{N}^*$:

$$\begin{aligned} \sum_{k=0}^{M} a_k h[k+m] &= \sum_{k=0}^{M} a_k \left(\sum_{j=1}^{M} c_j z_j^{k+m} \right) = \\ &= \sum_{j=1}^{M} c_j z_j^m \left(\sum_{k=0}^{M} a_k z_j^k \right) = \sum_{j=1}^{M} c_j z_j^m p(z_j) = 0. \end{aligned} \tag{4.18}$$

Using the sampled values of the signal $h[k]$, $k \in [0, 2M-1]$, this can be translated in a forward linear prediction system:

$$\sum_{k=0}^{M-1} a_k h[k+m] = -h[M+m], m \in [0, M-1], \tag{4.19}$$

which, in matrix form, becomes:

$$H_M(0) = \begin{pmatrix} x[0] & x[1] & \cdots & x[M-1] \\ x[1] & x[2] & \cdots & x[M] \\ \vdots & \vdots & \ddots & \vdots \\ x[M-1] & x[M] & \cdots & x[2M-2] \end{pmatrix} \begin{pmatrix} a[0] \\ a[1] \\ \vdots \\ a[M-1] \end{pmatrix} = - \begin{pmatrix} x[M] \\ x[M+1] \\ \vdots \\ x[2M-1] \end{pmatrix}. \tag{4.20}$$

where $H_M(0)$ is an invertible square Hankel matrix. The original Prony algorithm, then, consists in the following steps:

1. Solve the linear system 4.20, to find the Prony polynomial coefficients a_k;
2. Compute the zeros of the Prony polynomials 4.17, to find the frequencies $\omega_k = tan^{-1} \left[\mathrm{Im}(z_k) / \mathrm{Re}(z_k) \right] / T$ and the damping times $\tau_k = T / \log |z_k|$;
3. Solve the linear Vandermonde system 4.16, to get also the amplitudes $A_k = |c_k|$ and the phases $\phi_k = tan^{-1} \left[\mathrm{Im}(c_k) / \mathrm{Re}(c_k) \right]$.

Usually, however, one has more data points than $2M$, and they contain also a noise contribution. One simple solution to adapt Prony's method to the realistic case is to extend eq. 4.20, using a rectangular $[N - M \times M]$ Henkel matrix and solving it in the least-square sense. Unfortunately, this least-square Prony works only for very high signal to noise ratios. When the noise is a significant fraction of the sampled data, one has to resort to other formulations. There are a lot of variations published in the literature, but they all share the common trait of looking for a number of exponential components $L > M$, and, among them, find which one are due to the real signal and which one are due to noise. In the following analysis $L = N/3$ was used. Some of these techniques allow also

to estimate the value of M from the data, without needing to know it a priori, like in the original Prony method. In this work I adopted the ESPRIT technique (Estimation of Signal Parameters via Rotational Invariance Technique) [293–296]. It is closely related to the Matrix Pencil technique [297, 298], which was found to be the best in ref. [299] for balck holes quasi-normal modes. A comparison between the two, showing compatible results, was presented in ref. [294].

The starting point is the construction of the rectangular Hankel matrix

$$\begin{pmatrix} h[0] & h[1] & \cdots & h[L] \\ h[1] & h[2] & \cdots & h[L+1] \\ \vdots & \vdots & & \vdots \\ h[N-L-1] & h[N-L] & \cdots & h[N-1] \end{pmatrix}, \tag{4.21}$$

and the closely related matrix $H_{N-L,L}(1)$, which is obtained from $H_{N-L,L}(0)$ removing the first column and adding a $N-L$ vector of zeros as last column. Following from eq. 4.20, an *extended companion matrix* C_{L+1} can be constructed, which allows to transform $H_{N-L,L}(0)$ in $H_{N-L,L+1}(1)$:

$$H_{N-L,L+1}(0)C_{L+1} = H_{N-L,L+1}(1) \tag{4.22}$$

$$C_{L+1} = \begin{pmatrix} C_M(a) & \mathbf{0}_{M,L+1-M} \\ \mathbf{0}_{L+1-M,M} & V_{L+1-M} \end{pmatrix}, \tag{4.23}$$

where $C(M)$ is the companion matrix in the original Prony method:

$$C_M(a) = \begin{pmatrix} 0 & 0 & \cdots & 0 & -a_0 \\ 1 & 0 & \cdots & 0 & -a_1 \\ 0 & 1 & \cdots & 0 & -a_2 \\ \vdots & \vdots & & \vdots & \vdots \\ 0 & 0 & \cdots & 1 & -a_{M-1} \end{pmatrix} \tag{4.24}$$

and the bottom-right block is given by:

$$V_{L+1-M} = \begin{pmatrix} \mathbf{0}_{1,L-M} & 0 \\ I_{L-M} & \mathbf{0}_{L-M,1} \end{pmatrix}. \tag{4.25}$$

The companion matrix $C(M)$ has the M z_j, $j \in [1, M]$ as eigenvalues. Its extended version C_{L+1}, instead, has the same M eigenvalues, plus $L+1-M$ additional eigenvalues which are zero.

The key of the method, like many other Prony-like techniques, is to perform a singular value decomposition (SVD) of the Hankel matrix and the closely related matrix $H(1)$:

$$H_{N-L,L+1} = U_{N-L} S_{N-L,L+1} W^H_{L+1}, \tag{4.26}$$

where U and W are unitary matrices and S is a rectangular diagonal matrix, whose nonzero values $\sigma_i, i \in [1, L+1]$ are called the *singular values* of the Hankel matrix, arranged in a non-increasing order. For noiseless data, only M singular values are non-zero. For data with noise, instead, it is possible to define a threshold ϵ, depending on the desired accuracy (which depends also on the input data accuracy), to find *a posteriori*, from the sampled data, the number M of complex exponential components present in the signal, requiring

$$\frac{\sigma_M}{\sigma_1} \geq \epsilon. \tag{4.27}$$

In the present case, I chose $\epsilon = 10^{-2}$.

After the σ_i rearrangement, and finding M, it is possible to remove from S all the $L+1-M$ singular values linked with noise, setting them to zero, and building the rectangular diagonal submatrix $S_{N-L,M}$ At the same time, one defines accordingly the submatrix $W^H_{M,L+1}$. From those submatrices, which take into account only the signal-related singular values, one can reconstruct again $H_{N-L,L+1}$, and $H_{N-L,L+1}(1)$, taking also in this case only the largest M singular values. This allows to rewrite eq. 4.22 as:

$$S_{N-L,M} W^H_{M,L+1} C_{L+1} \;=\; S_{N-L,M} W^H_{M,L+1}(1). \tag{4.28}$$

Multiplying the conjugate transposed equation with $S^H_{N-L,M}$ from the left, and setting

$$W_{M,L}(s) \;=\; W_{M,L+1}(1:M, 1+s:L+s), s = 0, 1, \tag{4.29}$$

in order to remove the zero columns, one finally gets

$$C^H_L W_{M,L}(0) = W_{M,L}(1). \tag{4.30}$$

Since C_L has rank M, and its eigenvalues are the z_i we are looking for, one can find them solving eq. 4.30 in the least-square sense and computing the eigenvalues of the solution matrix

$$F_M \;:=\; W^\dagger_{M,L}(0) W_{M,L}(1), \tag{4.31}$$

where $W^\dagger_{M,L}$ is the Moore-Penrose pseudo-inverse

$$A^\dagger \;=\; A^H \left(A A^H\right)^{-1}. \tag{4.32}$$

Once one obtains the M z_i, as eigenvalues of F_M, it is possible to solve the (now overdetermined) Vandermonde system, again in the least-square sense, to get also the c_i, from which the modes amplitudes a phases can be computed.

In order to construct a *Prony spectrogram*, were computed, for each point in the post-merger gravitational wave strain, the c_i and z_i applying the ESPRIT Prony algorithm in an interval of 2 ms, centred in the given discrete time point. This allows to have at least two GW cycles for all emission at frequency larger than 1 kHz, as happens in every model in the post-merger phase. The results of these spectrograms are plotted in figure 4.19 (for the frequencies) and fig. 4.20 for the damping times and for the amplitudes, only for two simulated models: the equal mass one with the SLy EOS and $M = 1.4\,\mathrm{M}_\odot$ for each star and the unequal mass one, with the SLy EOS, the same total baryonic mass, and $q = 0.77$.

The different colors correspond to the main quadrupolar emission (red lines) and modes with higher (magenta lines) or lower (blue lines) frequencies. The horizontal lines in the frequency plots 4.19 have the same meaning of the corresponding lines in the Fourier spectrograms in fig. 4.15, 4.16, 4.17, 4.18.

The result of the Prony analysis are qualitatively close to what was found from the Fourier spectrograms, confirming the presence of different excited oscillation modes, with varying growing/-damping times. At this stage this can only be a qualitative comparison, since Prony's spectrograms are highly dependent on the choice for the length of the intervals in which Prony's fitting is performed. Further careful studies on the fine-tuning of the method parameters are needed before being able to draw also accurate quantitative inferences from it. For example, in the equal mass

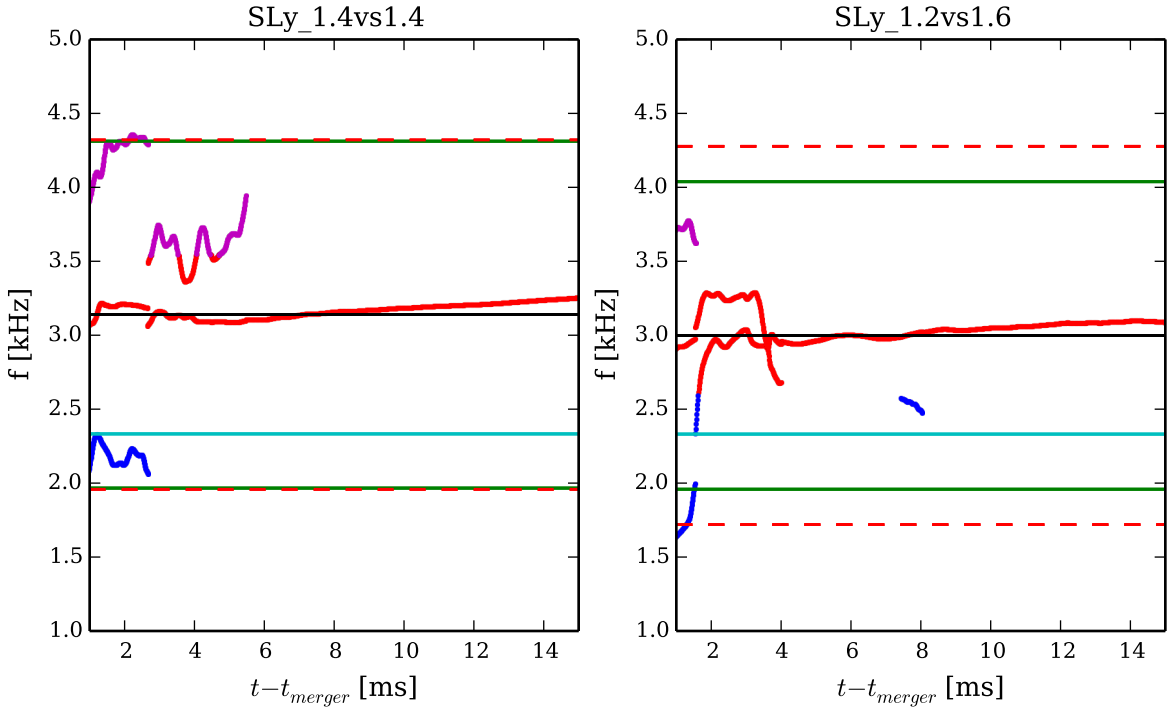

Figure 4.19: Frequency of the complex exponential modes fitted with the Prony method from the gravitational wave strain, for an equal and an unequal mass model with the same total baryonic mass ($2.8\,M_\odot$) and the SLy EOS. The *rolling Prony* method adopted assigns to every point in the graph the frequencies computed by an ESPRIT Prony algorithm in the 2 ms interval around it.

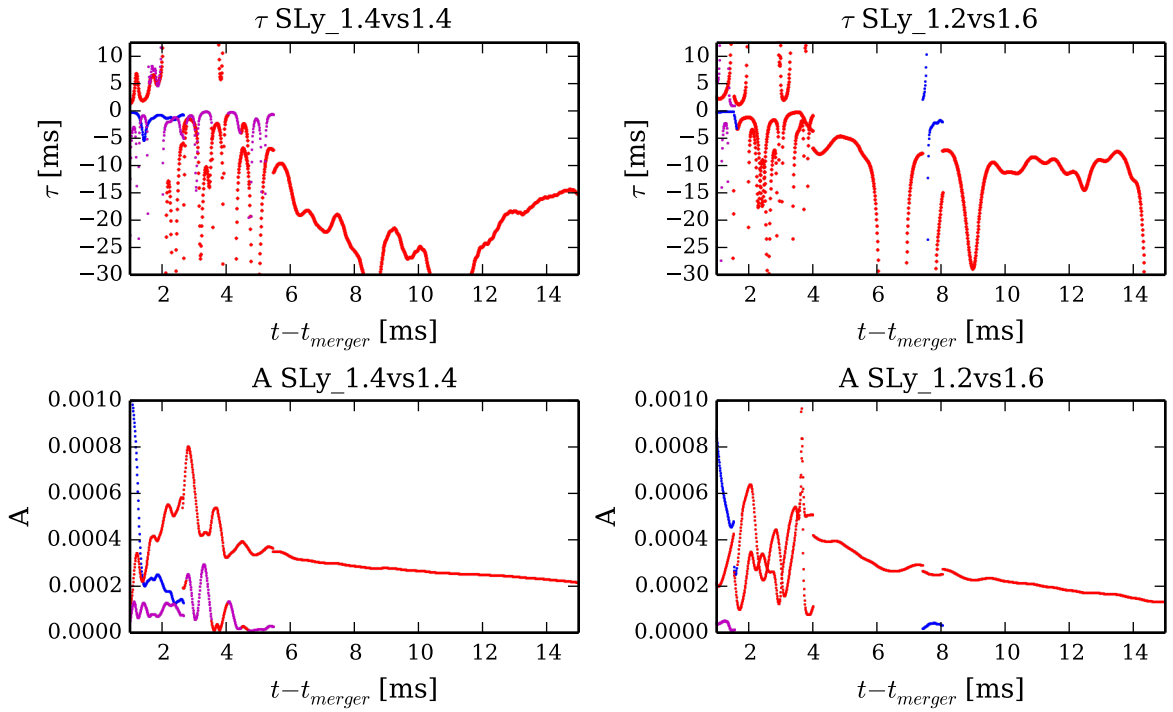

Figure 4.20: Damping times (upper panels) and amplitudes (lower panels) of the complex exponential modes fitted with the Prony method from the gravitational wave strain of the models in fig. 4.19.

model (left panel of figure 4.19), we do not see in the first milliseconds two separate low-frequency emission modes, like in the Fourier spectrogram, because the emission close to f_{spiral} lasts for less than the fitting interval. The result is a single mode at an intermediate frequency, just like it is reconstructed in the full 23 ms long spectrum (fig 4.13). Despite this problem with quickly-varying emission mechanisms, Prony's methods shows, instead, a better ability to recognize even very week modes, like the two subdominant modes in the $q = 0.77$ model, which are not visible either in the Fourier spectrogram or the full spectrum, but can be seen in the Prony spectrogram, instead, even if they last only just for the first two milliseconds of the post-merger.

The computed values for the damping times τ (fig. 4.20, upper panel), are less clear to read. This happens because a longer time window would be needed to more accurately evaluate the damping times, but it would prevent the recognition of the subdominant modes, which get damped in just a few milliseconds. However, still some interesting information can be gathered from fig. 4.20. The main GW emission mode have a positive τ (growing mode) in the first couple of milliseconds in the post-merger, when it gets seeded by the deformation produced in the merger phase. After that, it keeps a low, negative damping time (it gets quickly damped), until the end of the subdominant mode emission. After that, when there is also a rapid change of frequency in the dominant mode, as seen in the Fourier spectrograms, the damping time absolute value becomes much larger, between 20 and 30 ms for the equal mass model. In the unequal mass model, instead, the absolute value of the dominant emission mode damping time is much lower, always below 10 ms. This information is potentially very important for post-merger BNS GW detection, because a faster damping of the dominant mode means a lower integrated signal to noise ratio for the gravitational-waves post-merger signal from

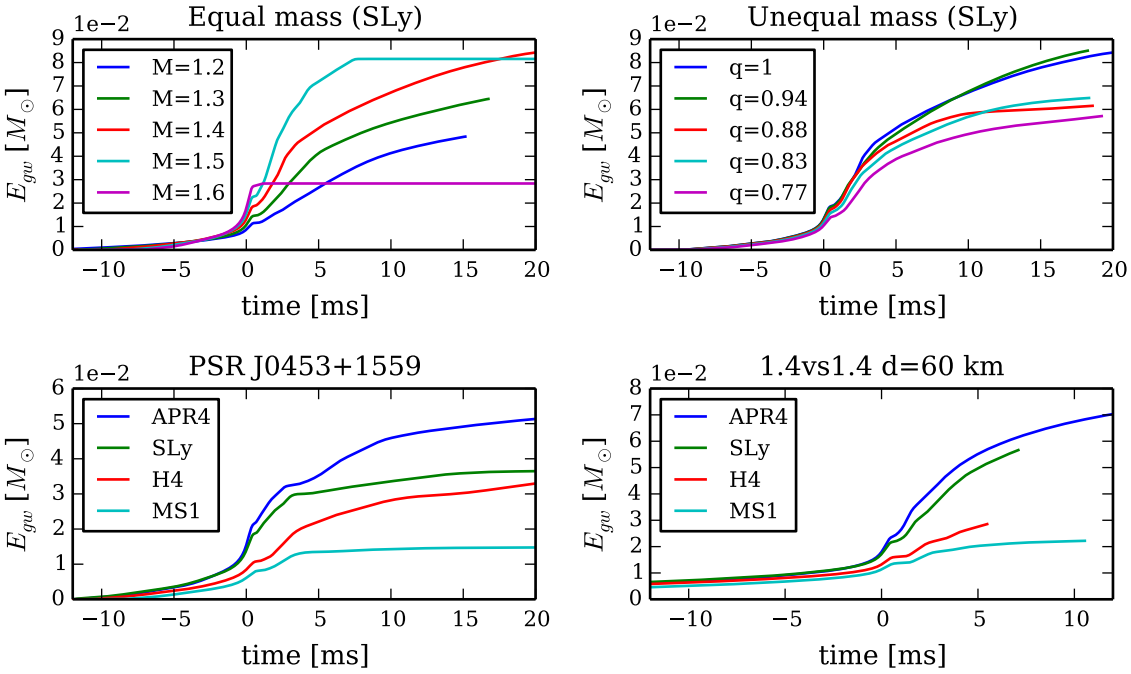

Figure 4.21: Total energy radiated in gravitational waves up to each point in retarded time.

unequal mass mergers.

The mode amplitude, plotted in figure 4.20 (lower panels), shows that in the first 2 ms after the merger the low-frequency subdominant mode is actually dominant (has more power) than the $m = 2$ oscillation mode.

4.2.2 Radiated energy

Another interesting aspect to evaluate from the merger and post-merger GW emission is the radiated energy. In particular, it is interesting to understand when most of the GW energy gets emitted, and how the total energy emitted in the different phases of a BNS merger change with the binary parameters.

Figure 4.21 represents the total energy emitted in gravitational waves up to a retarded time t, for the models analysed in this chapter. Its companion, figure 4.22, instead, depicts the instantaneous energy flux emitted in each discrete point in time of the binary evolution. From the energy fluxes (fig. 4.22), it is clear that most of the energy emission, in all models, is concentrated in two small time intervals: the merger moment, where the energy flux has its maximum peak, and an interval around $2 - 5ms$ after the merger. In the previous section, from the Prony analysis it was possible to notice that the dominant post-merger GW emission mode has an exponentially growing amplitude in the first 2 ms after the merger, after which there is a time interval characterized by a main emission at frequency f_{2i}, with a small damping time. After about 5 ms, when the energy flux decreases substantially in all models, there is also a drop in the dominant mode amplitude (see fig. 4.20), which switches to the frequency f_2, with now a larger damping time. This is reflected, again, also in the energy flux, which, after a sudden drop, slowly diminishes, in an almost linear way for many models (in particular, the equal mass ones with high total mass). The second energy

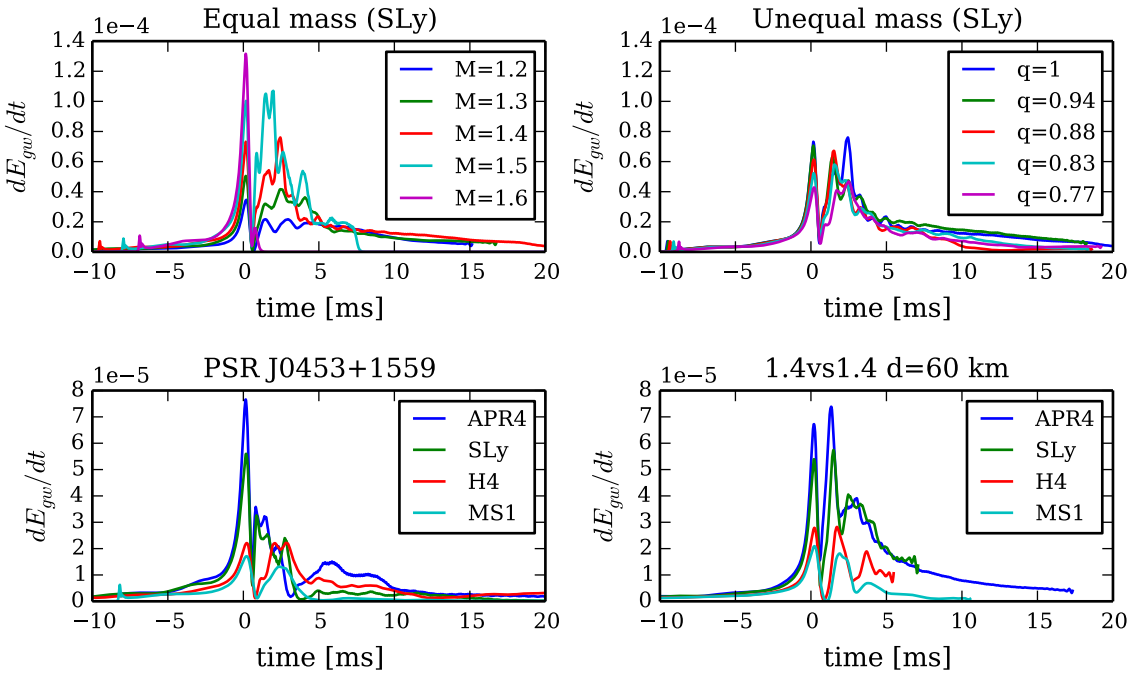

Figure 4.22: Energy flux $\frac{dE_{GW}}{dt}$ radiated instantaneously at each point in retarded time.

flux peak, during the post-merger, is higher increasing the total mass (it is almost not present in the SLy1.2vs1.2 model). Mass ratio does not seem to play a huge role in this early post-merger energy emission mechanism. There is, instead, an important effect of the EOS, with the softer models emitting much more energy than the stiffer ones. In the last part of the simulations, where only a single, slowly decaying mode is excited, total binary mass does not make too much of a difference, except for models collapsing to black holes, whose GW emission effectively stops, because BH quasi-normal modes and disc oscillations have a much lower amplitude than the bar-deformed NS remnant radiation. Mass ratio, instead, has a more important role in this phase; models with $q < 0.9$ show a much faster decay in the energy flux, consistent with the lower damping times of their dominant emission modes, as seen in figure 4.20.

To understand more intuitively the net effect of those differences in the energy fluxes, it is useful to look just at the total emitted energy (fig. 4.21). The top-left panel shows that the emitted energy, in both the inspiral and the post-merger phase, increases with the total mass of the system. It is interesting to note that the total energy emitted by high mass binaries collapsing to BH during the simulation time is quickly overcome by the not-collapsed models with lower total mass, due to the high efficiency of the $m = 2$ fundamental quardupolar mode in neutron stars. The top-right panel shows that mass ratio has a big effect only in the mid post-merger (about 5 to 15 ms after the merger), while it is not important for the radiated energy during the inspiral. The EOS (bottom panels), instead, has a big role in determining the total emitted energy. In particular, it is peculiar to note that in the unequal mass PSR J0453+1559 model, with some EOS (APR4, MS1) the energy emission seems to effectively stop after the post-merger peak in the energy flux, while for the other two EOSs employed (SLy and H4), it goes on, just like the other SLy models plotted in the top row. This effects points again to the need of performing new simulations and more careful analysis of the effects of the EOS and mass ration on the post-merger dynamics and GW emission in unequal

Model	E_{gw} [-10ms; -5ms] $M_\odot$	E_{gw} [-5ms; 0] $M_\odot$	E_{gw} [0; 5ms] $M_\odot$	E_{gw} [5ms; 10ms] $M_\odot$
SLy1.2vs1.2	0.002	0.006	0.018	0.015
SLy1.3vs1.3	0.002	0.008	0.031	0.015
SLy1.4vs1.4 (d=40)	0.003	0.011	0.039	0.015
SLy1.5vs1.5	0.002	0.013	0.056	0.009
SLy1.6vs1.6	0.002	0.016	0.010	4×10^{-7}
SLy1.35vs1.55	0.003	0.010	0.037	0.018
SLy1.3vs1.5	0.002	0.010	0.034	0.012
SLy1.25vs1.55	0.002	0.009	0.032	0.013
SLy1.2vs1.6	0.002	0.008	0.029	0.011
PSR J0453+1559 (APR4)	0.003	0.012	0.020	0.011
PSR J0453+1559 (SLy)	0.003	0.010	0.017	0.003
PSR J0453+1559 (H4)	0.002	0.006	0.014	0.006
PSR J0453+1559 (MS1)	0.001	0.005	0.007	0.001
APR4_1.4vs1.4_d60	0.002	0.009	0.037	0.012
SLy_1.4vs1.4_d60	0.002	0.008	0.033	-
H4_1.4vs1.4_d60	0.002	0.005	0.014	-
MS1_1.4vs1.4_d60	0.002	0.005	0.009	0.002

Table 4.11: Energy radiated in gravitational waves by the compared models in different intervals, respect to the merger time (here $t_{merger} = 0$). The missing values in the last column are because less than 10 ms after the merger were simulated for those models.

mass models, which we now know to exist, even in our galaxy.

In table 4.11 is reported the energy emitted in different time intervals by the different models, in order to confirm quantitatively what was just explained looking at the plots.

Another interesting observable to look at are the reduced energy vs reduced angular momentum curves (already introduced in sec. 4.1.1), plotted in figure 4.23, in particular for their gauge-invariance property, since a lot of other potentially interesting post-merger measurements, like the neutron star rotation profiles, are heavily influenced by the gauge choice, instead [57].

In this case, it is the total binary mass, and not the EOS, to make the biggest difference. The E(J) curves, in the inspiral phase, are lower (more emitted energy) decreasing the total mass, except for the SLy1.2vs1.2 case, which is very different form the other, having instead a much higher total energy respect to the total angular momentum, mainly due to the difference in the initial data, starting with a much higher angular momentum than all the other binaries. After the merger, the E(J) curves are straight lines, with a slope which contributes to invert the effects of the inspiral: the lower mass models emit energy more slowly in the post-merger, while they radiate angular momentum. At the end of the simulations, the models with mass $1.5, 1.4$ and $1.3 M_\odot$ pass trough a state with the same energy and angular momentum. Mass ratio (top-left panel) does not have, instead, a big effect, with most of the difference coming from the initial configuration. The EOS effect is very small during the inspiral, but the coalescence is longer for models with a softer EOS (which have a longer merger time). The post-merger E(J) slope is similar between the two soft EOS (APR4 and SLy) and the two stiff EOS (H4 and MS1). It would be interesting to check simulations

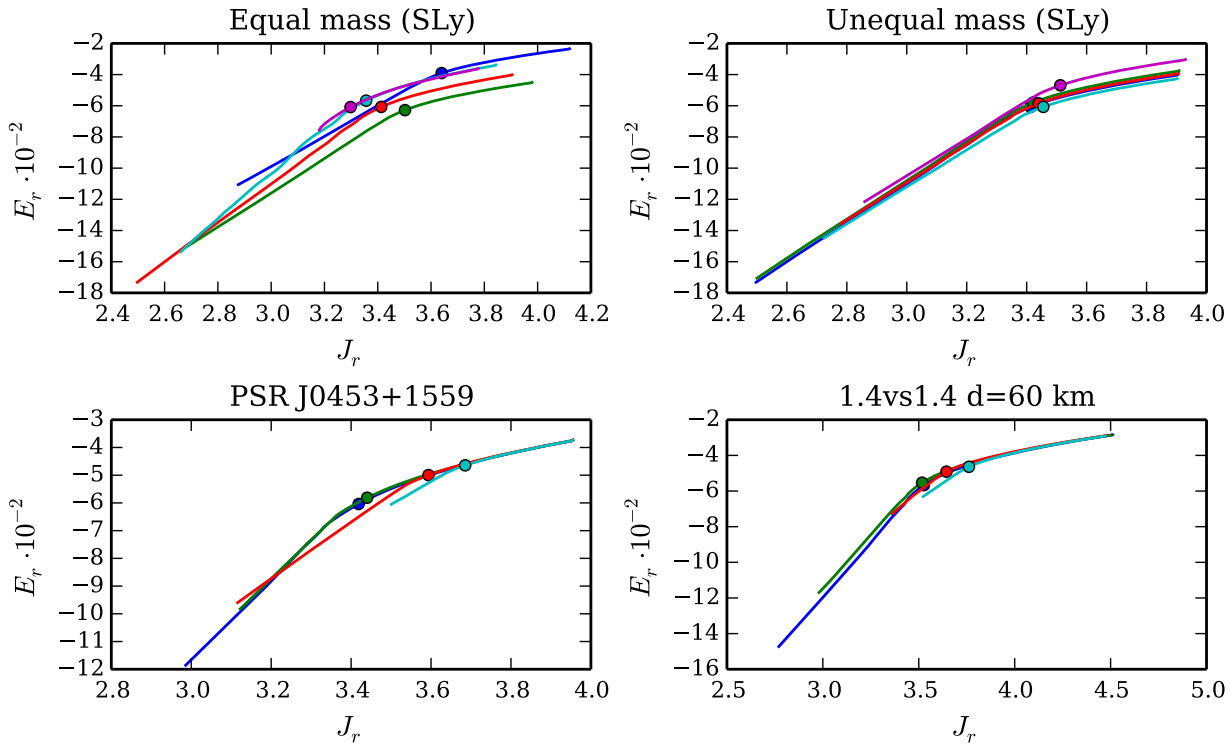

Figure 4.23: Reduced energy against reduced angular momentum curves, defined like for fig. 4.11.

with a wider set of EOS, in order to understand if there is a smooth transition in the E(J) slope, and if it can be correlated with some stellar parameter, like the radius of a non-rotating star, or its tidal deformability.

To end this subsection, it should be stressed that several microphysical ingredients, such as a full finite-temperature nuclear EOS, neutrino emission and absorption and magnetic fields, are missing in the simulations presented in this thesis. They could potentially have an important impact, in particular on the post-merger energy balance.

4.2.3 Effects of the initial interbinary distance on the post-merger evolution

In section 4.1.2, it was analysed in detail the effect of the initial interbinary distance on the inspiral phase of BNS mergers. Looking at figure 4.8, hinted already at some effects being present in the post-merger too. This is important, because most BNS merger simulations focusing on the post-merger phase start from very close configurations, to save computational time. It is therefore useful to understand which is the lowest possible initial distance which allows to investigate the post-merger evolution free of systematic numerical errors.

The first important difference can be seen in the emitted energy. Figure 4.24 shows the energy emitted during the last 5 ms of the inspiral phase and during the first 5 ms of the post-merger phase, for different EOS and initial separations. It is clear that in the early post-merger, when there is the second peak in the energy flux, and most of the radiated energy gets emitted, the simulations starting from $d = 60$ km consistently show a lower emitted energy, independently on the EOS, while no clear trend can be extrapolated from the other three initial distances considered. This systematic error source can potentially affect studies on the post-merger energy balance, like the ones in ref. []. This difference, as the inspiral ones, can be, again, linked with the higher accumulated numerical errors during the longer coalescence of $d = 60$ km models. Only repeating the same simulations with better resolutions and/or more accurate numerical methods we will be able to have a definitive answer on the source of this error, and on the lowest and highest initial stellar separation, at a given grid resolution, which can be used to safely analyse the post-merger dynamics without worrying about numerical errors coming from the inspiral or the initial data.

A second difference is seen in the post-merger GW spectrum. In figure 4.25 are represented the GW amplitude spectral densities, computed as in figure 4.12, but in the time window between 8 ms before and after the merger. Again, in every model, the $d = 60$ km simulations show a consistent deviation from the others, having, for every EOS, a lower frequency in the dominant post-merger peak. This is linked with the fact that they also have a lower value for the instantaneous frequency at merger, computed taking the derivative of the accumulated GW phase evolution. All the relevant peak frequencies and the merger frequencies are reported also in table 4.12. The difference in the merger frequency and in the frequency of the oscillation modes seeded during the merger phase is expected, because it was already shown in section 4.1.2 that stars at different initial separations merge, in numerical simulations, in a slightly different physical state, characterized by a difference in its energy and angular momentum (see figure 4.11). Again, while the change in the main peak frequency between $d = 60$ km simulations and the other three is always above the Fourier transform error, there are no clear differences or trends between the peak frequencies of simulations with the other three initial interbinary distances. This systematic error, like the one on the radiated energy, could be important in data analysis, in particular in building empirical relations for the peak frequencies, as extensively discussed in section 4.2.1. To conclude, it is interesting to remark that the post-merger peak frequencies results for the $d = 44.3$ km simulations, are compatible, within

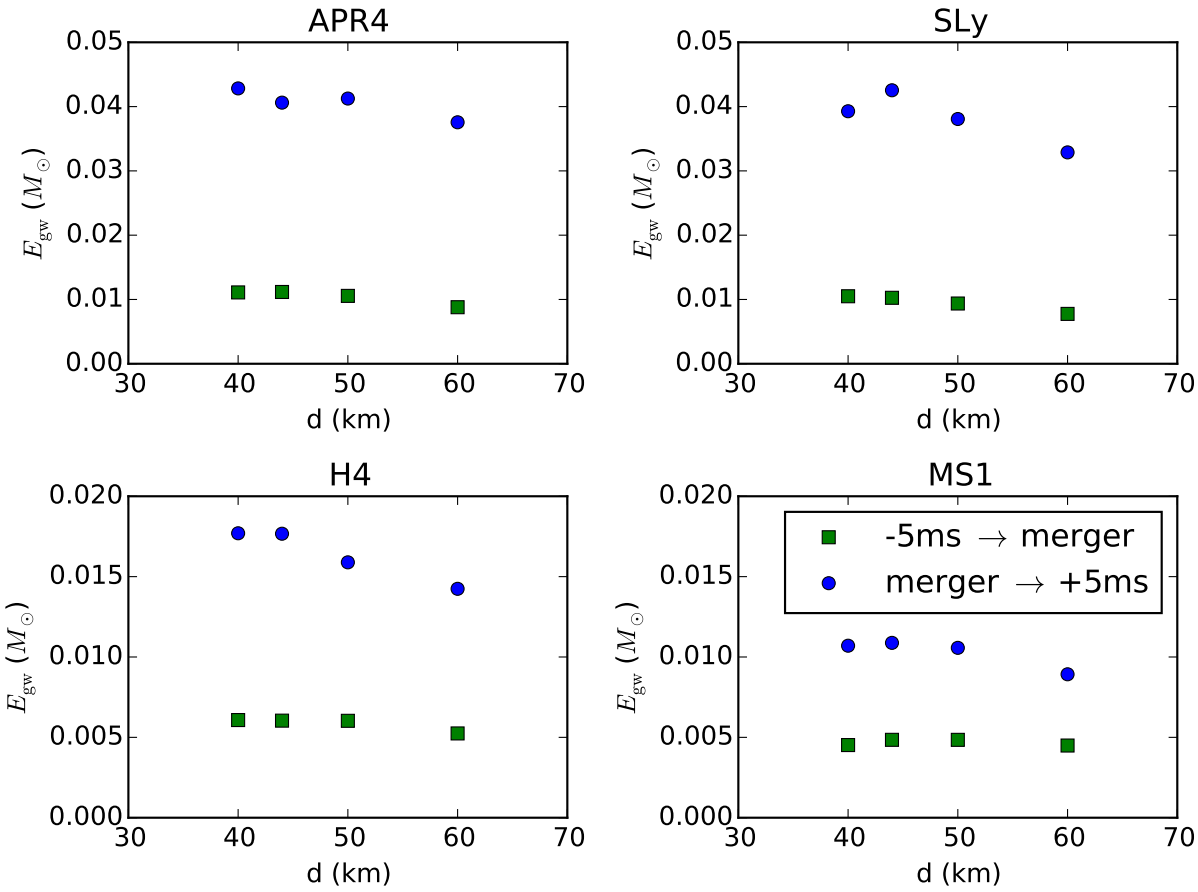

Figure 4.24: Radiated energy for all simulated models, computed integrating eq. 3.205 in time. Green squares represent the energy emitted in the last 5ms before the merger, while blue dots represent the energy radiated in the first 5ms after the merger.

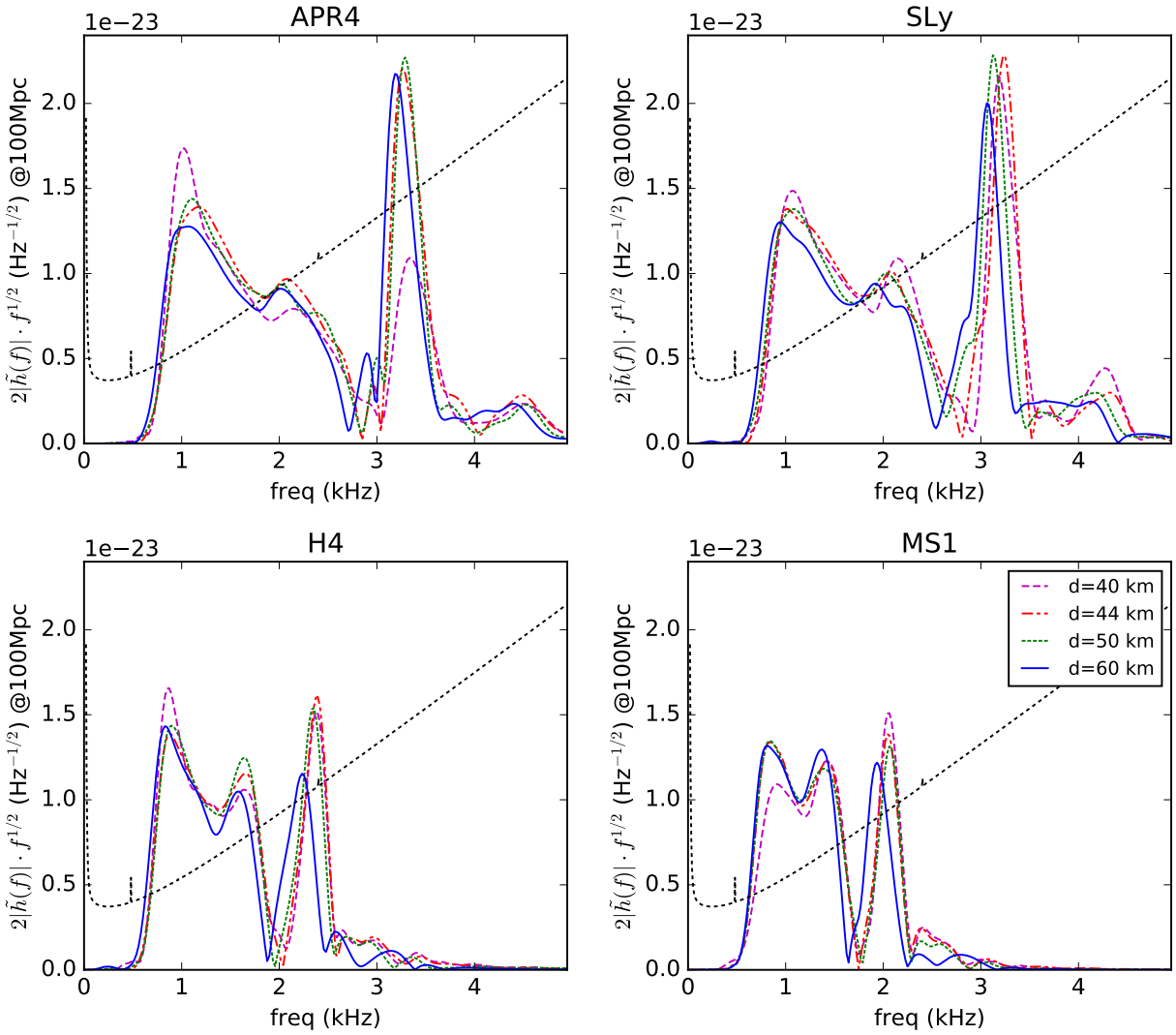

Figure 4.25: Amplitude spectral densities of the gravitational wave signal from 8ms before the merger to 8ms after it, for a source at 100Mpc. For some models the total signal power is lower either because the simulations were shorter in the post-merger phase (H4(d),APR4(a)), or because their merger time was less than 8ms (H4(a),MS1(a)). The black dashed curve represents the sensibility of Advanced LIGO in the Zero detuning-high power configuration

Model	f_2 (kHz)	f_1 (kHz)	$f_{\rm merger}$ (kHz)
APR4(d=40 km)	3.34	2.14	1.97
APR4(d=44.3 km)	3.26	2.08	1.97
APR4(d=50 km)	3.29	2.02	1.94
APR4(d=60 km)	3.19	2.02	1.87
SLy(d=40 km)	3.19	2.15	1.92
SLy(d=44.3 km)	3.24	2.08	1.88
SLy(d=50 km)	3.13	2.03	1.87
SLy(d=60 km)	3.07	1.92	1.72
H4(d=40 km)	2.38	1.64	1.44
H4(d=44.3 km)	2.39	1.66	1.46
H4(d=50 km)	2.35	1.64	1.44
H4(d=60 km)	2.24	1.58	1.41
MS1(d=40 km)	2.05	1.42	1.29
MS1(d=44.3 km)	2.05	1.43	1.33
MS1(d=50 km)	2.07	1.39	1.32
MS1(d=60 km)	1.93	1.37	1.26

Table 4.12: Results from the spectral analysis of models with different initial stellar separation. In the first column is reported the frequency of the dominant post-merger peak, calculated taking the frequency of the maximum of the amplitude spectral density after interpolation with a cubic spline. The second column shows the frequency of the left secondary peak f_1. In the third column is reported the instantaneous frequency at merger (f_{merger}) i.e., the frequency at the maximum of the gravitational waves amplitude, computed taking the derivative of the phase evolution. The uncertainty of the Fourier transform frequencies are in the interval $[62, 75]$ Hz. Some models have a higher frequency uncertainty because they either have shorter post-merger simulations (APR4(d=40 km), H4(d=60 km)) or they have a merger time less than 8ms (H4(d=40 km), MS1(d=40 km)).

the fft errors, with the results for similar BNS models simulations presented in ref. [14, 285], which have an initial interbinary distance of 45 km.

4.2.4 Collapse to black hole

To conclude this chapter about the post-merger BNS dynamics, it is interesting to take a closer look to models collapsing to black hole, during the simulated time. In order to do so, I will analyse, following ref. [68], two good representatives of the possible paths to collapse: the equal mass systems with the SLy EOS and a baryonic mass $M = 1.6\,{\rm M}_\odot$ for each star (which collapses promptly after the merger) or with $M = 1.5\,{\rm M}_\odot$ (which collapses after a short post-merger HMNS phase).

The black hole formation is captured looking at regular intervals for the formation of an apparent horizon, with the Einstein Toolkit module `AHFinderDirect` [300]. In models where a black hole collapse is expected (from the output of poorer resolution simulations), an additional grid refinement level, with resolution dx half of the finer grid resolution used during the inspiral evolution, is added, when the minimum lapse on the grid gets below a critical value.

Figure 4.26 shows a snapshots of the black hole-disc system evolution, at the end of each simulation, 30 and 34 ms after the merger. The most striking difference is that in the model with prompt collapse, very little mass is left in the disc around the black hole, which is quickly absorbed,

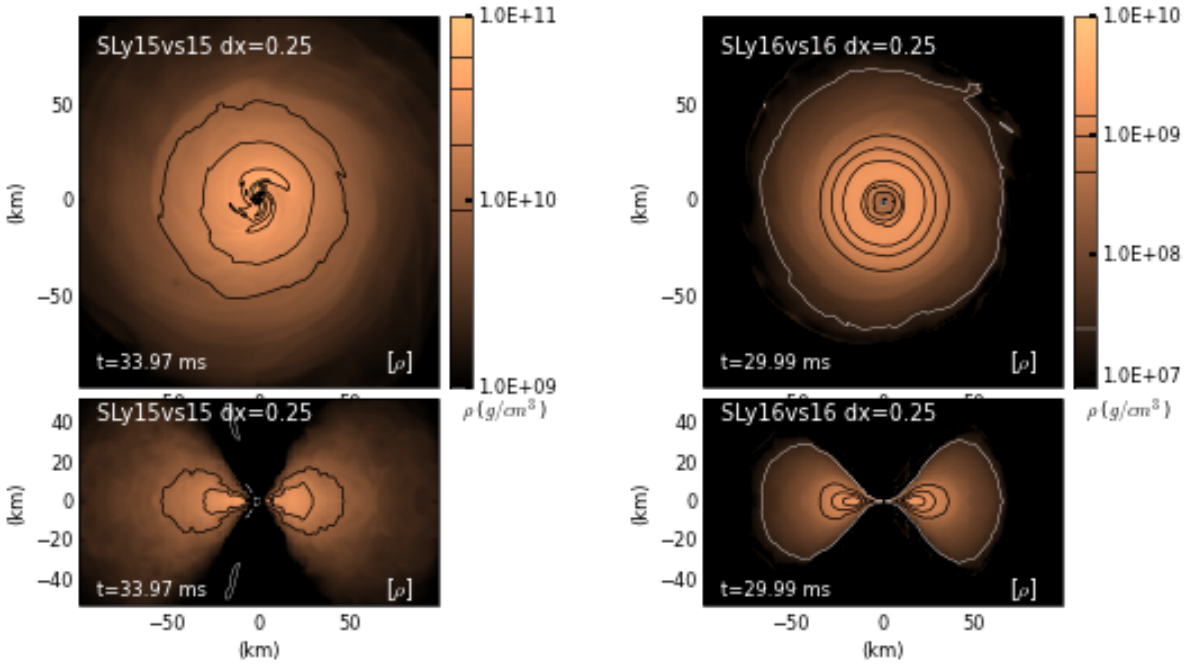

(a) Accretion disc density for model SLy1.6vs1.6 (b) Accretion disc density for model SLy1.5vs1.5

Figure 4.26: Density profiles for the accretion discs formed in a model promptly collapsing after the merger (SLy1.6vs1.6, left figure), or collapsing after a short HMNS phase (SLy1.5vs1.5, right figure). They are taken at the end of the simulations, at least 30 ms after the merger.

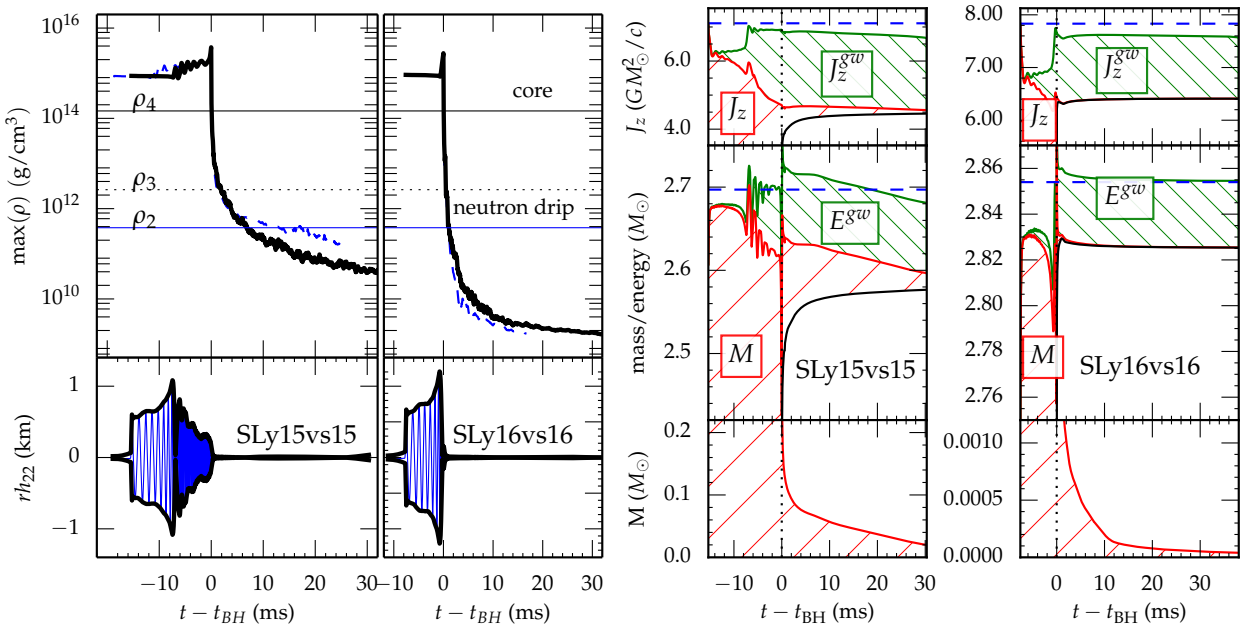

(a) Maximum density

(b) Energy and angular momentum budget

Figure 4.27: Properties of the black hole-disc system: the left figure shows the maximum density left on the grid, which is lower than the neutron drip level, independently on collapse time and grid resolution. The right figure, instead, shows the energy and z direction angular momentum contributions, before and after the collapse (see text for their computation).

forming a small disc, limited in space and axisymmetric. In the model with delayed collapse, instead, much more matter have been expelled from the central NS core during the HMNS evolution, causing the formation of a massive disc, with a large spatial extension, and which still has a spiral structure in its inner, higher density, region, even 30 ms after the collapse.

In figure 4.27a is reported the evolution of the maximum density on the numerical grid in both models. The most interesting feature to notice is that, independently of the path to collapse, the density of the leftover matter in the accretion disc quickly gets lower than the neutron drip line. This means that, for modelling collapsing BNS systems, it is important to use an equation of state able to give a realistic description also to low density matter. The simplest way, adopted in my work, is to use the full 7 pieces piecewise polytropic parametrization of [144], with the four lower-density segments taken from the SLy EOS [140]. This is different from what is done in most of the numerical relativity literature (see, for example, ref. [14, 64, 301]), where only the four highest density pieces are used, extrapolating the one which describes the inner crust down to the lowest frequencies, as already discussed in section 2.1.1. This approach is perfectly fine when studying a massive neutron star post-merger remnant, whose evolution is mainly driven by the high-density region dynamics, although some care should be taken when building empirical relations linking some GW signal characteristics to the initial star properties, since the stellar radius can be sensitive to the low density EOS. However, figure 4.27a proves that it could lead to wrong results when analysing also the accretion disc dynamics after collapse.

It is interesting to analyse the energy and angular momentum balance in collapsing models,

presented in figure 4.27b, in order to both verify the code ability to conserve those quantities throughout the evolution, even when a black hole appears on the numerical grid, and how the different components contribute to the overall energy and angular momentum balance. The initial values are taken from the output of the LORENE code, when importing BNS initial data on the evolution code numerical grid. The energy and angular momentum radiated in gravitational waves are computed integrating eq. 3.205 and 3.206, as already done several times, for example to construct the $E_r(J_r)$ curves of fig. 4.11. The disc mass and z angular momentum, instead, are computed tracking two quantities, which are exact only in the case of axial and temporal symmetry, and which can easily be computed during the numerical evolution:

$$M = \int (2T^{\mu}_{\nu} - \delta^{\mu}_{\nu} T^{\alpha}_{\alpha}) \, \xi^{\nu}_{(t)} d^3\Sigma_{\mu} \tag{4.33}$$

$$J_z = \int T^{\mu}_{\nu} \xi^{\nu}_{(\phi)} d^3\sigma_{\mu}, \tag{4.34}$$

where Σ_{μ} are the three-dimensional slices of fixed coordinate time t and ξ^{ν} are the two Killing vectors

$$\xi^{\nu}_{(t)} = (1, 0, 0, 0) \tag{4.35}$$

$$\xi^{\nu}_{(\phi)} = (0, \cos\phi, \sin\phi, 0). \tag{4.36}$$

This formalism have been already used in the case of isolated stars [194]. The required stationarity and axisymmetry conditions are almost satisfied at the end of the simulations discussed here. Finally, the mass of the black hole is computed on the apparent horizon surface using the isolated horizon formalism [302], implemented by the Einstein Toolkit thorn `QuasiLocalMeasures`.

For the promptly collapsing model, the accretion is already stopping at the end of the simulation time, while in the delayed collapse case the black hole mass is still increasing, and longer simulations are needed to reach an equilibrium configuration. Like in the previous section 4.2.2, it is necessary to remark that the simulations presented here do not take into account important effects like magnetic fields, neutrino emission and a proper treatment of the EOS thermal component, therefore they are only a first approximation, useful as a benchmark for future numerical studies involving a better treatment of microphysical aspects.

Another important remark is linked with the collapse time of models with a delayed collapse. It was found to be extremely sensitive to some simulation parameters, like the spatial grid resolution (the SLy1.5vs1.5 model collapses after , ms from the merger at resolutions ,, showing a non-convergent behaviour of the collapse time), or the choice for the EOS thermal component. That last consideration was also pointed out in ref. [64], where simulations with different choices for Γ_{th} were confronted. The difference in Γ_{th}, from 1.8 to 2.0, is the most probable cause also for the fact that in ref. [245] a BNS model similar to our SLy1.5vs1.5 does not collapse in their simulated 25 ms of post-merger evolution. It should also be noted that the results about the disc characteristics and the accretion process are likely to be influenced also by the choice for the artificial atmosphere density imposed by the hydrodynamics code. We did a conservative choice of $\rho_{min} = 6 \times 10^6 \, \mathrm{g/cm^3}$, but even lower values for the minimum accepted density should be tried in order to get more accurate estimates of the disc properties, in particular for promptly collapsing models.

Chapter 5

Conclusions

The work presented in this thesis focuses on the physical properties of the gravitational-waves signal emitted during the merger of binary neutron stars systems, in order to extract the signature of the signal that will be detected by the gravitational waves observatories LIGO/Virgo. To gain such insight an extensive set of numerical simulations of binary neutron star mergers was performed. The gravitational-waves signal was analysed through all the phases of binary neutron stars evolution: the coalescence, the merger, the post-merger (hyper) massive neutron star, and the possible collapse. The simulated models had different values of total mass, mass ratio, initial stellar distance and different choices for the high-density EOS, in order to infer the dependency of various observables on those parameters.

The main results obtained in this work are:

A procedure to extract the gravitational-waves signal from the numerical simulations was developed and tested, in order to guarantee a minimum possible extraction error, which was found to be less than the finite-resolution error in the time evolution, for every part of the simulated signal.

In order to obtain such result, it is necessary to adopt the second order perturbative extrapolation from ref. [262], to extrapolate to spatial infinity the Ψ_4 signal extracted at finite radii in the simulation domain, which, together with the spin correction, was tested for the first time on BNS simulations in this work. It was shown that, while the spin correction is mostly irrelevant, the second order "mass" correction allows to reduce the extraction error in the accumulated gravitational wave phase by a factor 2 respect to the first order one (which is already commonly adopted in BNS simulations). The error in radiated energy and angular momentum (which is linked to the gravitational waves amplitude error) was shown to be reduced, insted, by 1% (respect to the no extrapolation case) adopting the second order correction, and to be actually increased adopting only the first order one. Following these results, it is recommended the use of the full second order mass correction, if one does not want to employ the more complex and time-consuming CCE extraction [264, 303].
To have negligible waves extraction error, it is also necessary to implement an accurate solution for integrating the Ψ_4 signal, in order to compute the gravitational wave strain h, avoiding spurious GW amplitude oscillations, which come from high frequency noise aliased in the low frequency signal, amplified by the double integration. In this work was designed a new, simple, procedure for this task. The new solution consists in applying an appropriate high-pass Butterworth digital

filter to the GW strain, after the double integration. This solution shows a higher filtering power and leads to a cleaner GW amplitude signal, respect to the other procedures adopted so far in the literature [68, 251, 258]. In particular, the suppression of all spurious amplitude oscillations, even after the application of the perturbative extrapolation formula discussed above, which amplifies them because it contains integrals of Ψ_4, is mandatory for recognizing and studying oscillations coming from real physical processes, like the orbital eccentricity.

The post-merger emitted gravitational signal was studied in great depth, in order to check different emission mechanisms proposed in the literature, as well as the empirical relations developed to connect such signal to the merging stars properties, which could be used to constraint the neutron star equation of state with future gravitational waves detections.

In the cases in which the stars do not promptly collapse to black hole right after the merger, this work focused on the analysis of the gravitational waves spectrum and the radiated energy. Several relationships have been developed by the relativistic astrophysics community to link the post-merger GW spectral peaks to the neutron star EOS, through correlations with the stellar mass, radius, compactness or tidal deformability. Most of them do not, however, take into account unequal mass systems, which, however, we now know are present even in our galaxy [4]. The direct effect of mass ratio and the one of the EOS in highly unequal mass systems on the gravitational waves emitted by the merger remnant were analysed and quantified in this work, to serve as basis for future extensions of those relationships. In particular, the thesis main results are finding that, increasing the mass asymmetry, the main gravitational waves emission mode shifts towards lower frequencies, the subdominant modes gradually disappear, and the overall signal has a lower damping time than in the equal mass case, confirmed also by the radiated energy flux. A physical explanation was also proposed for all these observed effects.

In order to have a better investigation of the post-merger remnant temporal evolution, the Fourier and Prony's spectrograms were also analysed, confirming some proposed post-merger GW emission mechanisms [277], as well as showing some unexpected features, like signal components at frequencies very different from the ones predicted by current theoretical modelling.

For the inspiral phase, instead, the main obtained result was discovering differences in several observables between simulations of the same models with different initial separations between the stars centres. In particular, models starting from closer binary configurations showed an effective lower merger time. This effect is more pronounced looking at the difference from simulations starting with $d = 60$ km and all the others with $d \leq 50$ km. It is relevant only in the final part of the coalescence, after the start of the $d = 40$ km simulations. It was also found to be more important for the more compact models. Other than on the effective merger time, an effect of the initial stellar separation was also found in the gravitational waves phase evolution, the gauge-invariant reduced energy over reduced angular momentum curves, the post-merger gravitational waves spectrum and emitted energy. More studies will be necessary to pinpoint its dominant source, disentangling between the finite-resolution errors due to numerical viscosity and constraint violations accumulated in simulations with many orbits, errors in the initial data, possibly linked with the conformal flatness approximation, and physical effects in play linked with tidal deformations and

stars oscillation modes.

Among the other aspects investigated in this work, the presence of an orbital eccentricity, due to the Helical symmetry and conformal flatness imposed in the initial data computation, was examined. The eccentricity parameter was computed from the stars centres trajectory and the GW amplitude oscillations were confirmed to be an eccentricity effect, comparing the inspiral waveforms from numerical simulations with a recently developed eccentric orbits post-Newtonian approximant [278]. The impact of an orbital eccentricity of the order of the one found in simulations (0.01 in the stiff EOS models and 0.02 in the soft ones) was evaluated, computing its effect on the GW phase evolution and its detectability in current GW interferometers. There is a urgent need for a public code able to produce low-eccentricity BNS initial data [58, 95], towards which I will dedicate future works.

Finally, also models collapsing to black hole, both right after the merger, and following a short hyper mssive neutron star phase, were studied. The disk and accretion rate properties were computed, showing important differences in those two scenarios, which lead, respectively, to thin disks, occupying a limited region in space, and quickly accreated by the BH, or thick, massive disks, with a much larger spatial extension. In both cases, however, was recognized that the maximum density of the disk matter falls quickly below the neutron drip level. This indicates the need to adopt an appropriate prescription for the EOS also at low densities, avoiding to extrapolate the neutron star crust EOS to lower densities, when simulating models which can collapse in the dynamical timescale. The energy and angular momentum balance was analysed also in collapsing models, giving a further confirmation of the code accuracy.

All the simulations were performed with public, community codes, such as `The Einstein Toolkit` and the `LORENE` library, in order to ensure the reproducibility of the obtained results. The evolution code convergence properties were analysed, comparing different combinations of numerical methods. In particular, the concurrent use of the BSSN-OK formulation for the Einstein's equations and the WENO reconstruction method for hydrodynamics was found to be the best solution for entering in the convergent regime even at poor resolutions ($dx \geq 0.5 M_{\odot}$), allowing to run many qualitatively correct, low resolution, test simulations for a preliminary exploration of the parameter space, without the need of exceptional computational resources. Second order convergence, as theoretically expected from the adopted numerical methods, was confirmed looking at different observables: the merger time, the gravitational waves phase evolution, and the gauge-invariant reduced energy over reduced angular momentum curves.

Appendix A

Computational efficiency

A.1 Convergence

Verifying the convergence of a numerical code is an essential part in any numerical simulation data analysis. However, in complex simulations like general relativistic binary neutron star mergers, it could be difficult to uniquely define the code convergence order, finding the most appropriate observables to compute it. The classical notion of convergence states that, taking simulations with different grid spacing dx, any observable C should scale as

$$C(dx) = C(dx = 0) + \varepsilon\,(dx)^p\,, \tag{A.1}$$

where $C(dx = 0)$ represents the *true value* of the observable, at infinite resolution, and the second term represents the finite-resolution error, which, in a finite difference code like ours, should have a polynomial dependence on the grid resolution. The easiest way to compute the convergence order, given three simulations at different resolutions dx_{high}, Δx_{medium} and Δx_{low}, is to use the following relation (see, for example, ref. [179]):

$$\frac{|C_{medium} - C_{low}|}{|C_{high} - C_{medium}|} = \frac{\left|dx^p_{medium} - dx^p_{low}\right|}{\left|dx^p_{high} - dx^p_{medium}\right|}. \tag{A.2}$$

Using a zero-finding algorithm, such as the secant method, it is possible to extract the value of the convergence order p. This widely used technique has, however, the drawback that the result for p often changes choosing three different resolutions for the analysis [98]. It is also not possible to understand, just from three simulations, if the employed numerical algorithms are in the convergent regime, or which is the minimum resolution for which convergence at the nominal order is guaranteed. Another problem of grid-based codes convergence is that there could be some physical processes acting at low scales, which start to be detected only when the grid resolution is some times smaller the length scale of the effect one wants to observe. This is particularly troublesome in turbulent flows, like in the merger phase of binary neutron stars, where there is an inverse cascade of energy coming from smaller and smaller scales, as they are available to the numerical simulation at increasingly better resolutions, destroying any classical knowledge of convergence. For this reason (and also for the absence shocks, excluding the stars surfaces) convergence analysis of BNS simulations are often done only for the inspiral phase, like in ref. [68, 96–98].

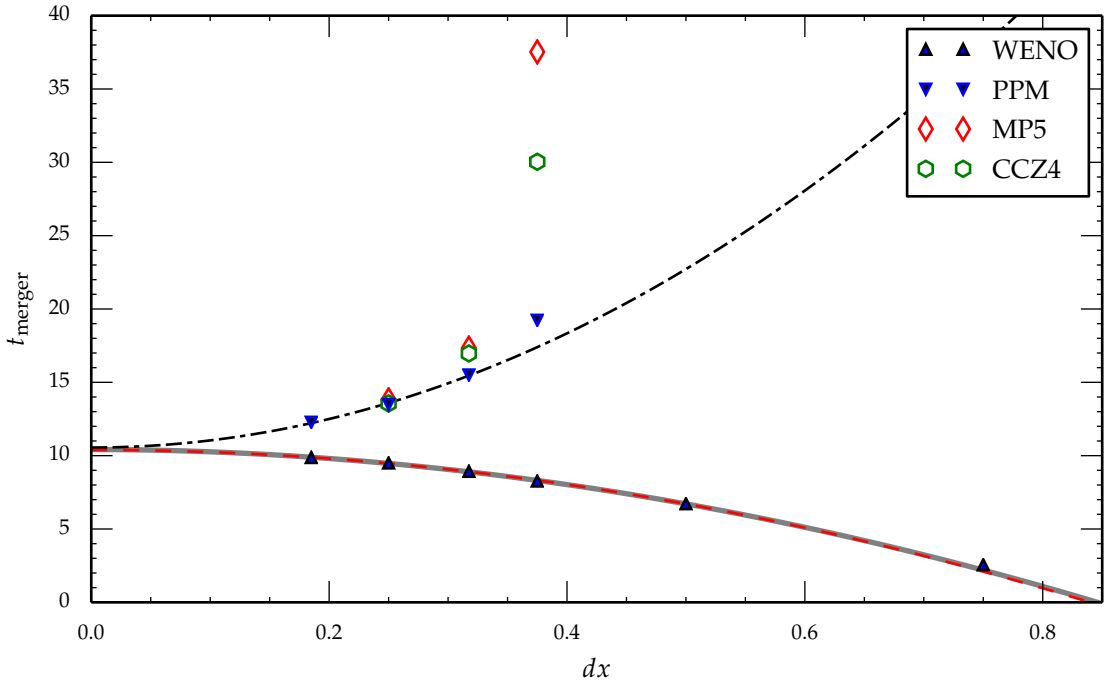

Figure A.1: Fits of the merger time $t_{\rm merger}$ as a function of the resolution dx using the PPM (dashed-dot black line) and the WENO (dashed red line) reconstruction methods, and the BSSN-NOK evolution methods for the gravitational variable assuming second order convergence. In the case of WENO reconstruction we also report (thick gray line) the fit were the convergence order p is computed. In this case the computed convergence order is $p = 1.96 \pm 0.14$. The values of the merger time extrapolated to $dx = 0$ are 10.39 ± 0.03 and 10.55 ± 0.20 for WENO and PPM data, respectively. Please note that the two fits corresponding to the WENO data are so close that they are on top of each other here.

A.1.1 Numerical methods comparison

In ref. [68] were compared the convergence properties, in the inspiral phase, of different numerical methods combinations, changing, in particular, the hydrodynamical variables reconstruction method (between PPM, MP5 and WENO, see sec. 3.2.1), and the formulations adopted for the Einstein equations (BSSN (sec. 3.1.1) or CCZ4 (sec. 3.1.2)). The comparison were done for a single model SLy1.4vs1.4, with an initial separation between the stars of 40 km. As observable the merger time was used, defined as the retarded time for which the amplitude of the GW emission is maximum. This global variable somewhat sums up all the effects in place during the inspiral.

Figure A.1 shows the merger times of simulations with different combinations of the mentioned methods from resolution $dx = 0.75\,\mathrm{M}_\odot$ to resolution $dx = 0.185\,\mathrm{M}_\odot$. The same results are also reported in the next appendix in table B.3. From these results, it is easy to conclude that the combination BSSN+WENO is the best for entering in the convergent regime even at very low resolutions. In particular, it is the only one for which even in simulations at resolution $dx = 0.5\,\mathrm{M}_\odot$ and $dx = 0.75\,\mathrm{M}_\odot$ the stars merge, leading to a qualitatively correct outcome, very useful to be able to run, even in regular workstations, many preliminary low-resolution simulations, in order to

select the most interesting models to evolve later at higher resolution. With all the other methods, instead, the stars do not merge in simulations with resolution $dx \geq 0.5\,\mathrm{M}_\odot$. One interesting thing to notice is that for all methods but BSSN+WENO the merger time decreases increasing the resolution. This difference, as explained also in ref. [], could be due to a different sign in the numerical errors introduced by different methods combinations, which lead to a different effect (in sign) on the resolution dependence of the merger time. Despite this difference, all three combinations with a merger time decreasing at better resolution (BSSN+PPM, BSSN+MP5, CCZ4+WENO) show compatible results for the merger time at $dx = 0.25\,\mathrm{M}_\odot$, which was chosen as standard resolution for the simulations in [68, 94, 99]. However, only BSSN+PPM appears to be in the convergent regime at these resolutions, while BSSN+MP5 and CCZ4+WENO are not. In the CCZ4 case, an explanation for the need of a higher resolution, respect to BSSN, to enter in the convergent regime was already given in ref. [220]: the Hamiltonian constraint, even if damped, enters in the evolution equations of the CCZ4 system, which are, then, more sensitive to numerical errors. More studies are instead needed to explain while the MP5 reconstruction method, which was found best in a TOV star test in ref. [225], performed so poorly in our BNS simulations. For the two combinations in the convergent regime, it is possible to perform a fit to equation (A.1), in order to obtain the merger time at infinite resolution and the convergence order (only in the case of WENO, because we have too few simulations in the convergent regime for PPM respect to the fitted parameters. Therefore, in the PPM case, a second order convergence was assumed in order to estimate the real merger time). The results are $p = 1.96 \pm 0.14$, compatible with second order convergence, and $t^{dx=0}_{merger} = 10.39 \pm 0.03$ in the WENO case, $t^{dx=0}_{merger} = 10.55 \pm 0.20$ in the PPM case. The two results for the merger time at infinite resolution are, therefore, compatible within the statistical error.

Second order convergence is indeed expected from the adopted numerical methods: the time evolution is done with a fourth order Runge-Kutta method, the curvature evolution with fourth-order finite difference, the reconstruction with fifth order (WENO and MP5) or third order (PPM) methods, but the limitation to second order convergence is given by approximating the cells volume averages with their values at cells centres (see sec. 3.2). Numerical GRHD codes able to go beyond second order convergence have been developed recently [96], even if it is proven difficult to get a convergence order higher than two in practical simulations with realistic EOSs [98].

Figure A.2 shows the impact of the numerical method choice on the GW signal, its spectrum and the radiated energy flux. All these observables do not change adopting different numerical techniques, confirming the robustness of HRSC finite-volume GRHD codes. The only difference is a faster dissipation of the post-merger GW signal using the MP5 reconstruction methods. As noted before, the MP5 implementation in `The Einstein Toolkit` would benefit from some more tests, in order to understand why it shows poor accuracy in real production applications.

A.1.2 Analysing convergence with different observables

Since the merger time can give only a global indication about the convergence order in the inspiral phase, it is useful to perform, on different observables, also a three-levels convergence test (eq. A.2) at each discrete point in time of the numerical evolution, before the merger.

This test is performed on the same equal mass model with SLy EOS and mass $1.4\,\mathrm{M}_\odot$ for each star, using the BSSN formulation of Einstein's equations and the WENO reconstruction method. Three triads of resolutions are used: the *High* one $dx = (0.125, 0.1875, 0.25)\,M_\odot$, the *Medium* one $dx = (0.1875, 0.25, 0.3125)\,M_\odot$, and the *Low* one $dx = (0.25, 0.3125, 0.375)\,M_\odot$. Since the convergence order can potentially change from one triad to another, it is mandatory to verify that

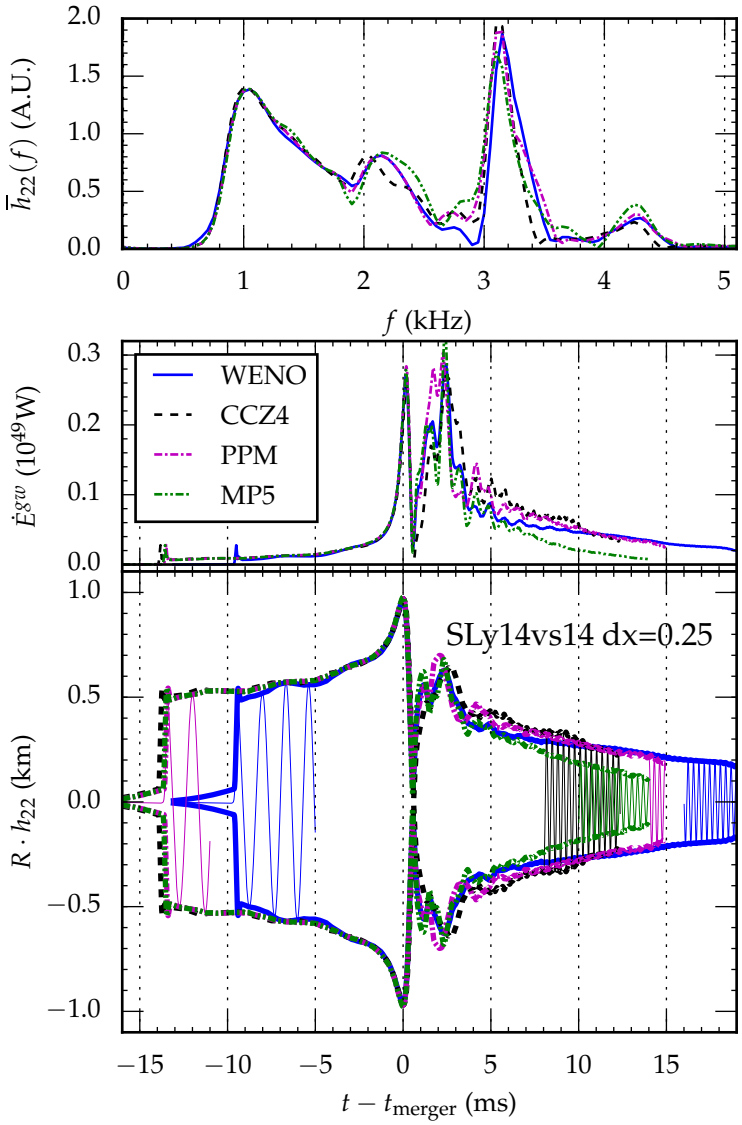

Figure A.2: Comparison of the evolution of model SLy1.4vs1.4 at resolution $dx = 0.25\,\mathrm{M}_\odot$, using different reconstruction methods for the hydrodynamics equations and different evolution scheme for the gravitational sector. Quantities are aligned in time at their respective (different) merger times. The upper panel shows the Fourier-transform (in arbitrary units) of the GW signal in the 22-mode of the whole signal from $t_{\rm merger} - 9$ ms to $t_{\rm merger} + 11$ ms, where a Blackman-windowing function has been applied. The second panel shows the total GW luminosity (energy flux). Finally, the bottom panel shows the envelop of the gravitational wave amplitudes and its real part, multiplied by the distance to the observer. Please note that the evolutions are all very similar to each other, and they differ mainly for the merger time, but not that much in the amount of total energy carried away by GW in this stage, and also not in the damping time of the final excitation of the merger remnant, except for the MP5 case (see text).

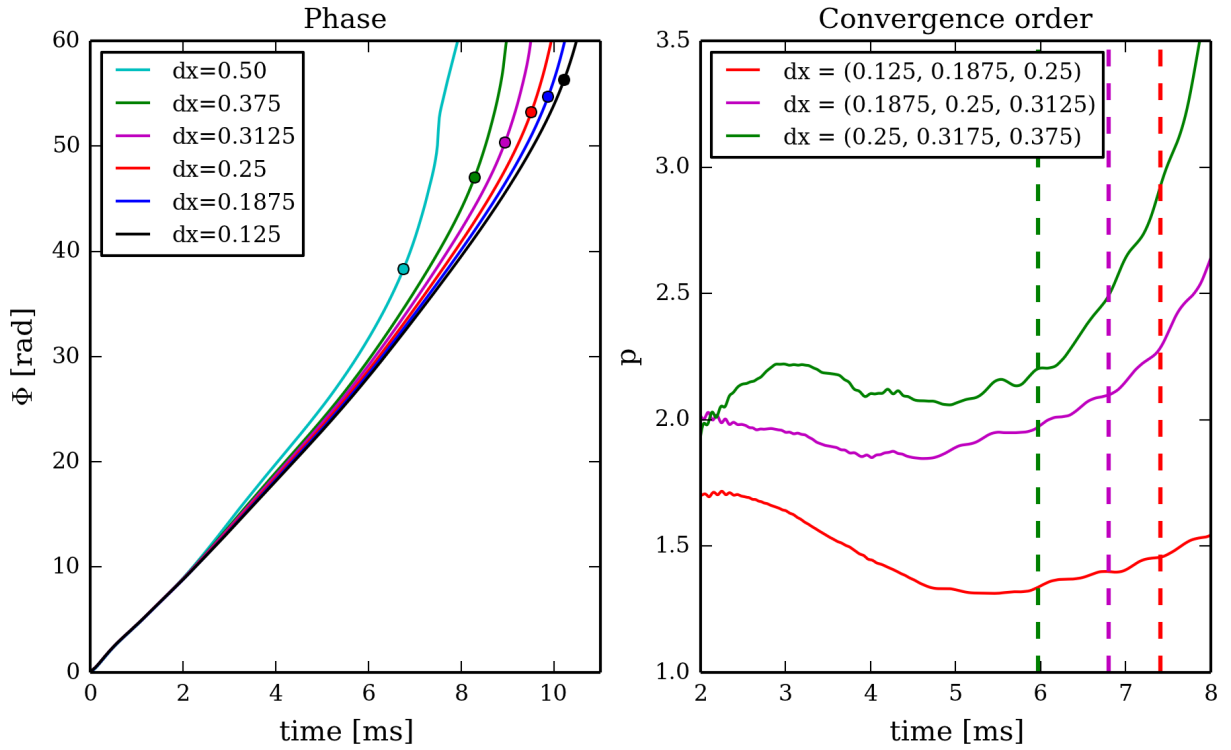

Figure A.3: Accumulated gravitational wave phase for simulations with different resolutions, of the same model SLy1.4vs1.4 (left panel). The coloured dots mark the merger time. The right panel, instead, shows the convergence order of the GW phase for three resolution triads (defined in the text). The vertical lines mark the time of contact of the crusts for the lowest resolution simulation of each triad.

it remains more or less the same, in order to be able to claim a certain convergence order for a numerical code [98].

In figure A.3, is reported the accumulated gravitational wave phase $\phi = arctan\frac{h_\times}{h_+}$, computed from zero retarded time, at the different resolutions (left panel), and the computed convergence order of the three resolution triads (right panel). The convergence order stays around two for the Low and Medium triad, from 2 ms (excluding the initial spurious radiation), until when the neutron stars crust, in the poorest of the three resolutions, come into contact (vertical lines). After the contact, a binary is in a totally different physical state than the ones still inspiralling, therefore no convergence is expected. This is consistent with what is reported also in ref. [96]. The contact times where extracted from the two dimensional density slices, taking the point in time when the fourth polytropic pieces, representing the inner crust ($\rho_3 = 2.6 \times 10^{12}\,\mathrm{g/cm^3}$, see table 2.1), come into contact for the first time. A lower convergence order is, instead, observed in the High triad. This is probably due to the presence of some subdominant error source. The dominant error scales with second order convergence, as expected; when the dominant errors becomes comparable with the subdominant one, increasing the resolution, the subdominant error scaling will impact the measured convergence order. One possible source of this subdominat error are the shocks formed at the stars surface, when they start to move inside the zero-velocity numerical atmosphere. These

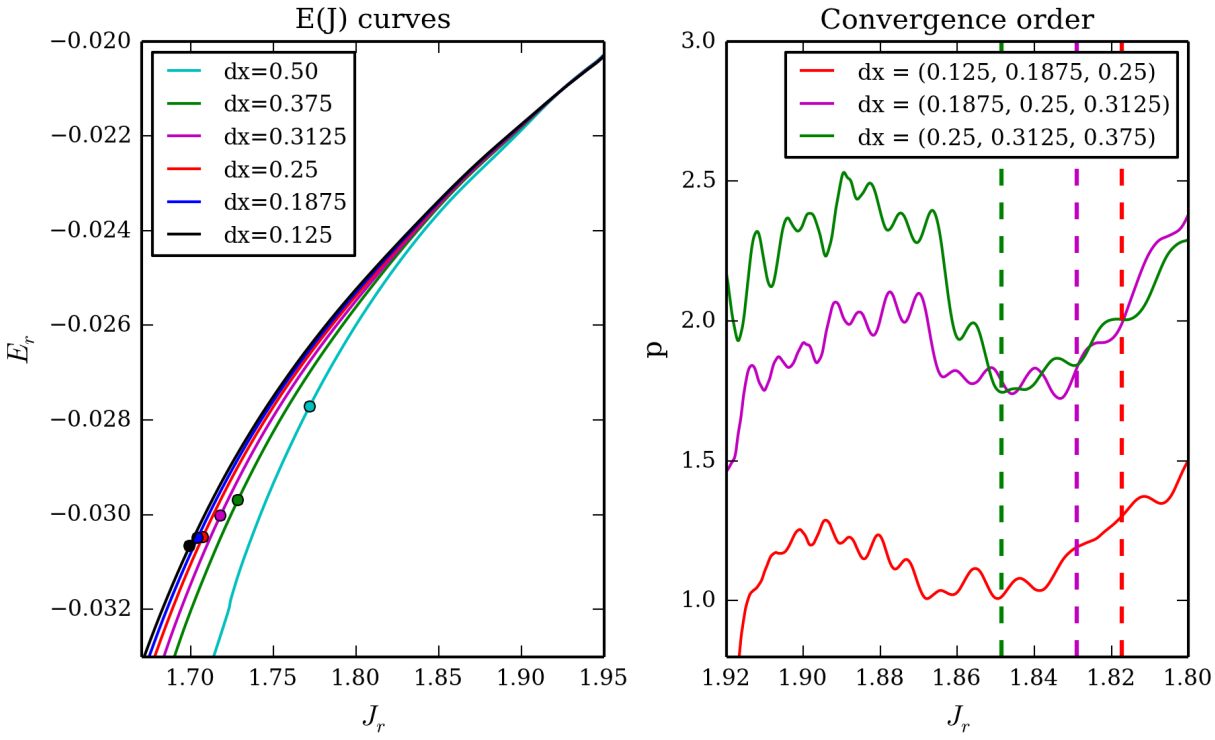

Figure A.4: Reduced energy over reduced angular momentum curves with different resolutions, of the same model SLy1.4vs1.4 (left panel). The coloured dots mark the merger time. The right panel, instead, shows the convergence order of the $E_r(J_r)$ curves for three resolution triads (defined in the text). The vertical lines mark the reduced angular momentum at contact of the crusts for the lowest resolution simulation of each triad.

shocks release thermal energy and eject low-density matter from the stars. In the recent ref. [304], in order to address this problem, the EOS thermal component was switched off for the most part of the inspiral phase, avoiding an extra unphysical thermal pressure at the star surface, but not guaranteeing thermodynamic consistency. A better solution would be to implement more advanced approximated Riemann solvers, like the HLLC solver [305], which are able to distinguish also contact discontinuities, not considered in the simple two-waves structure of HLLE (see sec. 3.2.2).

The same picture comes also from the convergence of the gauge-invariant $E_r(J_r)$ curves (see sec. 4.1.1 for details on their computation), plotted in figure A.4. The Low and Medium triads are around second order convergent, while the High one in only firs-order convergent. Again, the convergence is lost for J_r lower than the angular momentum which characterizes the moment in which the stars crust come into contact in the lowest resolution simulation. The average convergence order, from 2 ms to the contact point, are reported in table A.1.

Observable	dx = (0.25, 0.3125, 0.375)	dx = (0.1875, 0.25, 0.3125)	dx = (0.125, 0.1875, 0.25)
ϕ_{GW}	2.13	1.94	1.46
$E_r(J_r)$	2.24	1.86	1.11

Table A.1: Average convergence order, computed form 2 ms to the neutron star crusts contact, for three different triads of resolutions (see text) and two different observables, the accumulated gravitational wave phase and the gauge-invariant $E_r(J_r)$ curves.

Level	$\min(x/y)$ (CU)	$\max(x/y)$ (CU)	$\min(z)$ (CU)	$\max(z)$ (CU)	(N_x, N_y, N_z) $dx = 0.25$
1	-720	720	0	720	(185,185,96)
2	-360	360	0	360	(205,205,106)
3	-180	180	0	180	(205,205,106)
4	-90	90	0	90	(205,205,106)
5	-60	60	0	30	(265,265,76)
6	-30	30	0	15	(265,265,76)
(7	-15	15	0	7.5)	(265,265,76)

Table A.2: Simulation grid boundaries of refinement levels. Level 7 is only used for simulations forming a BH, once the minimum of the lapse $\alpha < 0.5$.

A.2 Computational infrastructures and the need for high performance computing

Three dimensional general relativistic simulations, like the ones presented in this thesis, require large computational resources. At each time-step, the code evolves in time 17 spacetime variables (including gauge variables) and 5 hydrodynamical variables (including their reconstruction, flux computation, and conservative to primitive conversion, which are all time-consuming algorithms). This is done for every point in the computational domain, which, at our standard resolution ($dx = 0.25\,\mathrm{M}_\odot$) and grid configuration (see table A.2) is made by 6 grids of around $\frac{180^3}{2}$ points each, where the division comes from bitant symmetry. In practice, the inner grids are smaller, also because they are not perfect cubes but have less points in the z direction. To this gridpoint number, one must add the buffer points needed for Runge-Kutta integration (see sec. 3) around the refinement boundaries. Table A.3 shows the computational cost of (relatively short) 30 ms simulation at different spatial resolution using the optimal run parameters on the Galileo machine. In the case of our standard resolution, a run of x days on 256 cores is needed.

Efficient parallel programming is essential for the code to be able to make out the most of the multi-cores and multi-nodes clusters we had allocations on. The code parallelism is handled in the Einstein Toolkit by the `Carpet` thorn. It implements an hybrid MPI-OpenMP parallelization. With MPI, the computational domain of each refinement level is divided among the requested processes, each running on one available core. Each process must evolve also some points at the boundary of its domain, called *ghost points*, which are evolved also by processes responsible for the adjacent domains. There are three ghost points in every direction, as the evolution finite differencing and reconstruction algorithms employed need a three points stencil. At each Runge-Kutta step in the evolution, just after applying the boundary conditions, the ghost points are synchronized between all

$\triangle x$ (CU)	0.75	0.50	0.375	0.25	0.185	0.125
# threads	16	64	128	256	512	2048
# MPI	2	8	16	32	64	256
Memory (GBytes)	3.8	19	40	108	237	768
speed (CU/h)	252	160	124	53	36	16
speed (ms/h)	1.24	0.78	0.61	0.26	0.18	0.08
cost (SU/ms)	13	81	209	974	2915	26053
total cost (kSU, 30 ms)	0.39	3.6	6.3	39	88	780

Table A.3: Computational cost of the simulations, for the example of using BSSN-NOK, with WENO reconstruction for the hydrodynamics. SU stands for service unit: one hour on one CPU core. The reported values refers to the "GALILEO" PRACE-Tier1 machine locate at CINECA (Bologna, Italy) equipped with 521 nodes, two-8 cores Haswell 2.40 GHz, with 128 GBytes/node memory and 4xQDR Infiniband interconnect. Also, these are only correct for evolutions that do not end with the formation of a BH, as an additional refinement level was used to resolve the BH surroundings, and more analysis quantities had to be computed (e.g., the apparent horizon had to be found). In addition, the simulations resulting in a BH were performed on facilities at Louisiana State University: SuperMike II (LSU HPC) and QB2 (Loni).

processes, via MPI communications. There communications take time which is subtracted from the computation time, so they should be reduced to a minimum. One way to try to do so, implemented in Carpet, is to "overlap computations and communications", using non-blocking MPI commands for exchanging messages between processes. OpenMP parallelization, instead, distributes the code computations inside loops to multiple threads, which are then reabsorbed in one single master thread after the loop's end. Most of the Einstein Toolkit is OpenMP parallelized, but some part of the code is inevitably not written in loops over the grid points, so should be executed in a serial manner.

Our production runs have been performed mainly in three similar machines, Cineca's Galileo cluster, thanks to the agreement between Cineca and INFN (specific initiative "Teongrav"), and on Louisiana State University clusters Mike and QueenBee, thanks to the allocations [...]. Galileo is a tier-1 cluster composed by 512 nodes, each mounting two eight-cores Intel Haswell processors and 128 GB of ram. The nodes are linked with an Infiniband network. Some nodes have also Nvidia K80 GPUs or Intel Phi 7120p accelerators, but the Einstein Toolikit is not yet able to take full advantage of them. QueenBee is as cluster at LSU made by 680 compute nodes, each mounting two quad-core Intel Xeon processors and 8GB of ram. Finally, the SuperMike cluster, also hosted at LSU, and now substituted by SuperMikeII, had 512 compute nodes with dual core Pentium IV Xeon processors and 2GB of ram each.

Figure A.5 shows the scaling features of our code on the Galileo cluster, representing, in the upper panel, the evolution time (in solar masses) computed every hour of code run, using a different number of physical cores, MPI processes and OpenMP threads for each process. The ideal scaling (dashed lines) is obviously not reached, since there are many factors limiting the actual code scaling, such as the presence of some serial parts in the code (as the output of 1D and 2D data, while the 3D data output is split among all MPI processes), which, following Ahmdal's low, set a limit to the overall maximum scaling, or the use of buffer zones or other kinds of grid points not really increasing the spatial resolution, or the MPI communication, which becomes more important increasing the

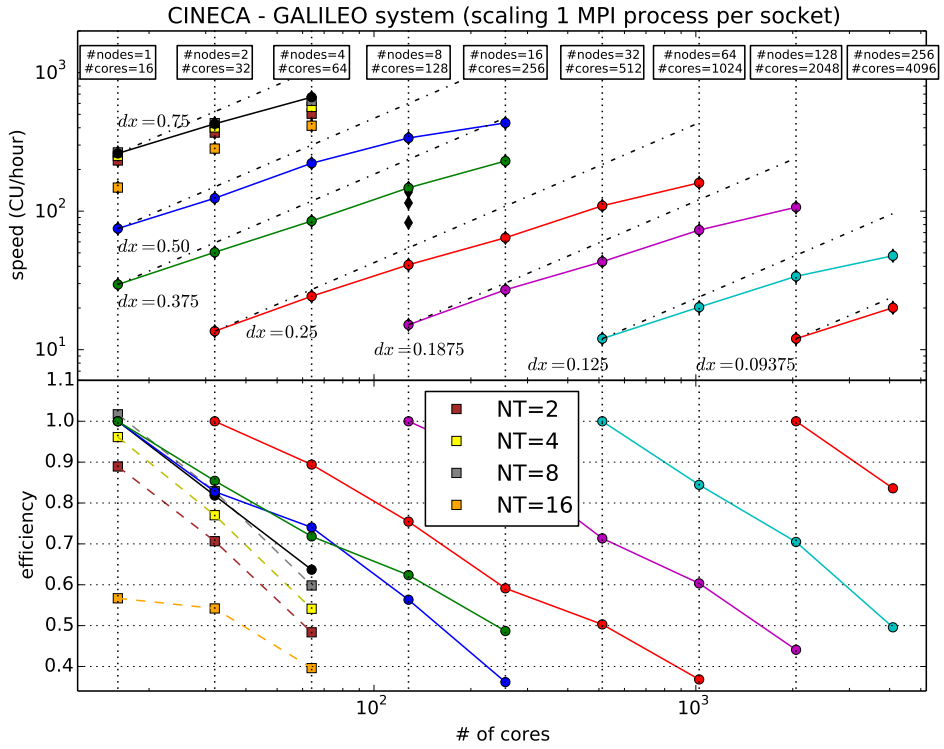

Figure A.5: Strong scaling performance of the Einstein Toolkit with our parameters, for a binary neutron star simulation, using different resolutions, number of physical cores and nodes, and number of threads for each MPI process. The best setup requires using 8 OpenMP threads each process. All the other thread number (NT) possibilities are shown for resolution $dx = 0.75\,\mathrm{M}_\odot$ only for simplicity. These test runs are performed on Cineca's Galileo machines, on Intel processors. Each node has two processors with 8 cores each.

number of processes requested. Nevertheless, the parallel efficiency, shown in the lower panel, is quite satisfactory for this kind of grid-based code, allowing to use a large number of cores without wasting too much computational resources for one's allocation. Such a good scaling could not be reproduced on more *exotic* computer architectures, such as the Fermi Blue Gene Q machine, also hosted at Cineca. When performing such kind of numerical simulations, we are not really interested in getting close to strong scaling, but instead we run in the so called week scaling regime. Week scaling means keeping constant execution time increasing the size of the computational problem and the number of used cores by the same amount. Running a simulation in a week scaling regime means using the least number of processors needed for providing the necessary memory for the application to run. This is the best strategy to spend efficiently the computing time allocation, especially for memory consumption intensive applications.

Appendix B

Simulated models

Table B.1 B.2 and B.3 list most of the simulated models presented in this thesis. The models in table B.1, alredy presented in [68], are binary neutron stars with a close initial distance between the stars centres (40 km), in order to focus the analysis on the merger and post-merger phase. They have different values for the stars mass and mass ratio, covering a large spectrum of the plausible BNS mass distribution (see sec. 2.1.2). The study of unequal mass systems, in particular, has been neglected in the literature until the last year, but, given the discovery of a $q = 0.75$ BNS system (PSRJ0473+1559, see table 2.3), it is very important for understanding the GW phenomenology one can expect to see in future LIGO/Virgo data and the characteristics of the physical environment formed after the merger, which are the basis for constructing electromagnetic emissions and multimessenger models (see sec. 2.3). The models in table B.2, instead, focus more on the study of the pre-merger part of the GW signal, analysing the effect of the neutron star EOS and enquiring if there is any difference in the results of simulations starting from a different interbinary distance (from 60 km to 40 km). This is an important check to evaluate the magnitude of the errors accumulated in many-orbits (≥ 10) simulations, which are a fundamental instrument to construct hybrid numerical-analytical waveforms and to analyse the impact of tidal effects (and, consequently, of the neutron star EOS) on the emitted GW signal, and the adequacy and precision of the adopted initial data, which currently rely on many approximations (see sec. 3.3). This study, presented in ref. [94], about simulations of the same model with a different initial distance (which is, equivalently, a different initial orbital frequency), can also help to reveal new physical processes contributing to the emitted GW signals, which are only developed during the dynamical evolution but not incorporated in the initial data of close-binary simulations. Finally, the models in table B.3, start from the same stars (equal mass $M = 1.4\,\mathrm{M}_\odot$, with the SLy EOS), but use different grid resolutions and/or numerical methods for their evolution. This allowed us to select the best combination of numerical methods for our scientific purposes (and our computational resources limitations), and to carefully study the convergence properties of the simulations in all evolution phases, in order to have a solid confidence in our physics results. All the simulations presented in this thesis have been performed imposing a mirror symmetry across the (x, y) plane, consistent with the symmetry of the problem, in order to reduce the computational cost by a factor 2. It was never forced, instead, a π symmetry around the z axis, in order to be able to simulate also unequal mass models and not to discard possible odd fluid perturbation modes.

Model name	M_b^1 $[M_\odot]$	M_b^2 $[M_\odot]$	M_g^1 $[M_\odot]$	M_G^2 $[M_\odot]$	q	M_{ADM} $[M_\odot]$	J_ADM $\left[\frac{GM_\odot^2}{c}\right]$	Ω_0 $\left[\frac{krad}{s}\right]$	R [km]	C
SLy1.2vs1.2_d40_r25	1.2	1.2	1.11	1.11	1	2.207	5.076	1.932	11.83	0.139
SLy1.3vs1.3_d40_r25	1.3	1.3	1.20	1.20	1	2.373	5.730	1.989	11.80	0.150
SLy1.4vs1.4_d40_r25	1.4	1.4	1.28	1.28	1	2.536	6.405	2.040	11.76	0.161
SLy1.5vs1.5_d40_r25	1.5	1.5	1.36	1.36	1	2.697	7.108	2.089	11.72	0.172
SLy1.6vs1.6_d40_r25	1.6	1.6	1.44	1.44	1	2.854	7.832	2.134	11.67	0.183
SLy1.35vs1.45_d40_r25	1.35	1.45	1.24	1.32	0.94	2.536	6.397	2.040	11.78 - 11.74	0.155 - 0.166
SLy1.3vs1.5_d40_r25	1.3	1.5	1.2	1.36	0.88	2.535	6.376	2.040	11.80 - 11.72	0.150 - 0.172
SLy1.25vs1.55_d40_r25	1.25	1.55	1.16	1.40	0.83	2.533	6.337	2.040	11.82 - 11.70	0.144 - 0.177
SLy1.2vs1.6_d40_r25	1.2	1.6	1.11	1.44	0.77	2.531	6.281	2.039	11.83 - 11.67	0.139 - 0.183
G275th1.4vs1.4_d40_r25	1.4	1.4	1.29	1.29	1	2.554	6.513	2.053	13.81	0.138
G300th1.4vs1.4_d40_r25	1.4	1.4	1.26	1.26	1	2.498	6.243	2.028	11.04	0.169

Table B.1: Evolved models from ref. [68]. All models except the last two use the piecewise polytropic approximation of the SLy equation of state presented in sec. 2.1.1. The last two models, instead, have initial data computed with a single polytrope EOS (with, respectively, $\Gamma = (2.75, 3.00)$ and $K = (18000, 80000)$). We fixed the star centres initial distance to 40 km, to have a relatively short inspiral phase, and the baryon masses of the stars to realistic values ranging from 1.2 to $1.6M_\odot$, with a mass ratio $q = M_g^1/M_g^2$ going from 1 (equal mass case) to 0.77 (close to the $q = 0.75$ of the recently discovered BNS system PSR J0573+1559). The first two columns shows the stars baryonic masses, the following two their gravitational masses at infinite separation, the fifth column is the mass ratio q (computed with the gravitational masses), the sixth and seventh columns report the initial ADM mass and z component of the angular momentum, the eighth column contains the initial orbital frequency, the nineth the star radius and the tenth its compactness $C = \frac{M_g}{R}$. Most of these quantities are given by the LORENE code output, except the gravitational masses and radii, which are computed with the code `rns` [306], constructing a sequence of non-rotating TOV stars.

Model name	d $[km]$	M_g $[M_\odot]$	M_{ADM} $[M_\odot]$	J_ADM $\left[\frac{GM_\odot^2}{c}\right]$	Ω_0 $\left[\frac{krad}{s}\right]$	R [km]	C pre-merger	# Orbits
APR41.4vs1.4_d40_r25	40	1.276	2.5255	6.359	2.036	11.33	0.166	15.5
APR41.4vs1.4_d44_r25	44	1.276	2.5275	6.577	1.767	11.33	0.166	9.5
APR41.4vs1.4_d50_r25	50	1.276	2.5297	6.860	1.492	11.33	0.166	6.5
APR41.4vs1.4_d60_r25	60	1.276	2.5329	7.339	1.153	11.33	0.166	4.5
SLy1.4vs1.4_d40_r25	40	1.281	2.5361	6.405	2.040	11.76	0.161	16
SLy1.4vs1.4_d44_r25	44	1.281	2.5382	6.623	1.770	11.76	0.161	9
SLy1.4vs1.4_d50_r25	50	1.281	2.5404	6.907	1.494	11.76	0.161	6
SLy1.4vs1.4_d60_r25	60	1.281	2.5435	7.388	1.155	11.76	0.161	4
H41.4vs1.4_d40_r25	40	1.300	2.5744	6.588	2.056	14.00	0.137	15
H41.4vs1.4_d44_r25	44	1.300	2.5764	6.802	1.782	14.00	0.137	8
H41.4vs1.4_d50_r25	50	1.300	2.5787	7.088	1.504	14.00	0.137	4.5
H41.4vs1.4_d60_r25	60	1.300	2.5819	7.574	1.163	14.00	0.137	3
MS11.4vs1.4_d40_r25	40	1.305	2.5833	6.643	2.063	14.90	0.129	12.5
MS11.4vs1.4_d44_r25	44	1.305	2.5852	6.850	1.786	14.90	0.129	6
MS11.4vs1.4_d50_r25	50	1.305	2.5875	7.131	1.506	14.90	0.129	3.5
MS11.4vs1.4_d60_r25	60	1.305	2.5907	7.616	1.164	14.90	0.129	2

Table B.2: Models evolved from [94]. All refer to equal mass stars with a baryonic mass of $1.4M_\odot$. The piecewise polytropic representations of the four EOS described in detail in section 2.1.1 have been used for generating the initial data. For each EOS, we run initial data from four different initial distances between the star centres, (60, 50, 44 and 40 km), reported in the first column. The last column shows the number of orbits each model completes from their initial configuration to the merger.

Curvature evolution	Reconstruction	dx	$t_{merger}[ms]$
BSSN-OK	WENO	0.75	2.56
BSSN-OK	WENO	0.50	6.72
BSSN-OK	WENO	0.375	8.27
BSSN-OK	WENO	0.3125	8.93
BSSN-OK	WENO	0.25	9.50
BSSN-OK	WENO	0.185	9.87
BSSN-OK	WENO	0.125	
BSSN-OK	PPM	0.375	19.23
BSSN-OK	PPM	0.3125	15.50
BSSN-OK	PPM	0.25	13.49
BSSN-OK	PPM	0.185	12.28
BSSN-OK	MP5	0.375	37.53
BSSN-OK	MP5	0.3125	17.34
BSSN-OK	MP5	0.25	13.81
CCZ4	WENO	0.375	30.03
CCZ4	WENO	0.3125	16.97
CCZ4	WENO	0.25	13.56

Table B.3: Models with different numerical methods and resolution. Most of them have been already presented in [68]. They refer to $1.4M_\odot$ stars with the SLy EOS and an initial interbinary distance of $40km$. The fourth column reports also their merger time, defined as the retarded time at which the GW amplitude is maximum. More analysis on this key parameter was presented in section A.1.

Appendix C

How to run a binary neutron star merger simulation using public codes

In this last appendix, are listed some simple instructions to perform general-relativistic binary neutron star mergers simulations, using only publicly available codes. Some of the codes and parameter files needed to reproduce this thesis results, should be downloaded from the Parma relativity group public Subversion repository:

```
$ svn --username=anonymous checkout \
        https://einstein.pr.infn.it/svn/numrel/pub/
password: anon
```

In order to run a BNS merger simulation, one needs, first, to generate appropriate initial data (crf. sec. 3.3). This can be done using the public `LORENE` library. It can be downloaded freely from its cvs repository, using the following commands in a bash shell:

```
$ cvs -d :pserver:anonymous@octane.obspm.fr:/cvsroot login
password: anonymous
$ cvs -z5 -d :pserver:anonymous@octane.obspm.fr:\
        /cvsroot checkout Lorene
```

Next, one needs to compile it, choosing appropriate configuration parameter in the file *local_settings* (which can be found in the main LORENE directory). Example configurations for the most common OSs can be found in the *Local_settings_examples* folder. The code to generate BNS initial configurations, using the conformal thin sandwich approximation, is contained in *Codes/Bin_star*. To generate the initial data it is necessary to run first the *init_bin* executable, in order to generate two isolated stars solutions, with the desired EOS, and, then, run *coal*, to compute the proper binary configuration. The output result is contained in a binary file called *resu.d*, which is readable by appropriate routines in `The Einstein Toolkit`, or codes contained in LORENE's *Export* subfolder. Before running the initial data code, its setting should be configured, modifying the files *par_grid.d* (to set the computational domain and its resolution), *par_eos.d* (to choose the EOS used, either a polytropic, one of the tabulated EOSs distributed with LORENE, or a user-defined table, in LORENE's or CompOSE format) and *parcoal.d* (to select, among other things, the initial distance between the stars centres and the stars baryonic mass). An example of LORENE's configuration files for the initial data of the simulations presented in this thesis can be found in the Parma relativity group public repository, under the *BNS_2015_work/InitialData* folder. In particular, the EOS was

set as a table file, generated from the piecewise polytropic parametrization of sec. 2.1.1. Examples of EOS table files in LORENE's format can be also found in the Parma group public repository, under the *BNS_2015_work/Eos_tables* folder.

To evolve the initial data, one needs to download, compile and run `The Einstein Toolkit`. For obtaining the current last version (May 2016), it is useful to download and run the script `GetComponents`. To be able to reproduce this thesis simulations, one should also download the Parma group minimal thornlist (the list of modules to download and compile) for BNS merger simulations, which includes also our modified version of some Cactus thorns (in particular, `EOS_Omni` and `Meudon_Bin_NS`, in order to be able to use piecewise polytropic EOSs) and our analysis modules (`GRHydro_Analysis`).

```
$ curl -kLO https://raw.githubusercontent.com\
      /gridaphobe/CRL/ET_2016_05/GetComponents
$ chmod a+x GetComponents
$ ./GetComponents --parallel \
      http://www.fis.unipr.it/gravity/Research/BNS2015.th
```

Then, it's important to set the proper configuration files. Four configuration files, found in the subdirectory *simfactory/mdb* of the main Cactus installation directory, are important for `simfactory`, the Python code responsible for the installation process and the simulations running:

- The optionlist (*simfactory/mdb/optionlists/*.cfg*), containing the compilation flags;
- The machine file (*simfactory/mdb/machines/*.ini*, containing information about the machine hardware;
- The submitscript (*simfactory/mdb/submitscripts/*.sub)*, containing the parameters to pass to the batch queuing system, when running on a shared cluster;
- The runscript (*simfactory/mdb/runscripts/*.run*), containing the command to run the setting the needed environmental variables.

The standard installation of The Einstein Toolkit already contains several examples of those files, for most OSs, Linux distributions, and many clusters around the world, including Galileo, Queenbee, and Mike, where this thesis simulations were performed.

After having found and eventually modified the correct configuration files, one can compile all the toolkit with the simple command

```
$ simfactory/bin/sim build CONFIGURATION_NAME\
      --thornlist THORNLIST.th --optionlist OPTIONLIST.cfg \
      --runscript RUNSCRIPT.run --submitscript SUBMITSCRIPT.sub \
      --machine MACHINE_NAME
```

where the upper case words should be substituted with the appropriate names or file paths. Multiple configurations, with different configurations names, and different parameters in the configuration files, can be created and compiled. After the compilation (which can require some minutes to several ours, depending on the platform), one still needs to set up a parameter file, before being able to run the desired simulation. A parameter file contains the list of the used module (called *active thorns*) and sets their parameters. For example, one should set the grid structure, through the parameters of the `CarpetRegrid2` thorn, or the numerical methods desired for the hydrodynamics,

with the `GRHydro` thorn parameters, or the variables one wants to output in 1D, 2D and 3D files. Other important things to set are the stars EOS (with the `EOS_Omni` thorn) and the path to the initial LORENE data file (the *resu.d* produced in the previous step). All the parameter files for this thesis simulations can be downloaded from the Parma group Subversion repository, in folder *BNS_2015_work/WorkBNS*.

To submit a simulation to the queuing system, one just needs to run the following command, from the main Cactus installation folder:

```
$ simfactory/bin/sim submit SIMULATION_NAME \
      --procs NP --num-threads NT --num-smt NS \
      --parfile PARFILE.par --configuration CONFIGURATION_NAME\
      --walltime hh:mm:ss
```

where NP is the total number of threads, NT is the number of threads for each MPI process, NS is the number of threads for each core, which can be greater than one in machines where hyperthreading is enabled, and walltime is the maximum running time, often imposed by the system administrators. In order to run long simulation, one can restart an interrupted simulation running the same submit command. It will start again from the last saved checkpoint file (checkpoint saving frequency can be set in the parameter file). Instead, to run a simulation directly on the machine one is logged in, the command *create-run* (for the first run), or simply *run* (for the subsequent restarts) can be used instead of *submit*. In this case, the option *walltime* will be ignored, using the one set in the parameter file (or its default value).

To analyse the results, several tools have been developed by different groups, listed on the webpage *https://docs.einsteintoolkit.org/et-docs/Analysis_and_post-processing*, but there is no single official Einstein Toolkit post-processing tool yet. I will illustrate some simple use-cases of the Parma group `PyCactus` code, which can be downloaded from its Git repository

```
$ git clone https://bitbucket.org/knarrff/pycactus.git
```

`PyCactus` is a Python code which heavily uses the *numpy*, *scipy* and *matplotlib* scientific libraries. It can be efficiently used in an interactive way with the *ipython* program. Just to give an example of its capabilities, I will illustrate the steps needed to extract and plot the gravitational waves signal from a Cactus simulation.

First, one needs to load the `PyCactus` modules:

```
from UtilityUnits import *
import CarpetASCIII as asc
import CarpetH5 as H5
import UtilityAnalysis as Analysis
import CarpetSimulationData  sim
from matplotlib import pyplot as plt
import numpy as np
```

To load all the scalar output from a simulation, and save it in an hdf5 file, one can use the following command (which, if the hdf5 file already exists, just reads its content):

```
d = sim.ReadAllScalarsSimulation(sim_name, basedir, folderH5)
```

Form there, to get the gravitational wave signal, extrapolated with the second order perturbative formula and integrated with our filtering procedure (see sec. 3.4), and to plot its h_+ component, one needs simply to use the following commands:

```
psi_inf=Analysis.second_order_extrapolation(d['PSI4'][r0]['l2m2'],
      int(r0),d['M0'],2,2,2,'filter',f0=f0)
h22  = Analysis.NIntegratePsi4_filter(psi_inf,f0,Nint=2,r=0,M=d['M0'])
plt.plot(d['time']*CU_to_ms,np.real(h22))
```

Acknowledgements

I wish to acknowledge the help received from some people and organizations during the three years of my Ph.D., which has been fundamental for the development of this thesis.
First and foremost, I must thank my supervisor, Prof. Roberto De Pietri, and our collaborator, Alessandra Feo, for accepting me in their research group, teaching me a lot about both physics and the academic system, guiding me in the transformation process form a lost student to someone able to carry on a Ph.D.-worth research. I could not have asked or hoped for a better guidance and better human connections inside my research group. I should thank them also for all the opportunities to participate to schools and conferences, even abroad, that I had.
I must thank also our collaborator Frank Löffler, whose contribution to the results presented in this thesis was fundamental and who guided me through the intricacies of the Einstein Toolkit source code.
I thank Professor José Antonio Font for his review, which was very helpful for improving the quality of this manuscript.
I thank INFN for giving me the support for travelling to conferences and schools and for the support in providing computational resources on CINECA's Fermi and Galileo clusters, without which this work would have been impossible. For the same reason, I should also thank the Louisiana Optical Network Initiative and the LSU HPC facilities, which granted to our group computing time allocations which were also used for some of the simulations presented in this work.
I want to thank all the developers of the free and public software that was used in this thesis, and, in particular, the `Einstein Toolkit` developers and maintainers.
Finally, I thank my wife Adriana, for supporting me during this intense three years, full of changes in our lives.

Bibliography

[1] Abbott et al B P 2016 *Physical Review Letters* **116** 061102 ISSN 0031-9007 (*Preprint* 1602.03837) URL http://arxiv.org/abs/1602.03837http://link.aps.org/doi/10.1103/PhysRevLett.116.061102

[2] The LIGO Scientific Collaboration, the Virgo Collaboration and Abbott et al B P 2016 (*Preprint* 1606.04856) URL http://arxiv.org/abs/1606.04856http://dx.doi.org/10.1103/PhysRevX.6.041015

[3] Abbott et al B P 2016 *Living Reviews in Relativity* **19** 1 ISSN 2367-3613 URL http://link.springer.com/10.1007/lrr-2016-1

[4] Martinez J G, Stovall K, Freire P C C, Deneva J S, Jenet F A, McLaughlin M A, Bagchi M, Bates S D and Ridolfi A 2015 *The Astrophysical Journal* **812** 143 ISSN 1538-4357 (*Preprint* 1509.08805) URL http://arxiv.org/abs/1509.08805http://dx.doi.org/10.1088/0004-637X/812/2/143http://stacks.iop.org/0004-637X/812/i=2/a=143?key=crossref.00c40b5651d73f94822d22bb60f5349c

[5] Ozel F and Freire P 2016 (*Preprint* 1603.02698) URL http://arxiv.org/abs/1603.02698http://dx.doi.org/10.1146/annurev-astro-081915-023322

[6] Hulse R A and Taylor J H 1975 *The Astrophysical Journal* **195** L51 ISSN 0004-637X URL http://adsabs.harvard.edu/doi/10.1086/181708

[7] Taylor J H and Weisberg J M 1989 *The Astrophysical Journal* **345** 434 ISSN 0004-637X URL http://adsabs.harvard.edu/doi/10.1086/167917

[8] Weisberg J M and Taylor J H 2004 (*Preprint* 0407149) URL http://arxiv.org/abs/astro-ph/0407149

[9] Baiotti L, Damour T, Giacomazzo B, Nagar A and Rezzolla L 2011 *Physical Review D* **84** 024017 ISSN 1550-7998 (*Preprint* 1103.3874) URL http://arxiv.org/abs/1103.3874

[10] Stergioulas N, Bauswein A, Zagkouris K and Janka H T 2011 *Monthly Notices of the Royal Astronomical Society* **418** 427–436 ISSN 00358711 (*Preprint* 1105.0368) URL http://arxiv.org/abs/1105.0368

[11] Bernuzzi S, Nagar A, Thierfelder M and Brügmann B 2012 *Physical Review D* **86** 044030 ISSN 1550-7998 (*Preprint* 1205.3403) URL http://arxiv.org/abs/1205.3403http://link.aps.org/doi/10.1103/PhysRevD.86.044030

[12] Hotokezaka K, Kyutoku K and Shibata M 2013 *Physical Review D* **87** 044001 ISSN 1550-7998 URL http://link.aps.org/doi/10.1103/PhysRevD.87.044001

[13] Read J S, Baiotti L, Creighton J D E, Friedman J L, Giacomazzo B, Kyutoku K, Markakis C, Rezzolla L, Shibata M and Taniguchi K 2013 *Physical Review D* **88** 044042 ISSN 1550-7998 URL http://link.aps.org/doi/10.1103/PhysRevD.88.044042

[14] Takami K, Rezzolla L and Baiotti L 2014 *Physical Review Letters* **113** 091104 ISSN 0031-9007 URL http://link.aps.org/doi/10.1103/PhysRevLett.113.091104

[15] Porciani C and Madau P 2001 *The Astrophysical Journal* **548** 522–531 ISSN 0004-637X URL http://stacks.iop.org/0004-637X/548/i=2/a=522

[16] Barthelmy S D, Chincarini G, Burrows D N, Gehrels N, Covino S, Moretti A, Romano P, O'Brien P T, Sarazin C L, Kouveliotou C, Goad M, Vaughan S, Tagliaferri G, Zhang B, Antonelli L A, Campana S, Cummings J R, D'Avanzo P, Davies M B, Giommi P, Grupe D, Kaneko Y, Kennea J A, King A, Kobayashi S, Melandri A, Meszaros P, Nousek J A, Patel S, Sakamoto T and Wijers R A M J 2005 *Nature* **438** 994–996 ISSN 0028-0836 URL http://www.nature.com/doifinder/10.1038/nature04392

[17] Norris J P and Bonnell J T 2006 *The Astrophysical Journal* **643** 266–275 ISSN 0004-637X URL http://stacks.iop.org/0004-637X/643/i=1/a=266

[18] Lee W H and Ramirez-Ruiz E 2007 *New Journal of Physics* **9** 17–17 ISSN 1367-2630 URL http://stacks.iop.org/1367-2630/9/i=1/a=017?key=crossref.ff9dd159a837eabe86e914e1169c90dc

[19] Belczynski K, Perna R, Bulik T, Kalogera V, Ivanova N and Lamb D Q 2006 *The Astrophysical Journal* **648** 1110–1116 ISSN 0004-637X URL http://stacks.iop.org/0004-637X/648/i=2/a=1110

[20] Metzger B D, Quataert E and Thompson T A 2008 *Monthly Notices of the Royal Astronomical Society* **385** 1455–1460 ISSN 0035-8711 URL http://mnras.oxfordjournals.org/cgi/doi/10.1111/j.1365-2966.2008.12923.x

[21] Rezzolla L, Giacomazzo B, Baiotti L, Granot J, Kouveliotou C and Aloy M A 2011 *The Astrophysical Journal* **732** L6 ISSN 2041-8205 URL http://stacks.iop.org/2041-8205/732/i=1/a=L6

[22] Ciolfi R and Siegel D M 2014 *The Astrophysical Journal* **798** L36 ISSN 2041-8213 (*Preprint* 1411.2015) URL http://arxiv.org/abs/1411.2015v2http://arxiv.org/abs/1411.2015http://dx.doi.org/10.1088/2041-8205/798/2/L36http://stacks.iop.org/2041-8205/798/i=2/a=L36?key=crossref.bebc4a32c6a8955bf93b7e0866d8a6c6

[23] Gompertz B P, O'Brien P T and Wynn G a 2014 *Monthly Notices of the Royal Astronomical Society* **438** 240–250 ISSN 0035-8711 (*Preprint* 1311.1505) URL http://arxiv.org/abs/1311.1505v1http://arxiv.org/abs/1311.1505http://dx.doi.org/10.1093/mnras/stt2165http://mnras.oxfordjournals.org/cgi/doi/10.1093/mnras/stt2165

[24] Kiuchi K, Sekiguchi Y, Kyutoku K, Shibata M, Taniguchi K and Wada T 2015 7 (*Preprint* 1506.06811) URL http://arxiv.org/abs/1506.06811

[25] Rezzolla L and Kumar P 2015 *The Astrophysical Journal* **802** 95 ISSN 1538-4357 (*Preprint* 1410.8560) URL http://arxiv.org/abs/1410.8560http://dx.doi.org/10.1088/0004-637X/802/2/95http://stacks.iop.org/0004-637X/802/i=2/a=95?key=crossref.8bcf0b822759fe19b17210ff726f346f

[26] Kawamura T, Giacomazzo B, Kastaun W, Ciolfi R, Endrizzi A, Baiotti L and Perna R 2016 (*Preprint* 1607.01791) URL http://arxiv.org/abs/1607.01791

[27] Ruiz M, Lang R N, Paschalidis V and Shapiro S L 2016 *The Astrophysical Journal* **824** L6 ISSN 2041-8213 URL http://stacks.iop.org/2041-8205/824/i=1/a=L6?key=crossref.d690eb72b069df40d2fb4582a5d35c4f

[28] Paschalidis V 2016 (*Preprint* 1611.01519) URL http://arxiv.org/abs/1611.01519

[29] Palenzuela C, Lehner L, Liebling S L, Ponce M, Anderson M, Neilsen D and Motl P 2013 *Physical Review D* **88** 043011 ISSN 1550-7998 URL http://link.aps.org/doi/10.1103/PhysRevD.88.043011

[30] Ponce M, Palenzuela C, Lehner L and Liebling S L 2014 *Physical Review D* **90** 044007 ISSN 1550-7998 URL http://link.aps.org/doi/10.1103/PhysRevD.90.044007

[31] Totani T 2013 *Publications of the Astronomical Society of Japan* **65** L12 ISSN 0004-6264 URL http://pasj.oxfordjournals.org/lookup/doi/10.1093/pasj/65.5.L12

[32] Falcke H and Rezzolla L 2014 *Astronomy & Astrophysics* **562** A137 ISSN 0004-6361 URL http://www.aanda.org/10.1051/0004-6361/201321996

[33] Siegel D M and Ciolfi R 2016 *The Astrophysical Journal* **819** 15 ISSN 1538-4357 URL http://stacks.iop.org/0004-637X/819/i=1/a=15?key=crossref.ba4e3a2d8a00e4bebac7fb8f3c2f1352

[34] Siegel D M and Ciolfi R 2016 *The Astrophysical Journal* **819** 14 ISSN 1538-4357 URL http://stacks.iop.org/0004-637X/819/i=1/a=14?key=crossref.42482ec984b60e189052721a74340fcc

[35] Tanvir N R, Levan A J, Fruchter A S, Hjorth J, Hounsell R A, Wiersema K and Tunnicliffe R L 2013 *Nature* **500** 547–549 ISSN 0028-0836 URL http://www.nature.com/doifinder/10.1038/nature12505

[36] Berger E, Fong W and Chornock R 2013 *The Astrophysical Journal* **774** L23 ISSN 2041-8205 URL http://stacks.iop.org/2041-8205/774/i=2/a=L23?key=crossref.ebd7c7cd171fc485d674306f4909d1a6

[37] Metzger B D 2016 (*Preprint* 1610.09381) URL http://arxiv.org/abs/1610.09381

[38] Berry et al C P L 2016 *Journal of Physics: Conference Series* **716** 012031 ISSN 1742-6588 (*Preprint* 1606.01095) URL http://arxiv.org/abs/1606.01095

[39] Buonanno A and Damour T 1999 *Physical Review D* **59** 084006 ISSN 0556-2821 URL http://link.aps.org/doi/10.1103/PhysRevD.59.084006

[40] Damour T, Nagar A, Hannam M, Husa S and Brügmann B 2008 *Physical Review D* **78** 044039 ISSN 1550-7998 (*Preprint* 0803.3162) URL http://arxiv.org/abs/0803.3162

[41] Buonanno A, Pan Y, Pfeiffer H P, Scheel M A, Buchman L T and Kidder L E 2009 *Physical Review D* **79** 124028 ISSN 1550-7998 URL http://link.aps.org/doi/10.1103/PhysRevD.79.124028

[42] The LIGO Scientific Collaboration, the Virgo Collaboration and Abbott et al B P 2016 18 (*Preprint* 1606.01210) URL http://arxiv.org/abs/1606.01210

[43] Damour T and Nagar A 2010 *Physical Review D* **81** 084016 ISSN 1550-7998 URL http://link.aps.org/doi/10.1103/PhysRevD.81.084016

[44] Hotokezaka K, Kiuchi K, Kyutoku K, Okawa H, Sekiguchi Y i, Shibata M and Taniguchi K 2013 *Physical Review D* **87** 024001 ISSN 1550-7998 URL http://link.aps.org/doi/10.1103/PhysRevD.87.024001

[45] Bernuzzi S, Nagar A, Dietrich T and Damour T 2015 *Physical Review Letters* **114** 161103 ISSN 0031-9007 (*Preprint* 1412.4553) URL http://arxiv.org/abs/1412.4553http://link.aps.org/doi/10.1103/PhysRevLett.114.161103

[46] Barkett K, Scheel M A, Haas R, Ott C D, Bernuzzi S, Brown D A, Szilágyi B, Kaplan J D, Lippuner J, Muhlberger C D, Foucart F and Duez M D 2015 7 (*Preprint* 1509.05782) URL http://arxiv.org/abs/1509.05782

[47] Hinderer T, Taracchini A, Foucart F, Buonanno A, Steinhoff J, Duez M, Kidder L E, Pfeiffer H P, Scheel M A, Szilagyi B, Hotokezaka K, Kyutoku K, Shibata M and Carpenter C W 2016 5 (*Preprint* 1602.00599) URL http://arxiv.org/abs/1602.00599http://dx.doi.org/10.1103/PhysRevLett.116.181101

[48] Steinhoff J, Hinderer T, Buonanno A and Taracchini A 2016 (*Preprint* 1608.01907) URL http://arxiv.org/abs/1608.01907

[49] Pretorius F 2005 *Physical Review Letters* **95** 121101 ISSN 0031-9007 URL http://link.aps.org/doi/10.1103/PhysRevLett.95.121101

[50] Campanelli M, Lousto C O, Marronetti P and Zlochower Y 2006 *Physical Review Letters* **96** 111101 ISSN 0031-9007 URL http://link.aps.org/doi/10.1103/PhysRevLett.96.111101

[51] Baker J G, Centrella J, Choi D I, Koppitz M and van Meter J 2006 *Physical Review Letters* **96** 111102 ISSN 0031-9007 URL http://link.aps.org/doi/10.1103/PhysRevLett.96.111102

[52] Bonazzola S, Gourgoulhon E and Marck J A 1997 *Physical Review D* **56** 7740–7749 ISSN 0556-2821 URL http://link.aps.org/doi/10.1103/PhysRevD.56.7740

[53] Taniguchi K, Gourgoulhon E and Bonazzola S 2001 *Physical Review D* **64** 064029 ISSN 05562821 (*Preprint* 0207098) URL http://link.aps.org/doi/10.1103/PhysRevD.63.064029

[54] Löffler F, Faber J, Bentivegna E, Bode T, Diener P, Haas R, Hinder I, Mundim B C, Ott C D, Schnetter E, Allen G, Campanelli M and Laguna P 2012 *Classical and Quantum Gravity* **29** 115001 ISSN 0264-9381 URL http://stacks.iop.org/0264-9381/29/i=11/a=115001?key=crossref.cc6d00612a26e4ca33a28de222784772

[55] Bernuzzi S, Dietrich T, Tichy W and Brügmann B 2014 *Physical Review D* **89** 104021 ISSN 1550-7998 URL http://link.aps.org/doi/10.1103/PhysRevD.89.104021

[56] East W E, Paschalidis V, Pretorius F and Shapiro S L 2016 *Physical Review D* **93** 024011 ISSN 2470-0010 (*Preprint* 1511.01093) URL http://arxiv.org/abs/1511.01093http://link.aps.org/doi/10.1103/PhysRevD.93.024011

[57] Kastaun W and Galeazzi F 2015 *Physical Review D* **91** 064027 ISSN 1550-7998 URL http://link.aps.org/doi/10.1103/PhysRevD.91.064027

[58] Dietrich T, Moldenhauer N, Johnson-McDaniel N K, Bernuzzi S, Markakis C M, Brügmann B and Tichy W 2015 *Physical Review D* **92** 124007 ISSN 1550-7998 (*Preprint* arXiv:1507.07100v1) URL http://arxiv.org/abs/1507.07100http://link.aps.org/doi/10.1103/PhysRevD.92.124007

[59] Gold R, Bernuzzi S, Thierfelder M, Brügmann B and Pretorius F 2012 *Physical Review D* **86** 121501 ISSN 1550-7998 URL http://link.aps.org/doi/10.1103/PhysRevD.86.121501

[60] East W E and Pretorius F 2012 *The Astrophysical Journal* **760** L4 ISSN 2041-8205 URL http://stacks.iop.org/2041-8205/760/i=1/a=L4?key=crossref.55c0b5849f3abe73e2c0e63333fc6239

[61] Radice D, Galeazzi F, Lippuner J, Roberts L F, Ott C D and Rezzolla L 2016 *Monthly Notices of the Royal Astronomical Society* **460** 3255–3271 ISSN 0035-8711 (*Preprint* 1601.02426) URL http://arxiv.org/abs/1601.02426http://mnras.oxfordjournals.org/lookup/doi/10.1093/mnras/stw1227

[62] Shibata M, Taniguchi K and Uryu K 2003 *Physical Review D* **68** 084020 ISSN 0556-2821 URL http://link.aps.org/doi/10.1103/PhysRevD.68.084020

[63] Rezzolla L, Baiotti L, Giacomazzo B, Link D and Font J A 2010 *Classical and Quantum Gravity* **27** 114105 ISSN 0264-9381 URL http://iopscience.iop.org/article/10.1088/0264-9381/27/11/114105

[64] Hotokezaka K, Kiuchi K, Kyutoku K, Muranushi T, Sekiguchi Y i, Shibata M and Taniguchi K 2013 *Physical Review D* **88** 044026 ISSN 1550-7998 URL http://link.aps.org/doi/10.1103/PhysRevD.88.044026

[65] Sekiguchi Y, Kiuchi K, Kyutoku K, Shibata M and Taniguchi K 2016 *Physical Review D* **93** 124046 ISSN 2470-0010 (*Preprint* 1603.01918) URL http://arxiv.org/abs/1603.01918http://link.aps.org/doi/10.1103/PhysRevD.93.124046

[66] Lehner L, Liebling S L, Palenzuela C, Caballero O L, O'Connor E, Anderson M and Neilsen D 2016 *Classical and Quantum Gravity* **33** 184002 ISSN 0264-9381 (*Preprint* 1603.00501) URL http://arxiv.org/abs/1603.00501http://stacks.iop.org/0264-9381/33/i=18/a=184002?key=crossref.04bdbcb9521ad8a6170295bb4ef6bb92

[67] Dietrich T, Ujevic M, Tichy W, Bernuzzi S and Bruegmann B 2016 (*Preprint* 1607.06636) URL http://arxiv.org/abs/1607.06636

[68] De Pietri R, Feo A, Maione F and Löffler F 2016 *Physical Review D* **93** 064047 ISSN 2470-0010 URL http://link.aps.org/doi/10.1103/PhysRevD.93.064047

[69] Foucart F, Haas R, Duez M D, O'Connor E, Ott C D, Roberts L, Kidder L E, Lippuner J, Pfeiffer H P and Scheel M A 2015 21 (*Preprint* 1510.06398) URL http://arxiv.org/abs/1510.06398

[70] Sekiguchi Y, Kiuchi K, Kyutoku K and Shibata M 2015 7 (*Preprint* 1502.06660) URL http://arxiv.org/abs/1502.06660

[71] Palenzuela C, Liebling S L, Neilsen D, Lehner L, Caballero O L, O'Connor E and Anderson M 2015 *Physical Review D* **92** 044045 ISSN 1550-7998 (*Preprint* 1505.01607) URL http://arxiv.org/abs/1505.01607http://link.aps.org/doi/10.1103/PhysRevD.92.044045

[72] Bernuzzi S, Radice D, Ott C D, Roberts L F, Mösta P and Galeazzi F 2016 *Physical Review D* **94** 024023 ISSN 2470-0010 (*Preprint* 1512.06397) URL http://arxiv.org/abs/1512.06397http://link.aps.org/doi/10.1103/PhysRevD.94.024023

[73] East W E, Paschalidis V and Pretorius F 2016 (*Preprint* 1609.00725) URL http://arxiv.org/abs/1609.00725

[74] Baumgarte T W, Shapiro S L and Shibata M 2000 *The Astrophysical Journal* **528** L29–L32 ISSN 0004637X URL http://stacks.iop.org/1538-4357/528/i=1/a=L29

[75] Tóth G 2000 *Journal of Computational Physics* **161** 605–652 ISSN 00219991 URL http://linkinghub.elsevier.com/retrieve/pii/S0021999100965197

[76] Del Zanna L, Bucciantini N and Londrillo P 2003 *Astronomy and Astrophysics* **400** 397–413 ISSN 0004-6361 URL http://dx.doi.org/10.1051/0004-6361:20021641

[77] Anton L, Zanotti O, Miralles J A, Marti J M, Ibanez J M, Font J A and Pons J A 2006 *The Astrophysical Journal* **637** 296–312 ISSN 0004-637X URL http://stacks.iop.org/0004-637X/637/i=1/a=296

[78] Del Zanna L, Zanotti O, Bucciantini N and Londrillo P 2007 *Astronomy and Astrophysics* **473** 11–30 ISSN 0004-6361 URL http://dx.doi.org/10.1051/0004-6361:20077093

[79] Font J A 2008 *Living Reviews in Relativity* **11** ISSN 1433-8351 URL http://www.livingreviews.org/lrr-2008-7

[80] Etienne Z B, Liu Y T and Shapiro S L 2010 *Physical Review D* **82** 084031 ISSN 1550-7998 URL http://link.aps.org/doi/10.1103/PhysRevD.82.084031

[81] Giacomazzo B, Rezzolla L and Baiotti L 2011 *Physical Review D* **83** 044014 ISSN 1550-7998 URL http://link.aps.org/doi/10.1103/PhysRevD.83.044014

[82] Etienne Z, Paschalidis V, Liu Y and Shapiro S 2012 *Physical Review D* **85** 024013 ISSN 1550-7998 URL http://link.aps.org/doi/10.1103/PhysRevD.85.024013http://journals.aps.org/prd/abstract/10.1103/PhysRevD.85.024013

[83] Kiuchi K, Kyutoku K, Sekiguchi Y, Shibata M and Wada T 2014 *Physical Review D* **90** 041502 ISSN 1550-7998 (*Preprint* arXiv:1407.2660v2) URL http://link.aps.org/doi/10.1103/PhysRevD.90.041502

[84] Etienne Z B, Paschalidis V, Haas R, Moesta P and Shapiro S L 2015 37 (*Preprint* 1501.07276) URL http://arxiv.org/abs/1501.07276

[85] Endrizzi A, Ciolfi R, Giacomazzo B, Kastaun W and Kawamura T 2016 31 (*Preprint* 1604.03445) URL http://arxiv.org/abs/1604.03445http://dx.doi.org/10.1088/0264-9381/33/16/164001

[86] Bucciantini N and Del Zanna L 2012 *Monthly Notices of the Royal Astronomical Society* **428** 71–85 ISSN 0035-8711 URL http://mnras.oxfordjournals.org/content/428/1/71

[87] Dionysopoulou K, Alic D and Rezzolla L 2015 *Physical Review D* **92** 084064 ISSN 1550-7998 (*Preprint* 1502.02021) URL http://arxiv.org/abs/1502.02021http://link.aps.org/doi/10.1103/PhysRevD.92.084064

[88] Andersson N, Dionysopoulou K, Hawke I and Comer G L 2016 (*Preprint* 1610.00449) URL http://arxiv.org/abs/1610.00449

[89] Kiuchi K, Cerdá-Durán P, Kyutoku K, Sekiguchi Y and Shibata M 2015 *Physical Review D* **92** 124034 ISSN 1550-7998 (*Preprint* 1509.09205) URL http://arxiv.org/abs/1509.09205http://link.aps.org/doi/10.1103/PhysRevD.92.124034

[90] Hinder et al I 2013 *Classical and Quantum Gravity* **31** 025012 ISSN 0264-9381 URL http://stacks.iop.org/0264-9381/31/i=2/a=025012

[91] Hotokezaka K, Kyutoku K, Sekiguchi Y i and Shibata M 2016 18 (*Preprint* 1603.01286) URL http://arxiv.org/abs/1603.01286

[92] Suh I, Mathews G J, Haywood J R and Lan N Q 2016 (*Preprint* 1601.01460) URL http://arxiv.org/abs/1601.01460

[93] Tsokaros A, Mundim B C, Galeazzi F, Rezzolla L and Uryū K 2016 *Physical Review D* **94** 044049 ISSN 2470-0010 (*Preprint* 1605.07205) URL http://arxiv.org/abs/1605.07205http://link.aps.org/doi/10.1103/PhysRevD.94.044049

[94] Maione F, Pietri R D, Feo A and Löffler F 2016 *Classical and Quantum Gravity* **33** 175009 ISSN 0264-9381 (*Preprint* 1605.03424) URL http://arxiv.org/abs/1605.03424http://dx.doi.org/10.1088/0264-9381/33/17/175009http://stacks.iop.org/0264-9381/33/i=17/a=175009?key=crossref.2efccecfc7de5de9c8d605df9a8478b7

[95] Kyutoku K, Shibata M and Taniguchi K 2014 *Physical Review D* **90** 064006 ISSN 1550-7998 URL http://link.aps.org/doi/10.1103/PhysRevD.90.064006

[96] Radice D, Rezzolla L and Galeazzi F 2014 *Monthly Notices of the Royal Astronomical Society: Letters* **437** L46–L50 ISSN 1745-3925 URL http://mnrasl.oxfordjournals.org/content/437/1/L46.shorthttp://mnrasl.oxfordjournals.org/cgi/doi/10.1093/mnrasl/slt137

[97] Hotokezaka K, Kyutoku K, Okawa H and Shibata M 2015 *Physical Review D* **87** 044001 ISSN 1550-7998 (*Preprint* 1502.03457) URL http://arxiv.org/abs/1502.03457http://dx.doi.org/10.1103/PhysRevD.91.064060

[98] Bernuzzi S and Dietrich T 2016 *Physical Review D* **94** 064062 ISSN 2470-0010 (*Preprint* 1604.07999) URL http://arxiv.org/abs/1604.07999http://link.aps.org/doi/10.1103/PhysRevD.94.064062

[99] Feo A, De Pietri R, Maione F and Löffler F 2016 (*Preprint* 1608.02810) URL http://arxiv.org/abs/1608.02810

[100] Lattimer J M and Prakash M 2004 *Science (New York, N.Y.)* **304** 536–42 ISSN 1095-9203 URL http://www.ncbi.nlm.nih.gov/pubmed/15105490

[101] Lackey B D, Nayyar M and Owen B J 2006 *Physical Review D* **73** 024021 ISSN 1550-7998 URL http://journals.aps.org/prd/abstract/10.1103/PhysRevD.73.024021

[102] Weissenborn S, Sagert I, Pagliara G, Hempel M and Schaffner-Bielich J 2011 *The Astrophysical Journal* **740** L14 ISSN 2041-8205 URL http://stacks.iop.org/2041-8205/740/i=1/a=L14?key=crossref.07c8c70150875fd2585ecdc3597b5374

[103] Oppenheimer J R and Volkoff G M 1939 *Physical Review* **55** 374–381 ISSN 0031-899X URL http://link.aps.org/doi/10.1103/PhysRev.55.374

[104] Tolman R C 1939 *Physical Review* **55** 364–373 ISSN 0031-899X URL http://link.aps.org/doi/10.1103/PhysRev.55.364

[105] Harrison B K, Thorne K S, Wakano M and Wheeler J A 1965 *Gravitation Theory and Gravitational Collapse, Chicago: University of Chicago Press, 1965*

[106] Burrows A and Lattimer J M 1986 *The Astrophysical Journal* **307** 178 ISSN 0004-637X URL http://adsabs.harvard.edu/doi/10.1086/164405

[107] Bethe H A and Wilson J R 1985 *The Astrophysical Journal* **295** 14 ISSN 0004-637X URL http://adsabs.harvard.edu/doi/10.1086/163343

[108] Ott C D, Abdikamalov E, Mösta P, Haas R, Drasco S, O'Connor E P, Reisswig C, Meakin C A and Schnetter E 2013 *The Astrophysical Journal* **768** 115 ISSN 0004-637X URL http://stacks.iop.org/0004-637X/768/i=2/a=115?key=crossref.3f02e11f85f457ab221aa94475a8a9f7

[109] Hanke F, Müller B, Wongwathanarat A, Marek A and Janka H T 2013 *The Astrophysical Journal* **770** 66 ISSN 0004-637X URL http://stacks.iop.org/0004-637X/770/i=1/a=66?key=crossref.67519a09268b611679c1e27dd77fcdab

[110] Mösta P, Richers S, Ott C D, Haas R, Piro A L, Boydstun K, Abdikamalov E, Reisswig C and Schnetter E 2014 *The Astrophysical Journal* **785** L29 ISSN 2041-8205 URL http://stacks.iop.org/2041-8205/785/i=2/a=L29?key=crossref.e3b14dfcbaec6843a01df483fa3551e1

[111] Mösta P, Ott C D, Radice D, Roberts L F, Schnetter E and Haas R 2015 *Nature* **advance on** ISSN 1476-4687 URL http://dx.doi.org/10.1038/nature15755

[112] Ott C D 2009 *Classical and Quantum Gravity* **26** 063001 ISSN 0264-9381 URL http://stacks.iop.org/0264-9381/26/i=6/a=063001?key=crossref.835129b71ce9a2c8bc8a352976c91109

[113] Ferrari V, Miniutti G and Pons J A 2003 *Monthly Notices of the Royal Astronomical Society* **342** 629–638 ISSN 0035-8711 URL http://mnras.oxfordjournals.org/cgi/doi/10.1046/j.1365-8711.2003.06580.x

[114] Burgio G F, Ferrari V, Gualtieri L and Schulze H J 2011 *Physical Review D* **84** 044017 ISSN 1550-7998 URL http://link.aps.org/doi/10.1103/PhysRevD.84.044017

[115] Fuller J, Klion H, Abdikamalov E and Ott C D 2015 *Monthly Notices of the Royal Astronomical Society* **450** 414–427 ISSN 0035-8711 URL http://mnras.oxfordjournals.org/cgi/doi/10.1093/mnras/stv698

[116] Pons J A, Reddy S, Prakash M, Lattimer J M and Miralles J A 1999 *The Astrophysical Journal* **513** 780–804 ISSN 0004-637X URL http://stacks.iop.org/0004-637X/513/i=2/a=780

[117] Camelio G, Gualtieri L, Pons J A and Ferrari V 2016 (*Preprint* 1601.02945) URL http://arxiv.org/abs/1601.02945http://dx.doi.org/10.1103/PhysRevD.94.024008

[118] Lorimer D R 2008 *Living Reviews in Relativity* **11** ISSN 1433-8351 URL http://www.livingreviews.org/lrr-2008-8

[119] Manchester R N, Hobbs G B, Teoh A and Hobbs M 2005 *The Astronomical Journal* **129** 1993–2006 ISSN 0004-6256 URL http://stacks.iop.org/1538-3881/129/i=4/a=1993

[120] et al Abdo A A 2013 *The Astrophysical Journal Supplement Series* **208** 17 ISSN 0067-0049 URL http://stacks.iop.org/0067-0049/208/i=2/a=17?key=crossref.c77d6b226f72328869f9f023cd2ff175

[121] Caraveo P A 2013 (*Preprint* 1312.2913) URL http://arxiv.org/abs/1312.2913http://dx.doi.org/10.1146/annurev-astro-081913-035948

[122] HEWISH A, BELL S J, PILKINGTON J D H, SCOTT P F and COLLINS R A 1968 *Nature* **217** 709–713 ISSN 0028-0836 URL http://www.nature.com/doifinder/10.1038/217709a0

[123] et al Özel F 2012 *The Astrophysical Journal* **757** 55 ISSN 0004-637X URL http://stacks.iop.org/0004-637X/757/i=1/a=55?key=crossref.2420cce00f9c869a1766fef3647a11c2

[124] Shapiro I I 1964 *Physical Review Letters* **13** 789–791 ISSN 0031-9007 URL http://link.aps.org/doi/10.1103/PhysRevLett.13.789

[125] Demorest P B, Pennucci T, Ransom S M, Roberts M S E and Hessels J W T 2010 *Nature* **467** 1081–1083 ISSN 0028-0836 URL http://www.nature.com/doifinder/10.1038/nature09466

[126] Heinke C O 2013 *Journal of Physics: Conference Series* **432** 012001 ISSN 1742-6588 URL http://stacks.iop.org/1742-6596/432/i=1/a=012001?key=crossref.719ff722bc4d2409ddfab6531dc6d0bc

[127] Özel F 2013 *Reports on Progress in Physics* **76** 016901 ISSN 0034-4885 URL http://stacks.iop.org/0034-4885/76/i=1/a=016901?key=crossref.5e0bbaec23532a4511e6917c3fa21199

[128] Pechenick K R, Ftaclas C and Cohen J M 1983 *The Astrophysical Journal* **274** 846 ISSN 0004-637X URL http://adsabs.harvard.edu/doi/10.1086/161498

[129] Brown E F, Bildsten L and Rutledge R E 1998 *The Astrophysical Journal* **504** L95–L98 ISSN 0004637X URL http://stacks.iop.org/1538-4357/504/i=2/a=L95

[130] Lewin W H G, Van Paradijs J and Taam R E 1993 *Space Science Reviews* **62** 223–389 ISSN 0038-6308 URL http://link.springer.com/10.1007/BF00196124

[131] Page D 1995 *The Astrophysical Journal* **442** 273 ISSN 0004-637X (*Preprint* 9407015) URL http://arxiv.org/abs/astro-ph/9407015http://dx.doi.org/10.1086/175439http://adsabs.harvard.edu/doi/10.1086/175439

[132] DeDeo S, Psaltis D and Narayan R 2001 *The Astrophysical Journal* **559** 346–352 ISSN 0004-637X URL http://stacks.iop.org/0004-637X/559/i=1/a=346

[133] Guillot S, Servillat M, Webb N A and Rutledge R E 2013 *The Astrophysical Journal* **772** 7 ISSN 0004-637X URL http://stacks.iop.org/0004-637X/772/i=1/a=7?key=crossref.652c69003ba407fafcfc19f1e37c57fd

[134] Lattimer J M and Steiner A W 2014 *The Astrophysical Journal* **784** 123 ISSN 0004-637X URL http://stacks.iop.org/0004-637X/784/i=2/a=123?key=crossref.cc02474952cd7f55e76e75faf4e96d87

[135] Barret D, Nandra K, Barcons X, Fabian A, den Herder J W, Piro L, Watson M, Aird J, Branduardi-Raymont G, Cappi M, Carrera F, Comastri A, Costantini E, Croston J, Decourchelle A, Done C, Dovciak M, Ettori S, Finoguenov A, Georgakakis A, Jonker P, Kaastra J, Matt G, Motch C, O'Brien P, Pareschi G, Pointecouteau E, Pratt G, Rauw G, Reiprich T, Sanders J, Sciortino S, Willingale R and Wilms J 2013 (*Preprint* 1310.3814) URL http://arxiv.org/abs/1310.3814

[136] Gendreau K C, Arzoumanian Z and Okajima T 2012 The Neutron star Interior Composition ExploreR (NICER): an Explorer mission of opportunity for soft x-ray timing spectroscopy ed Takahashi T, Murray S S and den Herder J W A (International Society for Optics and Photonics) p 844313 URL http://proceedings.spiedigitallibrary.org/proceeding.aspx?doi=10.1117/12.926396

[137] et al Feroci M 2012 *Experimental Astronomy* **34** 415–444 ISSN 0922-6435 URL http://link.springer.com/10.1007/s10686-011-9237-2

[138] Dey M, Bombaci I, Dey J, Ray S and Samanta B 1998 *Physics Letters B* **438** 123–128 ISSN 03702693 URL http://linkinghub.elsevier.com/retrieve/pii/S0370269398009356

[139] Lugones G and Horvath J E 2003 *Astronomy and Astrophysics* **403** 173–178 ISSN 0004-6361 URL http://www.edpsciences.org/10.1051/0004-6361:20030374

[140] Douchin F and Haensel P 2000 Inner edge of neutron-star crust with SLy effective nucleon-nucleon interactions

[141] Douchin F and Haensel P 2001 *Astronomy and Astrophysics* **380** 151–167 ISSN 0004-6361 URL http://dx.doi.org/10.1051/0004-6361:20011402

[142] Akmal A, Pandharipande V R and Ravenhall D G 1998 *Physical Review C* **58** 1804–1828 ISSN 0556-2813 URL http://journals.aps.org/prc/abstract/10.1103/PhysRevC.58.1804

[143] Müller H and Serot B D 1996 *Nuclear Physics A* **606** 508–537 ISSN 03759474 URL http://linkinghub.elsevier.com/retrieve/pii/037594749600187X

[144] Read J S, Lackey B D, Owen B J and Friedman J L 2009 *Physical Review D* **79** 124032 ISSN 1550-7998 URL http://link.aps.org/doi/10.1103/PhysRevD.79.124032

[145] Moore B, Favata M, Arun K G and Mishra C K 2016 49 (*Preprint* 1605.00304) URL http://arxiv.org/abs/1605.00304

[146] Keith M J, Kramer M, Lyne A G, Eatough R P, Stairs I H, Possenti A, Camilo F and Manchester R N 2009 *Monthly Notices of the Royal Astronomical Society* **393** 623–627 ISSN 00358711 URL http://mnras.oxfordjournals.org/cgi/doi/10.1111/j.1365-2966.2008.14234.x

[147] et al Faulkner A J 2005 *The Astrophysical Journal* **618** L119–L122 ISSN 0004-637X URL http://stacks.iop.org/1538-4357/618/i=2/a=L119

[148] Corongiu A, Kramer M, Stappers B W, Lyne A G, Jessner A, Possenti A, D'Amico N and Löhmer O 2007 *Astronomy and Astrophysics* **462** 703–709 ISSN 0004-6361 URL http://www.aanda.org/10.1051/0004-6361:20054385

[149] et al Lynch R S 2012 *The Astrophysical Journal* **745** 109 ISSN 0004-637X URL http://stacks.iop.org/0004-637X/745/i=2/a=109?key=crossref.e6dcab450cc6ec7b225bfc3be749ccfc

[150] Kramer M, Stairs I H, Manchester R N, McLaughlin M A, Lyne A G, Ferdman R D, Burgay M, Lorimer D R, Possenti A, D'Amico N, Sarkissian J M, Hobbs G B, Reynolds J E, Freire P C C and Camilo F 2006 *Science (New York, N.Y.)* **314** 97–102 ISSN 1095-9203 URL http://www.ncbi.nlm.nih.gov/pubmed/16973838

[151] Champion D J, Lorimer D R, McLaughlin M A, Cordes J M, Arzoumanian Z, Weisberg J M and Taylor J H 2004 *Monthly Notices of the Royal Astronomical Society* **350** L61–L65 ISSN 00358711 URL http://mnras.oxfordjournals.org/cgi/doi/10.1111/j.1365-2966.2004.07862.x

[152] et al Swiggum J K 2015 *The Astrophysical Journal* **805** 156 ISSN 1538-4357 URL http://stacks.iop.org/0004-637X/805/i=2/a=156?key=crossref.e253b061a2e7e20d0485e92556d26761

[153] et al Lorimer D R 2006 *The Astrophysical Journal* **640** 428–434 ISSN 0004-637X URL http://stacks.iop.org/0004-637X/640/i=1/a=428

[154] Wolszczan A 1991 *Nature* **350** 688–690 ISSN 0028-0836 URL http://www.nature.com/doifinder/10.1038/350688a0

[155] Anderson S B, Gorham P W, Kulkarni S R, Prince T A and Wolszczan A 1990 *Nature* **346** 42–44 ISSN 0028-0836 URL http://www.nature.com/doifinder/10.1038/346042a0

[156] Janssen G H, Stappers B W, Kramer M, Nice D J, Jessner A, Cognard I and Purver M B 2008 *Astronomy and Astrophysics* **490** 753–761 ISSN 0004-6361 URL http://www.aanda.org/10.1051/0004-6361:200810076

[157] Dewi J D M and Pols O R 2003 *Monthly Notices of the Royal Astronomical Society* **344** 629–643 ISSN 0035-8711 URL http://mnras.oxfordjournals.org/cgi/doi/10.1046/j.1365-8711.2003.06844.x

[158] van den Heuvel E P J 2007 (*Preprint* 0704.1215) URL http://arxiv.org/abs/0704.1215http://dx.doi.org/10.1063/1.2774916

[159] Beniamini P and Piran T 2016 *Monthly Notices of the Royal Astronomical Society* **456** 4089–4099 ISSN 0035-8711 URL http://mnras.oxfordjournals.org/lookup/doi/10.1093/mnras/stv2903

[160] Einstein A 1916 *Sitzungsber.Preuss.Akad.Wiss.Berlin (Math.Phys.)* **1916** 688–696

[161] et al Weisberg J M 2010 *The Astrophysical Journal* **722** 1030–1034 ISSN 0004-637X URL http://stacks.iop.org/0004-637X/722/i=2/a=1030?key=crossref.15104fd80ff1bc5009a11a53e5bcb142

[162] Boyle M, Brown D A, Kidder L E, Mroué A H, Pfeiffer H P, Scheel M A, Cook G B and Teukolsky S A 2007 *Physical Review D* **76** 124038 ISSN 1550-7998 URL http://link.aps.org/doi/10.1103/PhysRevD.76.124038

[163] Maggiore M 2008 Gravitational waves. Vol 1, Theory and Experiments

[164] Blanchet L 2014 *Living Reviews in Relativity* **17** ISSN 1433-8351 URL http://www.livingreviews.org/lrr-2014-2

[165] Pan Y, Buonanno A, Buchman L T, Chu T, Kidder L E, Pfeiffer H P and Scheel M A 2010 *Physical Review D* **81** 084041 ISSN 1550-7998 URL http://link.aps.org/doi/10.1103/PhysRevD.81.084041

[166] Steinhoff J, Hinderer T, Buonanno A and Taracchini A 2016 (*Preprint* 1608.01907) URL http://arxiv.org/abs/1608.01907

[167] The LIGO Scientific Collaboration and the Virgo Collaboration 2016 (*Preprint* 1606.04855) URL http://arxiv.org/abs/1606.04855http://dx.doi.org/10.1103/PhysRevLett.116.241103

[168] ANDERSSON N and KOKKOTAS K D 2001 *International Journal of Modern Physics D* **10** 381–441 ISSN 0218-2718 URL http://www.worldscientific.com/doi/abs/10.1142/S0218271801001062

[169] Andersson N 2003 *Classical and Quantum Gravity* **20** R105–R144 ISSN 0264-9381 URL http://stacks.iop.org/0264-9381/20/i=7/a=201?key=crossref.c949ee3aea1281c00094873424e8c219

[170] Ou S, Tohline J E and Lindblom L 2004 *The Astrophysical Journal* **617** 490–499 ISSN 0004-637X URL http://stacks.iop.org/0004-637X/617/i=1/a=490

[171] Shibata M, Baumgarte T W and Shapiro S L 2000 *The Astrophysical Journal* **542** 453–463 ISSN 0004-637X URL http://stacks.iop.org/0004-637X/542/i=1/a=453

[172] Watts A L, Andersson N and Jones D I 2005 *The Astrophysical Journal* **618** L37–L40 ISSN 0004-637X URL http://stacks.iop.org/1538-4357/618/i=1/a=L37

[173] Baiotti L, Pietri R D, Manca G M and Rezzolla L 2007 *Physical Review D* **75** 044023 ISSN 1550-7998 URL http://link.aps.org/doi/10.1103/PhysRevD.75.044023

[174] Corvino G, Rezzolla L, Bernuzzi S, De Pietri R and Giacomazzo B 2010 *Classical and Quantum Gravity* **27** 114104 ISSN 0264-9381 URL http://stacks.iop.org/0264-9381/27/i=11/a=114104?key=crossref.e48e4851fc51b124c9e9d695be0fcada

[175] Löffler F, De Pietri R, Feo A, Maione F and Franci L 2015 *Physical Review D* **91**

[176] Kotake K, Iwakami-Nakano W and Ohnishi N 2011 *The Astrophysical Journal* **736** 124 ISSN 0004-637X URL http://stacks.iop.org/0004-637X/736/i=2/a=124?key=crossref.d6f557ab90bd4afe8c17d25399a7fe19

[177] Andresen H, Mueller B, Mueller E and Janka H T 2016 (*Preprint* 1607.05199) URL http://arxiv.org/abs/1607.05199

[178] Shibata M and Sekiguchi Y i 2005 *Physical Review D* **71** 024014 ISSN 1550-7998 URL http://link.aps.org/doi/10.1103/PhysRevD.71.024014

[179] Reisswig C, Haas R, Ott C, Abdikamalov E, Mösta P, Pollney D and Schnetter E 2013 *Physical Review D* **87** 064023 ISSN 1550-7998 URL http://link.aps.org/doi/10.1103/PhysRevD.87.064023

[180] Cowperthwaite et al P S 2016 *The Astrophysical Journal* **826** L29 ISSN 2041-8213 (*Preprint* 1606.04538) URL http://arxiv.org/abs/1606.04538http://stacks.iop.org/2041-8205/826/i=2/a=L29?key=crossref.b1421e0dd349cd03be6011f729ee1e56

[181] Racusin et al J L 2016 (*Preprint* 1606.04901) URL http://arxiv.org/abs/1606.04901

[182] Patricelli B, Razzano M, Cella G, Fidecaro F, Pian E, Branchesi M and Stamerra A 2016 (*Preprint* 1606.06124) URL http://arxiv.org/abs/1606.06124

[183] Evans P A, Kennea J A, Palmer D M, Bilicki M, Osborne J P, O'Brien P T, Tanvir N R, Lien A Y, Barthelmy S D, Burrows D N, Campana S, Cenko S B, D'Elia V, Gehrels N, Marshall F E, Page K L, Perri M, Sbarufatti B, Siegel M H, Tagliaferri G and Troja E 2016 *Monthly Notices of the Royal Astronomical Society* **462** 1591–1602 ISSN 0035-8711 (*Preprint* 1606.05001) URL http://arxiv.org/abs/1606.05001http://mnras.oxfordjournals.org/lookup/doi/10.1093/mnras/stw1746

[184] Rosswog S 2015 43 (*Preprint* 1501.02081) URL http://arxiv.org/abs/1501.02081

[185] Just O, Obergaulinger M, Janka H T, Bauswein A and Schwarz N 2016 *The Astrophysical Journal* **816** L30 ISSN 2041-8213 (*Preprint* 1510.04288) URL http://arxiv.org/abs/1510.04288http://dx.doi.org/10.3847/2041-8205/816/2/L30http://stacks.iop.org/2041-8205/816/i=2/a=L30?key=crossref.636340c9e0376183e87b696161b4a6fa

[186] Lü H J, Zhang B, Lei W H, Li Y and Lasky P D 2015 *The Astrophysical Journal* **805** 89 ISSN 1538-4357 (*Preprint* 1501.02589) URL http://arxiv.org/abs/1501.02589http://stacks.iop.org/0004-637X/805/i=2/a=89?key=crossref.b7f8bdf850ab30b543e946129c58d929

[187] Blandford R D and Znajek R L 1977 *Monthly Notices of the Royal Astronomical Society* **179** 433–456 ISSN 0035-8711 URL http://mnras.oxfordjournals.org/cgi/doi/10.1093/mnras/179.3.433

[188] Balbus S and Hawley J 1991 *The Astrophysical Journal* URL http://scholar.google.com/scholar?hl=en{&}btnG=Search{&}q=intitle:No+Title{#}0

[189] Siegel D M, Ciolfi R, Harte A I and Rezzolla L 2013 *Physical Review D* **87** 121302 ISSN 1550-7998 (*Preprint* 1302.4368) URL http://arxiv.org/abs/1302.4368v3http://arxiv.org/abs/1302.4368http://dx.doi.org/10.1103/PhysRevD.87.121302http://link.aps.org/doi/10.1103/PhysRevD.87.121302

[190] Giacomazzo B, Zrake J, Duffell P C, MacFadyen A I and Perna R 2015 *The Astrophysical Journal* **809** 39 ISSN 1538-4357 (*Preprint* 1410.0013v1) URL http://arxiv.org/abs/1410.0013http://stacks.iop.org/0004-637X/809/i=1/a=39?key=crossref.f776b49146496dd9b89ccec0fa7b6e3b

[191] Arcones A and Thielemann F K 2013 *Journal of Physics G: Nuclear and Particle Physics* **40** 013201 ISSN 0954-3899 URL http://stacks.iop.org/0954-3899/40/i=1/a=013201?key=crossref.72412437c70b0c54caf0da5dbd94da36

[192] Just O, Bauswein A, Pulpillo R A, Goriely S and Janka H T 2015 *Monthly Notices of the Royal Astronomical Society* **448** 541–567 ISSN 0035-8711 URL http://mnras.oxfordjournals.org/cgi/doi/10.1093/mnras/stv009

[193] Korobkin O, Rosswog S, Arcones A and Winteler C 2012 *Monthly Notices of the Royal Astronomical Society* **426** 1940–1949 ISSN 00358711 URL http://mnras.oxfordjournals.org/cgi/doi/10.1111/j.1365-2966.2012.21859.x

[194] Franci L, De Pietri R, Dionysopoulou K and Rezzolla L 2013 *Physical Review D* **88** 104028 ISSN 1550-7998 URL http://link.aps.org/doi/10.1103/PhysRevD.88.104028

[195] Tanaka M 2016 *Advances in Astronomy* **2016** 1–12 ISSN 1687-7969 (*Preprint* 1605.07235) URL http://arxiv.org/abs/1605.07235http://www.hindawi.com/journals/aa/2016/6341974/

[196] Barnes J, Kasen D, Wu M R and Mart'inez-Pinedo G 2016 (*Preprint* 1605.07218) URL http://arxiv.org/abs/1605.07218

[197] Yang B, Jin Z P, Li X, Covino S, Zheng X Z, Hotokezaka K, Fan Y Z, Piran T and Wei D M 2015 8 (*Preprint* 1503.07761) URL http://arxiv.org/abs/1503.07761

[198] Runge C 1895 *Mathematische Annalen* **46** 167–178 ISSN 0025-5831 URL http://link.springer.com/10.1007/BF01446807

[199] Kutta W 1901 *Z. Math. Phys.* **46** 435–453

[200] Berger M J and Oliger J 1984 *Journal of Computational Physics* **53** 484–512 ISSN 00219991 URL http://www.sciencedirect.com/science/article/pii/0021999184900731

[201] Schnetter E, Hawley S H and Hawke I 2004 *Classical and Quantum Gravity* **21** 1465–1488 ISSN 0264-9381 URL http://stacks.iop.org/0264-9381/21/i=6/a=014?key=crossref.1c18ebd8d33db93ef2caf552a51407de

[202] Mongwane B 2015 *General Relativity and Gravitation* **47** 60 ISSN 0001-7701 (*Preprint* 1504.07609) URL http://arxiv.org/abs/1504.07609http://link.springer.com/10.1007/s10714-015-1903-7

[203] Arnowitt R, Deser S and Misner C W 2008 *General Relativity and Gravitation* **40** 1997–2027 ISSN 0001-7701 URL http://link.springer.com/10.1007/s10714-008-0661-1

[204] Nakamura T, Oohara K and Kojima Y 1987 *Progress of Theoretical Physics Supplement* **90** 1–218 ISSN 0375-9687 URL http://ptps.oxfordjournals.org/cgi/doi/10.1143/PTPS.90.1

[205] Shibata M and Nakamura T 1995 *Physical Review D*

[206] Baumgarte T and Shapiro S 1998 *Physical Review D* **59** 1–7 URL http://journals.aps.org/prd/abstract/10.1103/PhysRevD.59.024007

[207] Sarbach O, Calabrese G, Pullin J and Tiglio M 2002 *Physical Review D* **66** 064002 ISSN 0556-2821 URL http://link.aps.org/doi/10.1103/PhysRevD.66.064002

[208] Nagy G, Ortiz O E and Reula O A 2004 *Physical Review D* **70** 044012 ISSN 1550-7998 URL http://link.aps.org/doi/10.1103/PhysRevD.70.044012

[209] Bona C, Masso J and Stela J 1995 *Physical Review Letters*

[210] Alcubierre M, Brügmann B, Diener P, Koppitz M, Pollney D, Seidel E and Takahashi R 2003 *Physical Review D* **67** 084023 ISSN 0556-2821 URL http://link.aps.org/doi/10.1103/PhysRevD.67.084023

[211] Schnetter E 2010 *Classical and Quantum Gravity* **27** 167001 ISSN 0264-9381 URL http://stacks.iop.org/0264-9381/27/i=16/a=167001?key=crossref.1c378177f8dc06868dec59c41c07fb54

[212] Brown D, Diener P, Sarbach O, Schnetter E and Tiglio M 2009 *Physical Review D* **79** 044023 ISSN 1550-7998 URL http://link.aps.org/doi/10.1103/PhysRevD.79.044023

[213] Husa S, Hinder I and Lechner C 2006 *Computer Physics Communications* **174** 983–1004 ISSN 00104655 URL http://linkinghub.elsevier.com/retrieve/pii/S0010465506001020

[214] Gustafsson B, Kreiss H O and Oliger J 2013 *Time-Dependent Problems and Difference Methods* (Hoboken, NJ, USA: John Wiley & Sons, Inc.) ISBN 9781118548448 URL http://doi.wiley.com/10.1002/9781118548448

[215] Alcubierre M, Brügmann B, Dramlitsch T, Font J A, Papadopoulos P, Seidel E, Stergioulas N and Takahashi R 2000 *Physical Review D* **62** 044034 ISSN 0556-2821 URL http://link.aps.org/doi/10.1103/PhysRevD.62.044034

[216] Bona C, Ledvinka T, Palenzuela C and Žáček M 2003 *Physical Review D* **67** 104005 ISSN 0556-2821 URL http://link.aps.org/doi/10.1103/PhysRevD.67.104005

[217] Bona C and Palenzuela C 2004 *Physical Review D* **69** 104003 ISSN 1550-7998 URL http://link.aps.org/doi/10.1103/PhysRevD.69.104003

[218] Gundlach C, Calabrese G, Hinder I and Martín-García J M 2005 *Classical and Quantum Gravity* **22** 3767–3773 ISSN 0264-9381 URL http://stacks.iop.org/0264-9381/22/i=17/a=025?key=crossref.9cf07f21b6e1f51dc245073a74e4d736

[219] Bernuzzi S and Hilditch D 2010 *Physical Review D* **81** 084003 ISSN 1550-7998 URL http://link.aps.org/doi/10.1103/PhysRevD.81.084003

[220] Alic D, Bona-Casas C, Bona C, Rezzolla L and Palenzuela C 2012 *Physical Review D* **85** 064040 ISSN 1550-7998 URL http://link.aps.org/doi/10.1103/PhysRevD.85.064040

[221] Bona C, Bona-Casas C and Palenzuela C 2010 *Physical Review D* **82** 124010 ISSN 1550-7998 URL http://link.aps.org/doi/10.1103/PhysRevD.82.124010

[222] Alic D, Kastaun W and Rezzolla L 2013 *Physical Review D - Particles, Fields, Gravitation and Cosmology* **88** 1–15 ISSN 15507998 (*Preprint* arXiv:1307.7391v2)

[223] Hilditch D, Bernuzzi S, Thierfelder M, Cao Z, Tichy W and Brügmann B 2013 *Physical Review D* **88** 084057 ISSN 1550-7998 (*Preprint* arXiv:1212.2901v1) URL http://link.aps.org/doi/10.1103/PhysRevD.88.084057

[224] Ruiz M, Hilditch D and Bernuzzi S 2011 *Physical Review D* **83** 024025 ISSN 1550-7998 URL http://link.aps.org/doi/10.1103/PhysRevD.83.024025

[225] Mösta P, Mundim B C, Faber J a, Haas R, Noble S C, Bode T, Löffler F, Ott C D, Reisswig C and Schnetter E 2014 *Classical and Quantum Gravity* **31** 015005 ISSN 0264-9381 URL http://stacks.iop.org/0264-9381/31/i=1/a=015005?key=crossref.012018eea65fb29bf551cf95fd0a0522

[226] Martí J M, Ibáñez J M and Miralles J A 1991 *Physical Review D* **43** 3794–3801 ISSN 0556-2821 URL http://link.aps.org/doi/10.1103/PhysRevD.43.3794

[227] Font J A, Ibanez J M, Marquina A and Marti J M 1994 *Astronomy and Astrophysics (ISSN 0004-6361), vol. 282, no. 1, p. 304-314* **282** 304–314

[228] Banyuls F, Font J A, Ibanez J M, Marti J M and Miralles J A 1997 *The Astrophysical Journal* **476** 221–231 ISSN 0004-637X URL http://stacks.iop.org/0004-637X/476/i=1/a=221

[229] Martí J M and Müller E 2003 *Living Reviews in Relativity* **6** ISSN 1433-8351 URL http://www.livingreviews.org/lrr-2003-7

[230] Lax P and Wendroff B 1960 *Communications on Pure and Applied Mathematics* **13** 217–237 ISSN 00103640 URL http://doi.wiley.com/10.1002/cpa.3160130205

[231] Godunov S 1959 *Matematicheskii Sbornik* URL http://www.mathnet.ru/eng/sm4873

[232] Etienne Z B, Liu Y T and Shapiro S L 2010 *Physical Review D* **82** 084031 ISSN 1550-7998 URL http://link.aps.org/doi/10.1103/PhysRevD.82.084031

[233] Radice D and Rezzolla L 2012 *Astronomy & Astrophysics* **547** A26 ISSN 0004-6361 URL http://www.aanda.org/10.1051/0004-6361/201219735

[234] Colella P and Woodward P R 1984 *Journal of Computational Physics* **54** 174–201 ISSN 00219991 URL http://linkinghub.elsevier.com/retrieve/pii/0021999184901438

[235] Suresh a and Huynh H 1997 *Journal of Computational Physics* **136** 83–99 ISSN 00219991 URL http://linkinghub.elsevier.com/retrieve/pii/S0021999197957454

[236] Liu X D, Osher S and Chan T 1994 *Journal of Computational Physics* **115** 200–212 ISSN 00219991 URL http://linkinghub.elsevier.com/retrieve/pii/S0021999184711879

[237] Jiang G S and Shu C W 1996 *Journal of Computational Physics* **126** 202–228 ISSN 00219991 URL http://linkinghub.elsevier.com/retrieve/pii/S0021999196901308

[238] Muhlberger C D, Nouri F H, Duez M D, Foucart F, Kidder L E, Ott C D, Scheel M a, Szilágyi B and Teukolsky S a 2014 *Physical Review D* **90** 104014 ISSN 1550-7998 (*Preprint* 1405.2144) URL http://arxiv.org/abs/1405.2144v1http://arxiv.org/abs/1405.2144http://link.aps.org/doi/10.1103/PhysRevD.90.104014

[239] Baiotti L, Hawke I, Montero P J and Rezzolla L 2010 *arXiv preprint arXiv:1004.3849* **1** 210–219 (*Preprint* 1004.3849) URL http://arxiv.org/abs/1004.3849

[240] Yamamoto T, Shibata M and Taniguchi K 2008 *Physical Review D* **78** 064054 ISSN 1550-7998 URL http://link.aps.org/doi/10.1103/PhysRevD.78.064054

[241] Harten A, Engquist B, Osher S and Chakravarthy S R 1987 Uniformly High Order Accurate Essentially Non-oscillatory Schemes, III *Upwind and High-Resolution Schemes* (Berlin, Heidelberg: Springer Berlin Heidelberg) pp 218–290 URL http://link.springer.com/10.1007/978-3-642-60543-7{_}12

[242] Tchekhovskoy a, McKinney J C and Narayan R 2007 *Monthly Notices of the Royal Astronomical Society* **379** 469–497 ISSN 0035-8711 URL http://mnras.oxfordjournals.org/cgi/doi/10.1111/j.1365-2966.2007.11876.x

[243] Harten A, Lax P D and van Leer B 1983 *SIAM Review* **25** 35–61 ISSN 0036-1445 URL http://epubs.siam.org/doi/abs/10.1137/1025002

[244] Einfeldt B 1988 *SIAM Journal on Numerical Analysis* **25** 294–318 ISSN 0036-1429 URL http://epubs.siam.org/doi/abs/10.1137/0725021

[245] Takami K, Rezzolla L and Baiotti L 2015 *Physical Review D* **91** 064001 ISSN 1550-7998 URL http://link.aps.org/doi/10.1103/PhysRevD.91.064001

[246] Bonazzola S, Gourgoulhon E and Marck J A 1999 *Physical Review Letters* **82** 892–895 ISSN 0031-9007 URL http://link.aps.org/doi/10.1103/PhysRevLett.82.892

[247] Tsokaros A, Uryu K and Rezzolla L 2015 (*Preprint* 1502.05674) URL http://arxiv.org/abs/1502.05674

[248] Wilson J R and Mathews G J 1989 *International Workshop on Frontiers in Numerical Relativity, p. 306 - 314* 306–314

[249] Taniguchi K and Shibata M 2010 *The Astrophysical Journal Supplement Series* **188** 187–208 ISSN 0067-0049 URL http://stacks.iop.org/0067-0049/188/i=1/a=187

[250] Nagar A, Font J, Zanotti O and Pietri R 2005 *Physical Review D* **72** 024007 ISSN 1550-7998 URL http://link.aps.org/doi/10.1103/PhysRevD.72.024007

[251] Baiotti L, Bernuzzi S, Corvino G, De Pietri R and Nagar A 2009 *Physical Review D* **79** 024002 ISSN 1550-7998 URL http://link.aps.org/doi/10.1103/PhysRevD.79.024002

[252] Bishop N T and Rezzolla L 2016 (*Preprint* 1606.02532) URL http://arxiv.org/abs/1606.02532

[253] Campanelli M and Lousto C O 1999 *Physical Review D* **59** 124022 ISSN 0556-2821 URL http://link.aps.org/doi/10.1103/PhysRevD.59.124022

[254] Campanelli M, Kelly B and Lousto C O 2006 *Physical Review D* **73** 064005 ISSN 1550-7998 URL http://link.aps.org/doi/10.1103/PhysRevD.73.064005

[255] Boyle M and Mroué A H 2009 *Physical Review D* **80** 124045 ISSN 1550-7998 URL http://link.aps.org/doi/10.1103/PhysRevD.80.124045

[256] Zerilli F J 1970 *Physical Review Letters* **24** 737–738 ISSN 0031-9007 URL http://link.aps.org/doi/10.1103/PhysRevLett.24.737

[257] Moncrief V 1974 *Annals of Physics* **88** 323–342 ISSN 00034916 URL http://linkinghub.elsevier.com/retrieve/pii/0003491674901730

[258] Reisswig C and Pollney D 2011 *Classical and Quantum Gravity* **28** 195015 ISSN 0264-9381 URL http://stacks.iop.org/0264-9381/28/i=19/a=195015

[259] Berti E, Cardoso V, Gonzalez J A, Sperhake U, Hannam M, Husa S and Brügmann B 2007 *Physical Review D* **76** 064034 ISSN 1550-7998 (*Preprint* 0703053) URL http://arxiv.org/abs/gr-qc/0703053

[260] Bernuzzi S, Thierfelder M and Brügmann B 2012 *Physical Review D* **85** 104030 ISSN 1550-7998 URL http://link.aps.org/doi/10.1103/PhysRevD.85.104030

[261] Lousto C O, Nakano H, Zlochower Y and Campanelli M 2010 *Physical Review D* **82** 104057 ISSN 1550-7998 URL http://link.aps.org/doi/10.1103/PhysRevD.82.104057

[262] Nakano H, Healy J, Lousto C O and Zlochower Y 2015 *Physical Review D* **91** 104022 ISSN 1550-7998 (*Preprint* 1503.00718) URL http://arxiv.org/abs/1503.00718http://dx.doi.org/10.1103/PhysRevD.91.104022http://link.aps.org/doi/10.1103/PhysRevD.91.104022

[263] Bishop N T, Gómez R, Lehner L, Maharaj M and Winicour J 1997 *Physical Review D* **56** 6298–6309 ISSN 0556-2821 URL http://link.aps.org/doi/10.1103/PhysRevD.56.6298

[264] Babiuc M C, Szilágyi B, Winicour J and Zlochower Y 2011 *Physical Review D* **84** 044057 ISSN 1550-7998 URL http://link.aps.org/doi/10.1103/PhysRevD.84.044057

[265] Lousto C O and Zlochower Y 2013 *Physical Review D* **88** 024001 ISSN 1550-7998 URL http://link.aps.org/doi/10.1103/PhysRevD.88.024001

[266] Teukolsky S 1973 *Astrophysical Journal* **185** 635–647

[267] Nakano H 2015 7 (*Preprint* 1501.02890) URL http://arxiv.org/abs/1501.02890

[268] Berti E and Klein A 2014 *Physical Review D* **90** 064012 ISSN 1550-7998 URL http://link.aps.org/doi/10.1103/PhysRevD.90.064012

[269] Chu T, Fong H, Kumar P, Pfeiffer H P, Boyle M, Hemberger D A, Kidder L E, Scheel M A and Szilagyi B 2016 *Classical and Quantum Gravity* **33** 165001 ISSN 0264-9381 (*Preprint* 1512.06800) URL http://arxiv.org/abs/1512.06800http://dx.doi.org/10.1088/0264-9381/33/16/165001http://stacks.iop.org/0264-9381/33/i=16/a=165001?key=crossref.21ec2b47f6514802f3d0f934dc3527c2

[270] Damour T, Nagar A and Villain L 2012 *Physical Review D* **85** 123007 ISSN 1550-7998 URL http://journals.aps.org/prd/abstract/10.1103/PhysRevD.85.123007

[271] Zanotti O, Font J A, Rezzolla L and Montero P J 2005 *Monthly Notices of the Royal Astronomical Society* **356** 1371–1382 ISSN 00358711 URL http://mnras.oxfordjournals.org/content/356/4/1371.abstract

[272] Abramowicz M A and Fragile P C 2013 *Living Reviews in Relativity* **16** ISSN 1433-8351 URL http://relativity.livingreviews.org/Articles/lrr-2013-1/

[273] Daigne F and Font J A 2004 *Monthly Notices of the Royal Astronomical Society* **349** 841–868 ISSN 00358711 URL http://mnras.oxfordjournals.org/content/349/3/841.abstract

[274] Montero P J, Font J A and Shibata M 2010 *Physical Review Letters* **104** 191101 ISSN 0031-9007 URL http://link.aps.org/doi/10.1103/PhysRevLett.104.191101

[275] Mewes V, Galeazzi F, Font J A, Montero P J and Stergioulas N 2016 11 (*Preprint* 1605.02629) URL http://arxiv.org/abs/1605.02629

[276] Hirabayashi K and Hoshino M 2016 (*Preprint* 1603.04638) URL http://arxiv.org/abs/1603.04638

[277] Bauswein A and Stergioulas N 2015 *Physical Review D* **91** 124056 ISSN 1550-7998 (*Preprint* 1502.03176) URL http://arxiv.org/abs/1502.03176http://link.aps.org/doi/10.1103/PhysRevD.91.124056

[278] Tanay S, Haney M and Gopakumar A 2016 *Physical Review D* **93** 064031 ISSN 2470-0010 URL http://link.aps.org/doi/10.1103/PhysRevD.93.064031

[279] Loutrel N and Yunes N 2016 (*Preprint* 1607.05409) URL http://arxiv.org/abs/1607.05409

[280] Lindblom L, Owen B J and Brown D A 2008 *Physical Review D* **78** 124020 ISSN 1550-7998 URL http://journals.aps.org/prd/abstract/10.1103/PhysRevD.78.124020

[281] Boyle M, Buonanno A, Kidder L E, Mroué A H, Pan Y, Pfeiffer H P and Scheel M A 2008 *Physical Review D* **78** 104020 ISSN 1550-7998 (*Preprint* 0804.4184) URL http://arxiv.org/abs/0804.4184

[282] Suh I, Mathews G J, Haywood J R and Lan N Q 2016 URL https://inspirehep.net/record/1414186

[283] York J W 1999 *Physical Review Letters* **82** 1350–1353 ISSN 0031-9007 URL http://link.aps.org/doi/10.1103/PhysRevLett.82.1350

[284] Pfeiffer H P and York J W 2003 *Physical Review D* **67** 044022 ISSN 0556-2821 URL http://link.aps.org/doi/10.1103/PhysRevD.67.044022

[285] Rezzolla L and Takami K 2016 *Physical Review D* **93** 124051 ISSN 2470-0010 (*Preprint* 1604.00246) URL http://arxiv.org/abs/1604.00246http://link.aps.org/doi/10.1103/PhysRevD.93.124051

[286] Bauswein A, Stergioulas N and Janka H T 2016 *The European Physical Journal A* **52** 56 ISSN 1434-6001 (*Preprint* 1508.05493) URL http://arxiv.org/abs/1508.05493http://link.springer.com/10.1140/epja/i2016-16056-7

[287] Bauswein A and Janka H T 2012 *Physical Review Letters* **108** 011101 ISSN 0031-9007 URL http://link.aps.org/doi/10.1103/PhysRevLett.108.011101

[288] et al Punturo M 2010 *Classical and Quantum Gravity* **27** 194002 ISSN 0264-9381 URL http://stacks.iop.org/0264-9381/27/i=19/a=194002?key=crossref.bb1e57c8dd0d133fe6d9300567347626

[289] Sathyaprakash B and al E 2012 *Classical and Quantum Gravity* **29** 124013 ISSN 0264-9381 URL http://stacks.iop.org/0264-9381/29/i=12/a=124013?key=crossref.44198db7f226aee28bb644e9d3373305

[290] Bauswein A, Stergioulas N and Janka H T 2014 *Physical Review D* **90** 023002 ISSN 1550-7998 URL http://link.aps.org/doi/10.1103/PhysRevD.90.023002

[291] Bernuzzi S, Dietrich T and Nagar A 2015 (*Preprint* 1504.01764) URL http://arxiv.org/abs/1504.01764http://dx.doi.org/10.1103/PhysRevLett.115.091101

[292] Damour T, Nagar A and Villain L 2012 *Physical Review D* **85** 123007 ISSN 1550-7998 URL http://link.aps.org/doi/10.1103/PhysRevD.85.123007

[293] Hua Y and Sarkar T 1991 On SVD for estimating generalized eigenvalues of singular matrix pencil in noise *1991., IEEE International Sympoisum on Circuits and Systems* (IEEE) pp 2780–2783 ISBN 0-7803-0050-5 URL http://ieeexplore.ieee.org/lpdocs/epic03/wrapper.htm?arnumber=176121http://ieeexplore.ieee.org/document/176121/

[294] Potts D and Tasche M 2010 *Signal Processing* **90** 1631–1642 ISSN 01651684 URL http://linkinghub.elsevier.com/retrieve/pii/S0165168409004757

[295] Potts D and Tasche M 2013 *Linear Algebra and its Applications* **439** 1024–1039 ISSN 00243795 URL http://linkinghub.elsevier.com/retrieve/pii/S0024379512007665

[296] Plonka G and Tasche M 2014 *GAMM-Mitteilungen* **37** 239–258 ISSN 09367195 URL http://doi.wiley.com/10.1002/gamm.201410011

[297] Hua Y and Sarkar T 1990 *IEEE Transactions on Acoustics, Speech, and Signal Processing* **38** 814–824 ISSN 0096-3518 URL http://ieeexplore.ieee.org/lpdocs/epic03/wrapper.htm?arnumber=56027http://ieeexplore.ieee.org/document/56027/

[298] Sarkar T and Pereira O 1995 *IEEE Antennas and Propagation Magazine* **37** 48–55 ISSN 1045-9243 URL http://ieeexplore.ieee.org/lpdocs/epic03/wrapper.htm?arnumber=370583http://ieeexplore.ieee.org/document/370583/

[299] Berti E, Cardoso V, Gonzalez J A and Sperhake U 2007 *Physical Review D* **75** 124017 ISSN 1550-7998 (*Preprint* 0701086) URL http://arxiv.org/abs/gr-qc/0701086http://dx.doi.org/10.1103/PhysRevD.75.124017

[300] Thornburg J 2004 *Classical and Quantum Gravity* **21** 743–766 ISSN 0264-9381 URL http://stacks.iop.org/0264-9381/21/i=2/a=026?key=crossref.42ae08260b93c26e5ed3b56d930b84d3

[301] Dietrich T, Bernuzzi S, Ujevic M and Bruegmann B 2015 26 (*Preprint* 1504.01266) URL http://arxiv.org/abs/1504.01266

[302] Dreyer O, Krishnan B, Shoemaker D and Schnetter E 2003 *Physical Review D* **67** 024018 ISSN 0556-2821 URL http://link.aps.org/doi/10.1103/PhysRevD.67.024018

[303] Reisswig C, Bishop N T, Pollney D and Szilágyi B 2010 *Classical and Quantum Gravity* **27** 075014 ISSN 0264-9381 URL http://stacks.iop.org/0264-9381/27/i=7/a=075014

[304] Kastaun W, Ciolfi R and Giacomazzo B 2016 (*Preprint* 1607.02186) URL http://arxiv.org/abs/1607.02186

[305] White C J and Stone J M 2015 43 (*Preprint* 1511.00943) URL http://arxiv.org/abs/1511.00943

[306] Stergioulas N and Friedman J 1994 *The Astrophysical Journal* URL http://scholar.google.com/scholar?hl=en{&}btnG=Search{&}q=intitle:No+Title{#}0